UNIVERSITY OF SOUTHAMPTON

Faculty of Engineering and Physical Sciences
School of Engineering

Experimental studies on the critical current of REBCO coated conductors as a function of the magnetic field and temperature for a scaling law suitable for designing high field accelerator magnets

by

Giovanni Succi

ORCiD: 0000-0002-1729-1401

A thesis for the degree of
Doctor of Philosophy

June 2025

University of Southampton

Abstract

Faculty of Engineering and Physical Sciences
School of Engineering

Doctor of Philosophy

Experimental studies on the critical current of REBCO coated conductors as a function of the magnetic field and temperature for a scaling law suitable for designing high field accelerator magnets

by Giovanni Succi

REBCO coated conductors, or tapes, are innovative materials which are attracting major attention in the worldwide community of applied superconductivity. Their ability to work from the liquid helium temperature up to the liquid nitrogen temperature, combined with their high performance in magnetic fields, make them a potential game-changer not only in superconductivity, but also in the broader domain of electromagnetic machines. Nonetheless, the design and modelling of coils and other devices wound with REBCO tapes require an accurate knowledge of their electrical properties.

So-called scaling laws are needed to define tape properties and a thorough experimental campaign is needed to validate them. Scaling laws validated by the experimental effort are of the utmost importance for the design of coils and magnets. In this work, a formulation of an anisotropic scaling law that describes the field dependence of the critical current of REBCO tapes up to the irreversibility field and at temperatures of up to the critical temperature, is proposed. The law extends on previous formulations available in the literature.

The validation of this law is conducted by means of an experimental campaign of testing REBCO tapes from various manufacturers. Measurements of critical current were done via transport and magnetization methods at two facilities available at CERN. For the transport method, a sample holder with a 'U' shape was developed, to create a short straight region and expose tapes to a perpendicular field inside the bore of a solenoid station. Tests were conducted in liquid helium, at 4.2 K, and in magnetic fields of up to 15 T. Magnetization measurements have also been performed on small tape samples to extend the measurement range up to the critical temperature, using a vibrating sample magnetometer (VSM), in perpendicular fields of up to 10 T.

Matching of the two methods allows inferring the critical current as a function of field and temperature. The resulting scaling parameters of tapes are derived for various manufacturers. Different as well as common patterns in the temperature dependence

of the scaling parameters have been identified and a correlation with the known pinning landscapes has been discussed. The variations of the scaling law parameters and their temperature dependence could be helpful in further performance optimization, through correlation with the material science and production techniques of the different manufacturers. To conclude, the scaling law is validated for coated conductors exposed to perpendicular magnetic fields.

Contents

List of Figures

List of Tables

Declaration of Authorship

I declare that this thesis and the work presented in it is my own and has been generated by me as the result of my own original research.

I confirm that:

1. This work was done wholly or mainly while in candidature for a research degree at this University;
2. Where any part of this thesis has previously been submitted for a degree or any other qualification at this University or any other institution, this has been clearly stated;
3. Where I have consulted the published work of others, this is always clearly attributed;
4. Where I have quoted from the work of others, the source is always given. With the exception of such quotations, this thesis is entirely my own work;
5. I have acknowledged all main sources of help;
6. Where the thesis is based on work done by myself jointly with others, I have made clear exactly what was done by others and what I have contributed myself;
7. Parts of this work have been published as:

   G. Succi, A. Ballarino, S. C. Hopkins, C. Barth, and Y. Yang. Magnetic field and temperature scaling of the critical current of REBCO tapes. *IEEE Trans. Appli. Supercond., vol. 34, no. 3*, 2024

   G. Succi, A. Ballarino, S. C. Hopkins, and Y. Yang. Experimental validation of a scaling law for the critical current of commercial REBCO tapes as a function of magnetic field and temperature. *IEEE Trans. Appli. Supercond., vol. 35, no. 5*, 2025

Signed:..... Date: 27/05/2025

Acknowledgements

There are several people I would like to thank now that I have reached the end of this doctoral thesis. My first thought goes to my supervisor at CERN, Dr. Amalia Ballarino, and to Professor Yifeng Yang at the University of Southampton, who believed in me and accepted me to conduct this doctoral thesis. To Amalia, I am mostly grateful for your guidance all along the way and letting me free of exploring the subject on my own, even when I was not necessarily on the right track. To Yifeng, for making me understand how to conduct a research work, while sticking to a rigorous approach, both on the theoretical and experimental sides. I really admire the passion you both put in doing science and I am very proud to have worked with you during these four years.

Arnaud Devred has played a central role in this PhD. You made me understand the fundamental importance of experimental work in doing science and you kept caring and following the progress of my work even when you could have left. I am extremely grateful for that. The Magnet Group has been my 'home' throughout my entire time at CERN. A special thanks to Attilio Milanese for supporting my research in the two final years, and to Thierry Boutboul for the kind support with the laboratory activities.

To Simon Craig Hopkins, for the invaluable help with the VSM facility in building 163 at CERN. We managed to 'bring it back to life' and shown it is still capable of providing very accurate measurements, which eventually constitute a big chunk of this work. So many thanks for always welcoming me in your office and for the many conversations we had on the most varied topics, from the shape of flux vortices along the *ab*-planes to the more-than-sometimes delightful tennis matches.

To Christian Barth and Jerome Fleiter, for the technical discussions on many aspects of my sample holders, which helped me much while I was struggling during the second year of PhD. To Arnaud Vande Craen, who I call 'the man of providence': your help has been no less than incredible in setting back up the cryogenics of the VSM station and you were always patient to teach me everything about it from the basics. To Algirdas Baskys, who showed great interest in my work and with whom I shared many ideas on how to improve my experimental setups. To Nicolas Chritin and Pietro Rizzo, for the amazing sample holders we designed and built together, I really had a great chance of learning from your expertise!

Pierre François Jacquot, Anne Eychenne, Florian Girardot have been wonderful colleagues in the lab. Whether it was to allow me testing at any time of the day, multiple times per day, or in the weekends, your warmth and never declining optimism have

been invaluable to make me go through the difficult periods when nothing was working. Your technical support has also been very important and your experience in the field is really unrivaled.

The lab life is not always about technical work. I shared joyful conversations and coffees with Marina Malabaila, Angelo Bonasia, Simone Morisi, Alain Gharib, Florian Nicolot, Rabah Saoudi, Jean-Sebastien Denis, Julien Hurte, Marc-Philippe Careil, Aisha Saba, Norbert Gal, Josef Baumann, Julien Avronsart. With Kirtana Puthran and Joanna Kuczynska, I spent many long hours of testing, late in the evening and on weekends even. Whether it was about sharing thoughts about a steel mould or a laser glass fiber, I am happy we had those moments together.

A PhD is very different from all other academic or research work I conducted in the past. It is an extremely challenging time of life, which takes every ounce of energy from your own brain and body, pushes yourself constantly to revise your limits, and puts you in constant doubt about your abilities. I wouldn't have made it without the people that are very close to me in life.

I would like to start thanking my family. All of this wouldn't have been possible without the two people who saw me growing up and who always loved me. From the bottom of my heart, thank you to my mum and Roberto. And to my grandmother Maria, who gave me all her kindness. I also would like to mention Sauro, the real scientist of the family, for his constant support and advices.

My friends have just been incredible, they supported me and kept motivating me throughout the entire way. The list is maybe long, but I wish not to forget anybody here. To begin with, the first friends I met at CERN, who I still see in various occasions: Alexandre Louzguiti, Maxime Matras, Vera Korchevnyuk, Alessandro Cattabiani, Andrea Garcia Alonso, Victor Humbria, Dario Baffari, Jose Ferradas Troitino, Jaime Renedo Anglada, and Iole Falorio. A warm thanks to Enrico Felcini for inspiring me in pursuing a PhD while I was still a Master's student. I still share some great moments and conversations with Gianluca De Marzi, who I admire very much.

A special thanks goes to my friends back in Italy, who I grew up together with: Federico Ravagli, Riccardo Strada, Alessandra Zecchini, Mattia Venturini, Caterina Pezzi, Alessia Teresa Accoto, Cesare Ceccarelli, Sofia Orioli. And, of course, to my friends Gianni Rossi, Gianluca Mambelli, Daniele Biella, with whom we caught solar eclipses, northern lights and the beautiful southern sky!

To all the friends I met at CERN and in Geneva: Fabrizio Niccoli, Raffaello Secondo, Giulia Romagnoli, Salvatore Danzeca, Enrico Romagnoli, Sergio Di Giovannantonio, Ilenia Ferradino, Roberto Cittadini, Melissa Passari, Gianluca D'Antuono, Giancarlo D'Ago, Andrea Apollonio, Alice Moros, Antonella Chiuchiolo, and Giorgio Vallone.

How much fun we had together! And of course, to Aldo Rea, my tennis buddy, for the many rallies in basically all tennis courts around town.

One of the reasons why I enjoy CERN the most is the way people interact with and accept everybody, in spite of their different status. I would like to thank Lucio Fiscarelli, Carlo Petrone, and Christoph Wiesner for being so kind to me at all times, we shared many great coffees and lunches together. Unfortunately, not everyone who was here when I started is still with us: a special mention to Fabrizio Murtas, who gave me many previous advices in the beginning of this journey and always welcomed me at his house as a friend.

I had the opportunity to share my office with Marco Masci, a great engineer, who became also my friend. I learnt so much from your creative approach to this job! Recently, I also shared the office with Anastasija Popovic and Annika Bauerer. You are two rising stars and I wish you all the best of luck for your continuation.

And now. There is no greater emotion in mentioning three people who have been extraordinary throughout these years. Michela Lancellotti, Tessa Chiara Basso, and Marco Morrone. The more I think about it, the more I realize that this work wouldn't be here if it wasn't for the three of you. Together, we shared countless memorable moments, many of which have simply been hilarious. You have seen me through everything, you never stopped staying by my side, and you supported me in any possible way. In this sense, you have been my pillars and I couldn't wish to be more lucky to have you in my life.

To all of you, just thank you for supporting me, always. This thesis is dedicated to you.

"I didn't fail. I just found two thousand ways how not to make a lightbulb;
I only needed to find one way to make it work."
Thomas A. Edison

"When you measure what you are speaking about and express it in
numbers, you know something about it."
Lord Kelvin

"There's no supermarket where you can buy grit: you either have it or you
don't. You can have the best coach, the highest salary, and all the
motivation in the world, but when you're on the edge of exhaustion,
only your abilities will carry you through."
Marco Pantani

To my grandmother Maria,
and to all my friends.

Definitions and Abbreviations

$\vec{B}$	Magnetic flux density vector
$\vec{E}$	Electric field vector
$\vec{J}$	Current density vector
$\vec{H}$	Magnetic strength vector
$\vec{M}$	Magnetization vector
$\vec{A}$	Magnetic vector potential
$\vec{\Phi}$	Magnetic flux vector
J	Current density module
t	time
T_c	Critical temperature
B_c	Critical field
$B_{c,1}$	Lower critical field
$B_{c,2}$	Upper critical field
J_c	Critical current density
$B_{c,0}$	Critical field at zero kelvin
$B_{c,th}$	Thermodynamic critical field
E_c	Critical electric field
c_v	Volumetric specific heat
ρ	electrical resistivity
e	electron charge
m	electron mass
l_e	electron mean free path
v_F	Fermi velocity
Ψ	Wavefunction
φ	Phase
n_s	Density of superconducting charge carriers
n	Density of normal electrons
G	Gibbs free enthalpy
g	Gibbs free enthalpy density
U	internal energy
u	internal energy density
s	entropy density

α_{GL}, β_{GL}	Parameters in Ginzburg-Landau equations
λ	Magnetic penetration depth
ξ	Coherence length
$\hbar$	Planck constant
k_B	Boltzmann constant
Φ_0	Flux quantum
κ	Ginzburg-Landau parameter
F_p	Pinning force
a_0	Inter-flux line spacing
Ω_0	Hopping frequency of flux lines
R_{net}	Hopping rate
ΔW	Work spent to move a flux line
β_{visc}	Coefficient of viscous friction
B_{sat}	Saturation field in Bean critical state model
γ	Anisotropy factor of HTS materials
β, p	Parameters in Kramer's scaling
$I_{c,0}$	Critical current at zero applied field
α	Slope of Region II in the scaling law
B_0	Crossover field
q	Slope of Region III in the scaling law
b	Reduced field, expressed relative to B_{irr}
b'	Modified reduced crossover field
ω_k	Peak sharpness parameter
φ_k	Phase shift
B_ϕ	Matching field
χ^2	Least square parameter
APC	Artificial pinning centers

Chapter 1

Introduction

1.1 Historical background

The history of superconductivity began in 1911 when Heike Kamerlingh Onnes observed the abrupt drop of electrical resistance in a sample of mercury. As it often occurs in science, this discovery was made possible thanks to a number of previous remarkable achievements.

During the 19^{th} century, physicists were trying to liquefy the so-called 'permanent' gases. However, a small number of them, hydrogen, nitrogen, and oxygen resisted the efforts. In 1877, the French physicist Cailletet obtained oxygen in the liquid state at a temperature of 90.2 K, followed a few years later, in 1893, by the liquefaction of nitrogen, at 77.4 K.

In the end of the 19^{th} century, in 1898, Sir James Dewar went past beyond that point, liquefying hydrogen at only 20.4 K. In fact, he invented a double-walled vessel to contain liquid substances at low temperatures, where the gas in between the walls could be pumped to pressures lower than the atmospheric pressure. This type of vessel became the standard for low-temperature applications and it has been used up to the present day.

The final act of this story took place in 1908, when Heike Kamerlingh Onnes conducted his famous experiment to liquefy helium. The discovery of helium took place only in 1869 by astronomers, who inferred its existence by analysing the spectrum of the solar corona. Then, helium was found much later on the Earth as a gas released by certain minerals when heated up. Its liquefaction point was eventually discovered to be the lowest of all gases, 4.2 K, as observed by Onnes in his experiment of 1908.

This achievement allowed performing experiments on the electrical properties of several elements. Among these, Onnes observed that the electrical resistivity of mercury

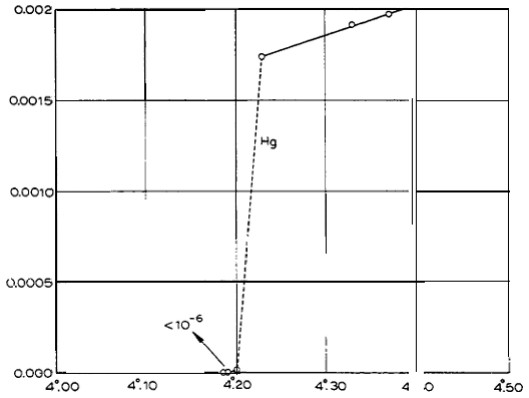

FIGURE 1.1: Discovery of the transition of mercury from the normal to the superconducting state [1].

disappeared *abruptly* at 4.2 K and he called this new state 'superconducting' [1], see Fig. 1.1. Following such a revolutionary discovery, Onnes and his team observed also the transition of tin, at 3.8 K, and lead, at 6 K.

In his Nobel lecture of 1913, Onnes already foresaw the possibility of using superconductors to build magnets:

'There is also the question as to whether the absence of Joule heat makes feasible the production of strong magnetic fields using coils without iron, for a current of very great density can be sent through very fine, closely wound wire spirals'

and as a conclusion:

'In the meantime there is plenty of work which can already be done, albeit with difficulty, in the neighbourhood of the liquefying apparatus, and which can contribute towards lifting the veil which thermal motion at normal temperature spreads over the inner world of atoms and electrons'.

Many elements have been discovered to be superconductors, see Table 1.1. Actually, some elements show a dependence of both the critical temperature, T_c, and of the critical field, B_c (we come back to these aspects later) upon the crystalline structure, such as for Hg, as reported in the table.

Element	T_c [K]	B_c [T]
Al	1.20	0.01
α-Hg	4.15	0.04
β-Hg	3.95	0.03
Nb	9.26	0.2
Sn	3.72	0.03
Ti	0.39	0.01

TABLE 1.1: Values of T_c and B_c for a few elements.

In addition, some elements like beryllium become superconducting only in the shape of thin films. This shed some light on the fact that superconductivity is a collective phenomenon determined by the structure of a given sample, rather than only by the property of isolated atoms. Another peculiar effect was that good conductors as gold, silver, and copper do not display any superconductivity, while some alloys are superconducting despite their single elements not being superconducting (such as CuS and Au_2Bi). This further supports the fact that the superconductivity is a collective phenomenon.

1.2 Meissner-Ochsenfeld effect

Superconducting materials are characterized by two distinctive properties. The first is the *absence of electrical resistivity* at temperatures below the T_c, the observation made by Onnes in 1911, shown in Fig. 1.1.

The second feature is the Meissner-Ochsenfeld effect, consisting in the *repulsion of the magnetic field lines*, namely B=0, from the inside of the material. This property cannot be deduced from the condition of infinite conductivity and is what makes the actual difference between a superconductor and a perfect (ideal) conductor. A perfect conductor is a conductor whose electrical resistivity becomes zero at zero kelvin. We distinguish between two conditions. To begin with, we consider a perfect conductor and a superconductor at a temperature below T_c (there is no T_c for a perfect conductor, which is considered to be at zero kelvin here) and the field is increased progressively from zero. This is referred as zero field cooling, ZFC. Both conductors expel the magnetic field lines to maintain the initial condition of zero field in their interior.

Then, we consider the condition of field cooling, FC, where a background field is first imposed to the two conductors and the temperature is lowered progressively. The perfect conductor just continues to be penetrated by the magnetic field lines when the temperature gets (ideally) to zero. The superconductor, instead, expels the external field from its interior when cooled below T_c. For the given reasons, a superconductor is both a perfect conductor and a diamagnetic material.

The Meissner-Ochsenfeld effect is employed to verify that a material is an actual superconductor. Fig. 1.2 shows the way this effect works: when the temperature is lowered below T_c, a superconducting material expels the field lines from its interior. To verify the argument, let us start from Ohm's law:

$$\vec{E} = \rho \vec{J} \tag{1.1}$$

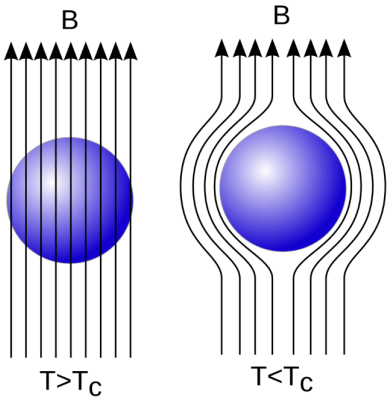

FIGURE 1.2: Magnetic field lines are expelled from the interior of a superconductor when the temperature is lowered below T_c.

where $\vec{E}$ is the electric field, ρ the resistivity, and $\vec{J}$ the current density. A zero resistivity implies no electric field in the material. Then, considering Faraday's law:

$$\vec{\nabla} \times \vec{E} = -\frac{\partial \vec{B}}{\partial t} \tag{1.2}$$

we get:

$$\frac{\partial \vec{B}}{\partial t} = 0 \tag{1.3}$$

namely the magnetic flux must remain constant in time. This implies that the final state of the sample is different if the initial condition is of zero field or rather of a non-zero field. Instead, the superconductor always expels the field from its interior. Namely, the superconductor remains in the same thermodynamic state, independent of the sequence used for cooling or applying the field. Before continuing, let us point out that the phenomenology described here is that of so-called *type-I* superconductors, the first ones to be discovered. In the following, the properties of this superconductor type are extended further. Then, *type-II* will be treated in Section 1.11.2.1.

In general, the mass of the atoms in the lattice, M, determines the frequency of vibrations in the lattice: $\Omega \sim M^{-1/2}$. Superconductivity, which is governed by the properties of the collection of electrons, is closely related to the state of the crystal lattice as well. Consequently, superconductivity results from the interaction of electrons with the lattice. Surprisingly, this is also at the origin of the usual electrical resistance, which is what made it so difficult for physicists to explain the phenomenon.

1.3 Critical parameters

Below the critical temperature, T_c, the 'effort' put in magnetic energy to expel an external magnetic field is overcome by the energy gain of the superconducting thermodynamic state. The maximum external field that can be expelled is the thermodynamic critical field, B_c, namely the field at which the material returns to the normal state. The temperature dependence of B_c is:

$$B_c = B_{c,0}\left[1 - \left(\frac{T}{T_c}\right)^2\right] \tag{1.4}$$

where $B_{c,0}$ is the critical field at zero temperature. This is also shown in Fig. 1.3. Below the red line is the Meissner state, where ρ=0 and B=0 in the inside of the superconducting material. Above the line is the normal state, instead, where $\rho > 0$.

The magnetic field in the superconductor can also be expressed in terms of the field strength, $\vec{H}$, of the external field and of the magnetization $\vec{M}$:

$$\vec{B} = \mu_0(\vec{H} + \vec{M}) \tag{1.5}$$

In the Meissner state, $\vec{B}$ = 0, therefore $\vec{M} = -\vec{H}$. Namely, the magnetization has the same value but opposite direction of the external field. Above H_c, the magnetization is zero, $\vec{M}$=0. Fig. 1.4 shows the resulting magnetization as a function of the external field strength.

Other factors are also capable of destroying the delicate superconducting state. One is the critical current density, J_c, which generates the H_c on the surface of the conductor.

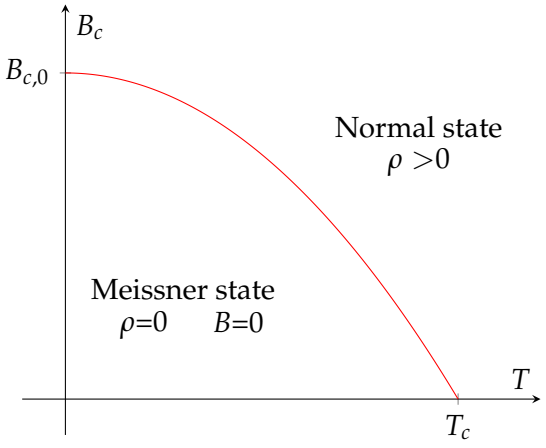

FIGURE 1.3: Critical field of type-I superconductors as a function of temperature and resulting Meissner and normal states.

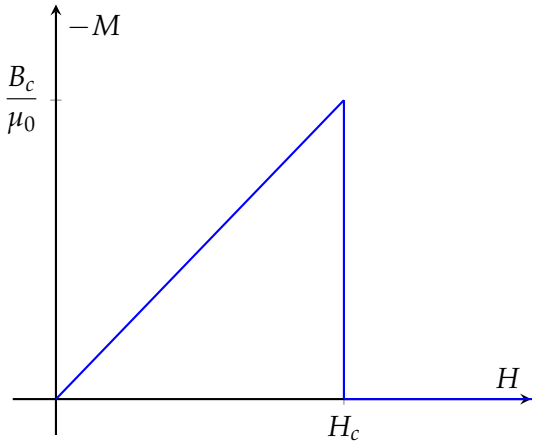

FIGURE 1.4: Magnetization of type-I superconductors as a function of the applied field.

Finally, there is also the critical frequency, f_c, which is the frequency at which photons have sufficient energy to depair the Cooper pairs, see later in section 1.6 (frequency is associated to energy by the Einstein relation, $E = h\nu$).

1.4 Heat capacity of superconductors

The transition of a material to the superconducting state has considerable impact also on its thermal properties. In particular, the specific heat 'jumps' suddenly at T_c, then it lowers below the expected values from the normal state.

The thermal conductivity in the normal state is described by the typical T^γ dependence, which decreases progressively with decreasing temperature following a parabolic shape. Below T_c, instead, the BCS theory (see also section 1.6) predicts Eq. 1.6.

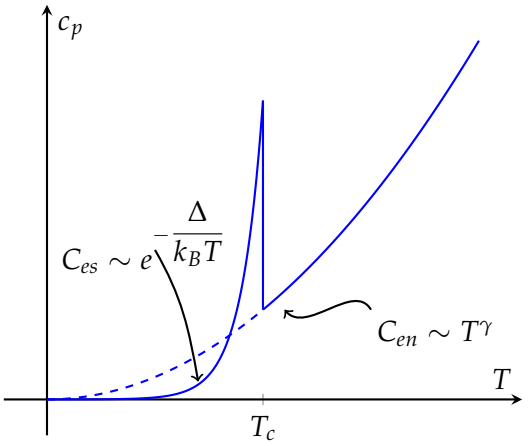

FIGURE 1.5: Specific heat of a superconductor below and above T_c.

$$c_v \propto e^{-\frac{\Delta}{k_B T}} \tag{1.6}$$

where 2Δ defines the energy gap of the material. This is the energy to spend in order to break a Cooper pair, which is in the order of a few meV (note that 1 K corresponds roughly to 12000 K); k_B in the formula is the Boltzmann constant. The energy gap is related to the T_c of the material by:

$$2\Delta = 3.5 k_B T_c \tag{1.7}$$

1.5 The isotope effect

An effect that greatly helped to progress the microscopic understanding of the nature of superconductivity is the so-called isotope effect.

In the early 1950s, the superconducting properties of samples containing different isotopes of mercury were studied. These revealed that, as the mass number M increased from 199.5 to 203.4, the T_c lowered from 4.185 K to 4.140 K. The following relationship was elaborated:

$$T_c M^{1/2} = constant \tag{1.8}$$

Electrons in a metal are very high in density ($n \sim 10^{23}$ cm^{-3}) and they behave as a gas of non-interacting particles which fills the space in between the ions of the crystalline lattice. An electric field applied to the metal makes the electrons flow in the direction of the field. At ambient temperature, the electrons interact with the lattice, giving rise to an electrical resistivity. In other words, this is the result of the *electron-phonon interaction*, which reduces progressively with decreasing temperature. Superconductivity is also the result of the interaction between electrons and phonons, however occurring in a very different way, as explained in the following section.

1.6 A quick hint into the BCS theory

The phonon contribution vanishes at zero kelvin, but a residual resistivity is observed, which is caused by the imperfections in the lattice, such as dislocations or impurities.

As a general rule, one can write that:

$$\rho(T) = \rho_i + \rho_P(T) \tag{1.9}$$

where ρ_i is the remanent resistivity given by the material impurities and ρ_P is from the phonon contribution, which is temperature dependent. From the elementary metal theory,

$$\rho_i = \frac{m v_F}{n e^2 l_e} \tag{1.10}$$

where v_F is the Fermi velocity of the electrons moving in the material (in the order of 10^6 m/s) and l_e is the electron mean free path. A high mean free path is obtained either at low temperatures or in high purity metals, for which one refers to the Residual Resistivity Ratio, RRR, namely the ratio between the resistivity at 300 K and the resistivity at 4.2 K.

Electrons in the superconducting state behave in a totally different way. They are bound in pairs and collectively act as a quantum fluid. In fact, below T_c, a conduction electron of given momentum and spin gets coupled with another electron of exact opposite momentum and spin, forming a so-called Cooper pair. The phonons, which are the elastic vibrations of the lattice of ions, allow the two electrons to be bound by an attractive force that overcomes the repulsive electromagnetic force.

Since the electrons forming a Cooper pair have opposite momenta, the net momentum of the pair is zero and the associated characteristic wavelength is infinite (due to the De Broglie relation, $\lambda = \hbar / p$, with p being the momentum). Such a wavelength does not result in scattering on the centers that scatter normal electrons. The typical distance separating the electrons in a Cooper pair can be approximated in the first order by the coherence length ξ.

In other terms, Cooper pairs are quasi-boson particles. Bosons obey the Bose-Einstein statistics, therefore they all occupy the same energy level. Instead, this is not the case with normal electrons, which are fermions and rather occupy different energy levels according to the Pauli exclusion principle.

One can then write a single wavefunction for all Cooper pairs:

$$\Psi(\vec{r}) = \sqrt{n_s(\vec{r})} e^{i\varphi(\vec{r})} \tag{1.11}$$

here, $n_s(\vec{r})$ is the density of superconducting electrons, which is the actual 'observable' quantity resulting from $\Psi(\vec{r})\Psi^*(\vec{r})$. Let us recall that, in quantum mechanics, $|\Psi(\vec{r})|^2$ is the probability of finding an electron in a point in space (Schrodinger's principle).

On the other hand, $\varphi(\vec{r})$ is the phase. Particles that are all in the same state (e.g. photons) and propagate in the same direction are described by a planar wave. The momentum of the associated particles is related to the gradient of the phase by the De Broglie relation, $\vec{p} = \hbar\vec{k}$, which can be developed into $\vec{v} = (\hbar/m)\vec{\nabla}\varphi$. Cooper pairs are also all in the same state and the gradient of the phase is a macroscopic quantity proportional to the current flowing in the superconductor, see section 1.8.

1.7 Digression on Gibbs free enthalpy

It is the purpose of this chapter to present the fundamental equations of the Ginzburg-Landau theory. These are based on the Gibbs free enthalpy of the system of superconducting charge carriers. In this section, the definition of the free enthalpy and how it is applied to both the superconducting and normal state is recalled.

Let us consider a system at a temperature T and subjected to a field strength $\vec{H}$, of module H. The equilibrium state of such a system corresponds to the minimum of the free enthalpy density, also called the Gibbs function, g. This is defined as:

$$g = u - Ts - \mu_0 MH \tag{1.12}$$

where u is the internal energy density, T is the temperature, s is the entropy density, and M is the magnetization.

If two phases co-exist together, their Gibbs functions at a particular temperature are the same. Let us examine the Gibbs functions of both the normal and the superconducting phases. To begin with, the differential form of Eq. 1.12 is:

$$dg = -sdT - \mu_0 M(H)dH \tag{1.13}$$

which expresses the variation of g as a function of the temperature variation dT and of the magnetic field variation, dH. At a fixed temperature T, one can integrate the field from H^*=0 to $H^* = H$:

$$g(T,H) - g(T,0) = -\mu_0 \int_0^H M(H^*)dH^* \tag{1.14}$$

in the normal state, with no hysteresis, $M(H)$=0, thus:

$$g_n(T,H) = g_n(T,0) \tag{1.15}$$

where the subscript n stays for the normal state. However, the superconducting state is characterized by $M(H) = -H$, which gives:

$$g_s(T,H) = g_s(T,0) + \mu_0 \frac{H^2}{2} \tag{1.16}$$

These two phases coexist at the critical field: $H = H_c(T)$,

$$g_s[T,H_c(T)] = g_n[T,H_c(T)] \tag{1.17}$$

namely the Gibbs free enthalpy density must be the same. Using Eq. 1.15 and Eq. 1.16:

$$g_s(T,H) = g_n(T,0) - \mu_0 \left[\frac{H_c^2(T)}{2} - \frac{H^2}{2} \right] \tag{1.18}$$

Therefore, the difference between the Gibbs free enthalpy density of the superconducting and normal states is made up of two terms:

1. The Gibbs free enthalpy density of *condensation*:

$$g_{s,cond} = -\mu_0 \frac{H_c^2(T)}{2} \tag{1.19}$$

   which is associated to the formation of the Cooper pairs at temperature T, per unit volume, which has negative sign.

2. The Gibbs free *magnetic* enthalpy density:

$$g_{s,mag} = \mu_0 \frac{H^2}{2} \tag{1.20}$$

   which corresponds to the increase in Gibbs free enthalpy density of the superconductor exposed to a field $\vec{H}$.

At $H = H_c$, the two Gibbs free enthalpy densities are the same, see also Fig. 1.6. Then, the superconducting state is favored for $H < H_c$.

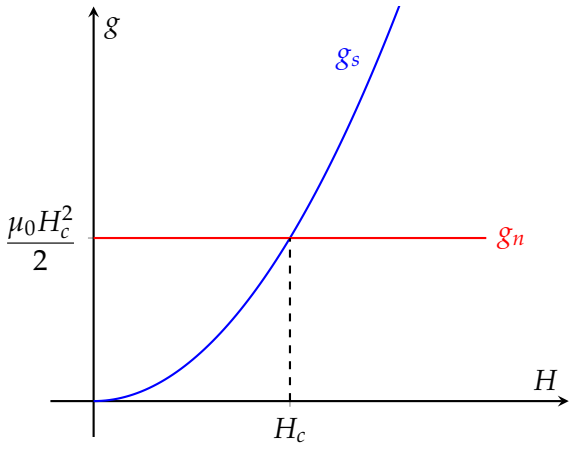

FIGURE 1.6: Gibbs free enthalpy density of the superconducting and normal states, at a specific temperature T.

1.8 Ginzburg-Landau theory

A step forward in the description of the phenomenology of superconductors was the theory of Ginzburg and Landau, sometimes also referred to as the GLAG theory, from Ginzburg, Landau, Abrikosov, and Gor'kov. The content of this chapter has been extracted from [3] and [2].

The reasoning behind the GLAG theory is that the transition from the normal to the superconducting state in the absence of a magnetic field is a second-order phase transition, for which Landau had already developed a theory. In particular, the theory requires a parameter (called the *order parameter*) to vary continuously from zero at T_c up to the value of 1 at T=0. The order parameter is assumed to be the wavefunction $\Psi(\vec{r})$ of the superconducting charge carriers, defined as:

$$\Psi(\vec{r}) = |\Psi(\vec{r})|e^{i\varphi(\vec{r})} \tag{1.21}$$

In fact, this is characterized by the following properties:

1. The modulus, $|\Psi\Psi^*| = |\Psi(\vec{r})|^2$, is interpreted as the density of superconducting charge carriers, n_s.
2. The phase, $\varphi(\vec{r})$ is proportional to the supercurrent that flows in the material below T_c.
3. $\Psi \neq 0$ in the superconducting state, but it is zero in the normal state.

Ginzburg and Laudau suppose the presence of superconducting charge carriers in the material, whose density is n_s, and of normal electrons, whose density is $n - n_s$, n being

the overall density of electrons. The Ginzburg-Landau theory extends Eq. 1.18 under the assumption that Ψ can vary in space, see Eq. 1.22.

$$g_s(T,H) = g_n(T) + \alpha_{GL}|\Psi|^2 + \frac{1}{2}\beta_{GL}|\Psi|^4 + \frac{1}{2m}\left|\left(-i\hbar\nabla - 2e\vec{A}\right)\Psi\right|^2 + \frac{1}{2}\left(\vec{H}_a - \vec{H}_i\right)^2 \tag{1.22}$$

where $\hbar$ is the reduced Planck constant. Only for Ψ=0, the Gibbs function of the superconducting state is equal to that of the normal state, $g_s = g_n$. Below T_c, $g_s < g_n$ so that $\alpha_{GL} < 0$ and $\beta_{GL} > 0$. Above T_c, both α_{GL}, β_{GL} >0 and $g_s > g_n$.

The two terms containing $|\Psi|^2$ and $|\Psi|^4$ account for the difference between superconducting charge carriers and normal charge carriers. Instead, the last two terms account for the Meissner effect. Let us note, in particular, that $\left(\vec{H}_a - \vec{H}_i\right)$ is the overall field given by the applied field and the internal field to the superconductor.

1.8.1 Ginzburg-Landau equations

This section is inspired from [2] and [31]. Eq. 1.22 takes into consideration that the order parameter, $\Psi(\vec{r})$, actually varies spatially. The order parameter and the vector potential in Eq. 1.22 determine the thermodynamic and electrodynamic properties of the superconductor, however they remain unknown. To derive them, one minimizes the Gibbs free enthalpy relative to both, obtaining:

$$\alpha_{GL}\Psi + \beta_{GL}|\Psi|^2\Psi + \frac{1}{2m}(-i\hbar\nabla - 2e\vec{A})^2\Psi = 0 \tag{1.23}$$

$$\vec{J}_s = \vec{\nabla}\times\vec{H} = -\frac{i\hbar e}{m}(\Psi^*\vec{\nabla}\Psi - \Psi\vec{\nabla}\Psi^*) - \frac{4e^2}{m}|\Psi|^2\vec{A} \tag{1.24}$$

These are the two Ginzburg-Landau equations and they should be solved simultaneously. The first returns the order parameter (wavefunction), whereas the second returns the supercurrent flowing in the superconductor.

1.8.1.1 Derivation of the coherence length

Considering the equilibrium value of the wavefunction sufficiently far away from any boundary, and calling it Ψ_∞, then the following relation holds: $n_s = |\Psi_\infty|^2$. Eq. 1.23 can now be normalized using $\psi = \Psi/\Psi_\infty$.

$$\alpha_{GL}\psi|\Psi_\infty| + \beta_{GL}|\psi|^2\psi|\Psi_\infty|^3 + \frac{1}{2m}\Big(-i\hbar\nabla - 2e\vec{A}\Big)^2\psi|\Psi_\infty| = 0 \tag{1.25}$$

At equilibrium and in the absence of fields, $g_s\big(|\Psi_\infty|\big)^2$ reaches a minimum [2]. From the condition $dg_s/d|\Psi_\infty|^2 = 0$, one gets $\beta_{GL}|\Psi_\infty|^2 = -\alpha_{GL}$. Then,

$$\alpha_{GL}\psi - \alpha_{GL}|\psi|^2\psi + \frac{1}{2m}\Big(-i\hbar\nabla - 2e\vec{A}\Big)^2\psi = 0 \tag{1.26}$$

Dividing by α_{GL} and re-ordering:

$$\frac{\hbar^2}{2m\alpha_{GL}}\Big(-i\nabla - 2\frac{e}{\hbar}\vec{A}\Big)^2\psi + \psi - |\psi|^2\psi = 0 \tag{1.27}$$

A new parameter comes out of these equations,

$$\xi^2(T) = \frac{\hbar^2}{2m|\alpha_{GL}|} \tag{1.28}$$

this is called *coherence length* and it expresses the length over which the order parameter $\Psi(\vec{r})$ varies in presence of a perturbation introduced at some point in the material.

1.8.1.2 Proof of flux quantization

Let us now normalize the second G-L equation, Eq. 1.24:

$$\vec{J}_s = -\frac{i\hbar e|\Psi_\infty|^2}{m}(\psi^*\vec{\nabla}\psi - \psi\vec{\nabla}\psi^*) - \frac{4e^2}{m}\vec{A}|\psi|^2|\Psi_\infty|^2 \tag{1.29}$$

recalling that $|\Psi_\infty|^2 = n_s$ and introducing the so-called London penetration depth, $\lambda_L = \sqrt{m/(\mu_0 n_s e^2)}$, we get:

$$\vec{J}_s = -\frac{i\hbar}{\mu_0\lambda_L^2 e}\big(\psi^*\vec{\nabla}\psi - \psi\vec{\nabla}\psi^*\big) - \frac{4}{\mu_0\lambda_L^2}|\psi|^2\vec{A} \tag{1.30}$$

We assume: $\psi = \psi_0 e^{i\varphi}$, then $(\psi^*\vec{\nabla}\psi - \psi\vec{\nabla}\psi^*) = 2i\psi_0^2\vec{\nabla}\varphi$,

$$\vec{J}_s = \frac{2\hbar}{\mu_0\lambda_L^2 e}\psi_0^2\vec{\nabla}\varphi - \frac{4}{\mu_0\lambda_L^2}\psi_0^2\vec{A} \tag{1.31}$$

reordering:

$$\vec{J}_s = \frac{2\psi_0^2\hbar}{\mu_0\lambda_L^2 e}\left(\vec{\nabla}\varphi - \frac{2e}{\hbar}\vec{A}\right) \tag{1.32}$$

Deep inside the superconductor, $\vec{J}_s = 0$, meaning the term between brackets in the previous expression is also zero. Then, for a quantity like $\vec{A}$, the magnetic vector potential, we apply the circulation and thus get the flux, which is the actual measurable quantity:

$$\oint_\Gamma \vec{\nabla}\varphi \cdot d\vec{l} = \frac{2e}{\hbar}\oint_\Gamma \vec{A}\cdot d\vec{l} \tag{1.33}$$

Using Stokes' theorem, the right-hand side is:

$$\frac{2e}{\hbar}\oint_\Gamma \vec{A}\cdot d\vec{l} = \frac{2e}{\hbar}\int_S \left(\vec{\nabla}\times\vec{A}\right)\cdot d\vec{S} \tag{1.34}$$

$$= \frac{2e}{\hbar}\int_S \vec{B}\cdot d\vec{S} \tag{1.35}$$

$$= \frac{2e}{\hbar}\Phi \tag{1.36}$$

whereas the left-hand side can only be a multiple of 2π:

$$\oint_\Gamma \vec{\nabla}\varphi \cdot d\vec{l} = 2\pi n \tag{1.37}$$

Putting everything back together:

$$2\pi n = \frac{2e}{\hbar}\Phi \tag{1.38}$$

namely:

$$2\pi n = \frac{2e}{\hbar}\Phi = \frac{\Phi}{\Phi_0} \tag{1.39}$$

meaning that the flux is the multiple of a fundamental quantity:

$$\Phi_0 = \frac{\hbar}{2e} = 2.07\cdot 10^{-15}\ Wb \tag{1.40}$$

The quantization of flux was confirmed experimentally in 1970 [32].

1.9 Magnetic penetration depth and coherence length

The Meissner effect is a characteristic feature of superconductors and acts in a way to prevent an external field from entering the material. Nevertheless, the drop in the magnetic field takes place over a layer of finite thickness below the surface of the superconductor:

$$B(u) = B_0 e^{-\frac{u}{\lambda}} \tag{1.41}$$

The thickness of this layer is λ, the magnetic penetration depth. The distance is expressed as u. Supercurrents (or superfluid currents) flow in such a layer and generate the magnetization that opposes the external field. The coherence length, ξ, also appears in the Ginzburg-Landau equations as the length over which the order parameter changes. A simplistic view attributes it to the mean distance between the electrons in a Cooper pair. In fact,

$$n_s(u) = n_{s,\infty}\left(1 - e^{-\frac{u}{\xi}}\right) \tag{1.42}$$

Type-I superconductors are characterized by $\xi > \lambda$. Fig. 1.7 shows the spatial variation of both quantities from the material surface, where the distance is expressed as u. Table 1.2 reports values of λ and ξ for a few superconductors.

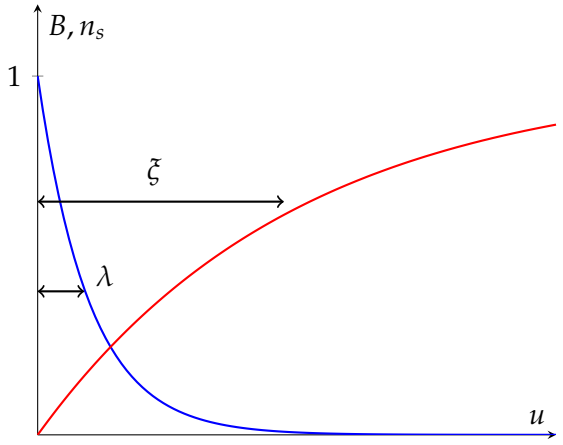

FIGURE 1.7: Field penetration (in blue) and coherence length (in red) in a type-I superconductor.

Compound	T_c [K]	$B_{c,2}$ [T]	λ [nm]	ξ [nm]
Al	1.1	0.02	50	1600
Nb	9.2	0.2	40	38
Nb-Ti	9.5	14.5	60	45
Nb_3Sn	18.0	30	80	3.5
$La_{1-x}Sr_xCuO_4$	38	$\sim$65	250	1.5
$YBa_2Cu_3O_{7-\delta}$	92	$\sim$120	400	1

TABLE 1.2: Penetration depth and coherence length of a few superconductors.

1.10 Ginzburg-Landau parameter

As introduced previously in section 1.11.2.1, the Ginzburg-Landau parameter, κ, is defined as the ratio of the magnetic penetration length and the coherence length.

$$\kappa = \frac{\lambda}{\xi} \tag{1.43}$$

which is characteristic of a given superconductor and does not depend on temperature nor field. This parameter is $\kappa < 1/\sqrt{2}$ for type-I superconductors and $\kappa > 1/\sqrt{2}$ for type-II superconductors, which are discussed in the following section.

1.11 Types of superconductors

1.11.1 Type-I superconductors

The early discovered superconducting materials belong to the so-called *type-I* category of superconductors, since they are characterized by the pure Meissner effect. Their features have already been described in the previous sections.

1.11.2 Type-II superconductors

Another type of superconductors have been discovered over the years. These are *type-II* superconductors and behave quite differently with respect to type-I superconductors. Just as a type-I superconductor, a type-II superconductor displays the pure Meissner state up to $B_{c,1}$, which is now called the lower critical field. Above $B_{c,1}$, the G-L theory foresees the spontaneous nucleation of microscopic vortices in the material. These vortices are interfaces between the superconducting bulk and cores of normal material. The following section is dedicated to the explanation for such difference.

1.11.2.1 Surface energy at the interface of normal and superconducting states

The previous expression, Eq. 1.18, is not fully realistic, since the underlying assumption is that the the superconducting region starts at the material surface. In fact, the magnetic field in the material vanishes from the surface, at B_0, as expressed in eq. 1.41:

$$B(u) = B_0 e^{-\frac{u}{\lambda}}$$

according to the magnetic penetration depth, λ. Then, one should define a *surface Gibbs free enthalpy density*, corresponding to the difference between the actual Gibbs free enthalpy and the previous Gibbs free enthalpy density, Eq. 1.16:

$$g_s^{mag,surf} = -\int_0^\infty \mu_0 \frac{H^2}{2} e^{-\frac{u}{\lambda}} du = -\mu_0 \lambda \frac{H^2}{2} \tag{1.44}$$

which accounts for the decrease in the magnetic enthalpy density close to the surface.

Let us now switch into considering the superconducting electrons. Their density does not jump from zero to the bulk value, call it $n_{s,\infty}$, but rather as described in Eq. 1.42:

$$n_s(u) = n_{s,\infty}\left(1 - e^{-\frac{u}{\xi}}\right)$$

which occurs over the length scale corresponding to ξ. Consequently, also the Gibbs free enthalpy density of condensation is reduced close to the surface, being:

$$g_s^{cond,surf} = \int_0^\infty \mu_0 \frac{H_c^2}{2} e^{-\frac{u}{\xi}} du = \mu_0 \xi \frac{H_c^2}{2} \tag{1.45}$$

Let us note that this surface quantity is positive. We can now sum up Eq. 1.44 and 1.45, giving the expression below and Fig. 1.8.

$$g_s^{surf} = -\mu_0 \left(\lambda \frac{H^2}{2} - \xi \frac{H_c^2}{2}\right) \tag{1.46}$$

The sign of this expression depends on the so-called Ginzburg-Landau parameter, $\kappa = \lambda/\xi$, giving:

$$\begin{cases} g_s^{surf} < 0, \quad if \;\; H > \dfrac{H_c}{\sqrt{\kappa}} \\ \\ g_s^{surf} > 0, \quad if \;\; H < \dfrac{H_c}{\sqrt{\kappa}} \end{cases} \tag{1.47}$$

To ensure $g_s^{surf} < 0$, the flux penetrates the material. The two vertical panels in Fig. 1.8 are for $\xi > \lambda$, typical of type-I superconductors (left), and $\lambda > \xi$ of type-II superconductors (right). In both panels, the condensation energy is negative and penetrates the material according to ξ, whereas the magnetic expulsion energy is positive and varies according to λ.

In the first case, the loss in condensation energy is smaller than the gain in magnetic expulsion energy (lower panel, on the left). Therefore, the resulting so-called *wall energy* must be provided to the material. The opposite is for the second case, where the *wall energy* is actually negative. When this occurs, thermodymically the system would tend to create as many domains as possible and minimize the energy. This is the root cause for the nucleation of vortices and thus for the partial diamagnetism resulting in the Abrikosov lattice (see later). In fact, one of the great successes of the Ginzburg-Landau theory was the prediction of the vortex state by Abrikosov.

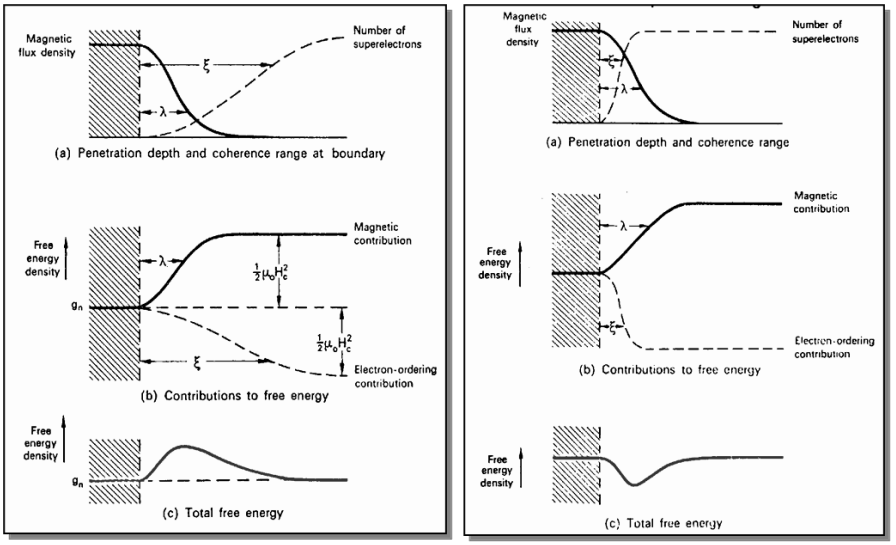

FIGURE 1.8: Spatial variation of the expulsion energy, here indicated as ε_B, and of the condensation energy, ε_C, per unit volume at the boundary, for both type-I (left) and type-II (right) superconductors. Credits: [2]

Therefore, we have two different thermodynamic regimes:

1. $\xi > \lambda$: the entire bulk is free of energy, which gives the Meissner effect.

2. $\xi < \lambda$: the flux penetrates the material and it is energetically favorable to have cores in the normal state. The primary effect of the minimization of energy is for the superconductor being more stable when the flux penetrates the material. The secondary effect is the nucleation of flux vortices.

Fig. 1.9 shows the resulting field and superconducting electrons distribution across a vortex flux line. A few early works [33], [34] proved that this is preferred way to maximize the surface to volume ratio of the normal regions, rather than, e. g. thin sheets. As shown in section 1.8.1, the flux is in the form of vortices which all carry the same flux:

$$\Phi_0 = \frac{h}{2e} = 2.067 \cdot 10^{-15}\ Wb \tag{1.48}$$

The density of vortices increases as the external field increases, until filling the entire material. This occurs at the upper critical field, $B_{c,2}$. Fig. 1.10 illustrates the evolution from the Meissner state ($B < B_{c,1}$), to the mixed state (between $B_{c,1} < B < B_{c,2}$), and the normal state ($B > B_{c,2}$). Fig. 1.11 shows the resulting phase diagram, where the so-called mixed state occupies the vast majority of the area below the critical surface. In this way, the material withstands very high applied fields, which can go even above 150 T in high temperature superconductors. The resulting magnetization is shown in Fig. 1.12. Above $B_{c,1}$ ($H_{c,1}$), the magnetization decreases progressively due to the penetration of vortices and it finally reaches zero at $B_{c,2}$.

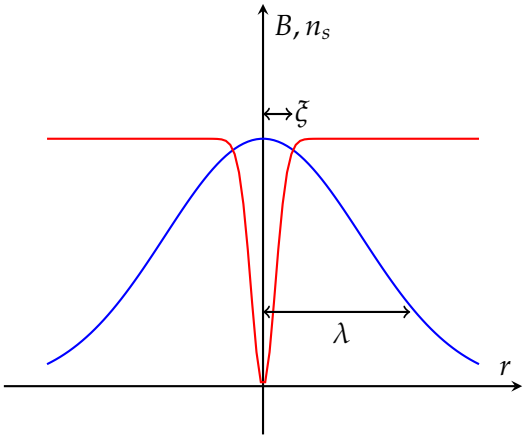

FIGURE 1.9: Field distribution around a vortex (in blue), for which the characteristic length is λ. The vortex has diameter ξ (in red). In the center of the vortex, the density of Cooper pairs is zero.

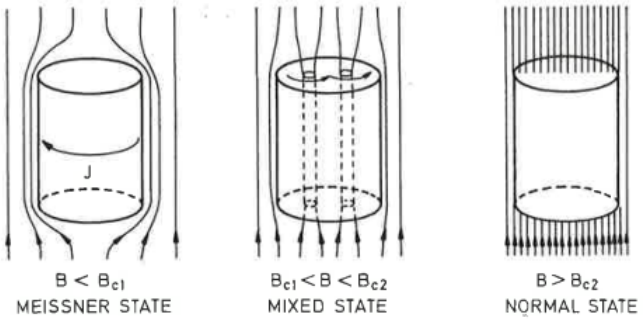

FIGURE 1.10: Flux penetration below $B_{c,1}$ on the left, in the mixed state between $B_{c,1}$ and $B_{c,2}$ at the center, and above $B_{c,2}$ on the right (from [3], referring to Decroux and Fischer, 1989).

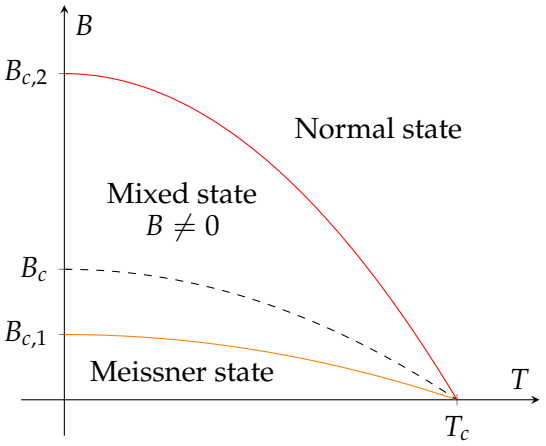

FIGURE 1.11: Upper and lower critical fields of type-II superconductors as a function of temperature and related states.

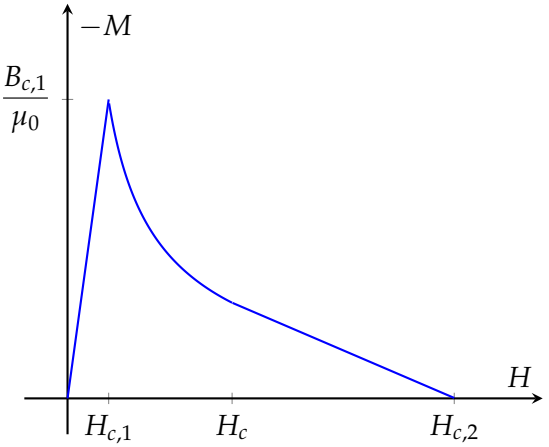

FIGURE 1.12: Magnetization of type-II superconductors as a function of field.

1.12 Further discussion on type-II superconductors

1.12.1 Lower critical field, $B_{c,1}$

Above $B_{c,1}$, it is energetically convenient for a type-II superconductor to let the external field enter the material in the form of flux tubes, rather than maintaining the entire bulk in the Meissner state. At $B_{c,1}$, vortices are far apart from each other, being at a distance of the order of λ. An expression for $B_{c,1}$ is derived accounting for the variation of the Gibbs free enthalpy when a density n of vortices enters the material. Vortices are far apart at this stage, therefore one can omit their interaction:

$$\Delta G = nU_v - BH \tag{1.49}$$

where U_v is the magnetic energy of a vortex, given by the sum of the magnetic field energy and of the kinetic energy of the supercurrents:

$$U_v = \int_V \frac{1}{2}\mu_0(h^2 + \lambda^2 J^2)dV \tag{1.50}$$

which is:

$$U_v = \frac{1}{4\pi\mu_0}\frac{\Phi_0^2}{\lambda^2} ln\frac{\lambda}{\xi} \tag{1.51}$$

The field in the material is just $B = n\Phi_0$, so:

$$\Delta G = B\left(\frac{U_v}{\Phi_0} - H\right) \tag{1.52}$$

The variation in the Gibbs free enthalpy must be negative for the vortices to enter the material:

$$H \geq H_{c,1} = \frac{U_v}{\Phi_0} \tag{1.53}$$

using Eq. 1.51, we derive:

$$B_{c,1}(T) = \frac{1}{4\pi}\frac{\Phi_0}{\lambda^2(T)} ln(\kappa) \tag{1.54}$$

For type-II superconductors, $B_{c,1}$ becomes very small.

1.12.2 Upper critical field, $B_{c,2}$

In simple terms, $B_{c,2}$ corresponds to the field at which the material is entirely filled with vortices, namely that their distance is equal to the vortex radius, ξ. The Ginzburg - Laudau theory provides some useful expressions relating the important quantities of superconductors. The first is:

$$B_c(T)\lambda(T)\xi(T) = \frac{\Phi_0}{2\pi\sqrt{2}} \tag{1.55}$$

For type-II superconductors, the upper critical field is related to the coherence length by the expression:

$$B_{c,2}(T) = \frac{\Phi_0}{2\pi}\frac{1}{\xi^2(T)} \tag{1.56}$$

considering Eq. 1.54 and 1.55, we have:

$$B_{c,1}B_{c,2} = B_c^2\, ln(\kappa) \tag{1.57}$$

The difference between type-I and type-II superconductors is explained in terms of the minimization of energy. In fact, it takes a considerable amount of enthalpy to completely expel the flux from the material interior in a type-I superconductor. In type-II superconductors, small cylinders are created, inside which superconductivity is destroyed. This costs enthalpy:

$$(G_s - G_n)\times \text{ Volume of the cylinder}$$

namely:

$$\frac{B_c^2}{2\mu_0\xi^2}d \tag{1.58}$$

However, the enthalpy gain is given by:

$$\frac{B^2}{2\mu_0\lambda^2}d \tag{1.59}$$

Consequently, the creation of vortices is favourable if $\lambda >> \xi$, or $\kappa >> 1$, explaining why type-I and type-II superconductors are so different.

1.12.3 Depairing current density

There is a limit current density the material can sustain while remaining in the superconducting state, called the depairing critical current. In fact, a current flowing in a superconductor carries energy, in a similar way that does a magnetic field. This is given by:

$$E_{kin} = \frac{1}{2} m v_s^2 n_s \tag{1.60}$$

which is just the kinetic energy of a charge multiplied by the density of charges. Considering that $\vec{J} = n_s e \vec{v}_s$, we have:

$$E_{kin} = \frac{1}{2} \frac{m}{n_s e^2} J^2 = \frac{1}{2} \mu_0 \lambda^2 J^2 \tag{1.61}$$

Clearly, this energy (positive) contrasts the binding energy of the Cooper pairs (negative). The energy gained with the superconducting state must remain higher than this kinetic energy. The limit current density, $J_{c,lim}$, is the current that gives a field B_c in the conductor, which is associated to an energy density $B_c^2/2\mu_0$.

Therefore, $J_{c,lim} = B_c/\mu_0\lambda$. The Ginzburg-Landau theory gives a similar result, just with a different numerical factor in front. In conventional superconductors, $B_c \sim 0.1$ T and $\lambda \sim 100$ nm, therefore

$$J_c \sim 10^{12} \frac{A}{m^2} = 10^6 \frac{A}{mm^2}$$

which is the maximum critical current density to be expected in conventional type-II superconductors in the case where vortices could be pinned up to filling the entire material.

1.13 Vortex pinning

The Abrikosov state is the result of a magnetic field applied to a type-II superconductor. Yet, an issue rises as soon as a current is injected in the superconductor. Given $\vec{J}$ the current density, a flux vortex is subjected to a lateral Lorentz force per unit length:

$$\vec{f}_L = \vec{J} \times \vec{\Phi}_0 \tag{1.62}$$

which, over the entire material, is a force per unit volume (considering n as a surface density):

$$\vec{F}_L = \vec{J} \times n\vec{\Phi}_0 \tag{1.63}$$

The material displays no dissipation until the Lorentz force surpasses the average pinning force density, $\vec{F}_p > \vec{F}_L$. In particular, one has:

$$\vec{F}_p = \vec{J}_c \times \vec{B} \tag{1.64}$$

Namely, the critical current density, J_c, is the current producing a Lorentz force that overcomes the pinning force. Once this happens, the displacement of vortices cuts the flux lines thus giving an electric field:

$$\vec{E} = \frac{d\left(n\vec{\Phi}\right)}{dt} \tag{1.65}$$

and a voltage. As shown in section 1.13.1 for the flux flow, $\vec{E}$ is along the same direction as $\vec{J}$, thus producing a dissipation as $\vec{E} \cdot \vec{J}$, which is equivalent to a resistivity.

Theoretically, the resulting critical currents in type-II superconductors are very weak. To surmount such an issue, the motion of vortices must be obstructed, which is achieved by vortex (or flux) pinning.

Vortex pinning consists in adding defects, such as inclusions or impurities in the superconducting material. These are normal regions in the material that act as potential holes, attracting vortices and counterbalancing the Lorentz force. The higher the pinning potential (i. e. the deeper the hole), the higher the transport current that can flow in the material. Efficient inclusions are typically of size comparable to ξ, the coherence length. Let us recall that the creation of vortices keeps the magnetic energy smaller than the condensation energy, so that the overall free energy of the mixed state remains thermodynamically more stable than the normal state up to even very high magnetic fields.

Type-II superconductors are either 'soft' or 'hard'. Hard superconductors are characterized by strong pinning which holds the flux vortices in position. These are the actual relevant materials for applications. They reach extremely high current densities, J_c, in the order of 10^3 A/mm^2 in Nb-Ti and Nb_3Sn and even up to 10^4 - 10^5 A/mm^2 in high temperature superconductors.

One can distinguish three pinning regimes:

- *Flux flow*. The Lorentz force overcomes the pinning force and $J > J_c$. The flux line lattice moves and one has dissipation inside the material, which is linear in B and resembles a normal state resistivity.
- *Hysteresis*. The pinning is stronger than the Lorenz force, therefore $J < J_c$ and the material is in the mixed state. The flux is trapped inside the material during a magnetic cycle, causing the hysteretic behavior. The amplitude of the cycle can be used to derive the J_c.
- *Flux creep*. If J is slightly lower than J_c and the temperature is sufficiently high, thermal fluctuations allow the flux vortices to move. The resistivity is not ohmic and depends on temperature.

In the following, we analyze these regimes in detail.

1.13.1 Flux flow

Let us consider a single flux vortex. The Lorentz force acting on it per unit length is given by Eq. 1.62. The mechanical balance on the vortices moving inside the material at constant velocity can then be written as the vectorial sum of the Lorentz and viscous forces. In this regime, the Lorentz force is considerably higher than the pinning force, so it can be neglected.

$$\vec{F}_L + \vec{F}_{visc} = \vec{0} \tag{1.66}$$

Namely:

$$\vec{J} \times \vec{B} - \beta_{visc}\vec{v} = \vec{0} \tag{1.67}$$

Reversing:

$$\vec{v} = \frac{\vec{J} \times \vec{B}}{\beta_{visc}} \tag{1.68}$$

where β_{visc} is the coefficient of viscous friction, variable depending on the vortex velocity. Let us suppose, for example, that the field generated by the flux vortices is oriented along x, $\vec{B} = B\hat{e}_x$, and that it has a non-uniform distribution along z: $dB/dz\ \hat{e}_z$, see Fig. 1.13. The resulting effect is a current density along the positive y-axis.

Applying Ampere's law:

$$\vec{\nabla} \times \vec{B} = \mu_0 \vec{J} \tag{1.69}$$

The LHS is:

$$\vec{\nabla} \times \vec{B} = \frac{dB}{dz} \hat{e}_y \tag{1.70}$$

Therefore:

$$\vec{J} = J_y \hat{e}_y = \frac{1}{\mu_0} \frac{dB}{dz} \hat{e}_y \tag{1.71}$$

The velocity in Eq. 1.68 results to be:

$$\vec{v} = -\frac{JB}{\beta_{visc}} \hat{e}_k \tag{1.72}$$

The electric field for negative charges is:

$$\vec{E} = \vec{B} \times \vec{v} \tag{1.73}$$

Substituting Eq. 1.68 and re-ordering:

$$\vec{E} = \frac{B^2}{\beta_{visc}} \vec{J} \tag{1.74}$$

Therefore, the motion of vortices corresponds to the generation of an electric field that is oriented in the same direction of the current. In particular, vortices 'leave' from the bottom and and 're-appear' from the top, maintaining the same macroscopic distribution seen in Fig. 1.13.

The previous equation resembles an Ohm's law: $\vec{E} = \rho \vec{J}$, where:

$$\rho = \frac{B\Phi_0}{\beta_{visc}} \tag{1.75}$$

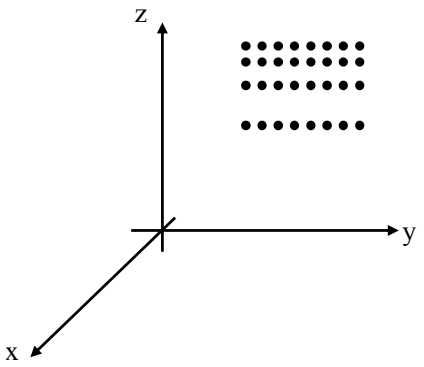

FIGURE 1.13: Non-uniform distribution of flux vortices, inducing an electric field and dissipation in the superconductor.

At $B_{c,2}$, we find:

$$\rho_n = \frac{B_{c,2}\Phi_0}{\beta_{visc}} \tag{1.76}$$

such that

$$\rho = \rho_n \frac{B}{B_{c,2}} \tag{1.77}$$

1.13.2 Hysteresis

The most important case is for $J < J_c$. As it was remarked above, flux vortices are subjected to the Lorentz force when a current flows in the superconducting layer, which leads to dissipation. As a result, J_c values are very low for soft type-II superconductors. To increase J_c, the solution is to disperse normal conducting regions of size comparable to ξ, such that flux vortices are pinned to their potential wells.

Pinning centers have the property to trap the magnetic flux inside the material even when the external magnetic field is switched off. This phenomenon is known as *hysteresis* and is very important in superconductors. A relatively simple way to describe hysteresis is the Bean critical state model.

1.13.2.1 The Bean critical state model

The first attempt to understand the irreversibility of the magnetization curves in type-II superconductors has been performed by Bean [35], who developed a simple model to deduce the critical current density in the superconductor. The content of this section is extracted from [36].

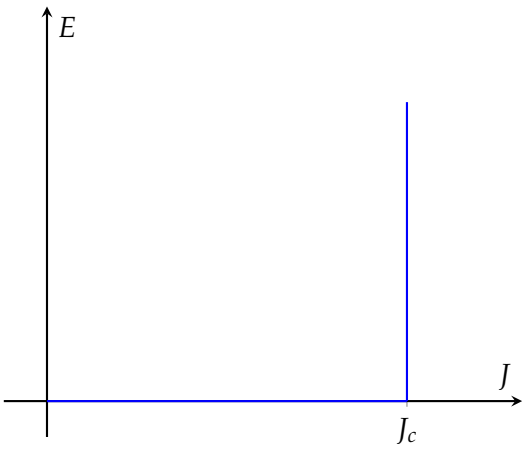

FIGURE 1.14: At J_c, the electric field jumps to an infinite value in Bean's critical state model.

The Bean model makes two basic assumptions:

1. There exists a limit value of J that the superconductor can carry, called the critical current density, J_c.
2. Any electric field in the material (no matter how small) induces the circulation of the full J_c, see Fig. 1.14.

These two hypotheses remain valid in any critical state model, which differentiate according to the magnetic field dependence of the J_c. An immediate consequence of the assumption that J_c is finite is diffusion and dissipation in the material.

We can write:

$$J(t) = \begin{cases} +J_c, & if\ \exists\ t' < t; E(t') > 0\ then\ \forall t'' \geq t', E(t'') \geq 0 \\ -J_c, & if\ \exists\ t' < t; E(t') < 0\ then\ \forall t'' > t', E(t'') \leq 0 \\ 0, & if\ E(t') = 0\ \forall t' \leq t \end{cases} \tag{1.78}$$

considering t as the present moment. Then, the two main descriptions are:

- Bean's model: J_c is constant, i.e. independent of the field.
- Kim's model: $J_c(B) = J_{c,0}/(1 + B/B_0)$

As a starting point, the Bean critical state model defines a saturation field, given as: $B_{sat} = \mu_0 J_c a$. The magnetization saturates above B_{sat} and remains constant up to the inversion point.

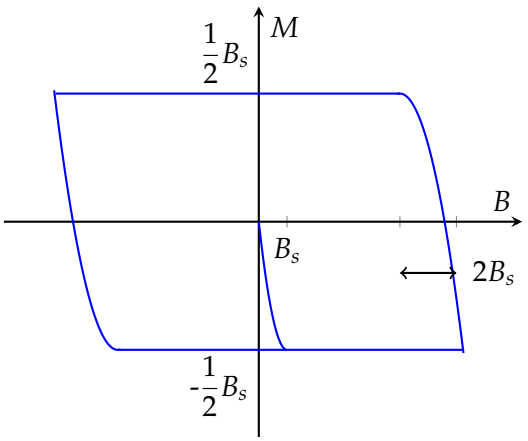

FIGURE 1.15: Magnetic hysteresis cycle resulting from Bean's model. B_s indicates the saturation field.

In the general case:

$$\mu_0 M = \frac{1}{2} B_{sat} \left[2\frac{\Delta B}{B_{sat}} - 2\left(\frac{\Delta B}{B_{sat}}\right)^2 - 1 \right] \tag{1.79}$$

This last formula is valid until $\Delta B \leq 2B_{sat}$. At inversion, the curve goes backwards and it stays constant until the next inversion, see also Fig. 1.15. This corresponds to the magnetization cycle, similarly to the case of traditional materials, which is also why the term 'hysteretic' has been adopted for superconductors as well.

The Bean model predicts that $M(B)$ has a wide hysteresis loop, which is proportional to the pinning strength and that it is directly related to the J_c, which is independent of the applied field. Here, we would like to mention that, in the more general case, the J_c is actually field dependent and the resulting magnetization plot changes. To provide

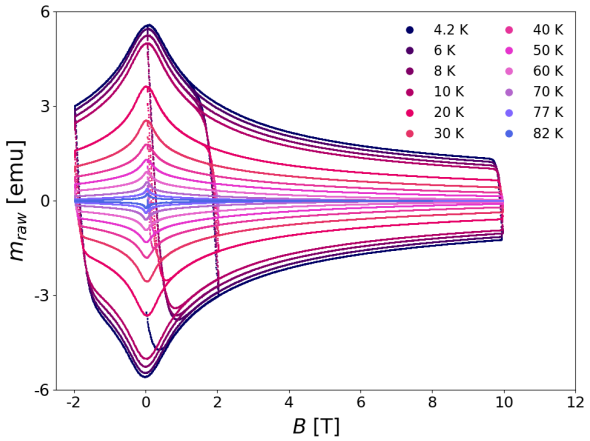

FIGURE 1.16: Magnetic hysteresis cycles for a tape of Shanghai Superconductor Technology from 4.2 K up to 82 K.

an example, Fig. 1.16 shows the measured magnetic cycle of a REBCO (RE: rare-earth, B: barium, C: copper, O: oxygen) tape tested for the scope of this work, from 4.2 K up to 82 K, see later in chapter 5. The measured magnetic moment, expressed in emu, is proportional to the J_c flowing in the superconducting layer. This justifies the cycles becoming progressively smaller with increasing temperature.

In the Appendix, the calculations for the Bean model in the case of the parallel slab geometry as well as the Brandt theory for the perpendicular strip geometry are derived and discussed in depth.

1.13.3 Flux creep

The regime of flux flow, corresponding to the collective detachment of flux lines being at the origin of strong dissipation in the material, is not the only phenomenon inducing losses. An additional source of losses are thermal fluctuations of the vortex lines that allow them to 'jump' from their pinning energy barriers. This is a local (non-collective) motion called *flux creep*.

The energy barrier holding a flux vortex in position is [37]:

$$U_0(T=0,B) = J_c(T=0,B)BV_c a_0 \tag{1.80}$$

It is expressed at zero kelvin, since at this temperature U_0 is directly related to the J_c. The energy is obtained from the force density, $J_c B$, multiplying by the flux line volume, V_c, and by the local displacement, a_0. In particular, a_0 corresponds to the inter-flux line spacing. Eq. 1.80 is also the work, ΔW, spent to move a flux line to the next available pinning center.

As the flux line moves, it generates an electric field, Eq. 1.73, whose module is $E = vB$. The velocity results from the product of the inter-flux spacing and the net hopping rate, R_{net} [37]:

$$R_{net} = 2\Omega_0 e^{-U/k_B T} \cdot sinh\left(\frac{\Delta W}{kT}\right) \tag{1.81}$$

where Ω_0 is the frequency of hopping. The electric field becomes:

$$E = R_{net} a_0 B = 2a_0 B\, \Omega_0 e^{-U/k_B T} \cdot sinh\left(\frac{\Delta W}{k_B T}\right) \tag{1.82}$$

If this is lower than the critical electric field, e.g. $E_c = 10^{-4}$ V/m, dissipation is not observed. Flux creep plays a much more important role in high-temperature superconductors than in low-temperature superconductors. In fact, the temperature is higher (T_c=90 K in YBCO) therefore thermal fluctuations are much stronger. Also, the coherence length ξ is smaller, resulting in a smaller energy barrier, U.

Chapter 2

Practical superconductors and their applications

2.1 Introduction

Practical superconductors are characterized by the ability of carrying very high current densities. While this is a necessary condition for magnet and cable applications, other conditions need to be satisfied as well. In fact, practical superconductors have other crucial requirements:

- Withstand high mechanical stresses, due to magnetic forces.
- Be protected in the case of quench, which demands for rapid detection.
- Have low magnetization, for applications to NMR, MRI, HEP magnets.
- Display consistent joint technology, again for NMR and MRI.
- Be stable against thermal perturbations.

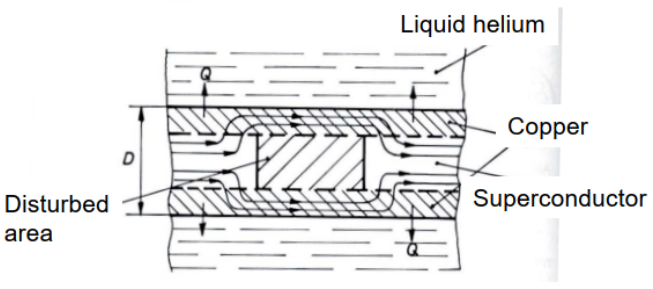

FIGURE 2.1: Copper is placed in parallel to the superconductor, to allow it recovering the superconducting state during a thermal disturbance [4].

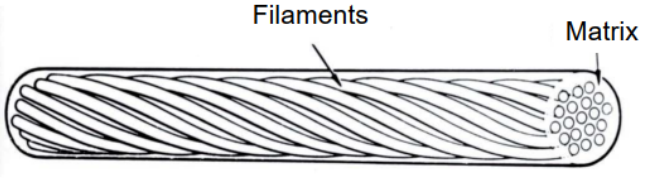

FIGURE 2.2: Sketch of a superconducting wire with twisted filaments embedded in a copper matrix [4].

In fact, a tiny internal or external disturbance (e.g. a strand movement in a cable) leads to the dissipation of heat. As a consequence, the superconducting material warms up, reducing the margin to the critical curve and even transiting to the normal conducting state. This might generate further dissipation into a positive feedback loop, which eventually quenches the superconductor.

To contrast this issue, copper or another electrical conducting material is put in parallel to the superconductor, such that the current can bypass the disturbed volume and the superconductor recovers the superconducting state, see Fig. 2.1. To make a practical superconductor working, wires in a cable must be made of multiple filaments inside a copper matrix, see Fig. 2.2. Filaments reduce the magnetization losses considerably with respect to a mono-block and their large surface-to-volume ratio guarantees efficient heat and current transfer to the matrix in case of a heat perturbation. The matrix itself has a low resistivity and occupies up to 50 % of the wire cross section, which allows it to take current during short transients without heating up much.

Filaments are also twisted to reduce the induction loops, see Fig. 2.3. Induction loops are undesired since they store energy that may trigger an instability and distort the field quality. Despite this filamentary nature, the effect of self-screening of the filaments cannot be avoided. The transport current flows in a small part of the filament when the magnet is ramped at low fields, while the remaining part of the filament screens the interior from any field change.

Current loops close over the resistive matrix and they are driven by the induction voltage. Twisting filaments shortens the current loops, thus reducing coupling between

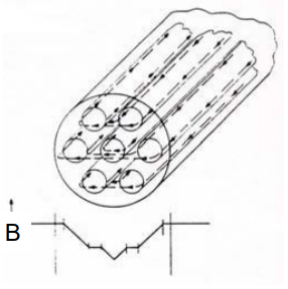

FIGURE 2.3: Induction loops and internal field profile in a multifilamentary wire with non-twisted filaments [4].

filaments efficiently. In turn, local disturbances release less energy into the superconductor.

2.2 Nb-Ti

To begin with, Nb-Ti has similar critical temperature to the Nb element, but much higher upper critical field:

Type II sc	T_c [K]	B_{c2} [T]
Nb	9.5	0.2
Nb-Ti	9.8	14.5

Nb-Ti has become the enabling technology for the large diffusion of Magnetic Resonance Imaging (MRI) machines, for an overall annual market value of roughly 5 billion euros. For the LHC magnets alone, more than 1200 tonnes of Nb-Ti have been manufactured.

The production process starts from a Nb-Ti billet (typically: 20.3 cm diameter x 76.2 cm height; total weight: 136.1 kg) surrounded by copper. This system is extruded at cold until obtaining an hexagonal bar. Several of these bars are then inserted in a copper cladding and further extruded at cold. The process includes intermediate stages of twisting, resulting in filaments having this advantageous geometrical feature. The final wire has a diameter of about 1 mm and it is hundreds of kilometers long [36]. The resulting wire cross section is shown in Fig. 2.4.

Nowadays, the typical composition of the metallic alloy is Nb-47wt%Ti. Pinning centers are α phases rich in Ti. Thermal treatments are alternated to mechanical stages such that the spacing between pinning centres equals that of flux lines.

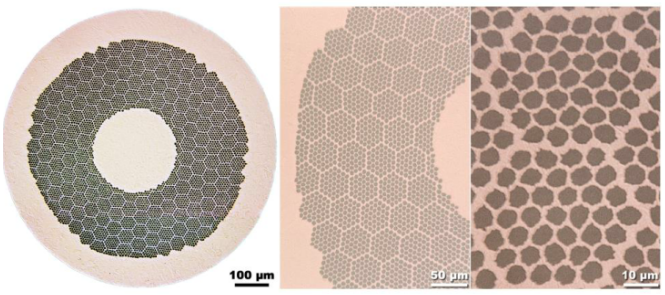

FIGURE 2.4: Cross section of a Nb-Ti wire containing thousands of filaments. Credits: [5].

2.3 Nb_3Sn

The critical temperature of Nb_3Sn is 18.2 K and its upper critical field is 30 T. In this sense, Nb_3Sn is the LTS used for high field applications (above 10 T).

The first important difference to note is that, while Nb-Ti is a metallic alloy, Nb_3Sn is an intermetallic compound having crystalline structure. The general chemical formula of the compound is $Nb_{3+x}Sn_{1-x}$ and the Sn content can vary greatly while still obtaining the superconducting compound. Nevertheless, the optimum T_c and $B_{c2,0}$ are seized for a 24.5% Sn content, see Fig. 2.5.

Many attempts have been conducted to maximize B_{c2} of Nb_3Sn by adding impurities. In fact, the higher the concentration of material impurities (thus disorder), the lower the electron mean free path, and the coherence length, ξ, as well. As a result, given the equation:

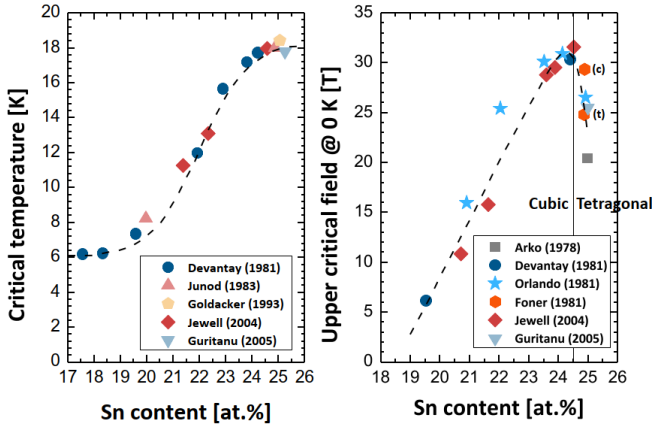

FIGURE 2.5: T_c and B_{c2} with varying Sn content. Credits: [5].

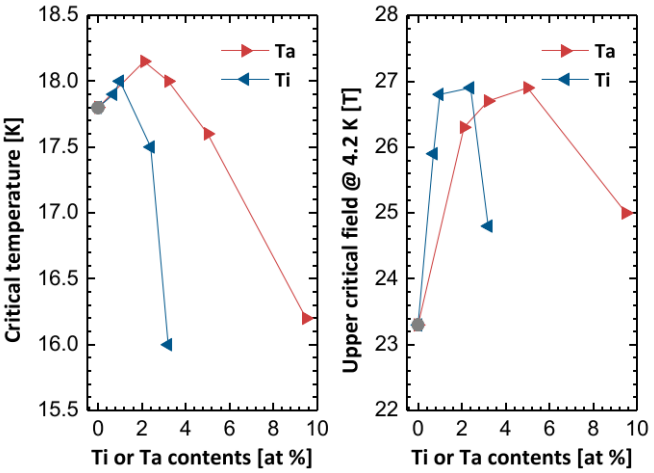

FIGURE 2.6: T_c and B_{c2} with varying Ta and Ti content. Credits: [5].

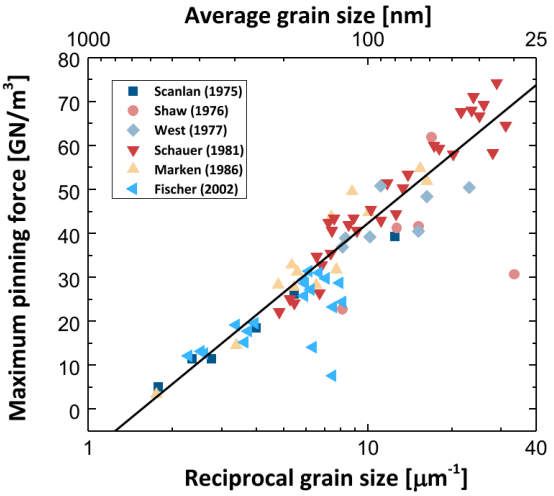

FIGURE 2.7: Maximum pinning force as a function of the reciprocal grain size in Nb_3Sn. Credits: [5].

$$B_{c2} = \mu_0 \frac{\Phi_0}{2\pi\xi^2} \tag{2.1}$$

the upper critical field is higher. Ta and Ti substitutions are particularly beneficial, see Fig. 2.6. Perhaps the most important feature is that grain boundaries play the role of pinning centers in Nb_3Sn. Fig. 2.7 shows that reducing the grain size, allows obtaining an increasingly higher pinning force.

2.3.1 Manufacturing processes

Three main processes have been developed at the industrial scale to manufacture Nb_3Sn, which differ according to the Sn source:

- Bronze route
- Internal Sn diffusion
- Powder-in-tube (PIT)

A feature that makes Nb_3Sn diverge from Nb-Ti is that the superconducting phase is formed through a heat treatment process lasting for roughly two weeks, which reaches a maximum temperature of 660 - 670 °C. The temperature cannot exceed 700 °C since the glass fiber insulation used in cables would degrade above such temperature. One could use ceramic insulators, but they are usually very expensive. Another reason is that the grain size increases at higher temperatures, therefore a compromise must be found. Let us also note that the different phases have different densities, so voids are

formed during the process. Finally, Nb_3Sn is very fragile, therefore the heat treatment must be the very last step in the magnet production: it is the so-called Wind-and-React technique.

2.3.1.1 Bronze route

The bronze process starts from single Nb-core billets stacked together in a bronze matrix rich in Sn (Cu13.4wt%Sn). On the outside is a Ta cladding acting as an anti-diffusive barrier, which is useful during the reaction stage. Then, several of these 'islands' are stacked together in a copper matrix and extruded until forming the multifilamentary wire, see Fig. 2.8.

During the heat treatment, the Sn in the bronze cladding diffuses into the Nb core of each filament, producing the actual superconducting Nb_3Sn phase. The Ta barrier prevents the Sn to diffuse into the external copper matrix, which must remain as pure as possible to have low electrical resistivity. Additions of Ti or Ta can be made in the inner Nb cores to enhance B_{c2}.

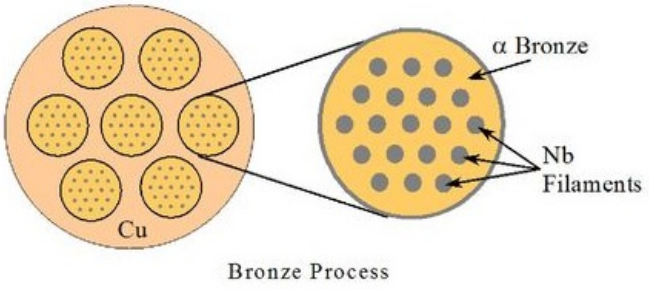

FIGURE 2.8: Sketch of the bronze route process. Credits: [6].

2.3.1.2 Internal tin diffusion

In the internal Sn process, see Fig. 2.9, the starting unit is a so-called 'Sn pool' placed inside a copper cylinder containing Nb bars as well. This unit is also surrounded by

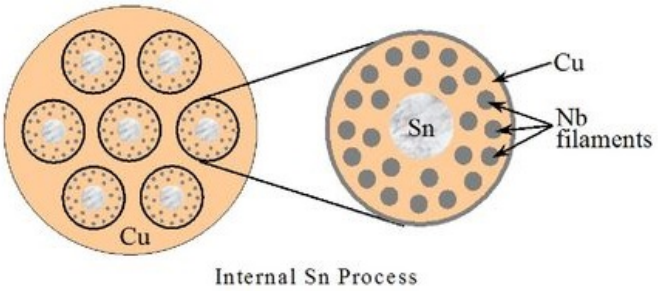

FIGURE 2.9: Sketch of the internal tin process. Credits: [6].

an anti-diffusive barrier. Multiple units are inserted in a copper matrix and extruded. During the reaction, Sn in the single unit diffuses in the Cu thus forming bronze, as well in the Nb, forming the superconducting phase.

2.3.1.3 Powder-in-tube (PIT)

The unit element is a Nb hexagonal bar inside which a mixed powder of Nb_2Cu and Cu is inserted. Here, the anti-diffusive barrier on the outside of the unit element is not needed, since the copper in the matrix between units remains at a high level of purity during the heat treatment. The resulting best performing wires obtained with these three manufacturing routes are shown in Fig. 2.11.

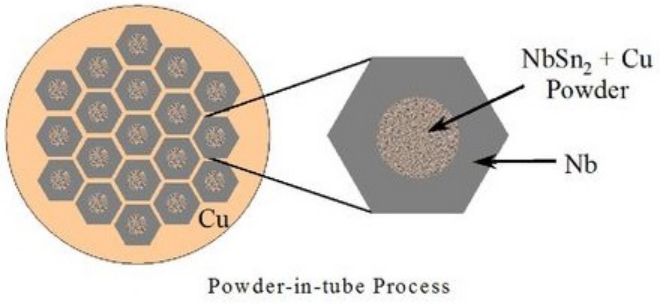

FIGURE 2.10: Sketch of the powder-in-tube process. Credits: [6].

2.3.2 Strain dependence

Unlike Nb-Ti, Nb_3Sn is subjected to degradation of performance when exposed to applied strain. Fig. 2.12 shows such an effect.

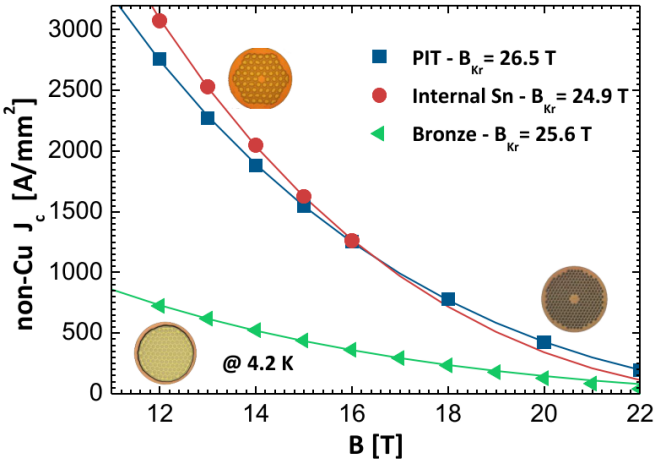

FIGURE 2.11: Performance comparison of the best wires manufactured with the bronze route, internal tin, and PIT methods listed above. Credits: [5].

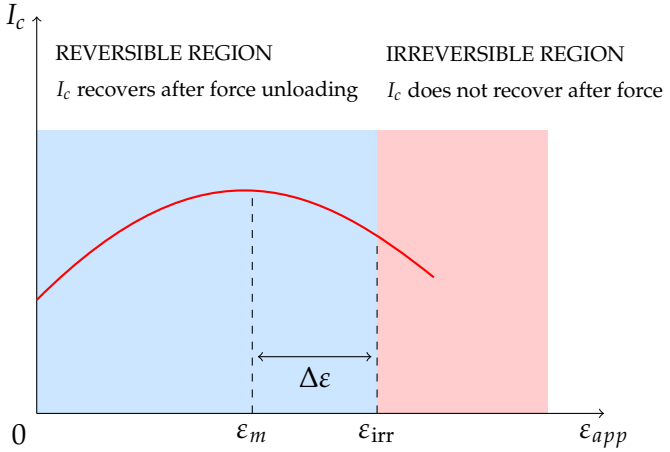

FIGURE 2.12: Reversible and irreversible effect of strain on Nb_3Sn performance. Adapted from [5].

Starting from the unloaded state, the performance increases initially with increasing applied strain, reaching a maximum at ε_m. This is explained by the fact that the material 'releases' the cumulated strain from the manufacturing process. Following the peak, the performance decreases up to ε_{irr}, at which one enters the irreversible region (in red, in Fig. 2.12), namely where the I_c does not recover after unloading the stress.

The irreversible limit for the axial strain is around 0.4% for both the PIT and Internal tin process, and slightly higher for the Bronze route at 0.62%. This corresponds to stresses of 160 MPa for PIT, 210 MPa for Internal tin, and 330 MPa for the Bronze route. The transverse stress limit, defined as the stress leading to 95% recovery of the initial I_c is σ_{irr}=110 MPa.

There are two issues to deal with in Nb_3Sn. On one side, the yield strength of copper is roughly 90 MPa, leading to the plastic deformation of copper when surpassing this limit. In turn, this imposes a stress state on the Nb_3Sn even after force unloading. On the other side, voids formed during the reaction heat treatment induce the concentration of localized stress where cracks can nucleate. As a matter of fact, Nb_3Sn is a brittle material characterized by a strong propensity to fracture.

2.4 MgB_2

Magnesium diboride, MgB_2, is a binary intermetallic compound which has been known since the 1950s, however it has been discovered to be superconducting only in 2001 [38]. MgB_2 has a simple layered structure composed of an hexagonal boron layer sandwiched between two magnesium layers, see Fig. 2.13.

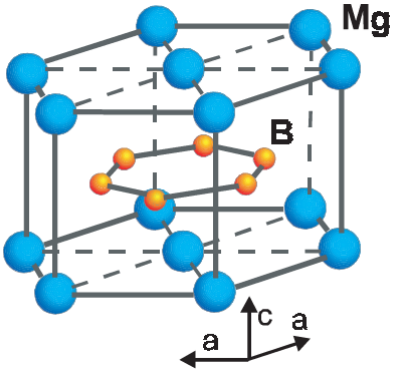

FIGURE 2.13: MgB_2 unit cell. Credits: [7].

The critical temperature, T_c = 39 K in MgB_2. This is exceptional as it far exceeds the highest T_c of LTS, namely of 23 K in Nb_3Ge. Additionally, this material exhibits a two-band superconductivity, namely two superconducting energy gaps coexist below T_c, resulting in anisotropic properties.

However, in contrast to cuprates (see the next section) there are no weak links, meaning grain boundaries are transparent to current and the manufacturing process is thus much facilitated compared to HTS. In addition, the coherence length, ξ, is between 25 - 40 nm both along the *ab*-planes and the *c*-axis, comparable to that of pure Nb. Being large with respect to the dimension of the unit cell, extended defects are needed to act as pinning centers.

Fig. 2.14a shows the upper critical field, B_{c2}, as a function of the reduced temperature for a pure MgB_2 single crystal; $B_{c2,0}$ results to be 17 T along the *ab*-planes, with the anisotropy being up to a factor 5. Doping using carbon (C) or C-related compounds shortens the mean free path and enables a great increase of B_{c2}, up to 32 T, as displayed in Fig. 2.14b [7].

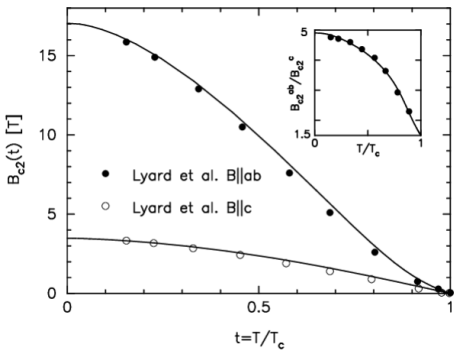

(A) Along the *c*-axis and *ab*-planes.

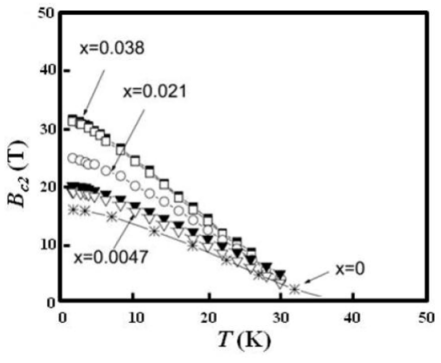

(B) C-related compounds addition.

FIGURE 2.14: Features of the upper critical field in the MgB_2 compound.

2.4.1 Manufacturing process

Two main methods are adopted to manufacture MgB_2 wires, which are either in-situ or ex-situ powder-in-tube. The in-situ process starts from a mixture of B and Mg powders. These are inserted into a cladding, which is then deformed and reacted to form the actual MgB_2. This process is used in the Wind-and-React technology and allows a high filling factor as well as easy doping with nanoparticles.

In the ex-situ process, already reacted MgB_2 powders are inserted into a cladding and heat treated. This is used in the React-and-Wind technology, which allows for a better control in granulometry and purity of the powders.

2.5 The discovery of high temperature superconductors

In 1986, Bednorz and Mueller discovered superconductivity in the La-Ba-Cu-O compound at the critical temperature of 35 K [39]. This led, in a few years only, to the discovery of multiple compounds having very high T_c, which were therefore named high temperature superconductors (HTS).

HTS are extreme type-II superconductors, characterized by $\lambda \approx 100$ - 1000 nm and $\xi \approx 1$ nm. Correspondingly, the Ginzburg-Landau parameter can be even up to $\kappa \approx 100$. The Ginzburg-Landau theory predicts:

$$B_{c2} = \frac{\Phi_0}{2\pi\xi^2} \tag{2.2}$$

and $T_c \propto 1/\xi$ as well. Therefore, the very low ξ results in high values of the upper critical field and critical temperature.

In addition to these considerations, HTS display anisotropic properties, in the sense that the effective mass of the charge carriers depends on the crystallographic orientation (see the discussion on unit cells in section 2.5.1). This can be either along the CuO_2 planes, usually referred to as *ab*-planes, or in the perpendicular direction to the planes, the *c*-axis. One defines the so-called anisotropy parameter as:

$$\gamma = \sqrt{\frac{m_c}{m_{ab}}} = \frac{\lambda_c}{\lambda_{ab}} = \frac{\xi_{ab}}{\xi_c} \tag{2.3}$$

where the ratio m_c/m_{ab} varies between 50 - 10,000 in HTS. In the above expression, m_{ab} and m_c are the masses of the charge carriers along the *ab*-planes and the *c*-axis, respectively.

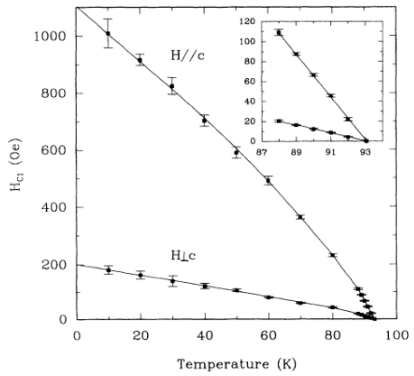

FIGURE 2.15: Lower critical field of a YBCO film along the *c*-axis and *ab*-planes, as a function of temperature. Extracted from [8].

The anisotropy parameter can then be expressed in terms of the ratii between the upper and lower critical fields:

$$\gamma = \frac{B_{c2}^{ab}}{B_{c2}^{c}} = \frac{B_{c,1}^{c}}{B_{c,1}^{ab}} \tag{2.4}$$

The anisotropy of the three practical HTS (discussed later in the chapter) is shown in Table 2.1.

Anisotropy	*Bi-2212*	*Bi-2223*	*YBCO*
γ	$\sim$150	$\sim$30	$\sim$5 - 7

TABLE 2.1: Anisotropy of the three practical HTS.

Furthermore, the anisotropy of $B_{c,1}$ in a YBCO crystal has been shown experimentally in [8], see Fig. 2.15. The corresponding plot of B_{c2} is reversed; $B_{c2,0}$ has been measured to approximately 120 T for $B \parallel c$-axis [40], while $B_{c2,0} \approx 250$ T for $B \parallel ab$-plane [41]. To conclude this part, let us specify that the actual formulae for the upper critical field are:

$$B_{c,2,c} = \frac{\Phi_0}{2\pi\xi_{ab}^2} \tag{2.5}$$

and

$$B_{c,2,ab} = \frac{\Phi_0}{2\pi\xi_{ab}\xi_c} \tag{2.6}$$

2.5.1 Unit cells

The general formula for BSCCO compounds is: $Bi_2Sr_2Ca_{n-1}Cu_nO_{4+2n+\delta}$. This allows up to three CuO_2 planes in the unit cell and the resulting T_c is reported in Table 2.2. The

Compound	*No. planes*	T_c [K]
Bi-2201	1	15
Bi-2212	2	91
Bi-2223	3	110

TABLE 2.2: T_c of the three BSCCO compounds.

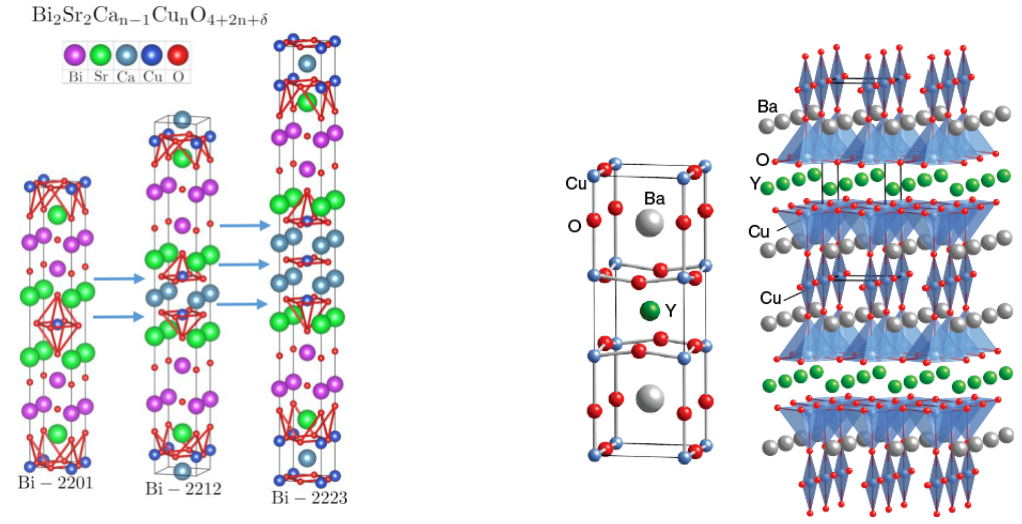

(A) The three BSCCO compounds. (B) YBCO

FIGURE 2.16: Unit cells of HTS compounds.

schematic unit cells of the three types of BSCCO are displayed in Fig. 2.16a. Instead, only one composition exists for YBCO: $Y_1Ba_2Cu_3O_{7-\delta}$. The corresponding unit cell is represented in Fig. 2.16b.

2.5.2 Phase diagrams of vortices

The lowest enthalpy and thereby the stable state of vortices is attained with a triangular lattice with one flux quantum at each lattice site [2]. This condition is also valid for vortices in the mixed (Shubnikov) phase of HTS. We note that several of the previously listed properties have a strong impact on this state: 1) the very small coherence length, ξ, 2) the high T_c, and 3) the layered structure of the CuO_2 planes.

One can consider the *coherence volume*, $V_c = \xi_{ab}^2 \xi_c$ as the volume element in which the Cooper pair density changes only very little, while it can change much more on larger scales. This volume is a few orders of magnitude smaller in HTS compared to LTS. Then, the condensation energy per unit volume can be written as: $E_c = B_{c,th}^2 / 2\mu_0$.

On the other hand, the thermal energy is estimated as $k_B T_c$, with k_B being the Boltzmann constant. Comparing the thermal energy with the condensation energy, one has $k_B T_c / (E_c V_c)$, which indicates the superconductor sensitivity to thermal fluctuations.

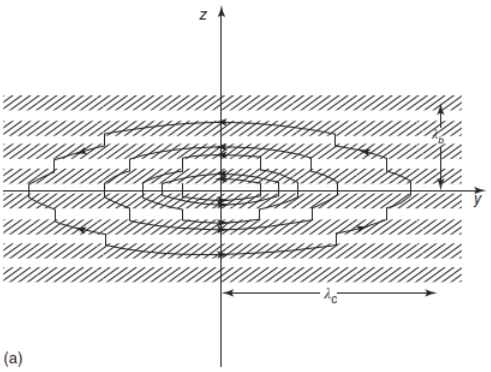

FIGURE 2.17: Circulation of currents around a vortex in a superconducting layered structure. Credits: [2].

The *Ginzburg number* can be defined:

$$G_i = \frac{1}{2}\left(\frac{k_B T_c}{E_c V_c}\right)^2 \tag{2.7}$$

This is around 10^{-2} in YBCO and Bi-2212, while it is typically smaller by five or more orders of magnitude in LTS. We can infer that thermal fluctuations play a very relevant role in HTS.

The layers are only weakly coupled with each other in YBCO and BSCCO compounds. In the case of a field applied perpendicular to the layers (higher than $B_{c,1,\perp}$), supercurrents can flow only within the separated *ab*-planes, therefore one ends up with stacks of 2-D vortices (called 'pancakes'). Let us note that planar vortices from different planes attract each other, since the currents sustaining them flow in the same direction. Pancakes align along common axes in the perpendicular field configuration. Eventually, one obtains again a triangular lattice of flux lines penetrating the material as for LTS (see more in detail in the next section).

Let us now consider a field applied parallel to the layers (higher than $B_{c,1,\parallel}$). Currents flow along the *c*-axis, however the entity of these currents is much lower than those along the *ab*-planes. Also, the magnetic penetration depth, $\lambda_c > \lambda_{ab}$, therefore $B_{c,1,\parallel} = (\lambda_{ab}/\lambda_c)B_{c,1,\perp}$. Since, λ_c can be up to 1000 times higher than λ_{ab}, $B_{c,1,\parallel}$ is very small.

As a result, vortices have a dimension of about $2\lambda_c$ in the planes and of $2\lambda_{ab}$ perpendicular to the planes. λ_{ab} is higher than the *ab*-plane spacing, therefore vortices extend into several planes, however they are still very flat objects, see Fig. 2.17. Additionally, these vortices, referred to as *Josephson vortices* are very different with respect to Abrikosov vortices or either pancake vortices along the perpendicular direction. In fact, the axis of a Josephson vortex is located along a non-superconducting layer, therefore the Cooper

pair density is not suppressed as in the other two cases. Josephson vortices are also arranged in a triangular lattice.

2.5.3 Irreversibility line

The very short coherence length, ξ, combined with the high temperatures in HTS gives rise to various regimes of vortices, which are not foreseen by the Ginzburg-Landau theory (see chapter 1). In fact, the pancakes discussed above are easier to move, which results in different vortex phases:

1. A crystalline state. Pancakes among different planes form a triangular flux-line lattice. However, this state practically does not occur in available materials;
2. A quasi 2-D vortex solid, called vortex glass. Pancakes still form a triangular lattice within the single planes, but the lattice is easily shifted among different planes;
3. A flux-line liquid. Pancakes among different planes align with each other to form flux lines, but these are mobile (a 'spaghetti'-like behaviour);

In HTS, there exists a line at which the glass state of flux vortices transitions into the liquid state, thus generating dissipation. The critical current density, J_c=0 at such transition.

Fig. 2.18 shows the actual phase diagram of HTS, which includes the so-called irreversibility line (in blue). The Abrikosov lattice does not exist in HTS, and flux vortices are arranged in a 'glass' structure below the irreversibility line, where only creep (see section 1.13.3) takes place. Above the line, vortices are in a 'liquid' state and they move

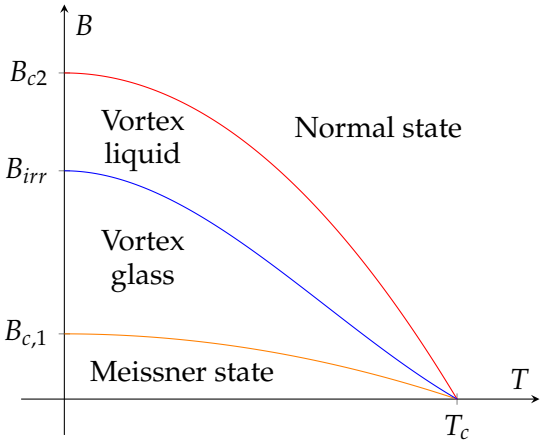

FIGURE 2.18: Full phase diagram of HTS, showing the irreversibility line (in blue), the actual limit for applications.

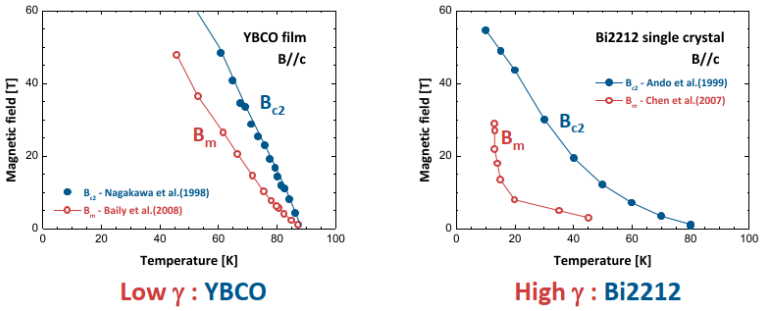

FIGURE 2.19: Comparison of anisotropy between a YBCO crystal and Bi-2212. Credits: [9].

under the action of an external current producing dissipation. The irreversibility line is extremely important as it defines the actual limit for applications.

In particular, the higher the anisotropy γ, the lower the irreversibility line, see Fig. 2.19. The J_c of Bi-2212 drops rapidly to zero with temperature, becoming too low for applications already at 50 K. Instead, YBCO maintains a relevant J_c even above 77 K.

2.5.4 Bi-2212

The manufacturing process of Bi-2212 differs from the other technical HTS as it is produced in the form of round wires, see Fig. 2.20, which is the case of LTS. The process starts from Bi-2212 powders which are melt during a heating stage above the peritectic temperature to form liquid Bi-2212 and (Sr, Ca) oxides. Slow cooling and an intermediate 'dwell' stage at a lower temperature allows the mixture to solidify and nucleate Bi-2212 grains below ∼872 °C. This is followed by an oxygenation stage for further stabilization of the Bi-2212.

The wire ends up to be multifilamentary, with a filling factor comprised between 25 - 30 %. The advantage of these wires is the resulting absence of anisotropy, since the

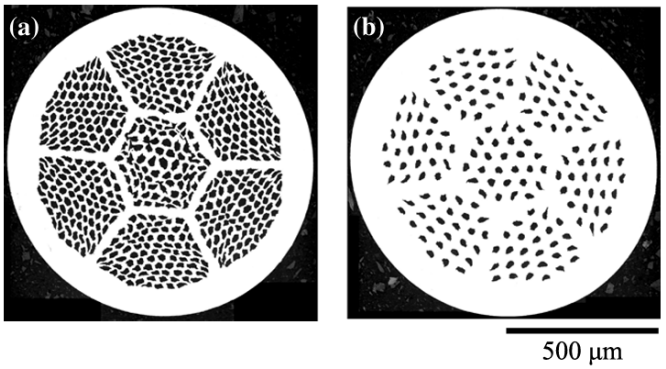

FIGURE 2.20: Transverse cross-section images of Ag-sheated PIT multifilamentary Bi-2212 round wires with (a) 85x7 and (b) 27x7 architectures. Credits: [10].

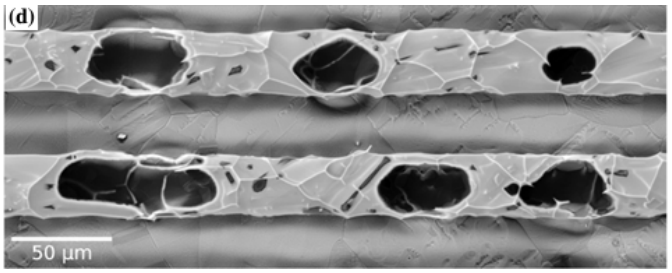

FIGURE 2.21: Bubbles in Bi-2212 filaments. Credits: [10].

c-axis of grains is oriented along all directions. Unfortunately, the melting results in a multiple-phase assemblage with gas bubbles agglomerating from the porosities as well as filaments bonding together, see Fig. 2.21.

This issue has been solved adopting an overpressure process which can go up to 100 MPa, that prevents the formation of bubbles and increases the current-carrying cross section [42]. The process also allowed obtaining optimally doped grain boundaries and over-doped intragrain regions, something that is not possible with Bi-2223 and YBCO [43]. These improvements led to a large enhancement of the critical current density, see Fig. 2.22.

The J_{eng}(4.2 K) of the Bi-2212 strand is greater than that of the HL-LHC Nb_3Sn strand above 11 T and it has a much less field-sensitive characteristic, achieving 1365 A/mm^2 at 15 T, which is twice the target desired for Nb_3Sn strands for the FCC. Additionally, it goes up to 1000 A/mm^2 at 27 T, being 65 % higher than the previous Bi-2212 record performance.

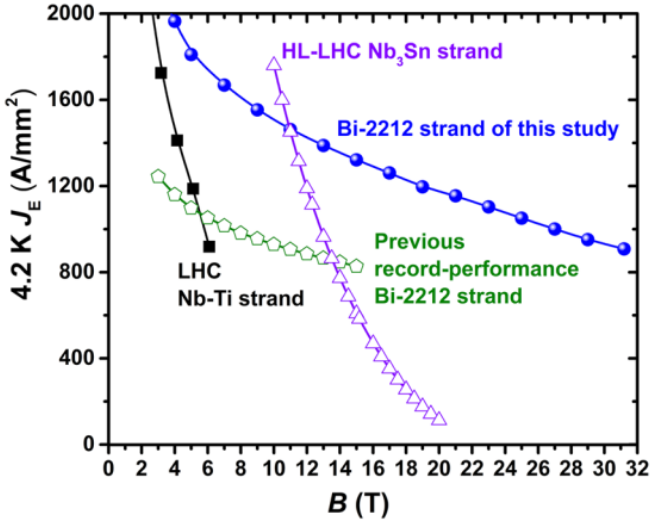

FIGURE 2.22: Record J_{eng} in Bi-2212 wires, compared to previous record performance, Nb-Ti LHC strands and Nb_3Sn for the HL-LHC project. Credits: [11].

2.5.5 Bi-2223

The compound $Bi_2Sr_2Ca_2Cu_3O_{10}$ is fabricated using the powder-in-tube (PIT) process. The process starts from a mixture of Bi_2O_3, PbO, $SrCO_3$, $CaCO_3$, and CuO powders that are hand-grinded and heat treated at 700 - 800 °C in air to form Bi-2212 (75-80 %), Bi-2201 ($\sim$5 %), Ca_2PbO_4 (10 %) and CuO [44]. The reacted powders are then packed into an Ag tube and the resulting composite is drawn to form a wire. Subsequently, the wire is cut into many straight longitudinal sections, which are re-bundled into another Ag tube. The resulting multifilamentary wire is drawn to thinner diameters and deformed into the shape of a tape.

This stage is of absolute importance as it generates the texturing, namely the platelet-like Bi-2212 grains are aligned to each other along the *c*-axis by the deformation. The process continues with a heat treatment at temperatures of 830 - 850 °C in a 7.5 % O_2 atmosphere during which the Bi-2223 phase is formed (in-situ). An unwanted side product of the reaction is the formation of CO_2, which leads to the formation of bubbles lowering the overall density. The process is completed by two final stages, during which the tape is deformed further to densify the ceramic core and an overpressure treatment at up to 30 MPa removes the voids.

While conventional Bi-2223 reaches roughly 85% density, the density is 100% in the so-called DI-BSCCO obtained in the way described above. This process was employed by Sumitomo, the only worldwide manufacturer of Bi-2223 on an industrial scale [45]. The resulting tape cross section is displayed in Fig. 2.23.

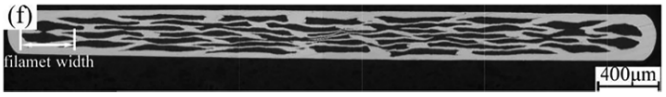

FIGURE 2.23: Bi-2223 tape cross section by PIT. Credits: [12].

2.5.6 REBCO

The relevant advantages of REBCO fabricated in the form of coated conductors are:

- High T_c
- High B_{c2} and B_{irr}
- High J_c

while the disadvantages are:

- Brittle ceramic nature

- Low coherence length
- Deleterious effect of grain boundaries
- High thermal excitations
- Large penetration depth
- Anisotropy

Additionally, REBCO coated conductors are complex materials in which many defects are involved at the same time.

2.5.6.1 Historical development and general features

REBCO is a quaternary system and its variable oxygen stoichiometry has a decisive impact on its functional properties, which are anisotropic and highly correlated.

REBCO coated conductors (CCs) are characterized by a low superconducting coherence length, ξ, causing the grain boundaries to be connected by weak links. In addition, pinning defects, necessary to allow the high critical currents of REBCO CCs, need to be of the nanoscale size both to not disrupting the superconducting continuity across the boundaries as well as to match the vortex core and save its condensation energy [46].

In the early 2000s [26], coated conductors had reached the same self-field J_c values at liquid nitrogen temperatures as those of similar films deposited on single crystal substrates, which were considered as the reference at the time. This meant that the current flow in those coated conductors was uniform rather than percolative, and therefore that the source of limitation of the J_c was the intragrain bulk pinning rather than the weak links among grain boundaries [13].

The 2-D structure of the crystalline lattice causes a poor electronic transport perpendicular to the planes. Therefore, very high grain alignment is required to allow the current transfer among the grains, without any obstruction along the length of the conductor.

To resume, nanoscale defects need to be engineered in the material without disrupting the superconducting planes and without blocking the current transfer through the grain boundaries. To achieve such required grain alignment as well as the nanoscale defect microstructure, REBCO conductors must be manufactured by epitaxial thin film growth methods. At the same time, the material must be deposited on a long and flexible support to facilitate handling, which is why a metallic substrate is used.

High vortex pinning energies must exceed thermal excitation. This tightly depends on the ability to generate a pinning landscape that adapts to the temperature, magnetic

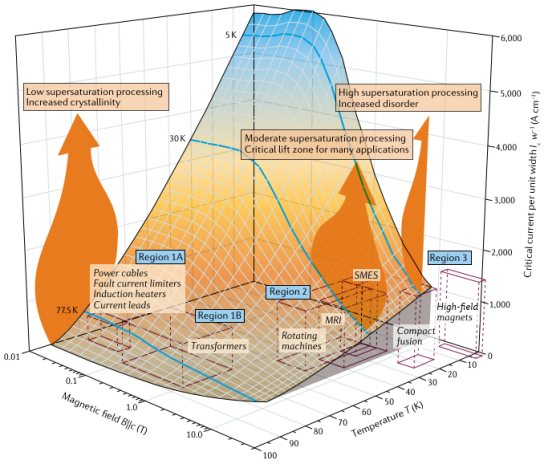

FIGURE 2.24: Critical curve, $I_c(B,T)$, separating the three regions relevant for applications. These are: Region 1A, for power cables and fault current limiters, Region 1B for transformers, Region 2 for rotating machines and MRI, and Region 3 for high-field magnets. Credits: [13].

field strength and orientation. In turn, this has a decisive impact on the application range, see Fig. 2.24.

A very useful concept for the following considerations is *supersaturation*. This is the concentration of REBCO chemical species above the equilibrium level. The level of supersaturation drives nucleation and it is related to the growth rate: low supersaturation leads to low nucleation rates and larger crystallites, whereas high supersaturation leads to high nucleation rates and finer crystallites.

2.6 Manufacturing routes of REBCO coated conductors

2.6.1 Early struggles

An issue that limited the performance of REBCO in the early days was the weak-link effect, since it caused an exponential decrease of J_c with increasing misorientation angle between adjacent grains [47]. This was the reason why critical current densities in single crystals exceeded currents in polycrystalline HTS by several orders of magnitude.

This issue was overcome by having a crystalline template on which to grow the REBCO layer epitaxially. The involved processes were IBAD and RABiTS, which allow to approximate a very long single-crystal substrate by inducing a biaxial texturing in the REBCO layer [14]. The difference between IBAD and RABiTS process is shown in Fig. 2.25.

Initially, IBAD was used to form YSZ films on low roughness metal substrates, on which then YBCO was deposited either by PLD, chemical vapour deposition (CVD), or

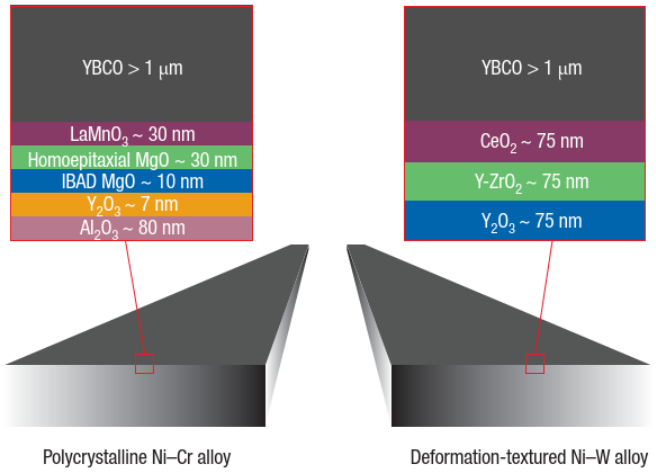

FIGURE 2.25: Left: Polycrystalline Ni-Cr substrate where texturing is obtained by IBAD. Right: Polycrystalline Ni-W substrate where texturing is obtained by RABiTS. Credits: [14].

electron-beam coevaporation methods. YSZ involves a rather slow mechanism, since it requires 500 - 1000 nm thickess deposited at ∼0.1 nm/s [48]. A few years later, MgO was found capable of achieving good texturing at much higher deposition rate of ∼300 nm/min with much lower thickness, using ISD [49], [15] as well as IBAD [50].

Already in the beginning of the 2000s, coated conductors based on YBCO deposited on biaxially textured substrates were foreseen to be an alternative to powder-in-tube (PIT) Bi-2212 and Bi-2223 [51].

2.6.2 The substrate

Hastelloy metals and alloys are known for their resistance to corrosion, strength, as well as ductility under stress. They are used in aerospace, chemical and nuclear industries, and they have been widely used as substrates for manufacturing 2G-HTS REBCO tapes with the IBAD process [52]. The RABiTS process, instead, rather uses strong non-magnetic Ni-W alloys.

2.6.3 Tape architecture

The architecture of REBCO coated conductors is made up of several layers, each having a specific purpose, see Fig. 2.26. The starting point is a non-magnetic stainless-steel or Hastelloy substrate, on top of which lies a series of buffer layers preceding the REBCO layer. A thin silver layer completes the ensemble. This 'sandwich' is then electroplated by a layer of copper for electrical stabilization.

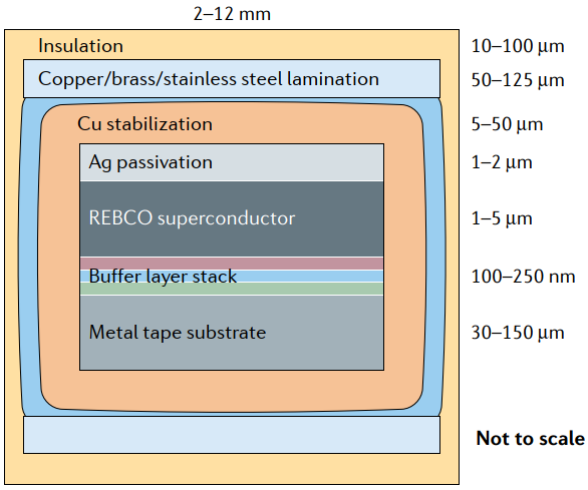

FIGURE 2.26: Typical architecture of a REBCO tape. This is composed of a metal substrate, a series of thin buffer layers, the superconducting REBCO layer, and an Ag layer. This sandwich is surrounded by a uniform copper layer for electrical stabilization. Other external layers of copper, stainless steel and insulation can be further added for a cable configuration. Credits: [13]

Each layer in the stack of the buffer layers has a specific purpose, creating an interface between the substrate and the REBCO layer. The objective of the manufacturing process is to induce a bi-axial alignment in the REBCO layer, which reduces grain misalignment thus allowing high currents to flow in the tape. The bi-axial alignment can be achieved by two different methods: the ion-beam assisted deposition (IBAD) of a bi-axially textured buffer layer onto an untextured substrate, or a rolling-assisted biaxially textured substrate (RABiTS) [47].

In the IBAD process, an oxide layer, typically MgO, is deposited onto a polycristalline non-magnetic Hastelloy or stainless steel substrate, while an ion beam simultaneously induces the biaxial texturing in the growing layer through orientationally selective etching. Variations of IBAD are the alternating beam assisted deposition (ABAD) process [53] employed by Bruker HTS, and the inclined substrate deposition (ISD), adopted by Theva.

In the RABiTS process, instead, a Ni-W alloy working as a substrate is rolled producing a bixial texture with 5 - 7° average grain misorientation. Then, the buffer layers can be either vapour-deposited or solution-deposited, whereas the REBCO layer is solution-deposited and thermal processing is used to crystallize and biaxially texture the grains as well.

Various methods are employed to manufacture REBCO conductors. The method employed determines the types, dimensions, and density of the artificial pinning centres, intrinsic defects, and grain sizes in the REBCO. Common to all methods are the principles of nucleation and growth, the ease to nucleate REBCO and the speed and direction of grain growth. These depend on the degree of supersaturation and on the kinetics

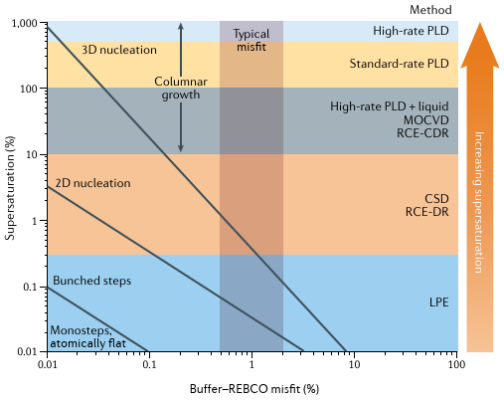

FIGURE 2.27: Supersaturation resulting from buffer to REBCO layer misfit, depending on the manufacturing process. Credits: [13].

and direction of the grain growth. In general, an indirect link exists between supersaturation and the kinetics of film growth. Also, the nucleation density of the REBCO grains depends on the supersaturation of the REBCO species, however a correlation between supersaturation and the density of inclusions has not been established yet.

In general, finding a link between the degree of supersaturation and the regions in the $I_c(B,T)$ diagram is extremely relevant to understand conductor performance and enlightens the way to improve it. Both the supersaturation level and the crystallographic lattice misfit with the upper buffer surface on which the REBCO is grown determine the REBCO microstructure, see Fig. 2.27. Growing the REBCO layer by the epitaxy from the underlying buffer layers is of crucial importance to achieve high grain orientation, thus maintaining the inter-grain J_c very high [46].

2.6.4 High supersaturation methods

In high supersaturation methods, which are mainly standard-rate or high-rate PLD, fast growth of the REBCO layer is achieved thanks to the delivery of highly energetic atomic species onto the substrate. Long columnar defects do not manage to develop in this case, and a high density of 3-D nuclei is formed, instead. The layer is characterized by a high level of disorder associated with fine columnar grains.

For example, this is the case observed in [54], where a high density of segmented and splayed nanorods rather than continuous straight nanorods were observed. A high density of stacking faults were also characteristic of the coated conductors manufactured in [54]. The fast vertical growth ensures grain alignment, which results in highly columnar grains providing pinning from the grain boundaries and the associated dislocations, at low temperatures.

A considerable disadvantage of these methods is that they require vacuum deposition coupled with laser ablation in order to obtain the high degree of supersaturation [55].

This translates into a high manufacturing cost, however this has not posed a particular threat for commercial operation, thanks to the other several advantages of PLD.

The crystal and texture quality of REBCO films worsens with increasing film thickness under deposition conditions at high growth rates, because of the formation of secondary phases and grains with non-preferable orientation. To maintain high phase purity and not degrade texture with increasing film thickness, the deposition process must be carefully controlled to obtain the desired microstructure.

2.6.4.1 PLD

In the physical vapour deposition (PLD), a high power laser vaporizes a REBCO target, which forms a plasma plume deposited on a substrate. The duration of time during which the target material is supplied by the laser plume to the growth surface is considerably shorter than the time between the pulses. Such a remaining time between pulses allows the ad-atoms in the growing media to diffuse and find appropriate sites for crystallization [55].

2.6.4.2 Advanced PLD

This technique uses hot-wall PLD (see later in Fig. 2.32) with $BaHfO_3$ artificial pinning centres. A high density of nanocolumns is achieved, however the performance remains slightly lower than for Advanced-MOCVD, due to the lower density of RE_2O_3 nanoparticles.

2.6.4.3 ISD

Inclined substrate deposition (ISD) is another method of achieving biaxial texturing of buffer layers on metallic substrates, which is crucial to grow REBCO thin films [49]. ISD is used in combination with PLD.

In this process, the substrate is mounted above a deposition source and placed inside a heater. An electron beam is used to evaporate the target material from the deposition source, which is usually MgO forming the first epitaxial layer. The substrate can be rotated in such a way that the deposition takes place in angles ranging from 0 - 70° with respect to the substrate normal, see Fig. 2.28.

Analyses show that the top plane of the MgO buffer layer is tilted towards the deposition direction and it is proportional to the inclination angle of the process [49]. This first deposition stage occurs at low temperatures below 100 °C, however a second stage

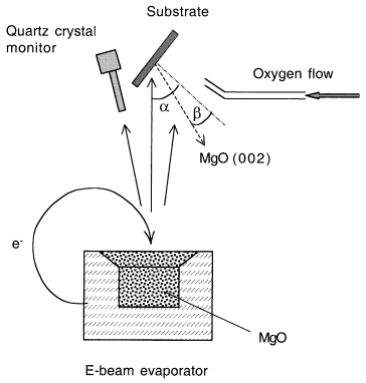

FIGURE 2.28: Schematics of the ISD system for REBCO deposition. Credits: [15].

at much higher temperature, 700 °C, is used to generate the epitaxial layer on which to grow the (Y,Gd)BCO layer by PLD.

2.6.4.4 TLAG

In the transient liquid-assisted growth (TLAG), a metal-organic fluorine-free precursor solution is deposited on a substrate and pyrolized [46]. The solid phase of RE_2O_3, $BaCuO_3$ and CuO are heated rapidly in a moderate O_2 pressure environment. The REBCO layer is grown in a non-equilibrium liquid where the RE ions are dissolved, by applying a fast pressure ramp.

2.6.5 Moderate supersaturation methods

Tapes manufactured by moderate supersaturation methods, such as RCE-CDR (Reactive Co-Evaporation - Cyclic Deposition and Reaction) and MOCVD, show similar performance as those produced by PLD, with the exception of the high-field region. Moreover, they do not present similar inherent pinning microstructure and crystallinity typical of high supersaturation methods, since the achievable layer thickness is limited.

2.6.5.1 MOCVD

In the metal organic chemical vapour deposition (MOCVD), volatile precursors are injected into a reactor chamber by means of a non-reactive carrier gas. These precursors decompose onto the substrate forming the REBCO layer.

2.6.5.2 Advanced MOCVD

In advanced (A-) MOCVD [56], high volume fractions of Zr, up to 15%mol, are added to the REBCO layer, resulting in a variety of pinning defects. These are 1-D $BaZrO_3$ nanorods, 3-D RE_2O_3 nanoparticles, and 2-D stacking faults of CuO planes.

2.6.5.3 Metal Evaporation

Metal evaporation (ME) consists in heating up a REBCO polycrystalline pellet and vaporizing it under high vacuum conditions. Then, the molecules travel from the source to the substrate, where they nucleate to form the REBCO layer.

2.6.5.4 Metal-Organic Deposition

This is a liquid-phase deposition technique which uses organic precursors. It was typically employed in the RABiTS process.

2.6.6 Low supersaturation methods

REBCO is formed by a post-deposition reaction (ex-situ) in low supersaturation methods. Grains tend to develop along the planar direction in this case, since these methods lack of an actual driving force as in simultaneous (in-situ) methods.

2.6.6.1 CSD

In the chemical solution deposition (CSD), a liquid is placed on the film surface for a transient period of time. Slow growth rates are needed in CSD to ensure a controlled reaction and prevent random nucleation of misoriented grains. This also leads to coarser pinning centers, which are not effective at high fields. The advantage of CSD is that it does not require vacuum processing.

2.6.6.2 TFA-CSD

In the tri-fluoro-acetate (TFA) method, BaF_2 forms hydrogen fluoride (HF) in presence of a humid atmosphere. In turn, this volatile gas controls the growth of the REBCO layer, obtained by means of the reaction between CuO and RE_2O_3.

2.6.6.3 RCE-DR

In the reactive co-evaporation and direct reaction process, an amorphous precursor layer is formed at low temperature and low partial oxygen pressure, p_{O_2}, using electron beam co-evaporation. Then, the composite passes continuously through a high temperature zone and two different p_{O_2} zones in series to one another, providing the conversion of the precursors to the superconducting phase [20]. In this sense, this method is simpler than CSD.

Overall, low supersaturation methods are very suitable for tapes in Region 1a and 1b applications. As it has been mentioned already, the supersaturation level is closely related to the optimal operating regime. As a general rule, high supersaturation methods are well suited for high-field, low-temperature performance, whereas the performance is limited at high temperatures. Moderate supersaturation techniques provide intermediate J_c both at 4.2 K and high fields, 77 K and low fields. Finally, low supersaturation processes (RCE-DR and CSD) are best suited for self-field applications at 77 K, see Fig. 2.29. Introducing artificial pinning centres helps improving the performance, thus inducing a shift of the processes towards Regions 2 and 3.

2.6.7 Oxygenation process

Each manufacturing method, in general, is followed by an oxygenation stage in which the REBCO layer becomes superconducting. There are three oxygenation regimes in REBCO: the underdoped, the optimally doped, and the overdoped.

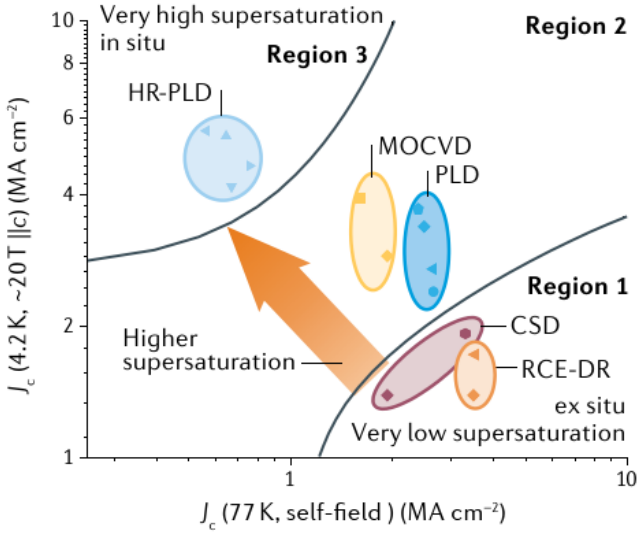

FIGURE 2.29: J_c at 4.2 K and 20 T ($B \parallel c$) versus self-field J_c at 77 K and application regions of the various manufacturing methods. Credits: [13].

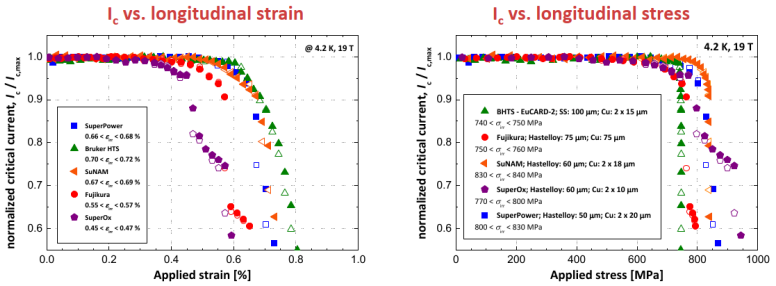

FIGURE 2.30: Stress and strain dependence of various industrial REBCO tapes. Credits: [16]

The critical temperature is the highest in the optimally doped regime, corresponding to 0.16 holes/CuO_2 plane. However, the maximum critical current is expected to be located at slightly overdoped oxygen concentrations, which can be up to the limit 0.19 holes/CuO_2 plane at which the Fermi surface changes. This kind of effect has been directly observed in [24].

2.6.8 Strain dependence

Before concluding this part, it is interesting to point out that REBCO tapes are inherently strong, thanks to ∼50 % of the cross section being a high strength alloy. Fig. 2.30 shows the data for five manufacturers, from [16]. Stress has very low effect on tape performance, expressed as $I_c / I_{c,max}$, and the irreversible limit is in the range 600 - 700 MPa.

2.7 Tape manufacturers

The core feature of coated conductor tape fabrication is the biaxial highly textured substrate on which to grow the REBCO layer epitaxially. This is achieved by three main methods: rolling-assisted biaxially textured substrates (RABiTS), ion beam assisted deposition (IBAD), and inclined substrate deposition (ISD).

2.7.1 American Superconductors

The approach followed by the American Superconductor Corporation (AMSC) consisted in the RABiTS method combined with metal-organic deposition (MOD).

The RABiTS method starts from a 40 mm wide and 75 μm thick NiW substrate (5% Ni) on which texturing is imposed through a deformation-recrystallization process. Buffer layers of yttria, YSZ, and ceria, of 75 nm thickness are deposited by high-rate reactive sputtering and grown epitaxially on the underlying textured substrate [57]. The YBCO precursor film, which is tri-fluoro-acetate (TFA) doped with rare earth, is coated onto

the RABiTS template, pyrolized to remove the organic compounds and converted into the epitaxial YBCO. At the present day, AMSC is not active on the market.

2.7.2 Bruker HTS

Bruker HTS adopted a non-magnetic CrNi stainless steel substrate. Following chemical and mechanical polishing, the substrate was buffered by means of an yttria-stabilized-zirconia (YSZ) layer having 1.1 - 2 μm thickness [58], deposited through the ABAD process [53]. The resulting YSZ presented the necessary biaxial texture to allow epitaxial growth of the subsequent layers.

A 'cap' layer of CeO_2 (ceria) was then inserted between the YSZ and the YBCO layer to avoid lattice mismatch between the two. Both the ceria and YBCO layer were deposited by means of PLD. A peculiarity of the Bruker process was the so-called 'dynamic' drum, which differed with respect to the more traditional reel-to-reel system, but was capable of similar throughput [58]. At the present day, Bruker HTS is also not active on the market.

2.7.3 Shanghai Superconductor Technology

As early as 2012, Shanghai Superconductor Technology (SST) switched from RABiTS to IBAD-MgO process [17].

The process currently adopted by SST involves a 10-mm wide and 50-μm thick Hastelloy C-276 substrate. The substrate is first polished and then an alumina (Al_2O_3) layer and an yttria (Y_2O_3) layer are deposited in sequence, the first being 80 nm thick to act as a diffusion barrier for the oxygen, the other being 20 nm thick to serve as a seed layer for the further MgO nucleation by reel-to-reel IBAD. This MgO layer, being 5 nm thick, is the 'core' layer implementing the biaxial texturing. A thin 20 nm layer of $LaMnO_3$ deposited by sputtering and a thick 200 nm ceria layer deposited by PLD follow. This latter layer is added to have little lattice mismatch with the further REBCO layer.

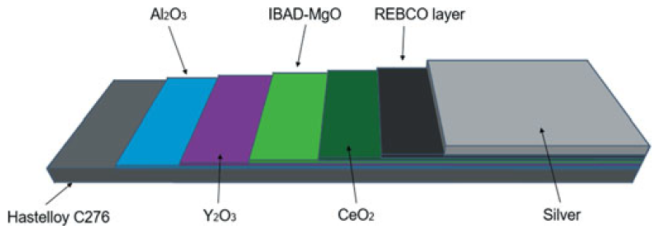

FIGURE 2.31: Typical architecture of SST tapes. Credits: [17].

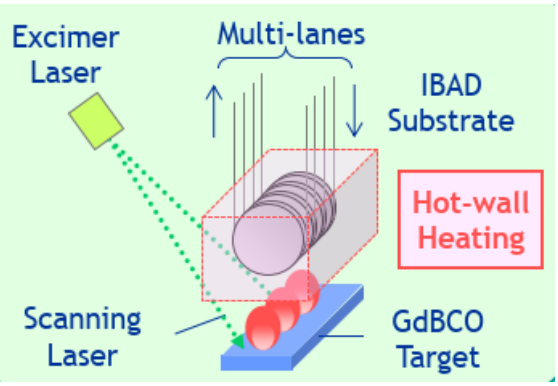

FIGURE 2.32: Representation of the hot-wall PLD technique by Fujikura. The process uses a laser to hit a GdBCO target and thus release a plasma plume on a rotating and heated drum including several tapes mounted in parallel. Credits: [18].

SST uses three different compositions for the REBCO layer, which are selected depending on the application. In particular, GdBCO is used for 77 K, self-field applications, while EuBCO + $BaHfO_3$ or (Y,Gd)BCO are for low temperature and high fields [59], [54]. A thin silver layer of 1-2 μm thickness and $\sim$20 μm copper are deposited by magnetron sputtering to close this sandwich sequence. Fig. 2.31 displays the slided open tape layer structure of SST tapes.

In recent years, SST managed in the successful attempt to increase J_{eng} of tapes both by reducing the Hastelloy substrate thickness to 30 μm and achieving even better tape I_c than with thicker substrates, by assuring a more homogeneous temperature distribution over the deposition zone [54].

2.7.4 Fujikura

The starting point of Fujikura for manufacturing coated conductor tapes is a 10-mm wide Hastelloy substrate. Originally, the polished substrate was treated by IBAD to form a biaxially textured $Gd_2Zr_2O_7$ (GZO) buffer layer. Later, it was found that a much thinner MgO layer grown on alumina (in direct contact with the substrate) could considerably reduce the buffer layer thicknesses and manufacturing time with it [60].

An intermediate ceria layer, similarly to the manufacturing process of SST, is deposited as an interface with the REBCO layer, and the rare earth element is Gd in this case. To improve tape performance, Fujikura implemented the so-called *hot-wall* PLD [61], where the region of film formation is surrounded by heaters, see Fig. 2.32 from [18].

2.7.5 SuperPower

SuperPower tapes are based on IBAD combined with MOCVD on either 50 μm or 100 μm Hastelloy C-276 polished substrates. The typical architecture of SuperPower

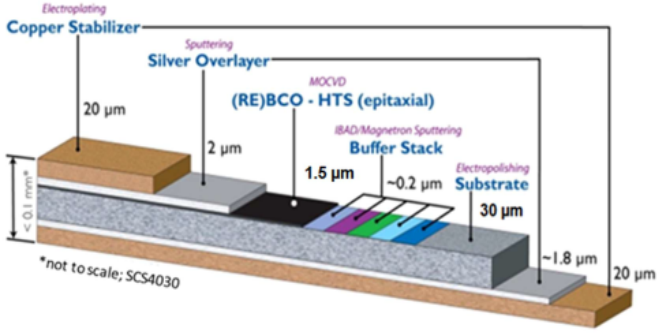

FIGURE 2.33: Typical architecture of SuperPower tapes. Credits: [19].

tapes is shown in Fig. 2.33.

Such architecture closely resembles that of Faraday Factory, Fujikura, and SST tapes. Namely, the substrate is first deposited with two thin layers of alumina and yttria by magnetron sputtering. 80 nm of alumina prevent the diffusion of atoms from the substrate to the REBCO layer, whereas 7 nm of yttria are useful for the nucleation of the subsequent 10-nm MgO layer by IBAD.

The MgO layer texture is improved by growing an additional 20 nm MgO layer epitaxially by magnetron sputtering of Mg. A 30-nm cap layer of LMO ends the sequence of buffer layers, and it is used to provide good lattice match with the REBCO film [19]. This was changed with respect to the original $SrTiO_3$ (STO) layer envisaged by LANL because of the higher stability provided by the LMO [50].

In SuperPower's process, the REBCO layer is deposited by MOCVD using a 7.5% Zr-doped precursor. A 2-μm silver layer completes the architecture, providing a path for oxygen diffusion during the annealing stage.

2.7.6 SuNAM

Fig. 2.34 displays the manufacturing process at SuNAM, which relies on RCE-DR, see Section 2.6.6.3. This process is capable of high deposition rates.

The tape architecture starts from a Hastelloy substrate that is electropolished, on top of which a succession of layers is deposited by IBAD. The first one is a ∼40 nm alumina layer serving as a diffusion barrier, while the second is a ∼7 nm yttria layer. Then, two MgO layers are grown in succession, the first being ∼10 nm thick having random texture and the second being ∼20 nm thick, the actual epitaxial layer on which to grow the REBCO.

A 20 nm LMO cap layer is grown just before the REBCO, to minimize the lattice mismatch with the underlying layers, similarly to SuperPower. For the REBCO layer, an amorphous precursor is deposited by evaporating three different metal sources of Gd,

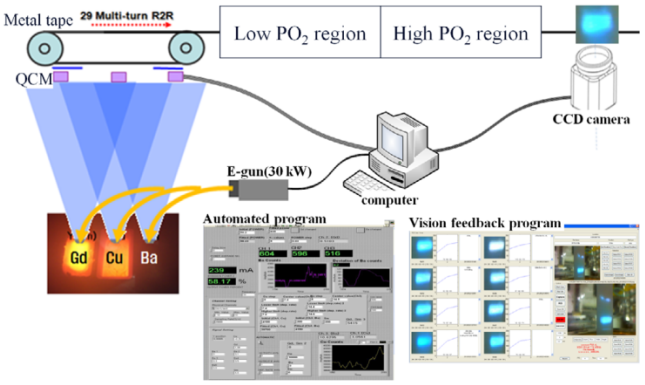

FIGURE 2.34: RCE-DR process adopted by SuNAM. The process involves an electron gun to hit different spots for various precursors, which are then deposited onto the textured substrate. A low and high oxygen pressure regions are used to complete the reaction. Credits: [20].

Ba, and Cu simultaneously. This precursor film is then transferred in a lower oxygen pressure environment at high temperature, and then further moved in a higher oxygen pressure environment to allow the conversion into the GdBCO phase. Therefore, the liquid layer is steadily residing on the surface of the growing film. The thickness ends up to be 1.5 nm and a silver protecting layer is added by DC sputtering.

2.7.7 Faraday Factory

The manufacturing route adopted by Faraday Factory closely resembles that of SST and Fujikura. In fact, the layer structure is: Hastelloy/Al_2O_3/Y_2O_3/IBAD-MgO/LMO/Ce_2O_3 [55]. The deposition is conducted in a low-pressure environment at 70 Pa. Gd has been usually adopted as the rare earth element.

The production process of coated conductors also involves silver sputtering on top of the REBCO layer and a final annealing phase in pure oxygen atmosphere, which is indicated to be at 420° for 7 hours, in [55], followed by furnace cooling.

A recent advancement in tape production at Faraday Factory [24], showed that selecting YBCO instead of GdBCO improves the $J_c(B)$ dependence. On one side, having Y instead of Gd in the crystalline structure gives higher charge carrier (hole) density in the superconductor, resulting in slightly higher CuO_2 plane concentration and better performance. On the other, YBCO allows much higher density of Y_2O_3 nanoparticles with respect to GdBCO, which is attributed to their respective phase diagrams.

2.7.8 Theva

Theva adopts an alternative way with respect to the other manufacturers. This is the inclined substrate deposition (ISD), introduced around the turn of the 2000s [49], [15].

The peculiarity of tapes manufactured by Theva is that the peak performance is at ∼30°, which in combination with other standard tapes might reveal helpful to maintain the tapes aligned to the field lines in magnetic devices.

In the last few years, another manufacturer, Subra [62] has been using the ISD process from Theva to manufacture tapes using a multifilamentary substrate.

2.8 Pinning centers in REBCO

A complex relationship exists between material defects and J_c in REBCO coated conductors. The pinning force exerted by one single defect depends on its type and size, as well as on its composition and interaction with the matrix.

Pinning centers can be divided into two main categories. The first is that of 'correlated' pinning, which act along the same spatial direction and therefore are effective when an external field is applied parallel to them. These can be either linear or planar defects and their signature is a peak in the $J_c(\theta)$ profile.

The second category is that of 'uncorrelated' or 'random' pinning, consisting of randomly-distributed defects which act uniformly along all field directions. Even if one would think of random defects as a weak form of pinning, such as point-like defects, these are also 3-D nanoparticles acting as strong pinning centers.

Defects are also classified according to their dimensionality and pinning strength. They can be pointwise, linear, planar, or spherical:

- 0-D weak defects: isotropic, usually atomic and cluster vacancies.
- 1-D strong defects: anisotropic, such as dislocations and nanorods.
- 2-D strong defects: anisotropic, typically twin boundaries and stacking faults.
- 3-D strong defects: isotropic, such as nanoparticles and nanostrain.

Vortices are thermally stable when pinned to strong defects, whereas even low thermal fluctuations (at low temperatures) make them very unstable when they are pinned to weak defects. The temperature dependence of the critical current density follows two different trends:

$$J_c^{wk}(T) = J_{c,0}^{wk} \cdot e^{-T/T_0} \tag{2.8}$$

$$J_c^{str}(T) = J_{c,0}^{str} \cdot e^{-3\left(T/T^+\right)^2} \tag{2.9}$$

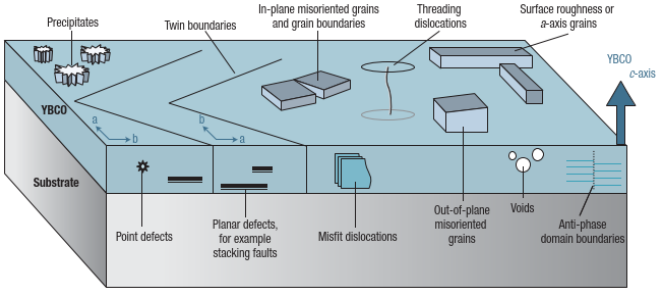

FIGURE 2.35: Types of pinning defects in REBCO. Credits: [14].

The first expression is for weak pinning centres [63], whereas the second is for strong pinning centres [64]. In the expressions, $J_{c,0}^{wk}$ and $J_{c,0}^{str}$ are the values at 0 K in the absence of creep. T_0 and T^+ are associated with the characteristic pinning energy of weak and strong pinning centres. In other terms, these two parameters account for the density and effectiveness of the pinning potentials with respect to the thermal energy.

High values of $J_{c,0}^{wk}$ and $J_{c,0}^{str}$ mean high density of pinning defects, whereas high T_0 and T^+ are a sign of higher stability to thermal fluctuations. In fact, $T_0 \approx 5$ - 20 K for weak pinning centres, and $T^+ \approx 50$ - 90 K for strong centres, and even 70 - 130 K for long anisotropic defects [46].

In the following, we discuss the pinning landscape existing in the REBCO layer, which is displayed in Fig. 2.35 from [14].

2.8.1 Stacking faults

The first type of intrinsic defects we discuss are stacking faults, which consist in the intergrowth of planes parallel to the *ab*-planes. The region surrounding the stacking fault is sparsed with partial dislocations, thus inducing a localized strain state in the lattice. A double CuO chain structure appears, and a cluster of Cu and O atoms fills the vacancies created by the presence of the stacking fault itself. These act as point defects [65].

2.8.2 Threading dislocations

This type of defect occurs at the boundaries between two growth islands and literally threads through the thickness of the REBCO layer, acting as 1-D linear defect. Their density can be increased by reducing the size of the growth islands. The work in [66] was the first one to show a direct relationship between the density of this type of defects and the resulting J_c of a thin film. In particular, it was shown that increasing the density of threading dislocations extended the single-vortex pinning regime (low-field plateau, see later) to higher fields.

2.8.3 Twin boundaries

The crystalline lattice of REBCO is orthorhombic. During the growth of the superconducting layer, it may happen that crystals with different *ab*-plane orientations meet: twin boundaries are the defects arising at the meeting planes of these domains.

2.8.4 Misfit dislocations

The REBCO layer and the substrate on which it is deposited have different lattice spacing. The mismatch between the two is compensated, in general, by elastic strain in the REBCO. However, when this is not sufficient, dislocations form to relieve the stress, as missing or extra planes of atoms [67].

2.8.5 Anti-phase boundaries

When the layers of two REBCO crystals meet imperfectly (at different 'heights'), an anti-phase boundary is formed. This can act as a pinning center [68], [23].

2.8.6 Point defects

Point defects are disruptions in the crystal structure at the atomic scale. They can be either vacancies, interstitials (extra atoms), or impurities. Sometimes, the rare earth element and barium atoms can exchange places, especially in the case of Eu, Yb, and Sm which are very similar in size to Ba.

2.8.7 Precipitates

Precipitates can either form by intrinsic growth of the REBCO layer or by extrinsic action. In the first case, secondary phases such as RE_2O_3 or Ba-Cu-O might precipitate because of deviations from the stoichiometric composition of the REBCO layer [14]. In the second case, precipitates such as $BaZrO_3$ are intentionally added to the material. The study in [69] on tapes manufactured by MOCVD shows that both of these types of defects can be produced and co-exist in the same thin film, enhancing performance both for $B \parallel c$-axis and $B \parallel ab$-planes. Planar arrays fall in this category. In fact, films often present self-assembled RE_2O_3 precipitate planar arrays aligned along the *ab*-planes [23].

2.8.8 Nanoparticles

Nanoparticles can be of various kinds, such as BZO, RE_2O_3, and Y_2BaCuO_5 [70]. Recently, a simple pinning scheme involving *intrinsic* Y_2O_3 nanoparticles rather than extrinsic nanorods has demonstrated to be capable of achieving extremely high performance tapes while being highly reproducible [24].

2.8.9 Nanorods

These are correlated pinning centers, which can be along any direction. As a result, the conduction properties are much enhanced in the direction parallel to the defects, as it is usually desired along the *c*-axis or the *ab*-planes.

Examples are BZO nanorods which enhance J_c in the high temperature regime where thermal fluctuations are strong and the contribution of weak pinning centers disappears. As mentioned earlier, the diameter of the nanorods should be in the order of the coherence length, ξ, in order to efficiently pin the flux vortices. Relevant work has been conducted about this in [55].

2.8.10 Nanostrain

Typically, the insertion of APC in the material can induce a strain state because of the mismatch between the REBCO lattice and the inclusions (e.g. BSO/BZO nanocolumns), which have larger unit cell parameter [55]. This is a typical feature of in-situ deposition methods.

2.8.11 Alternative ways to improve performance

It is relevant to remark that, even though multiple types of pinning centers coexhist in the REBCO layer, their combined effect does not necessarily sum up linearly. Actually, they can even cancel each other out [14].

A variety of alternative approaches has been studied to increase tape performance, both at 77 K, self-field conditions, as well as at low temperatures and high fields. One of these consists in the substitution and combination of rare earth elements in the crystalline lattice.

An MOCVD process was used in [71], to form a REBCO layer made either of: Yb, Y, Ho, Dy, Gd, Eu, Sm, as well as combinations of these elements. Interestingly, the study reports an increase of T_c with the rare earth ionic radius. This went from 85.2 K for

Yb up to 93.4 K for Eu, following a linear trend. Additionally, the J_c at 77 K and self-field increases with the ionic radius of the rare earth element/mixture. However, an opposite trend was observed at low temperatures and in high magnetic fields.

The data presented in [71] suggests that combinations of (Eu,Y)BCO, (Gd,Y) BCO, and (Sm,Y)BCO are good choices for applications at intermediate to high temperatures of 40 - 77 K, in self-field, and down to very low magnetic fields (<0.1 T). In between 65 - 77 K and fields below 3 T, EuBCO and GdBCO show high J_c, with (Gd,Eu)BCO being also useful for applications in this range. In the intermediate temperature interval, 20 - 40 K, YBCO appears as the best, whereas (Gd,Yb)BCO is applicable in average fields of 3 - 5 T and between 10 - 20 K, something that can be attributed to the high density of vertical and horizontal aligned defects. Additional ways of improving performance are through non-stoichiometric compositions.

2.9 Applications of HTS

Thanks to the features discussed so far, REBCO coated conductors enable energy efficient and high power density delivery of electricity, making them key materials for power transmission, clean energy generation, transportation, solenoid magnets, fusion experiments, and particle accelerators [13].

2.9.1 Power transmission

Transmission lines made of HTS cables have been installed since many years now. A three-phase cable built out of Bi-2223 tapes was one of the earliest applications [72]. Tapes in this cable were wound around a central former of 7 cm in diameter, and could carry an overall 3 kA RMS at 73 K. The actual cable was made of three of these sub-cables, one for each phase. A similar cable [73] was wound out of YBCO tapes and could carry 800 A RMS per phase at 69 K, for a total cable diameter of 3.5 cm (per phase).

The CORC architecture has been proposed more recently [74] and it has been demonstrated to be very promising to use REBCO coated conductors for power transmission applications as well. One recent example of HTS for power transmission in a scientific environment is the superconducting (SC) link project at CERN [75]. The cable for the SC link is roughly 80 meters long and it is composed of a Nb-Ti section, an MgB_2 section, as well as of a REBCO section. The cable is made of a bundle of cables that are capable of carrying up to 120 kA at a temperature of 50 - 60 K in helium gas at the level of the REBCO section.

On the societal side, it is worth mentioning the case of the project for the Montparnasse train station in Paris, where a superconducting line carrying 5.3 MW will be installed to meet the growing energy demand [76].

2.9.2 Energy generation in wind turbines

REBCO coated conductors can be employed in the generation of electric energy. Not later than five years ago, the EcoSwing project aimed at building the first superconducting generator for wind turbines [77]. The project successfully built a new generator, composed of a conventional stator and a superconducting rotor to produce 3.6 MW of mechanical input power at 15 rpm rotation speed. The generator was installed and operated successfully in a wind farm in Denmark.

2.9.3 Magnetic levitation

Non-conventional trains operating by the principle of magnetic levitation are generally referred to as Maglevs [78]. Maglevs use two different sets of magnets for levitation and propulsion. A few examples of Maglevs have been constructed during the 1980s and 1990s, however this type of transportation was typically conceived for short distances, in the order of 10 km, and low speeds, below 150 km/h.

Many efforts have been conducted in recent years to build Maglevs that could travel at higher speeds (above 300 km/h). In fact, the electrodynamic suspension configuration is particularly suitable to employ superconducting coils. This configuration uses a set of superconducting coils on board of the train, while an active coil for propulsion is powered on the track and a passive coil for levitation and guiding is also present on the track. A clear interactive explanation of the working principles of this system is available at [79].

The Central Japan Railway company is developing a superconducting Maglev operating with Nb-Ti coils to start operations in 2027. REBCO coated conductors and HTS more in general have a huge potential also in this type of application. A first trial in this direction has been conducted by the German company Boegl in collaboration with the Southwest Jiaotong University in China who built a prototype, called the Super Bullet Maglev, which reached a cruise speed of 620 km/h [80].

2.9.4 Solenoids

2.9.4.1 NMR magnets

The limit of LTS technology to build solenoid magnets for research applications such as Nuclear Resonance Imaging (NMR) is 23.5 T, corresponding to a 1 GHz frequency, which is given by Nb_3Sn ($B_{c2,0}$ = 30 T). Solutions to go beyond this magnetic field value usually employ an LTS outsert combined with a HTS insert. Currently, the record field of a commercial application has been established at 28.2 T by adopting this hybrid solution by Bruker [81].

2.9.4.2 Research magnets

Research magnets are also solenoid magnets that can reach even higher fields than NMR. This is thanks to smaller bore diameters which allow achieving the same stress state as in the lower-field, wider-bore configuration.

A remarkable reference for research magnets is the full-superconducting 32 T solenoid built at NHMFL [82], [83]. This is composed of a 15 T LTS outsert (wound with both Nb-Ti and Nb_3Sn) plus a 17 T insert wound with REBCO tapes. Another useful reference is the REBCO insert designed by the Seoul National University which generates 14.4 T inside the bore of a 31.1 T resistive Bitter magnet, to attain the largest DC magnetic field available worldwide, 45.5 T [84].

2.9.5 Fusion experiments

The irreversibility field of REBCO coated conductors enables them to generate much higher magnetic fields than their main LTS 'competitor', Nb_3Sn. This constitutes a considerable advantage in the design of fusion devices of small size, in order to achieve the poloidal field/plasma current needed for sufficient stability [85]. The fusion power per unit volume scales as B_0^4, with B_0 being the magnetic field in the plasma. In addition, the plasma confinement improves at higher magnetic field strength. The ARC design foresees to have demountable TF coils generating 9.2 T on the torus axis, and 23 T peak field on the coil. This is much higher than ITER, which will have roughly 5.5 T in the plasma and 12 T peak field on the coil.

Furthermore, the operation will be at 20 K, which has several advantages compared to 4.2 K. First, the cost of cooling is drastically reduced, thanks to Carnot's law. Second, the thermal stability of the coil would be much higher, because of the higher specific heat of materials (which is almost 80 times for copper, 5 - 10 times for Hastelloy and

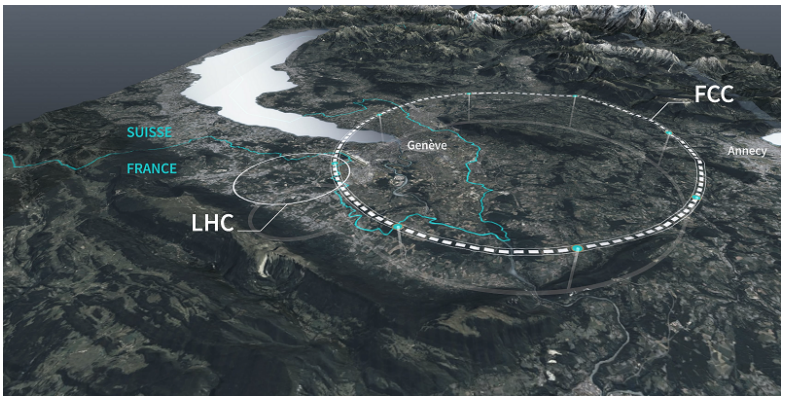

FIGURE 2.36: Representation of the Future Circular Collider around the Geneva area. Credits: [21].

steel). Third, other coolants other than liquid helium could be used, such as gaseous helium, liquid hydrogen, or liquid neon.

Several other projects involving REBCO coated conductors to achieve the magnetic confinement of fusion in relatively small-sized reactors came to life in recent years. Many efforts are in the direction of spherical tokamaks [86] as well as stellators [87].

2.9.6 Particle accelerators

The enhanced performance of REBCO coated conductors and HTS, in general, is being considered to build high-energy physics (HEP) experiments worldwide.

At present, two main projects aim at achieving a 100-TeV class hadron-hadron (h - h) collider in the center-of-mass. The first is the so-called Future Circular Collider (FCC) at CERN [88]. This will likely be preceded by an electron-positron machine, similarly to what happened with the LEP and LHC. The second is the CEPC project in China [89]. Both projects foresee the construction of a 80 - 100 km underground tunnel with 20 T class dipole magnets to achieve the 100 TeV proton collisions. While it is foreseen that the FCC h-h collider will employ magnets with either Nb_3Sn or REBCO, the CEPC might opt for iron-based superconductors [90].

Chapter 3

Scaling laws and experimental methods

3.1 Scaling laws

3.1.1 Introduction

High temperature superconductors (HTS) in the form of coated conductor (CC) tapes have increasingly been employed in recent years for high-field magnet applications, thanks to their very good ability to transport current in high fields.

Originally, applications of REBCO CCs were envisaged for power transmission cables, following the example of first-generation (1G) Bi-2223 wires for which in-field performance was limited [91]. Then, the driver of development became the design and construction of solenoids, such as the case of the 32 T hybrid configuration combining a 15 T low-temperature superconducting (LTS) magnet with a 17 T insert of HTS [83]. In recent years, fusion experiments [92] have also been leading the way, thanks to the remarkable improvement of the performance of REBCO CCs in high magnetic fields [24]. Particle accelerators [93], [94] have also sparked considerable activities on this subject.

REBCO, and HTS in general, is a complex material and its critical current, I_c, depends on the magnetic field intensity, B, temperature, T, and orientation angle, θ, of the magnetic field with respect to the tape, $I_c(B, T, \theta)$ [95]. This results from the anisotropic features of the crystalline lattice of REBCO, which induces much better electrical conduction along the *ab*-planes than along the *c*-axis, due to the mass anisotropy.

Furthermore, REBCO CCs can include a variety of engineered defects for improving the electrical properties. These can be differentiated into two types. The first type are uncorrelated (random) defects, such as precipitates and point defects, which enhance the conduction at all angles. Alternatively, there can be correlated defects such

as nanorods, twin boundaries and dislocations that enhance the performance at specific angles [14].

Such an intrinsic material complexity is augmented by the manufacturing route, which determines the growth rate of the REBCO layer and the artificial pinning landscape, which in turn impacts considerably on the critical current dependence upon field, temperature, and angle [46]. This influence has been reported to be originated from the supersaturation, namely the discrepancy in concentration of the REBCO species from the equilibrium level [13], which drives nucleation and is highly dependent on the manufacturing route.

At present, the design of a device is constrained, basically, to the choice of a single type of tape from a specific manufacturer and it demands for the full characterization of the tape performance over the ranges of interest. Moreover, the full experimental characterization of the $I_c(B, T, \theta)$ of a tape over a wide field, temperature, and angular domain is a complex and time consuming procedure [96].

So-called *scaling laws* are needed to describe the tape properties and a thorough experimental campaign is needed to validate them [97]. Scaling laws validated by experimental effort are of the utmost importance for the design of coils and magnets. In this chapter, we propose an extension of an existing scaling law for the complete description of the critical current of REBCO tapes, which is applicable to tapes from any manufacturing method.

3.1.2 Review of past scaling laws for LTS and REBCO

A full magnetic field dependence of the I_c of REBCO CCs lacks at present, unlike for Nb-Ti and Nb_3Sn [98].

The behaviour of REBCO is comparable to that of LTS, although data are not available, in general, at low fields for REBCO. In fact, demagnetization effects are small for LTS, as they are manufactured in thin filaments, therefore losses induced by magnetization are very little. This is not the case for REBCO, which is produced in wide single filaments and a similar scaling law as for LTS would result in the underestimation of magnetization losses. This is why a more complete description is of primary importance.

Most previous works on scaling laws [95], [96], [97] focused only on the intermediate field region, typically between 2 T to 10 T, presenting a phenomenological scaling of the field dependence of I_c of the type $B^{-\alpha}$. This description has been particularly useful for magnet design and a satisfactory match with experimental datasets was obtained over a limited range of magnetic fields.

Plots are usually reported in double logarithmic scale, such that this law is a straight line with slope $-\alpha$, see for example the dashed line in Fig. 3.1, where α was set to

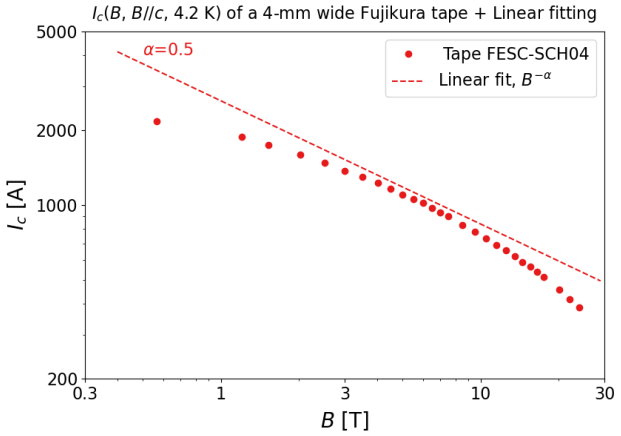

FIGURE 3.1: Non-linear I_c field dependence of a Fujikura tape. Reproduced from [22].

0.5 for simplicity. The match is already satisfactory in the intermediate field region. However, the low and high field region are overlooked in the phenomenological scaling and experimental data diverge considerably from the constant slope, both for $B < 2$ T and $B > 10$ T, as again can be grasped from Fig. 3.1.

A Kramer-like expression [98], [99] allows incorporating the high field region in the description of tape performance, Eq. 3.1. The scaling law from Kramer was originally defined for the pinning force, F_p. Usually, this is expressed in N/m^3 or N/mm^3, but here it is intended as integrated over the cross section and expressed in N/m. In this way, the critical current can be derived as $I_c = F_p/B$.

$$F_p = \beta \cdot \left(\frac{B}{B_{c,2}}\right)^p \cdot \left(1 - \frac{B}{B_{c,2}}\right)^q \tag{3.1}$$

The knowledge on this high-field region is essential for the design of solenoids, fusion experiments, and particle accelerators, as mentioned in the Introduction. Based on Kramer's approach, Fleiter and Ballarino [100] proposed:

$$I_c(B) = \frac{\beta}{B} \cdot b^p \cdot (1-b)^q \tag{3.2}$$

where b is the reduced field, defined as the ratio between the magnetic field and the irreversibility field, B/B_{irr}, while β, p, and q are the fitting parameters. The relevant feature of this equation is that it can be applied to the I_c parameterization along the c-axis and ab-plane directions as well.

Eq. 3.2 has solid foundations in the physics of pinning, since it is a typical Kramer expression, where the critical current has been derived explicitly by dividing the equation for the integrated pinning force by the magnetic field, B. Moreover, Eq. 3.2 has

the advantage of containing B_{irr} instead of the upper critical field $B_{c,2}$ (commonly used for LTS), which is the quantity of interest for HTS. In fact, B_{irr} is almost equal to $B_{c,2}$ for LTS, while HTS suffer more for the reduction of B_{irr} from $B_{c,2}$, due to the much shorter coherence length, ξ.

Both the phenomenological expression, $B^{-\alpha}$, and the pinning approach, Eq. 3.2, deal with intermediate fields as this is interesting for most applications. However, they suffer from singularities at low fields. Indeed, I_c in the phenomenological description tends inevitably to infinity when B approaches zero; something similar occurs in Eq. 3.2 since B is at the denominator.

Clearly, I_c cannot be infinite because of the physical constraints imposed by the depairing of the Cooper pairs [3]. This is why the validity of these laws is generally provided starting from roughly 1 T at 4.2 K. There is also an upper field limit for the validity, as curves depart from the linear behavior, typical of the log-log plot, at relatively small fractions of the ratio $B/B_{irr} \approx 0.1$ - 0.15. Tape quality can also affect the validity of these laws, as well as the angular orientation of the field.

Besides the critical current, the pinning force should also be zero at zero field. In fact, it is zero in the pinning approach, while it should be $\alpha < 1$ for it to be zero in the phenomenological approach [101]. The opposite condition, $\alpha > 1$, is not acceptable as it would result in the pinning force being infinite.

Only the description of the low field region is missing, at this point. The reason for such an interest is for: 1) elaborating the effect of the self-field on the I_c, and 2) computing magnetization effects in REBCO at low fields.

From the conventional Kramer expression [98], [99] and the work of Fleiter and Ballarino [100], our proposal is to substitute b in the second term with the expression $(1 + b/b_0)$, where $b_0 = B_0/B_{irr}$. Also, p is replaced with the expression $1 - \alpha$. The resulting most complete mathematical description of the I_c field dependence of REBCO tapes is proposed in Eq. 3.3.

$$I_c(B, T^*, \theta^*) = I^*_{c,0} \cdot \left(1 + \frac{B}{B^*_0}\right)^{-\alpha^*} \cdot \left(1 - \frac{B}{B^*_{irr}}\right)^{q^*} \tag{3.3}$$

The equation presents only the magnetic field dependence. For compactness, it is expressed for a generic temperature T^* and orientation of the external field, indicated as θ^*. For example, one could think of T^*= 4.2 K and θ^*= 0°.

Let us note that each parameter in Eq. 3.3 depends on the temperature and/or the angle. To begin with, $I^*_{c,0} = I_c(T^*, B = 0)$ regardless of the angle. Then, the crossover field, $B^*_0 = B_0(T^*, \theta^*)$ is a function of both the temperature and the angle. Something similar occurs for the other parameters in the formula, namely the slope of the linear region,

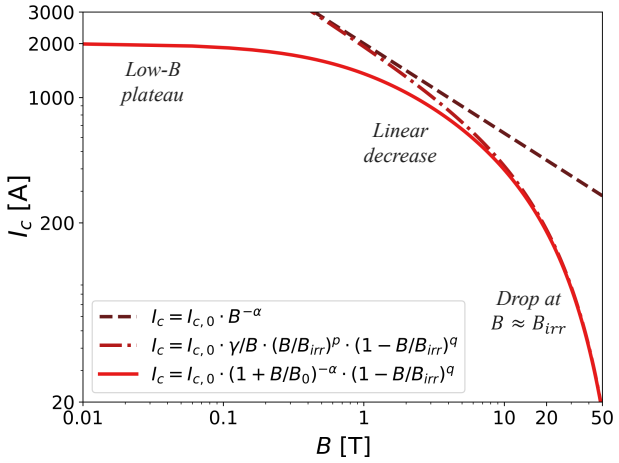

FIGURE 3.2: Comparison of scaling curves. Parameters are set to representative values.

$\alpha^* = \alpha(T^*, \theta^*)$, the irreversibility field, $B^*_{irr} = B_{irr}(T^*, \theta^*)$, and the slope associated to the further drop in performance, $q^* = q(T^*, \theta^*)$.

In particular, $I^*_{c,0}$ is the intercept defining the initial height of the curve, while α^* in the second term defines the slope of the linear region: the higher α^*, the faster the decline. Introducing B^*_0 allows a finite I_c at zero field, while resulting in the pinning force being zero, see Fig. 3.3b. Let us emphasize that the purpose of the third term is to account for the discrepancy of experimental data to the scaling law $B^{-\alpha}$ at high fields. The value of q^* in the third term determines the rapidity of the further performance drop at high fields. For example, $q^* = 1$ results in a linear dependence, while $q^* = 2$ in a parabolic shape in a linear plot.

Here, we focus on the field part only. In general, parameters very according to the manufacturer, depending on the deposition process of the REBCO layer and by the pinning centers introduced in the material. Let us note that the orientation angle is defined with respect to the tape normal. The direction parallel to the *ab*-planes, usually θ=90°, gives the highest critical current.

Fig. 3.2 helps visualizing the difference between the three scaling laws. The dashed curve is for the phenomenological scaling $B^{-\alpha}$, where the slope $-\alpha$ remains always constant. The dashdot curve corresponds to Eq. 3.2, which displays the drop at high fields. Finally, the solid curve is the proposed scaling, Eq. 3.3, which has the potential to describe all the three regions of the curve.

3.1.3 Foundations in the physics of pinning

The scaling law proposed in Eq. 3.3 is solidly derived from the physics of pinning. Multiplying it by B allows obtaining the actual expression for the pinning force. The

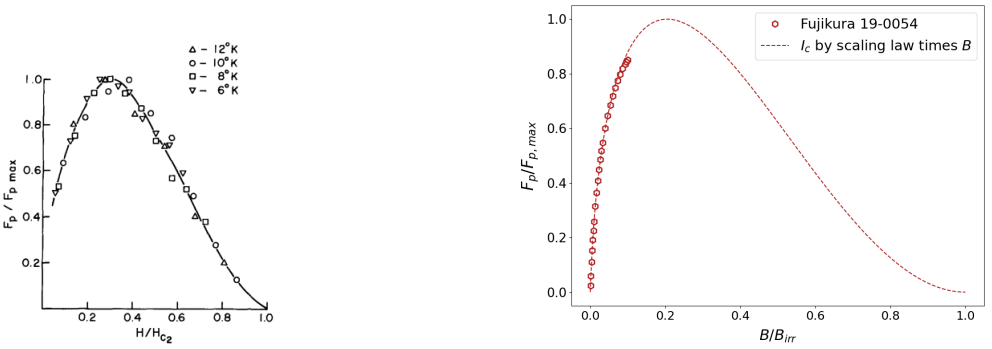

(A) For Nb_3Sn [98]. (B) For a REBCO tape tested here.

FIGURE 3.3: Normalized pinning force versus normalized field.

result, after a number of transformations, is:

$$F_p = F_{p,0} \cdot \left(\frac{1+b'}{b'} \right)^{p^*-1} \cdot b^{p^*} \cdot (1-b)^{q^*} \tag{3.4}$$

where $F_{p,0} = I^*_{c,0} \cdot (B^*_0)^{\alpha^*} \cdot (B^*_{irr})^{1-\alpha^*}$, expressed in N/m, $b = B/B_{irr}$ is the reduced field, $b' = B/B^*_0$ is the modified reduced crossover field, and $p^* = 1 - \alpha^*$. Note that one could have defined b' as B^*_0/B and get the term $(1+b')^{p^*-1}$ in Eq. 3.4, but a definition similar to b is preferable.

Fig. 3.3a displays the shape of the normalized pinning force for Nb_3Sn as presented in [98]. Instead, Fig. 3.3b displays the shape of the scaling law applied to the actual data of a Fujikura tape tested in the scope of this work (see chapter 4 and 5).

Let us note that the pinning force is zero at zero field, as expected from the physics. This is the actual advantage with respect to the phenomenological and pinning approaches described above, given by the presence of the

$$\left(1 + \frac{B}{B_0} \right)^{-\alpha}$$

term. Measured data stop at a reduced field of 0.1, where B_{irr} was assumed to be 150 T. The curve peak is located at 20 % of the irreversibility field.

3.1.4 Full field dependence

The field dependence of I_c is the combination of three regions when looking at a double logarithmic plot. For example, shown in Fig. 3.4 are the data of a SuperPower tape

tested from 10 K up to 77 K for an applied magnetic field ranging from 0.2 T up to 16 T, reproduced from [23]. The J_c in Fig. 3.4 was derived in [23] from four-probe transport current measurements on bridges of 10 - 50 μm width.

Eq. 3.3 has been applied to the dataset reported in [23] and the resulting fitting is shown in Fig. 3.4 by using dashed lines. An optimization algorithm was used to find the values of the fitting parameters $I^*_{c,0}$, B^*_0, α^*, B^*_{irr}, and q^* in Eq. 3.3. The fitting gave a maximum least square parameter, $\chi^2 = 5.4$, corresponding to the 10 K curve. In general, χ^2 is acceptable up to a value close to the number of datapoints, which is around twenty for the curves in Fig. 3.4. Therefore, this result seemed promising.

In this work, we discuss about the I_c, rather than the critical current density, J_c, as presented in Fig. 3.4. In fact, the I_c is the actual practical quantity measured in tapes. The same considerations derived for the I_c, nonetheless, can be applied to the J_c as well as to the non-copper engineering current density, $J_{eng,nonCu}$, taking into account constant factors given by the cross section of the REBCO layer and of the non-copper layers, respectively.

The three regions are represented schematically by the two dashed diagonal lines. *Region I* is characterized by a constant value of the critical current near zero external field, which is a function of temperature, $I_{c,0}(T)$. At intermediate temperatures, such region extends from 10^{-3} to 10^{-1} T, the lower limit of Fig. 3.4, where a mild slope characterizes the subsequent low-field region. However, at 10 K, this regime extends up to ~0.3 T.

Vortices barely interact with each other in *Region I*, as their density is much lower than the density of the pinning centers [102]. The pinning energy is much larger than the energy associated to vortex-vortex interactions, which is why this regime is called the

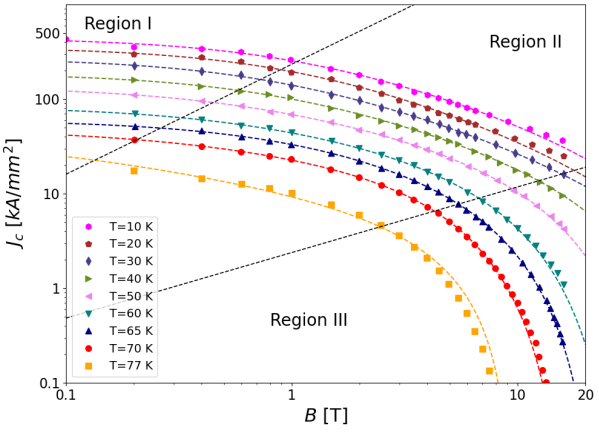

FIGURE 3.4: $J_c(B, B \parallel c\text{-axis})$ dependence of a SuperPower tape tested in [23]. Overlapped are the dashed lines with the fitting resulting from the proposed scaling law at each temperature level.

'single vortex' pinning regime. The value of $I_{c,0}$ can be improved by acting on interfacial misfit dislocations, as shown in [14] and [67]. In addition, Dam et al. [66] found that inter-island threading dislocations can be used to extend the plateau region.

The so-called 'kink', 'crossover', or 'accommodation' field, B_0, marks the transition to *Region II* where I_c is controlled by the collective interaction of vortex bundles confined in a fixed volume. This causes the linear field dependence in the log-log plot. Another relevant quantity is the matching field, B_ϕ, namely the field corresponding to the density of APCs. This is given by $n \cdot \phi_0$, with n being the density of APCs and ϕ_0 the flux quantum.

The matching field is an intrinsic property of the material, therefore it does not depend on temperature. Conversely, the crossover field is a function of temperature, $B_0(T)$, which explains the slope of the upper diagonal line in Fig. 3.4. It is relevant to note that $B_0 \leq B_\phi$. Specifically, B_0 is the field value corresponding to the crossing between the two constant slopes of *Region I* (flat) and *Region II*. Particle-induced dislocations reduce the slope of the linear region, as shown in [70].

Finally, the performance drops even more rapidly in *Region III*, as the field approaches the irreversibility field, B_{irr}, the practical limit of HTS. This is referred to as the thermal activation regime since thermal fluctuations are very effective in de-pinning the weak pinning centers from intermediate temperatures (30 K - 40 K), leaving only the strong centers such as 1-D columnar defects, which are much lower in density. The lower dashed line in Fig. 3.4 is an indication that B_{irr} is a function of temperature as well, see for example [103].

3.1.5 Lack of data at low fields

To complement this part, it is useful to mention that measurements on 4 mm tapes available in the literature are typically limited in current. Fig. 3.5, which is reproduced from [24], shows the results of the testing of tape samples from the same manufacturer, performed by three different institutes. The first tape, tested by Tohoku University (represented in black) had a 40 μm substrate and 2.55 μm thick YBCO layer. The second tape, tested by the University of Geneva, had a 60 μm substrate and 2.82 μm YBCO layer. Finally, the tape tested by NHMFL (in blue) had a 100 μm substrate and 3.28 μm YBCO layer.

Fig. 3.5 clearly shows that the region below 3 T is empty of data. In turn, this corresponds to currents exceeding 1800 A. Coated conductors have reached extremely high performance, which makes it challenging to fully characterize them even in 4 mm widths. Overlapped to the datapoints in the plot is the fitting obtained with the scaling law, Eq. 3.3. The absence of data in the low-field region does not allow the transition

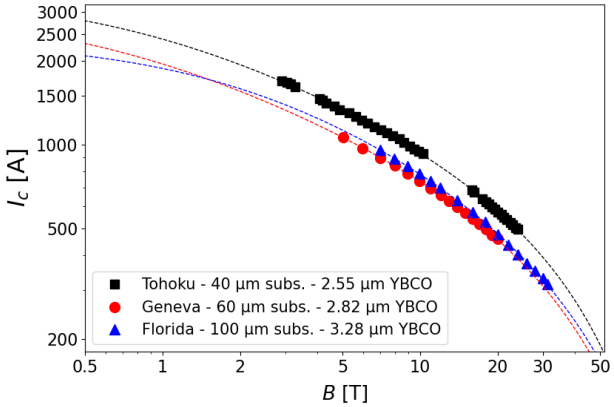

FIGURE 3.5: 4 mm tapes from S-Innovations tested by three different institutes. Testing is limited to 3 T, 1800 A. The plot is adapted from [24] and dashed lines are for the fitting with the relevant scaling law, showing that performance is overestimated below 2 T.

from *Region I* to *Region II*, namely the B_0, to be observed. As a result, the fitting routine overshoots the value of $I_{c,0}$, which becomes unrealistic below the 0.5 T shown in Fig. 3.5.

In this context, it is relevant to mention the database from the Robinson Research Institute [104]. Data are publicly available for multiple tapes, however the temperature is limited to 12.5 K at most, and currents to 1 kA [105]. While this is a very useful reference, the aim of this work is to explore directly the properties down to 4.2 K, as this information is crucial to design high-field accelerator magnets.

To summarize, we have pointed out, on one side, that the full $I_c(B)$ dependence is characterized by three regions due to different pinning regimes. The need for a comprehensive scaling law stems from the fact that only partial descriptions are currently available in the literature. Such a law has been proposed in this work, as an extension of an existing law that is valid for LTS and it is based on the physics of pinning. Therefore, the next step is to validate the law against experimental data, to prove its general character and apply it to tapes from different manufacturers. The high performance of commercial tapes, together with the variety of pinning centers, makes it necessary to conduct an independent experimental campaign to investigate the electrical properties of tapes and validate the proposed scaling law.

3.2 Experimental methods

Two different experimental methods have been employed to test REBCO tapes. The first method consists in injecting a transport current in a tape immersed in a liquid

helium bath at 4.2 K and exposed to background magnetic fields of up to 15 T, perpendicular to the broad face of the tape. The second method relies on a Vibrating Sample Magnetometer (VSM) and measures the magnetic moment of tapes which oscillate rapidly inside a slowly ramping background magnetic field.

One of the objectives of this measurement campaign was also to assess the agreement between these two different methods. By checking that the same field dependence is measured at 4.2 K with both, the transport method is useful to establish the absolute value of $I_{c,0}$(4.2 K) to scale the curves obtained at the other temperature levels by the magnetization method. Eventually, this enables the temperature dependence of the scaling parameters to be determined for each tape, which is fundamental for the full description of Eq. 3.3. The features of the experimental set-ups are described in the following.

3.2.1 Transport current

Starting from the transport method, a U-shaped sample holder was developed, similar in concept but different in construction with respect to the one reported in [106], with the aim to measure the I_c of tapes in liquid helium at 4.2 K as a function of the applied magnetic field. In particular, the goal was to explore the region down to low field levels (<2 T), where the critical current surpasses 1500 A [107] and the relevant fitting parameter B_0 is directly accessible. The testing has been conducted thanks to a solenoid test station available in the laboratory at CERN that allows up to 3 kA to be injected in the samples, in background magnetic fields of up to 15 T.

Fig. 3.6 shows a photograph of the sample holder. This is constituted of three parts: two copper bars connected to a central G10 piece. A 4.5 mm-wide groove runs along the entire length of the sample holder, both in the copper and in the G10, which is used

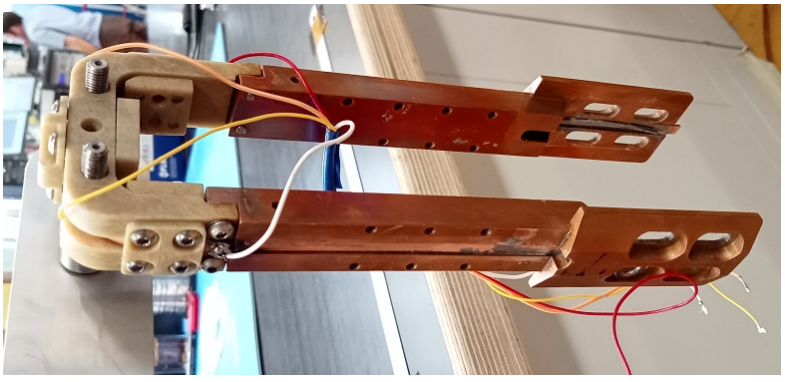

FIGURE 3.6: Photograph of the U-shape sample holder. The holder is composed of two copper bars for current injection and extraction, and of a central G10 part. The length where the sample is exposed to perpendicular field is 15 mm.

FIGURE 3.7: U-shape sample holder mounted on the solenoid insert. The white piece is used to add rigidity to the holder, but later revealed to be unnecessary.

to host the tape. The tape itself is soldered onto the copper bars by means of a 60%Pb - 40%Sn solder (melting temperature: 180 °C) along the full length of the bars, 15 cm.

From Fig. 3.6, one may notice that the copper bars have wider and thinner terminations (visible on the right of the figure) with respect to the main body. The copper bars are directly screwed onto the current leads of the solenoid insert, see Fig. 3.7. This way, the current enters the sample through the copper bars and it is then transferred into the REBCO tape through the soldering.

During the design stage, a white 'filling' piece had been also conceived, see again Fig. 3.7. This piece was slid onto the U-shape, then the two pieces were mounted together onto the solenoid insert. Let us note that the design of this piece was intended to match the features of the insert. For example, it presented four grooves for matching the G10 'fingers' of the insert, two of which are visible in Fig. 3.7. The scope of the filling block was to keep the U-shape tightly in position during testing. Later during the measurement campaign, it was observed that the U-shape was sufficiently stable onto the current leads, therefore mounting of this piece could be omitted.

The reason for choosing the central region in G10 insulating material rather than a single block of copper or another electrical conducting material was to avoid current sharing with the holder in the region of interest for the measurement, which had been observed in some initial trials using a single-block stainless steel holder.

The central U-shape creates a short straight region ($\sim$15 mm long) where the tape broad face lies perpendicular to the background field generated by the solenoid. The design implemented an inner 1.5 mm groove and six transversal holes into an already existing 4.5 mm groove that hosts the tape, to improve the heat exchange between the tape and the liquid helium. This has been the essential feature to surpass the barrier of 2000 A injected in the sample, that was particularly limiting during the early stages of the work. Fig. 3.8 is a closeup of the mentioned inner groove in the central G10 piece.

We would like to mention that the design of the sample holder was greatly influenced by the configuration of the solenoid insert, see the lower part of it in Fig. 3.9. In fact, the

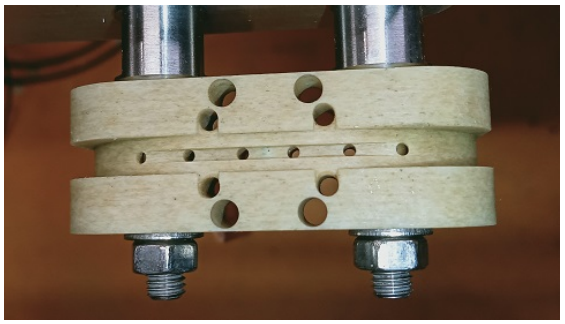

FIGURE 3.8: Inner 1.5 mm groove with six transversal holes for improving the cooling between the tape and the liquid helium. These are inside a 4.5 mm wide groove hosting the tape in the central G10 piece.

insert was originally conceived for testing Nb-Ti and Nb_3Sn wires using the so-called VAMAS sample holder, a short cylindrical bar around which the superconducting wire is wound in a solenoid-like geometry. A central bar is used for installing two VAMAS holders on the insert, to allow testing two wires at a time. Four 'fingers' made of G10, used to contain the VAMAS externally, complete the assembly. It was a tight requirement of the design of the U-shape sample holder to not introduce any modification to the solenoid insert, because of the importance of the inserts for the laboratory activities.

A first idea consisted to design a holder that could fit only on one side of the insert cross section, namely that it would fully lie on one side of the central bar. This would have allowed for two different holders (i.e. tape samples) to be tested at the same time.

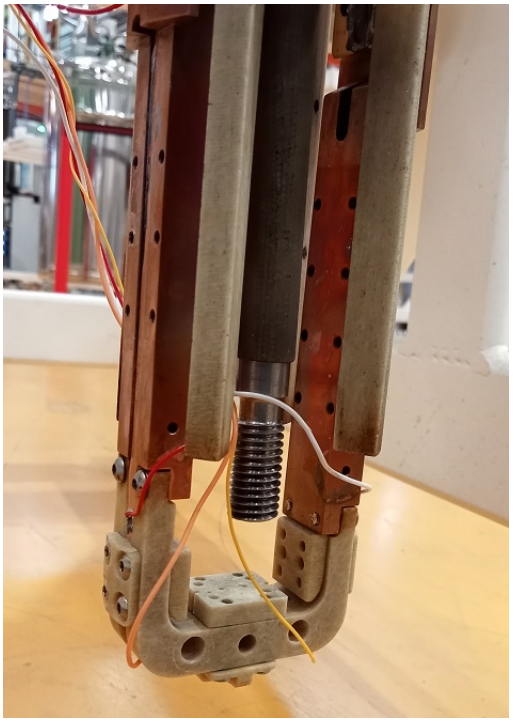

FIGURE 3.9: U-shape mounted on the insert, without the filling piece. The holder bypasses the central bar, typically used for mounting the VAMAS sample holders.

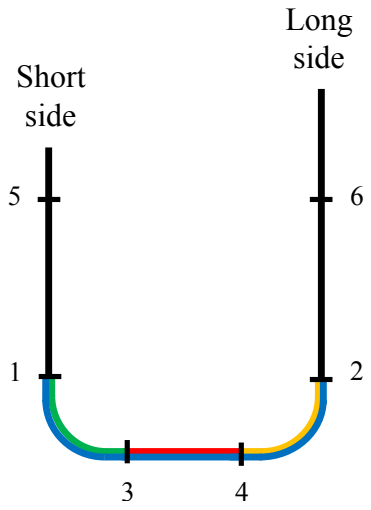

FIGURE 3.10: Schematics of the voltage taps on the U-shape. They can also be seen in the actual holder in Fig. 3.9. Color codes correspond to plots presented later in chapter 4.

However, such a configuration would have granted only ∼40 mm of total transversal length. This would have resulted in a very tight bending diameter, likely inducing tape degradation at each new mounting of a tape sample, as well as in a too short measurement region.

For these reasons, such a solution would have been highly impractical to design and operate, and eventually it was discarded. Then, it was decided to bypass the central bar and use the full available bore diameter of 67 mm. The complication was that, then, the sample would have been outside the high- and homogenized field region. To solve this issue, a wedge to be installed at the top of the cold region was designed to compensate for the difference in height.

As a result, the designed bending radius of the holder was 18 mm, a compromise between exceeding the minimum bending radii of commercial tapes, typically around 15 - 20 mm, having a sufficiently long straight region transversal to the field, and fitting the holder inside the magnet bore (67 mm).

Two voltage taps are located at the extremities of the straight region (indicated as 3 and 4, in Fig. 3.10), and the resulting voltage signal is extracted to derive the critical current. Other pairs of voltage taps are located across the bent regions (1 - 3 and 4 - 2) and the copper bars (5 - 6) to monitor the status of the superconductor all over the sample holder. Three small plates over the G10 region complete the assembly. They are also made of G10 and they keep the tape inside the groove both during the sample preparation procedure and measurement.

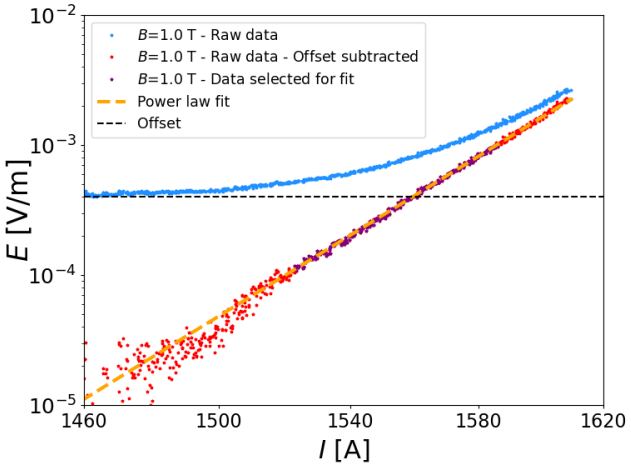

FIGURE 3.11: Raw data (in blue) and raw data after subtraction of the offset (in red) used to extract the I_c and the n-value for a 1 T background field of the tape from Faraday Factory. Highlighted in purple are the data in the relevant electric field range from 10^{-4} to 10^{-3} V/m fitted using the power law.

The list of released technical drawings produced for the parts of this sample holder is available at `https://edms.cern.ch/document/2795729/1`. Following the manufacturing of the pieces, the procedure for mounting and dismouting the assembly was also defined. This can be found in CERN EDMS document no. 3223386 [108].

Fig. 3.11 presents the raw data (in blue) of the testing of a 4 mm wide tape from Faraday Factory, measured in a 1 T background field. The offset (black dashed line) has then been subtracted and the result (in red) has been fitted using the power law, deriving the I_c and the *n-value*. Repeating the procedure for all magnetic field levels, one obtains Fig. 3.12, where the two quantities are plotted as a function of the applied magnetic field (scale is linear).

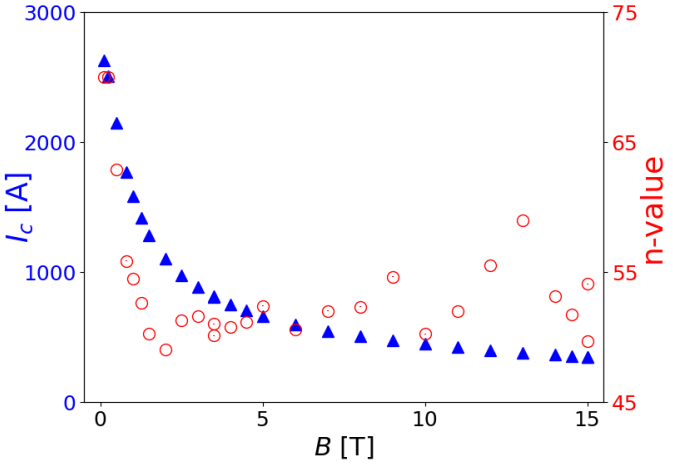

FIGURE 3.12: Resulting field dependence of both the I_c and the n-value for the same tape discussed in Fig. 3.11. Error bars are comprised within the symbols.

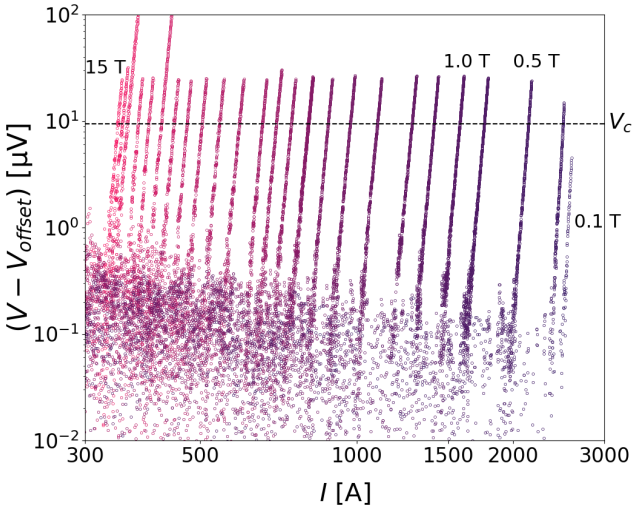

FIGURE 3.13: Raw data cleaned by the offset from a transport current test of a 4 mm tape from Faraday Factory. Curves are for field levels from 15 T (left) down to 0.1 T (right), corresponding to roughly 2600 A injected in the tape.

Fig. 3.13 shows the voltage 'cleaned' by subtraction of the offset for all the background field levels, from 15 T (on the left) to 0.1 T (on the right). We injected up to 2600 A in the final test at 0.1 T, at which current level the tape burnt. No copper shunt was included in parallel to the REBCO conductor. Following transition, curves showed even higher slopes due to heating. Heating is supposed to originate from the copper bars, despite the considerable copper cross section available (180 mm^2). This might also be at the origin of the tape burning observed in the last run at 0.1 T background field, which occurred in the segment in contact with the copper bars.

3.2.2 Magnetization

Magnetization measurements have also been performed to cross check the data from the transport current method at 4.2 K, and to extend the measurement range to higher temperatures, using a vibrating sample magnetometer (VSM) at CERN. A couple of references about this station can be found at [109] and [110].

Fig. 3.14a shows a schematic of the VSM facility. To begin with, the background field coil is depicted in orange. This is a superconducting coil that provides the uniform field in which the sample is immersed. The magnet of the VSM is wound out of Nb-Ti and it generates a maximum field of 10.5 T. In a typical magnetic cycle, the field is ramped from zero up to 10.5 T, lowered to -2 T, then up to 2 T, and finally decreased again to zero. In fact, the magnetization cycle is symmetric at negative fields with respect to positive fields, thus it is valuable to study the region down to only -2 T, to verify that the return branch of the curve overlaps to the virgin one up to 2 T. The ramp rate is usually set between 200 - 350 mT/min.

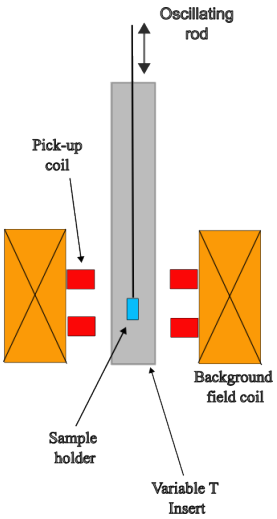

(A) Schematic.

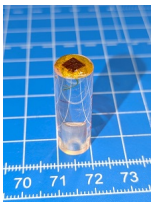

(B) VSM sample mounted on its holder.

FIGURE 3.14: VSM station installed at CERN.

A sample with its holder (see Fig. 3.14b) is attached at the end of a vertical rod, which oscillates at a fixed frequency, selected in the range between 10 - 50 Hz (but typically set to 20 Hz). The oscillation causes a variation of the magnetic flux seen by the sample over time, which induces currents to flow in the sample to counteract the external field and shield the sample interior. The variable magnetic flux generated by these currents is recorded by the pick-up coils as a voltage and it is then converted to a magnetic moment.

The sample with its sample holder is located in the Inner Helium Vessel (IHV), also called Variable Temperature Insert (VTI). The temperature and pressure of the VTI are controlled such that the sample experiences the conditions between the minimum

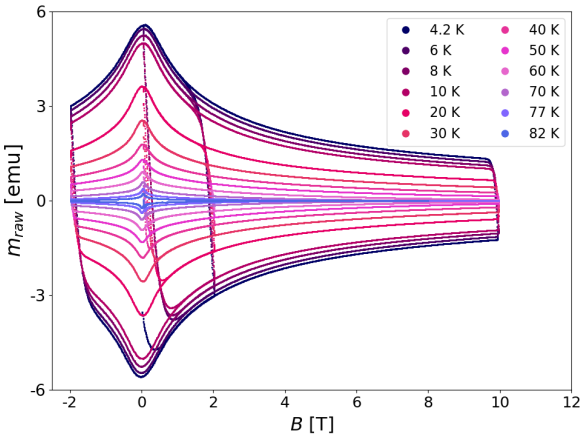

FIGURE 3.15: Magnetic hysteresis cycles measured on an SST tape, from 4.2 K up to 82 K.

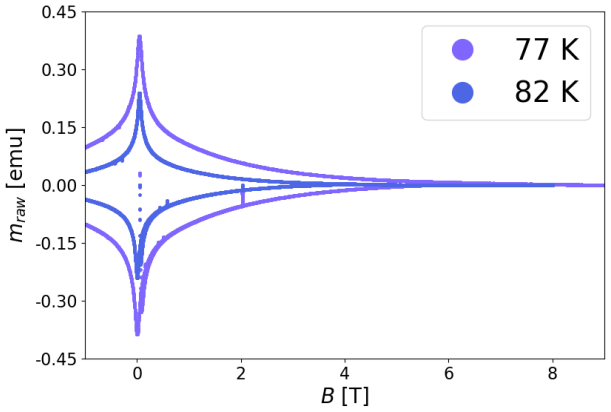

FIGURE 3.16: Irreversibility field at 77 K and at 82 K, for the SST tape.

available temperature, 1.7 K, for the system under consideration, up to the critical temperature, T_c, which is around 90 K for REBCO coated conductors.

Fig. 3.15 shows the magnetization cycles obtained for a tape of Shanghai Superconductor Technology (SST, see again later in chapter 5), from 4.2 K to 82 K. The ability of this method to measure at various temperature levels allows to directly observe the irreversibility field. See for example, Fig. 3.16, where this is 7 T at 77 K and 3.5 T at 82 K.

3.3 Angular scaling

We add another layer of complexity to Eq. 3.3 that is, the angular dependence. It is well known that the anisotropic crystalline lattice of REBCO at the microscale induces different electrical properties along different directions. In fact, the conduction of the charge carriers in the superconducting layer takes place much more efficiently along the *ab*-planes than along the *c*-axis.

Nevertheless, adding inclusions to the material helps improving the electrical properties. Random (uncorrelated) defects enhance conduction at all angles, while correlated defects act at specific angles (e.g. parallel to the *c*-axis).

Fig. 3.17 reports an example of a multiple-peak angular dependence of two YBCO films [25]. In this work, the phenomenological angular scaling from Hilton et al. [95] is adopted, see Eq. 3.5.

$$I_c(\theta) = I_0 + \sum_{k=1}^{n} I_{c,k} \cdot \frac{1}{\omega_k \cdot \varepsilon(\omega_k; \theta - \varphi_k)} \tag{3.5}$$

where n is the number of peaks in the curve; $I_{c,k}$ is the intensity of each peak; ω_k is called the peak sharpness parameter. The higher ω_k, the sharper the peak. Finally, φ_k is the phase shift.

I_0 is the base value, common to all peaks. It could also be seen as an additional term of the summation associated to $\omega_0 = 1$, therefore it does not present any angular variation. Then, the ε function in Eq. 3.5 is defined as:

$$\varepsilon(\omega_k; \theta - \varphi_k) = \left[cos^2(\theta - \varphi_k) + \frac{1}{\omega_k^2} \cdot sin^2(\theta - \varphi_k) \right]^{\frac{1}{2}} \tag{3.6}$$

Eq. 3.6 is inspired by the effective electronic mass anisotropy of the Ginzburg-Landau theory, but only its mathematical form is adopted here, where the factor ω_k is a fit

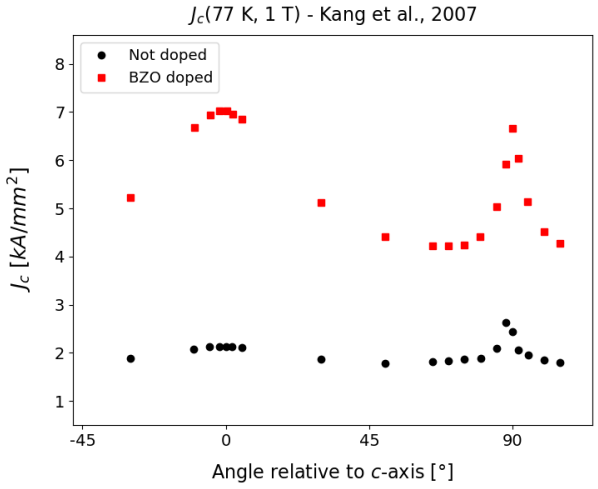

FIGURE 3.17: Multiple-peak angular dependence of two YBCO films. Reproduced from [25].

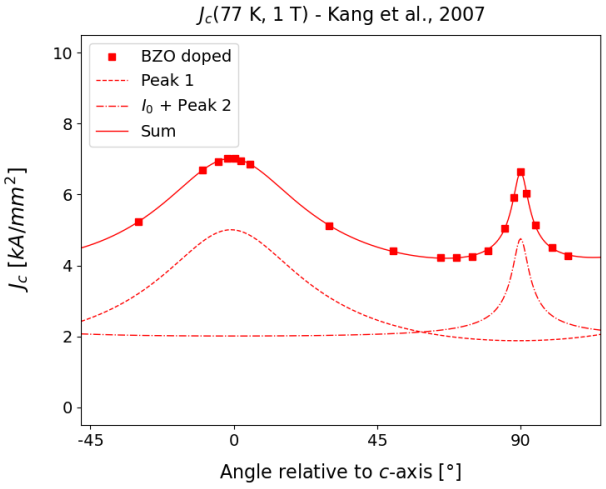

FIGURE 3.18: Peak contribution separation for the BZO doped tape in Fig. 3.17.

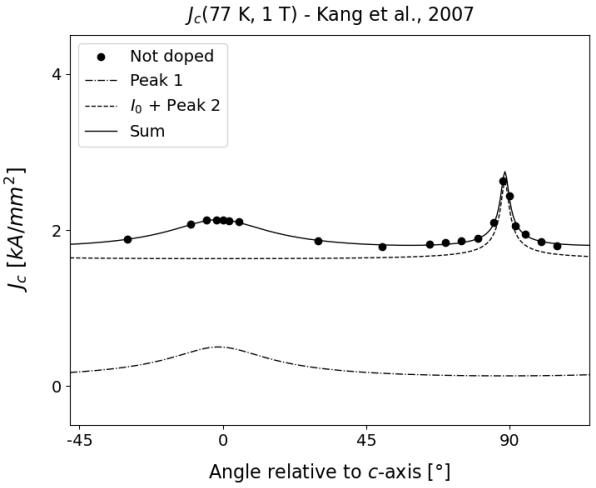

FIGURE 3.19: Peak contribution separation for the non-doped tape in Fig. 3.17.

	I_0	$I_{c,1}$	ω_1	φ_1	$I_{c,2}$	ω_2	φ_2
Not doped	1.6	1.0	45.9	-1.3°	0.5	3.9	88.5°
BZO doped	1.9	2.9	23.4	-0.9°	5.0	2.7	90°

TABLE 3.1: Resulting scaling parameters for both the non-doped and BZO doped tapes.

parameter free to vary.

Let us isolate the two curves in the plot and show the contributions given by each peak, see Fig. 3.18 and 3.19. Let us specify that both curves have two peaks, corresponding roughly to the direction parallel to the *ab*-planes and the *c*-axis. Note that I_0 is summed to the second peak to have it at the same level of the first peak in both plots. Table 3.1 reports the resulting fitting parameters obtained applying Eq. 3.5.

The range of application of Eq. 3.5 is vast. Let us show another example, from Civale et al. [26], where the J_c angular dependence of a YBCO tape is reported at (76 K, 5 T),

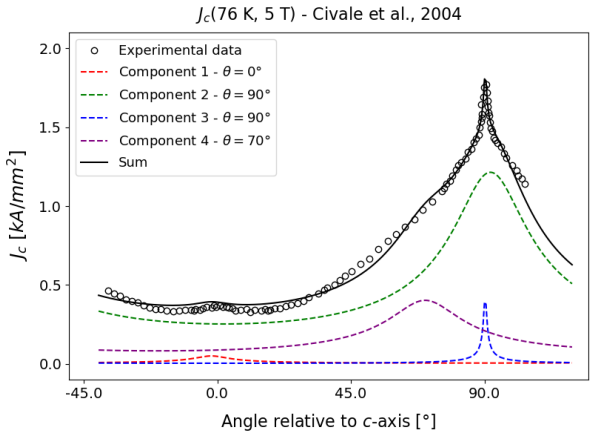

FIGURE 3.20: Separation of contributions resulting in four peaks. Adapted from [26].

see Fig. 3.20.

As a start, a broad maximum can be identified at $\theta = 90°$, namely for $B \parallel ab$, which is due to the combination of mass anisotropy and random defects: this is modeled by the green dashed line. A sharper peak, represented in blue, appears on top of the broad one at this angular position. This is associated to intrinsic pinning and extended planar defects. Another small peak is centered on the c-axis, θ=0°, arising from correlated defects (e.g. twin boundaries and edge dislocations), shown with the red dashed line. The best fitting of the experimental data is actually achieved adding a fourth peak, placed at 70° (purple dashed line). The black solid line is the sum of the four mentioned curves and it constitutes a valid fitting of the experimental data.

Chapter 4

Experimental results: Transport current

4.1 Description of a typical test with the U-shape sample holder

The test of 4 mm tape samples using the U-shape holder starts from the background field of 15 T, the highest available in the solenoid facility. This is chosen since the current level involved is the lowest, thus minimizing the risk of tape burning during the early runs. In turn, this allows efficient testing since more data can be extracted from each test. An example of unsuccessful testing from the low-field, high-current regime will be presented later in the discussion.

Fig. 4.1a shows the *pure* raw data of the test of a SuperPower tape sample at 15 T background field. The y-axis is for the voltage in microvolts and the x-axis for the current

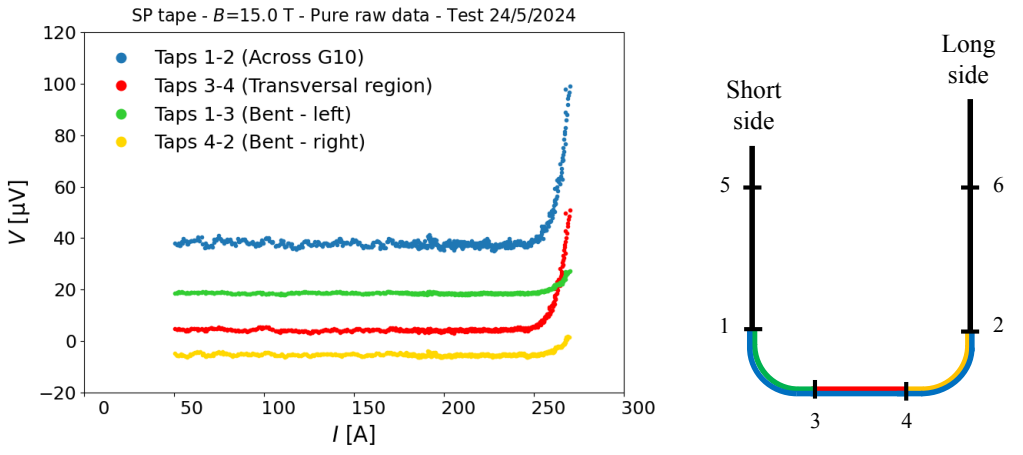

(A) Raw data

(B) Schematics of the voltage taps.

FIGURE 4.1: Pure raw data of the test of a SuperPower tape sample at 15 T background field (left). Color codes correspond to the same locations in the schematics (right).

V taps	*Offset* [μV]	*Distance* [mm]	*Protection* [mV]
1-2	38	89	20
3-4	5	18	5
1-3	18	28	5
4-2	-5	28	5

TABLE 4.1: Features of the different pairs of voltage taps.

in amperes. Let us note that the data recording starts from 50 A, which is why data are absent at lower currents. Fig. 4.1b summarizes the layout of the six voltage taps installed along the U-shape. Four of these (1 to 4) are on the G10 part, while the other two (5 and 6) are located on the copper bars. Color codes in the two figures correspond.

The curves are recorded using different voltmeters. Therefore, each curve is characterized by a different offset, which is $\sim$ -5 μV for the yellow curve (taps 4 - 2), 5 μV for the red curve (taps 3 - 4), 18 μV for the green curve (taps 1 - 3) and 38 μV for the blue curve (taps 1 - 2). Table 4.1 reports these values together with the settings for the protection system.

In the test runs, the current injected in the sample is increased by the 'measure' method. This latter method consists in rising the current in small steps and waiting at each step for the inductive signal to disappear. The setting for the first run at 15 T is reported in Table 4.2. The 'M' stays for the measure method while 'S' stands for 'step'. Basically, the testing is divided into three phases. The first phase goes from zero current up to 180 A and it is performed at a pace of '0.8'. This stays for a current increase by 0.8 A per step. Since each step lasts roughly 0.3 s, the equivalent ramp rate is 2.5 A/s.

In the second phase, the current increases from 180 A to 500 A at 0.2 A/step. This is done to avoid a rapid stress cumulation on the tape, while acquiring sufficient data during transition to later apply the power law. Finally, once either the upper 500 A limit or the limit of the protection system is reached, the current is cut automatically by the

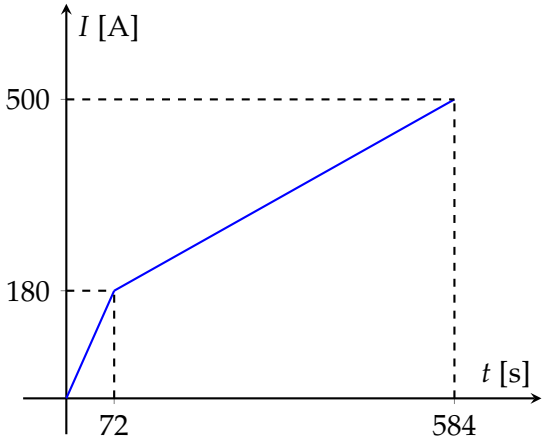

FIGURE 4.2: Applied current vs time

M	0	180	0.8
M	180	500	0.2
S	500	0	

TABLE 4.2: Software settings

protection system. This is the step drop, 'S', indicated above, which is also represented in Fig. 4.2.

The offsets are compensated to compare the curves directly, see Fig. 4.3a, which displays voltage data from 220 A, namely 80 % of I_c. All curves lie around the zero at such currents, then they depart from each other when approaching transition. The red curve, which corresponds to the transverse region to the field (3 - 4) is the first to experience transition: this occurs at 265 A. Then, the red curve follows a power-law behavior and its voltage reaches $\sim$50 μV at 270 A.

At that moment, the current is cut manually even before the protection system. In the meantime, also the green (1 - 3) and yellow (4 - 2) curves undergo a voltage increase, as they end up at 8 - 9 μV when the powering is cut. In fact, the tape passes from the parallel to the perpendicular configuration over the bent regions. Consequently, the transition is slower due to the average angular contribution from each differently oriented location. It does not come as a surprise that these two curves have very similar slopes, as they are symmetric to each other. Finally, the blue curve is the signal over the entire region 1 - 2, which is basically the sum of the previous three regions.

Fig. 4.3b is the associated normalized plot. Namely, the current is divided by the I_c and the voltage by the critical voltage, V_c. This latter quantity is calculated as the product of the critical electric field, $E_c = 10^{-3}$ V/m, with the distance between the different pairs of voltage taps, reported in Table 4.1. Then, it does not come as a surprise that the normalized voltage is highest for the transversal region 3-4.

Let us specify that the tape is subjected to the Lorentz force during testing. This force pushes the tape laterally against one of the groove edges in the transverse region to the field. The voltage signal used to be quite noisy during the first trials with the U-shape, which was attributed to small tape movements. Therefore, it was decided to align the tape during mounting against the edge where the Lorentz force was expected to act (see the mounting procedure in [108]).

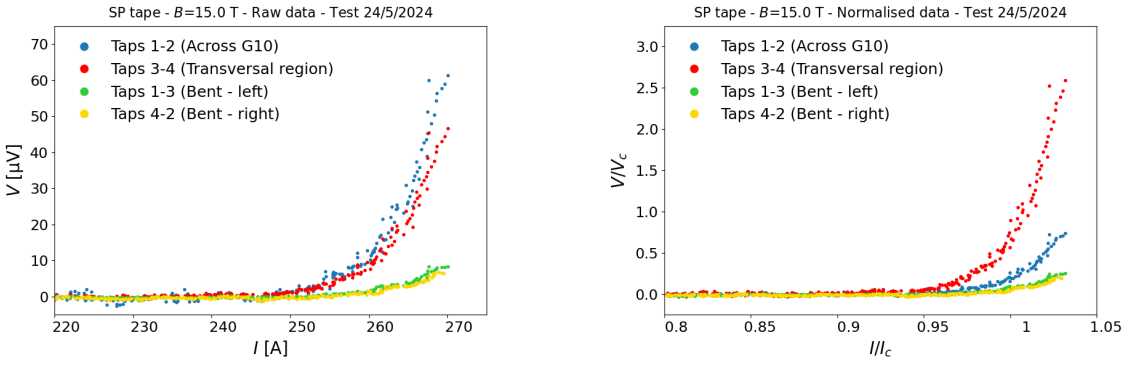

(A) Raw data (B) Normalized data

FIGURE 4.3: Test of a SuperPower tape sample at 15 T background field.

Implementing this detail in the sample preparation, the voltage signals tend to be noisy only during the very first test run, which is attributed to the tape still slightly adjusting itself in position. In fact, as shown also later, the Lorentz force is the highest at 15 T, namely the worst condition occurs at the very beginning of the test. The measurement at 15 T is usually repeated a couple of times to let the tape fully stabilize. As the test progresses, the Lorentz force acting on the tape reduces with decreasing field, even if this corresponds to a current increase.

The test continues by lowering down the field to 5 T in steps of 1 T. An intermediate step is conducted at 14.5 T, since the ramp of the background field solenoid is quite slow between 14 T and 15 T, which does not add much time to the testing while adding a precious point to the dataset. Let us specify that the ramp is set in a similar way to the one described in Fig. 4.2, where the current level at which the ramp rate lowers is set roughly 100 A before the expected transition at each field level.

Fig. 4.4a shows a detail of the test at 5 T in the final ∼90 A (scale is log-log). The behavior is very similar to the one described in Fig. 4.3a for the first test at 15 T. Clearly, the I_c is higher, passing from 265 A to 585 A. Fig. 4.4b is the normalized plot, also in log-log scale, where the curve from the region transversal to the field stands out. Below

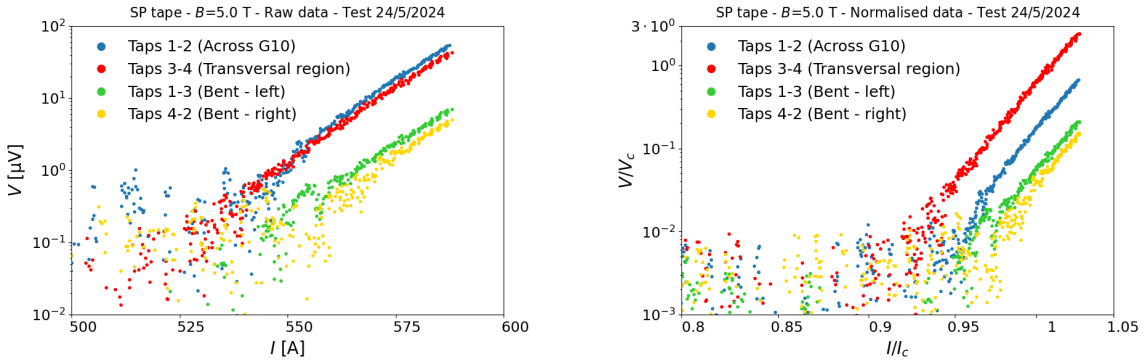

(A) Raw data (B) Normalized data

FIGURE 4.4: Test of the SuperPower tape sample at 5 T background field.

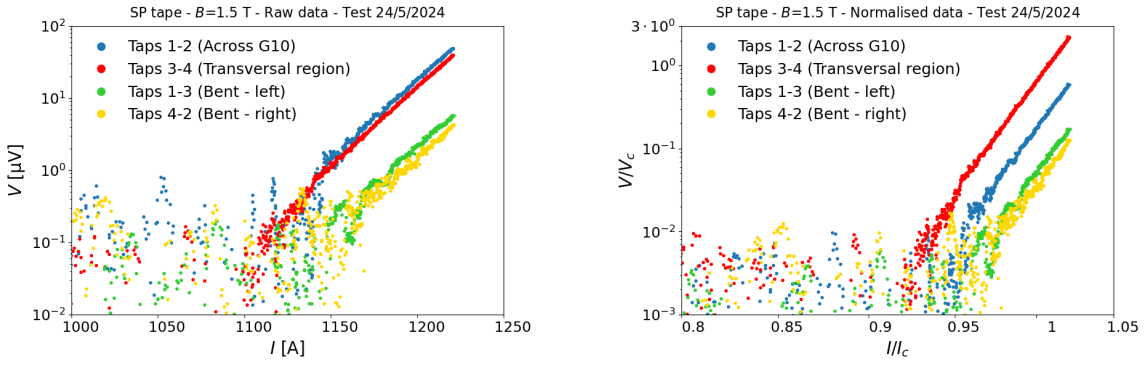

(A) Raw data (B) Normalized data

FIGURE 4.5: Test of the SuperPower tape sample at 1.5 T background field.

5 T, the field is further lowered in steps of 0.5 T down to 1.5 T. This is done to refine the number of data points, since the transition from *Region II* to *Region I* of collective pinning occurs between 2 - 3 T.

Then, again, Fig. 4.5a is for the 1.5 T background field. The overall behavior remains the same, where now the green curve for the bent region 1-3 displays a slightly higher signal than the yellow curve for the bent region 4-2. The I_c = 1220 A. The test continues

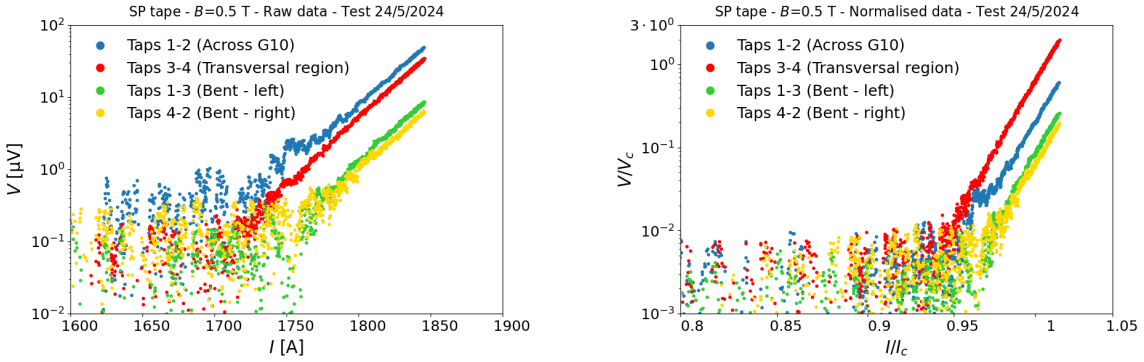

(A) Raw data (B) Normalized data

FIGURE 4.6: Test of the SuperPower tape sample at 0.5 T background field.

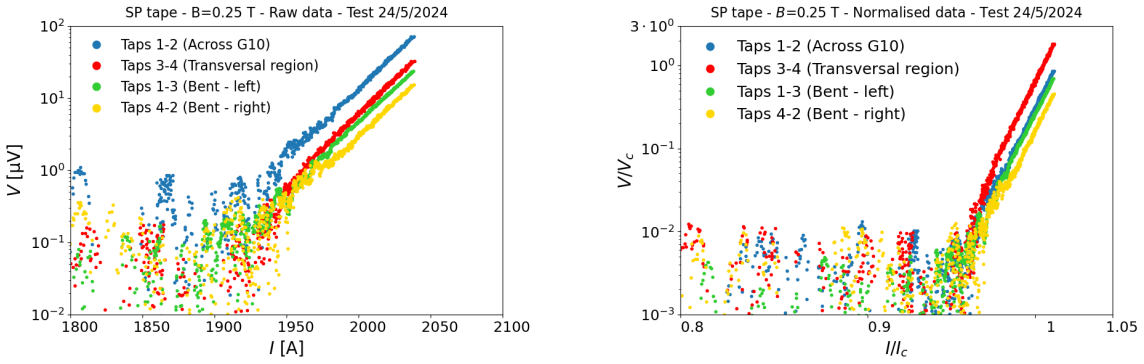

(A) Raw data (B) Normalized data

FIGURE 4.7: Test of the SuperPower tape sample at 0.25 T background field.

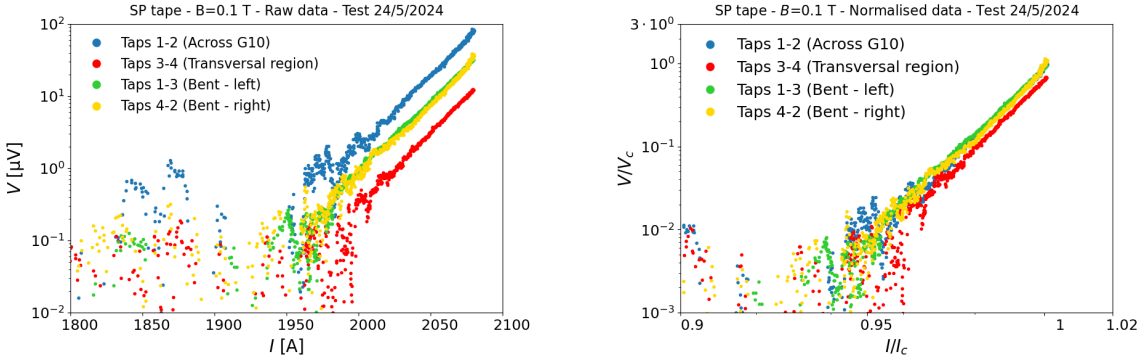

(A) Raw data (B) Normalized data

FIGURE 4.8: Test of the SuperPower tape sample at 0.1 T background field.

further by lowering the field to zero in steps of 0.25 T since the current increases considerably at each step. Fig. 4.6a shows the situation at 0.5 T background field. The tape I_c = 1850 A.

It is now relevant to look at the evolution of signals in the two final runs, at 0.25 T and 0.1 T background field, see Fig. 4.7a and Fig. 4.8a, as well as at their associated normalized plots, Fig. 4.7b and Fig. 4.8b. Signals are very low at first, being 10^{-2} - 10^{-1} μV below 1950 A.

Then, all curves lie parallel to each other, i.e. they have the same constant slope. In Fig. 4.7, the red curve for the region transverse to the field still lies above the green and yellow for the two bent regions. However, the gap with the green curve is considerably reduced. Jumping to Fig. 4.8, the red curve lies lowest this time while the green and yellow are a factor five to six higher.

This has been interpreted as the result of partial degradation, which might be attributed to local imperfections in the crystalline lattice inducing an early transition. Another reason might be due to excessive heating originating from the copper bars and descending into the tape along the bent regions (the closest to the copper bars). However, it is unlikely that heating might have such a relevant impact and the first motivation is considered to be more probable. In any case, the signal from the central region was still high enough to evaluate the I_c, which is 2078 A.

We note from Fig. 4.4 to Fig. 4.8 that slopes are constant all the way up to transition, regardless of the applied field. Fig. 4.9 sums up the signal only from taps 3-4 from the previous normalized plots. This allows visualizing the difference in slope, which is the n-value, through the power law relation $E = E_c(I/I_c)^n$. Then, Fig. 4.10 shows the resulting linear plot for the I_c field dependence as well as the n-values. This is very high around zero field, being 93.9 at 0.1 T and 87.6 at 0.25 T, then drops to ∼50 at 2.5 T,

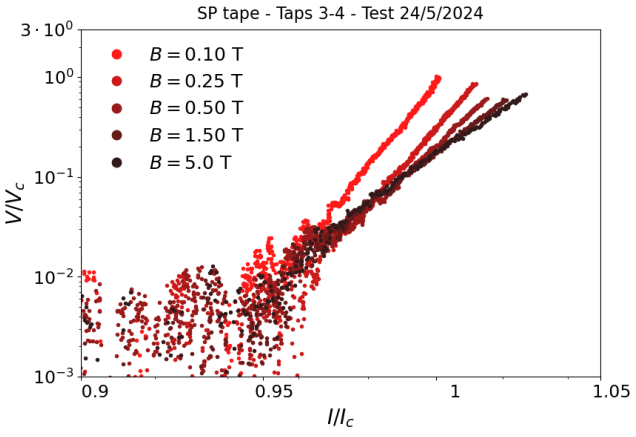

FIGURE 4.9: Comparison of the normalized signal for taps 3-4 from 0.1 T to 5 T, showing the decreasing slope and thus n-values, with increasing field.

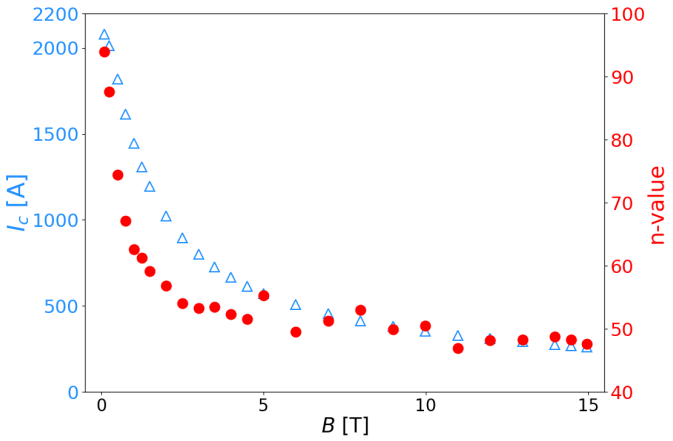

FIGURE 4.10: I_c and n-value field dependence for the SP tape. Error bars are comprised within the symbols.

and it remains between 45 - 55 up to 15 T. Eventually, the tape burnt next to one voltage tap on the inside of region 3 - 4, see Fig. 4.11.

For the sake of completeness, the signal along the copper bars is displayed. One voltage tap is installed in the left bar and another one in the right bar (5 and 6, as shown in Fig. 4.1b). In total, six taps are installed in the sample holder. However, the test station is equipped with four nano-voltmeters, meaning that only four signals can be acquired during a test run. Consequently, specific runs during the test are dedicated to monitor the behavior of the copper bars, which occurs typically at 15 T, at an intermediate field (e.g. 5 T), and at lower field (2 T) levels. Fig. 4.12 shows the raw data of a run at 5 T for the same test conducted on 24/05/24.

Four combinations of voltage taps are described. The first is 5-1, represented in light blue, which covers the straight section on the left, comprising most of the copper bar and the first centimeter on the G10 piece. The second is 5-3, represented in dark blue, which encompasses the same as 5-1 plus the bent region on the left (1-3). The third is

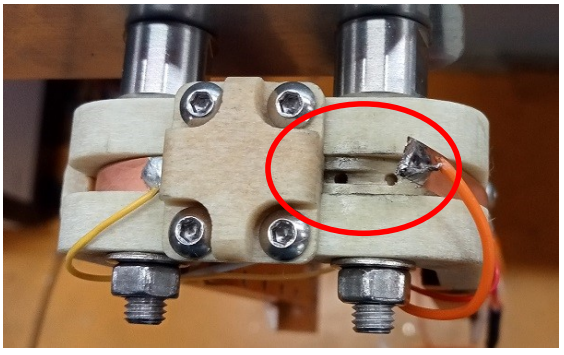

FIGURE 4.11: Visual inspection after testing on 24/05/24. The inspection revealed that tape burning occurred between taps 3 - 4 in the central region of the holder. See the red oval where the tape on the right side of the central plate stands out of the groove.

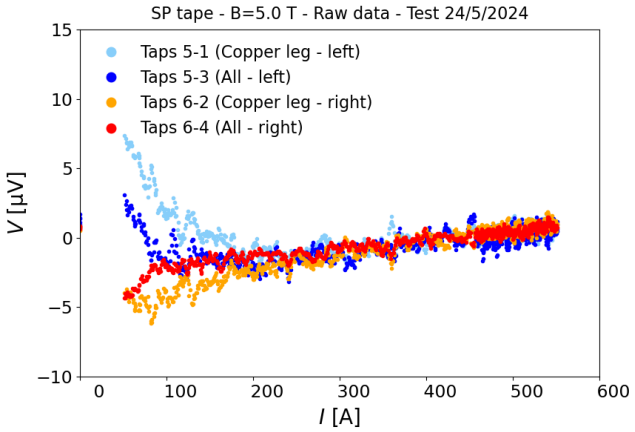

FIGURE 4.12: Raw data of the resistive signal generated along the copper bars in the test of a SuperPower tape sample at 5 T background field.

6-4, represented in orange, which covers the straight section on the right, comprising most of the copper bar and the first centimeter on the G10 piece. Finally, there is 6-4, represented in red, which covers the same region as 6-2 plus the bent region on the right (4-2).

A residual inductive signal is observed below ∼200 A, which vanishes as the measurement progresses and it does not play an important role. At even higher currents, the voltages align to each other and increase with roughly constant slopes. In fact, the voltage increases by roughly 2 μV from 300 A (when the voltages align to each other) to 550 A, the level of current cut. Therefore, we estimate the resistance of the copper bars to be 10 - 15 nΩ. This value is rather satisfying, considering that this system has not been designed to minimize the contact resistance while rather to allow the I_c measurement.

4.2 $I_c(B)$ dependence

The most important outcome of this test is the $I_c(B)$ dependence, displayed in double logarithmic scale in Fig. 4.13. This test was chosen as it provides the full description of the evolution during testing. In particular, we highlight the presence of both *Region I* and *Region II*, the latter having constant slope up to 15 T. Let us observe the remarkable performance which surpasses 1800 A below 0.5 T. This was precisely the objective set in Chapter 3 and shows the ability of our measurement setup in exploring beyond the limits in the literature.

Furthermore, data are available down to 0.1 T background field, which is of primary importance for the scaling. We must bear in mind that such a high current in the tape generates a self-field. Two different scenarios must be taken into consideration:

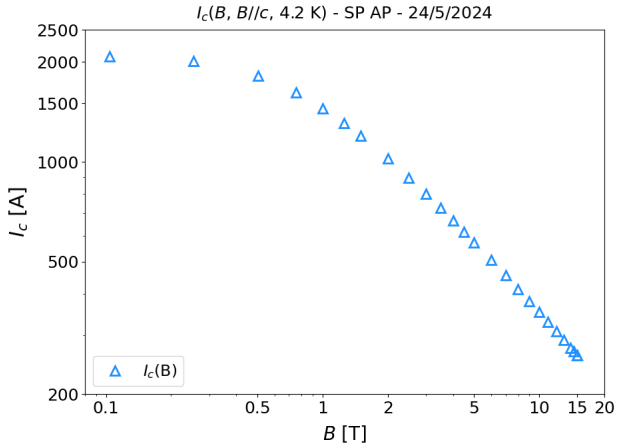

FIGURE 4.13: Field dependence of the transport critical current of the SP AP tape tested on 24/05/24.

1. The effect of self-field is negligible, therefore 'B' indicated in the plot is the actual (total) field. Then, the maximum value of $I_{c,0}$ is constrained to be at maximum 1 - 2 % higher than the I_c(0.1 T) to account for a slight transport current improvement down to zero field.

2. This effect is not negligible, therefore 'B' in the plot is only the background field, different from the actual field. Nevertheless, the field is not uniformly distributed across the tape width [111] and it is not straightforward to estimate its effect on the critical current.

To further elucidate on this, Table 4.3 analyses three scenarios. The first is called 'free' scaling, where the $I_{c,0}$ has no imposed constraints. The third is the 'fully constrained', where the $I_{c,0}$ is imposed to be 2 % higher than I_c(0.1 T) at most. The second case is somehow intermediate between the previous two, where the $I_{c,0}$ is imposed to be 5 % higher than I_c(0.1 T).

In fact, Table 4.3 also shows the resulting ratio between the $I_{c,0}$ and the data point at the lowest available applied field, I_c(0.1 T). This is 10.6 % higher for the free scaling, while it corresponds to the maximum limit imposed on the $I_{c,0}$ for the other two. Finally,

	$I_{c,0}$ [A]	α	B_0 [T]	$I_{c,0}/I_c$(0.1 T)	χ^2
Free scaling	2309	0.82	1.33	1.106	29.1
Half free	2193	0.91	1.75	1.050	52.4
Fully constrained	2130	0.96	2.05	1.020	73.8

TABLE 4.3: Variability of scaling parameters in the three scenarios. The error margin of both the slope of the linear region and the crossover field is estimated to be up to 25 % for the fully constrained case, 15 % for the half free, and less than 10 % for the free scaling (while it is less than 1 % for the $I_{c,0}$ in all cases).

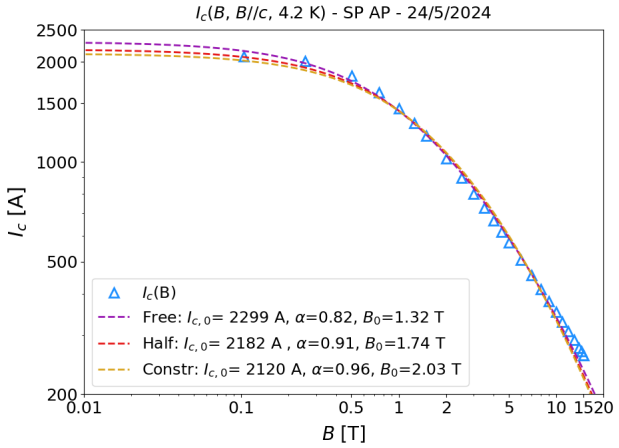

FIGURE 4.14: Field dependence of the critical current of the SP AP tape tested on 24/05/24. Three different fits of the data are proposed: the free scaling (in purple), the half-free (in red), and the fully constrained (in yellow).

Table 4.3 also displays the least square parameter, χ^2, which results to be lowest for the free scaling, and it is the only acceptable value for a representative fit.

The discrepancy among the three types of scaling is limited to 2 - 3 % above 0.75 T. Much of the discrepancy lies, instead, below this field level. In fact, all the three scalings underestimate the I_c(0.5 T), only the free scaling estimates the I_c(0.25 T) correctly, while the other two are more appropriate for the I_c(0.1 T).

Regarding the scaling parameters, the variation is by 8.4 % on the $I_{c,0}$, by 17 % on the α, and by 54 % on the B_0. The resulting slope of the linear curve, α, and the crossover field, B_0, are very helpful to understand which approach to prefer. The slope of the linear region is quite high for all the three cases. The higher this parameter, the faster the performance drop, which is governed by $B^{-\alpha}$ for $B >> B_0$.

On one hand, the free scaling results in the highest discrepancy to the first data point, I_c(0.1 T). On the other, the fully constrained and half-free conditions tend to underestimate the region between 0.25 T and 0.75 T. The free scaling also has the lowest χ^2, meaning it is preferable in general, compared to the other approaches. In addition, it is the best candidate to account for the correction by the self-field below $\sim$1 T. For all these reasons, it is the preferred choice for estimating the $I_{c,0}$ in the following.

4.3 Categories of issues with tape testing

The sample testing reported and commented above belongs to an actual minority of tests running smoothly from the beginning to end. In fact, testing of over 70 samples has shown that they usually display several issues.

4.3.1 Premature tape burning

As explained earlier in this chapter, the test of tape samples with the U-shape generally starts at 15 T. This is done to let the tape adjusting itself in the groove of the sample holder, while minimizing the risk of tape burning.

In fact, it was observed in a number of tests that, while the tape samples seem to behave properly from high down to intermediate field levels, suddenly current could not be injected anymore. Tapes were observed to have burnt upon extraction of the solenoid insert from the cryostat. For example, this was the case of the SuperPower HM tape. Fig. 4.15 shows the results of the testing of two samples: the data stop at 2 T, 1330 A, for the test on 17/12/2024 and at 1.5 T, 1440 A, for the test on 15/01/2025.

In both cases, the tape burnt across the central region, similarly to what showed in Fig. 4.11. It is not easy to explain why the tape should burn at such an intermediate current level. The main cause could be the presence of a microscopic defect in the REBCO layer. As the current injected increases, the heating associated to the presence of the defect increases even more rapidly because of Ohm's law.

Considering a voltage of 10 μV generated across the defect (as measured from region 3 - 4), a 1500 A current generates 15 mW of power dissipation. The copper layer on the adjacent side to the REBCO layer plays a pivotal role in diverting the current and mitigating the Joule heating, thus letting the helium bath lowering the local temperature. The size of the defect might play a major role, too. Therefore, tape burning in this region of the sample holder might be attributed to a series of causes.

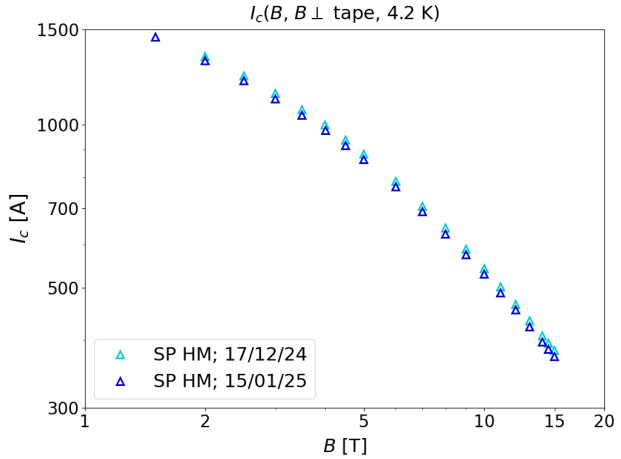

FIGURE 4.15: SP HM tape tested two times, showing a performance limitation between 1300 - 1400 A.

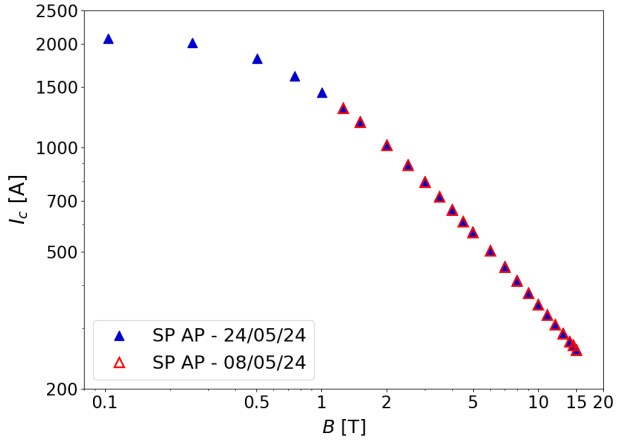

FIGURE 4.16: Two SP AP tape samples tested in 2024. In particular, the sample tested on 08/05/24 displayed a performance limitation at 1.25 T.

4.3.2 Sudden degradation, no visual counterpart

Let us continue with the SP AP tapes discussed above, since they present a varied phenomenology. The dataset displayed in blue in Fig. 4.16 is for the same test conducted on 24/05/24. In red, is the data from the testing on 8/05/24, which had a very close performance to the test on 24/05/24, however the data stop at 1.25 T.

In fact, the testing revealed a similar behaviour to the one described in Fig. 4.3 to Fig. 4.5, then a sudden degradation appeared at 1 T from the central region, see the raw signal in Fig. 4.17. This obliged to stop the current injection at 140 A. We suppose that such a degradation might have been induced by excessive heating during the previous run at 1.25 T. Visual inspection after the testing did not reveal any particular feature in the damaged region.

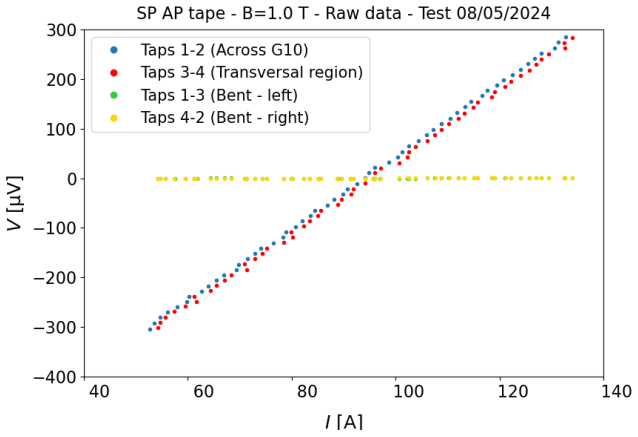

FIGURE 4.17: Sudden performance degradation in the test on 08/05/24 from the central region, represented in red.

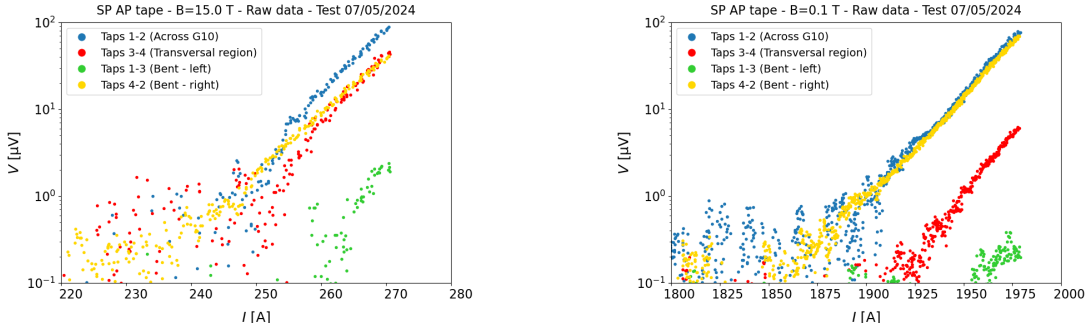

(A) Starting at 15 T.

(B) Takes over at 0.1 T.

FIGURE 4.18: Degradation in region 4-2 in the test of 07/05/24.

4.3.3 Permanent degradation from the start, test continued

Another two SP AP samples were measured down to very low field levels as well. The test on 07/05/24, in yellow in Fig. 4.38, presented a considerable degradation from the bent region 4 - 2 from the very beginning of the test. In fact, the voltage from this region was already comparable to that of region 3 - 4 at 15 T, see Fig. 4.18a.

The entity of the degradation from this bent region increased progressively with the testing, see Fig. 4.18b which is at 0.1 T background field. Nevertheless, it was always possible to extract the I_c from the transverse region to the field, which is why the curve is reported in Fig. 4.38. A huge increase in degradation arose from region 4 - 2 at $\sim$760 A in the final run, preventing to continue the testing further. We suggest that this degradation was present already in the tape, which worsened with the electromagnetic cycling.

4.3.4 Permanent degradation from the start, test stopped

A permanent degradation was observed in many cases from one of the bent regions, starting from the first test run. Fig. 4.19 shows such an example, for the test of a Fujikura tape conducted on 28/06/24. The phenomenology remained the same repeating the testing at other field levels. No transition originated from the transversal region to the field. We suspect that this issue has been due to the tape mounted with the superconductor on the outside. The following test, on 03/07/24 was conducted successfully from 15 T down to 3 T, then one of the bent regions reported a sudden degradation, similar to what described in section 4.3.2.

4.3.5 Potential intrinsic, however stable, degradation

The test on 17/05/24, represented in green in Fig. 4.38, was run smoothly all over the field domain. The signal from the two bent regions was always flat at transition, in the

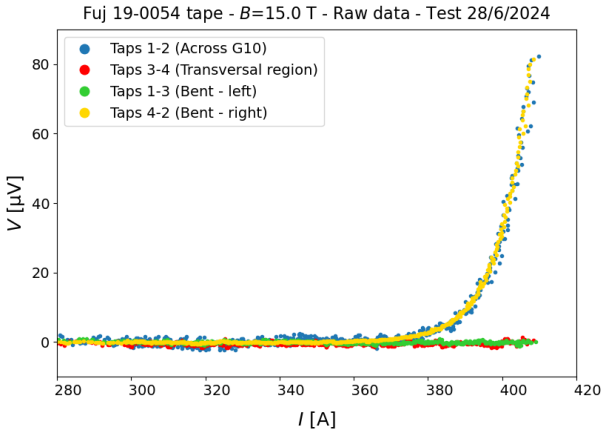

FIGURE 4.19: High signal from bent region 4-2 from the first test run in the test on 28/06/24, an indication of permanent degradation.

transversal region to the field, see Fig. 4.20. Nevertheless, it is rather expected for these regions to display the beginning of a transition when the central region reaches the full transition. This might be the sign of a partial degradation of this tape sample with respect to the others tested from the SP AP batch. This potential degradation remains stable throughout the test, which is also supported by the I_c of this sample being lower at all field levels by 6% compared to the other samples.

4.3.6 Limitation from the power supply

It is worth reporting that a few tape samples had such a high performance that the critical curve could not be explored in full in the available facility. This was the case of a Faraday Factory tape shown in Fig. 4.21, which is for a test conducted at 0.55 T background field where the beginning of the transition was observed at 3000 A. In

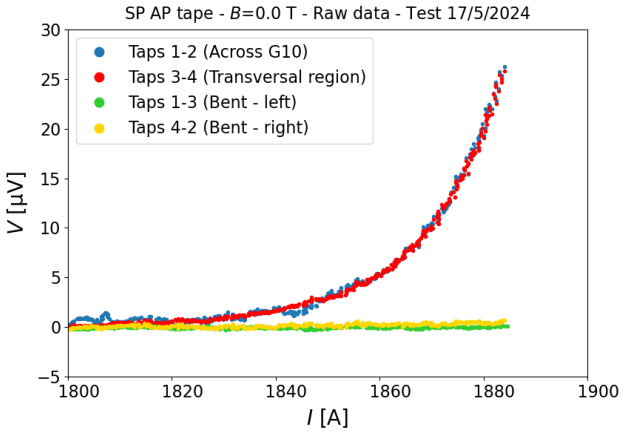

FIGURE 4.20: The absence of transition of the yellow and green curves upon transition of the red curve suggests the presence of intrinsic tape degradation in the test on 17/05/24.

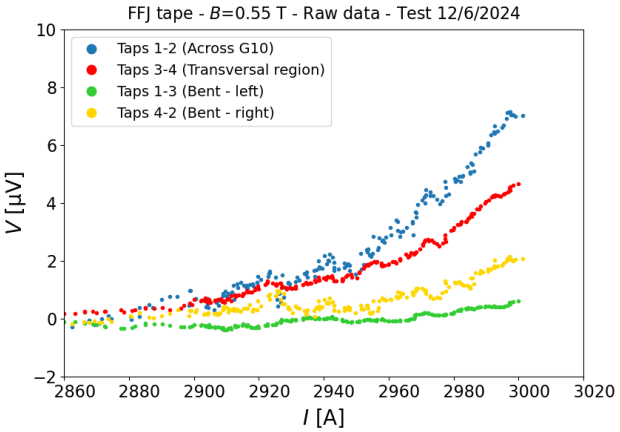

FIGURE 4.21: Test on the tape from Faraday Factory displaying the beginning of transition at 3000 A (at the background field of 0.55 T), the limit of the power supply.

fact, the I_c could be extrapolated to 3040 A. The results obtained with this tape will be discussed also later.

4.3.7 Tests started from low fields and high currents

It was mentioned in the beginning that tests are usually started at 15 T to both let the tapes stabilize into the groove, as well as to avoid burning the tapes during the early runs. While this choice was preferred from the first tests, as it was based on such assumptions, it later revealed to be the appropriate one.

Alternatively, the test conducted on 08/07/24 was started at 0.5 T field, giving an I_c of 1916 A, see Fig. 4.22a. Then, a high resistive signal appeared in the following run, obliging to cut the current at ∼1000 A, see Fig. 4.22b. Another case was that of the test on 16/07/24. The first run at 0.1 T showed a high signal from region 1 - 3, resembling a strong degradation. This behavior extended up to 1 T, see Fig. 4.23a. At 2 T, the signal from 1 - 3 remained considerably lower, then it disappeared at 2.5 T and the transition was induced by the central region 3 - 4, see Fig. 4.23b. Going back down to 0.5 T, the signal from 1 - 3 appeared again. A similar phenomenology was observed also in the test of a Fujikura tape on 22/03/24.

The tape tested in the examples shown here was type 19-0054 from Fujikura, mounting the superconducting layer facing inward. For comparison, the result of another test on the same tape performed on 9/07, however starting from 15 T as usual, is shown. The test proceeded smoothly down to 0.5 T and 1950 A, which is similar to the current level in the first run of the test on 8/07. Fig. 4.24 proposes the comparison of the voltage signals from region 3-4 in the first run of the test on 08/07/24 and in the last run of the test on 09/07/24. This clarifies on the advantages of starting the characterization tests from high fields and low currents.

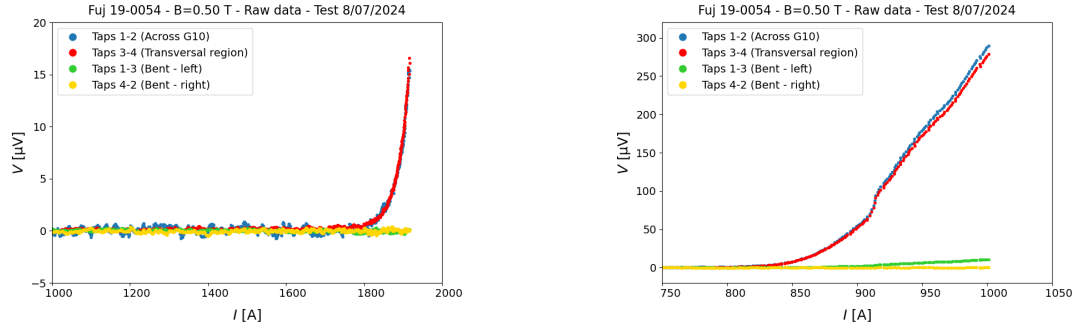

(A) Typical transition in the first run.

(B) Performance loss in second run.

FIGURE 4.22: Test on 08/07/24 started at 0.5 T.

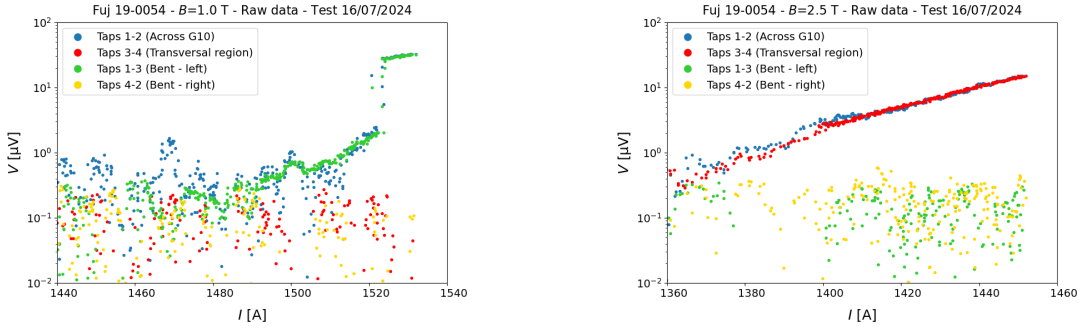

(A) At 1 T.

(B) Increasing to 2.5 T

FIGURE 4.23: Test on 16/07/24, started from low fields.

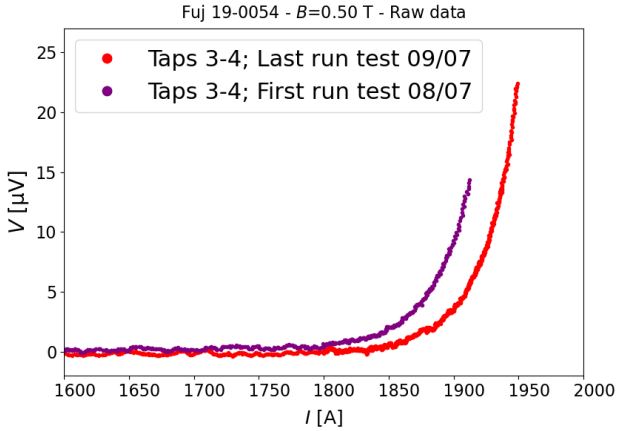

FIGURE 4.24: Comparison of the signal from the central region 3-4 in the two tests on 08/07 and 09/07/24 at 0.5 T.

4.4 Results

4.4.1 Scaling of data measured over the whole field range

This section is dedicated to the presentation of data from the transport current measurements and to the fitting of such data by means of the scaling law. Fig. 4.25 and Fig. 4.26

display the results of the transport current measurements conducted in liquid helium at 4.2 K on five tapes from four different manufacturers [29]. These tapes were: two ST-4-E tapes from Shanghai Superconductor Technology (SST), S-Innovations, SCS4050-AP from SuperPower, and TPL4421-HP from Theva.

Tapes from SST and S-Innovations are fabricated by means of IBAD + PLD on a 50-μm and a 40-μm Hastelloy substrate, respectively; SuperPower is fabricated by means of IBAD + MOCVD on a 50-μm substrate. Finally, the Theva tape uses a 48-μm substrate adopting ISD + PLD. All tapes are electroplated with a 20-μm copper layer on each side, except for Theva which has only a 10-μm copper layer.

All tapes have been delivered in spools of roughly 20 m length, either during 2022 or early 2023. Typically, two samples per spool were tested for each of the tapes displayed

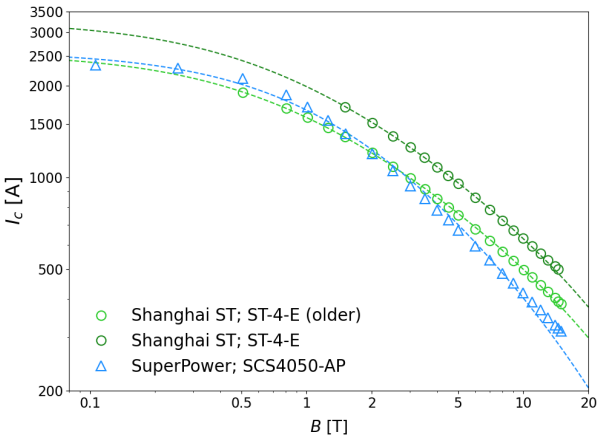

FIGURE 4.25: Critical current data (4.2 K, $B \perp$ tape) as a function of field for a SP tape and two SST tapes, listed in Table 4.4. Dashed lines are for the fitting with the proposed scaling law.

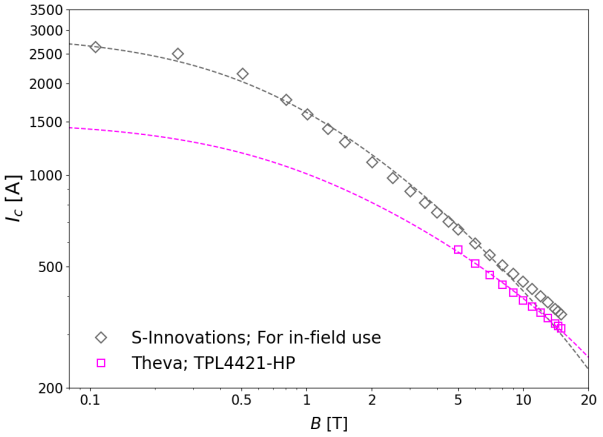

FIGURE 4.26: Critical current data (4.2 K, $B \perp$ tape) as a function of field for an S-Innovations and a Theva tape, listed in Table 4.4. Dashed lines are for the fitting with the proposed scaling law.

Fitting parameters		$I_{c,0}$ [A]	α	B_0 [T]	χ^2
Allowed ranges		$\leq$3500	0 - 1	-	-
Manufacturer	**Tape type**				
Shanghai ST	ST-4-E	3272	0.56	0.73	1.4
Shanghai ST	ST-4-E (older)	2547	0.56	0.73	1.5
S-Innovations	For in-field use	2894	0.67	0.74	75.0
SuperPower	SCS4050-AP	2589	0.86	1.56	49.3
Theva	TPL4421-HP	1500	0.45	0.75	0.8

TABLE 4.4: Scaling parameters of the tapes tested in 2023. Let us specify that q is set to 2 to match the exponent in Kramer's law and B_{irr}=150 T from past estimates on the $B_{c,2}$ on cuprates [27], for all tapes. The quality of the fitting, χ^2, is also reported. The error bars can be accounted for a 10 - 15 % for each scaling parameter.

in Fig. 4.25 and Fig. 4.26. The I_c of tapes from the same spools differed by less than 5 %, meaning the data shown are reproducible. The only exception was the 'older' SST tape, which was tested once, since only a 0.5 m length of this tape was available. In two cases, the test was conducted down to a background field of 0.1 T, corresponding to remarkable I_c values of 2337 A and 2600 A for the SuperPower and the S-Innovations tapes, respectively.

The 'older' tape from SST was tested down to 0.5 T, while the most recent one, which showed better electrical performance, only down to 1.25 T. The reason for this limited testing is that both tapes burnt prematurely, interestingly at similar current levels of $\sim$1800 A. Fig. 4.26 also reports the data for the Theva tape, which was tested down to 4 T. Degradation appeared from the bent regions of the sample holder at this field level, which did not allow further data to be collected. This degradation might be attributed to to the bending radius of the holder, which is slightly higher than the minimum bending radius of these tapes (20 mm).

The scaling proposed was applied to the present datasets: the result is shown by the dashed lines in Fig. 4.25 and Fig. 4.26, while the scaling parameters are listed in Table 4.4. Parameters were allowed to span over relatively wide ranges in the fitting routine, imposed only by physical constraints. For example, B_{irr} was limited to 150 T because of some past estimates on the upper critical field, B_{c2}, on cuprates [27]. The slope q was set between 2, to match the exponent in Kramer's law, and 5 to allow an even faster performance drop in *Region III*.

Then, Fig. 4.27 shows the data of tape samples from three manufacturers, tested in 2024 [30]: SuperPower AP (in blue), SST ST1910-19 (in green), and Fujikura FESC-SCH04 (in red). Data are complemented with the fitting by the scaling law, represented by dashed lines.

The availability of I_c data down to 0.1 T applied field is of great relevance for fitting using the scaling law as it allows the intercept, $I_{c,0}$, and the crossover field, B_0, to be derived precisely. This was also the case of the S-Innovations tape in Fig. 4.28. This

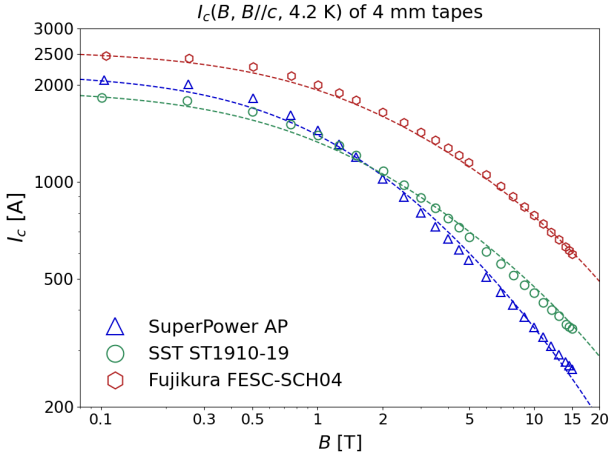

FIGURE 4.27: Transport data of three tapes from different manufacturers, all tested down to 0.1 T background field. The tapes are 4 mm wide. The magnetic field is perpendicular to the tapes.

is extremely valuable for scaling the data of other tape samples from the same manufacturers obtained with similar methods (e.g. introducing the same pinning structure). This information is often lacking when testing is limited to intermediate fields. Table 4.5 reports the resulting scaling parameters for each of the three curves as well as for a fourth curve shown in Fig. 4.28.

The $I_{c,0}$ in Table 4.5 varies quite substantially among the different tapes. However, most of the interest here is on the slope of the linear region, α, and on the crossover field, B_0. As mentioned also in the previous chapters, B_0 is related to the so-called matching field, B_ϕ, which is determined by $n \cdot \Phi_0$, n being the density of the pinning centres in the superconducting layer, and Φ_0 the flux quantum. In Table 4.5, B_0 is in the range from 0.84 T and 1.42 T.

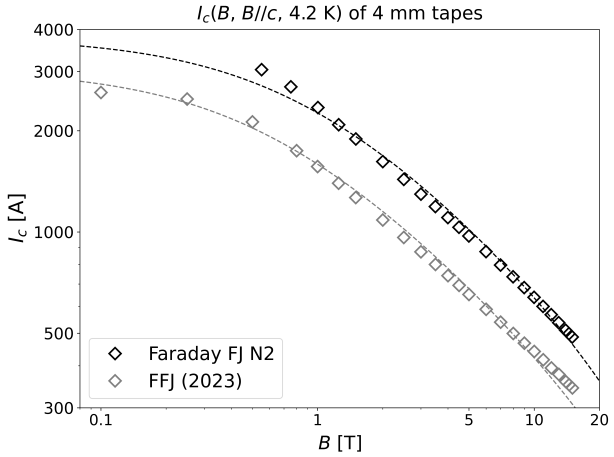

FIGURE 4.28: Transport data of the FFJ tape (in black), tested down to 0.55 T background perpendicular field, as it reached the 3000 A limit of the power supply. For comparison, data of the S-Innovations tape tested in 2023 is also reported (in grey).

Manufacturer	$I_{c,0}$ [A]	α	B_0 [T]	χ^2	$\Delta\alpha$	ΔB_0 [T]
Shanghai ST	1974	0.56	1.06	28.2	$\pm$0.05	$\pm$0.08
SuperPower	2284	0.85	1.42	32.5	$\pm$0.36	$\pm$0.44
Fujikura	2650	0.51	1.39	7.0	$\pm$0.05	$\pm$0.11
Faraday FJ	3794	0.64	0.84	86.9	$\pm$0.18	$\pm$0.19

TABLE 4.5: Resulting scaling parameters for the curves in Fig. 4.27 and Fig. 4.28. Error margins are also reported for the slope of the linear region and the crossover field (they are just of a few amperes for the $I_{c,0}$). In particular, the high uncertainties of SP and FFJ are attributed to the limited testing only up to 7 T (see also later in chapter 5). Let us specify that q is set to 2 to match the exponent in Kramer's law and B_{irr}=150 T from past estimates on the $B_{c,2}$ on cuprates [27], for all tapes.

Before continuing, it is worth spending a few words on the last two columns in Table 4.5, which report the error bars both for the α and B_0. While these are relatively limited for SST and Fujikura, the uncertainties are much higher for the SP and FFJ tapes. This is attributed to the limited testing in the magnetization experiment (which is used to define these error bars) and that was only up to 7 T for these two tapes, while it was up to 10 T for SST and Fujikura. This is explained in depth in chapter 5.

A relative variability is observed also on the slope of the linear region. It resulted to be as low as 0.51 for the Fujikura tape and up to 0.81 for the SuperPower tape. The difference in slope is evident from the crossing between the SP and SST tapes in Fig. 4.27. Although SP starts from a higher $I_{c,0}$, its α is considerably higher than SST, therefore its performance drops faster. The crossing occurs at roughly 1 T and the performance ends up being considerably higher for the SST tape above 5 T. The engineering critical current density of the Fujikura tape is J_{eng}(4.2 K, 15 T) = 1500 A/mm^2 and J_{eng}(4.2 K, 5 T) = 2850 A/mm^2, which is higher than the Bi-2212 wires developed in the past years [112].

The case of the FFJ tape is now analysed separately. This tape has also been tested successfully in our solenoidal facility. However, it reached the current limit of the power supply of 3000 A. The beginning of transition was observed at such current level down to 0.55 T applied field and the I_c was extrapolated to 3040 A. Fig. 4.28 shows the result of the testing, where data for this tape are represented in black. The scaling is challenging, as insufficient data are available in the relevant region below 0.5 T, where the second term in the scaling law plays the most important role.

To estimate $I_{c,0}$, data of the similar tape from S-Innovations, shown in Fig. 4.26 and displayed in grey in Fig. 4.28, was used. The $I_{c,0}$ of this tape was 1.25 times higher than the measured I_c(0.5 T). The same factor was applied to the recent tape. The resulting fitting applying the scaling law is reported by the dashed line. The scaling is 10.4 % lower than the datapoints at 0.55 T, 4.1 % higher at 2 T, and 4.7 % lower at 15 T.

4.4.2 Scaling of data measured over a partial field range

It is now of great relevance to provide the reliable scaling of transport data in all cases, especially when these are available only over a partial field range.

4.4.2.1 SuperPower

Let us start from SuperPower. First, a SP AP tape is considered, which was also presented above in the discussion, see Fig. 4.29, which is the same as Fig. 4.16, where the dashed lines represent the fitting with the scaling law.

Values in Table 4.5 were derived for the full test conducted on 24/05/24, namely of B_0=1.42 T and α=0.81. The tape sample tested on 08/05/24 was from the same spool as the sample tested on 24/05/24. Actually, they were less than 2 m apart since they were extracted consecutively. Therefore, the same density of pinning centers and the same scaling parameters (with the associated uncertainties) are assumed. This results in $I_{c,0}$= 2164 A, slightly lower than 2182 A of the other test. In fact, data points for the test on 08/05/24 are a few amperes lower than for the test on 24/05/24.

Data of a different tape, SuperPower HM, are also presented, see Fig. 4.30. The performance of this tape differs considerably from type AP shown so far. In fact, the I_c = 380 A vs 260 A at 15 T (46 % higher) and it remains much higher down to 2 T. However, the crossover field is considerably higher, resulting in the performance increasing at a lower rate with decreasing field.

Scaling is even more challenging, since reference values for the scaling parameters are not available for this tape. This is mostly due to the underlying pinning mechanisms,

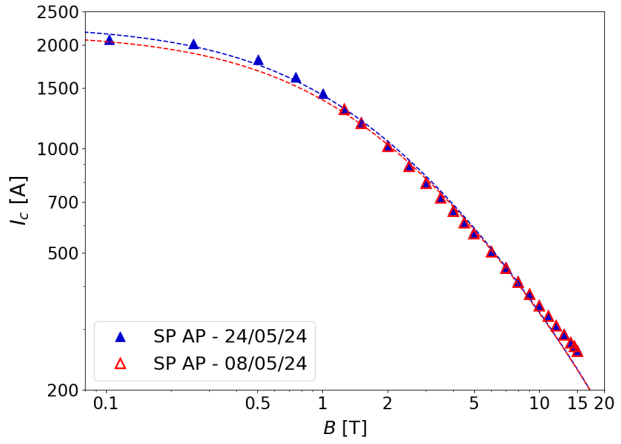

FIGURE 4.29: Two SP AP tape samples tested in 2024. In particular, the tape tested on 08/05/24 showed a limitation of performance at 1.25 T, corresponding to ~1300 A. Data have been fitted using the scaling law.

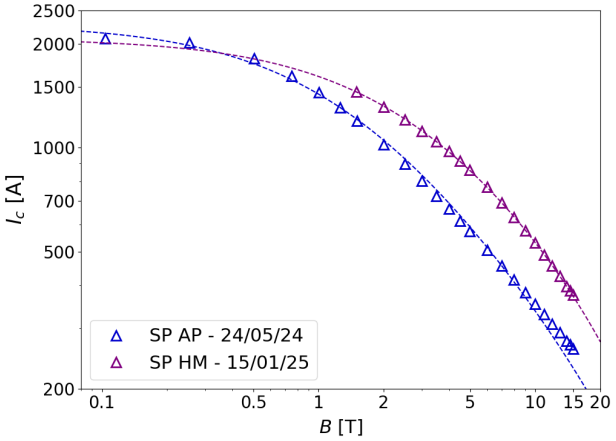

FIGURE 4.30: The performance of SP HM tape, tested on 15/01/25 and shown in purple, is considerably different from SP AP, in blue.

which might differ considerably with respect to the SP AP tape. As usual, we keep q=2 and B_{irr} =150 T at 4.2 K and let the other parameters vary. The result is $I_{c,0}$ = 2037 A, α = 0.89, and B_0 = 3.44 T. The slope of the linear region is even higher than for SP AP. Then, the crossover field is also considerably higher, which is why the $I_{c,0}$ ends up to be lower than for the SP AP tape. Because of these reasons, the SP HM tape is recommended for high field applications.

4.4.2.2 Fujikura

We now consider tape FESC-SCH04 type 19-0054 from Fujikura, which has been tested successfully on 23/07/24 as presented in Fig. 4.27. Many other samples of this tape

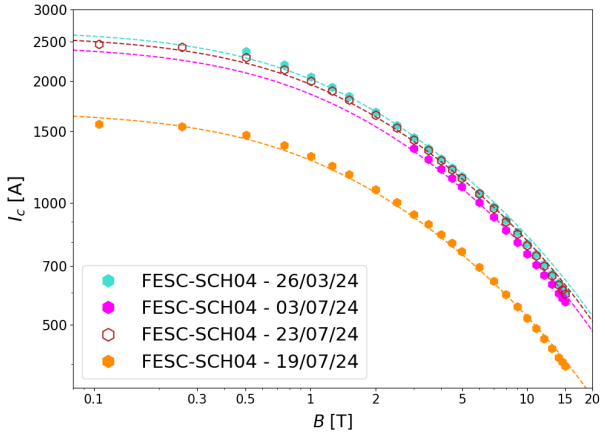

FIGURE 4.31: Performance of four samples of the Fujikura tape 19-0054, extracted sequentially along the same spool. The fitting of each dataset using the scaling law is reported by dashed lines.

Test	$I_{c,0}$ [A]	*var*
26/03/24	2670	3.1 %
23/07/24	2590	0 %
03/07/24	2450	-5.4%
19/07/24	1684	-35 %

TABLE 4.6: Resulting intercept, $I_{c,0}$, of Fujikura tape samples shown in Fig. 4.33, and percentage variation with respect to the test on 23/07/24. Note: the intrinsic uncertainty on the $I_{c,0}$ is up to 5 A at most.

have also been tested, which have shown different absolute performance. Moreover, in some cases, data are available only over a limited field range. Fig. 4.31 still shows the test on 23/07/24 (in dark red, open symbols) together with the results of three other tests, conducted on 26/03/24 (in cyan), 03/07/24 (in pink), and 19/07/24 (in orange). These tapes were extracted consecutively from each other on the same spool.

The same assumption contemplated for scaling the partial data of the SP AP tape is maintained here: that the types and density of pinning centers remain the same, therefore that the scaling parameters (as well as the related uncertainties) do not change. The only exception is on the $I_{c,0}$, which accounts for the variation in the absolute performance. Then, the α and B_0 are assigned to 0.51 and 1.39 T, respectively. The resulting variation on $I_{c,0}$ is reported in Table 4.6.

Table 4.6 also reports the percentage variation with respect to the test of 23/07/24. While this is rather within the expected range ($\pm$5 %) for two samples, the difference is huge with respect to the test on 19/07/24. This aspect is also treated later in section 4.4.3.

A further case is analyzed, namely that of a different Fujikura tape (type 24-0032). This is displayed in Fig. 4.32, where the 'reference' tape 19-0054 is reported for comparison.

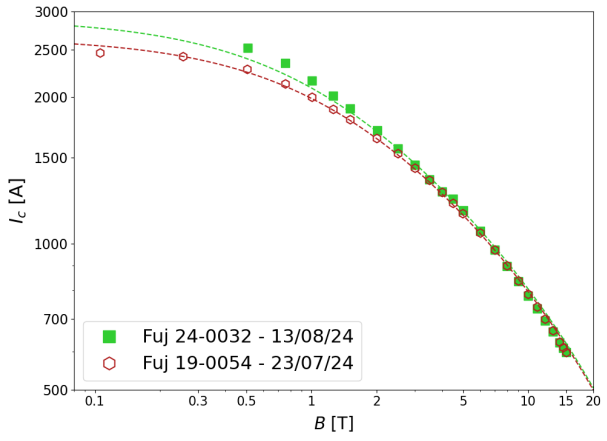

FIGURE 4.32: Performance of a different Fujikura tape (type 24-0032), and related scaling, compared to type 19-0054 shown previously.

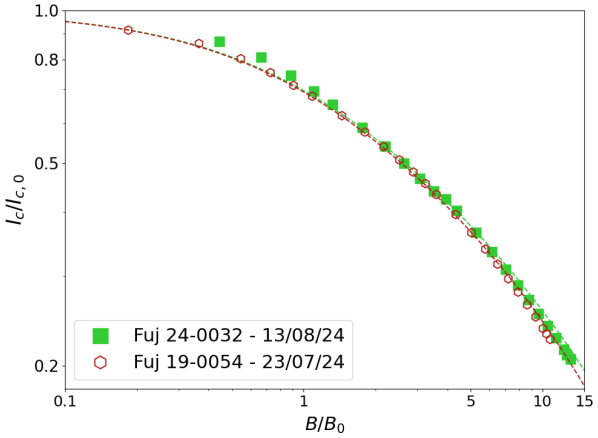

FIGURE 4.33: Plot of the normalized I_c and B of the same data in Fig. 4.32.

The field dependence of this new tape tested on 13/08/24 is considerably different, therefore 'guess' values of the scaling parameters cannot be inferred based on the testing of other tapes.

Nevertheless, to achieve a realistic scaling and avoid the fitting algorithm overshoot the $I_{c,0}$, which always occurs when data are not available down to zero field, the only condition was to set the limit on $I_{c,0}$ to a 15 % higher, at most, than the first data point, I_c(0.5 T). This is generous, considering for comparison that the limit was only 10 % for tape 19-0054. The result is $I_{c,0}$ = 2901 A, α = 0.5 and B_0 = 1.14 T, with the related uncertainties being comprised within a 15% for each of these parameters.

While the crossover field of this more recent tape is quite close to that of the previous tape (1.14 T versus 1.39 T), the intercept is higher and the slope of the linear region is similar. This can be better visualized in Fig. 4.33, where both the I_c and B have been normalized by their respective $I_{c,0}$ and B_0. Both tapes are effective at retaining the critical current in *Region II* thanks to the low α values, and they end up having the same I_c at 15 T.

4.4.2.3 Faraday Factory

The Faraday Factory manufacturer is considered in this section. As shown in Fig. 4.28, the type N2 tape had very high I_c = 3040 A at 0.55 T background field. The most relevant aspect was the I_c field dependence being still in *Region II*, barely showing any sign of transition into *Region I*. Therefore, the performance of a similar tape from S-Innovations tested in 2023 was used to estimate the upper limit on $I_{c,0}$ and thus provide a realistic scaling.

Another FFJ tape of type 6919-C has been tested, of which data are available only down to 1 T, see Fig. 4.34. In this case, the only available quantity of reference for both tapes is

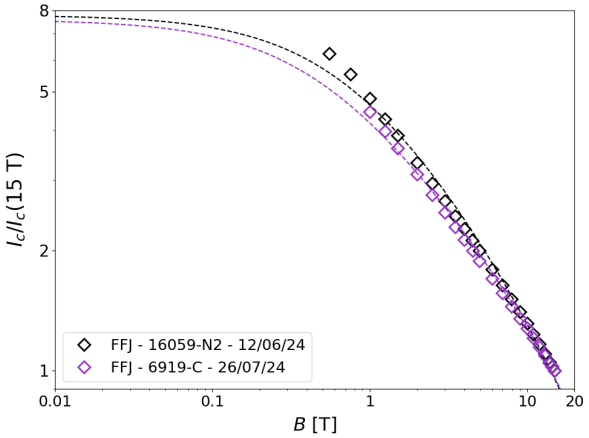

FIGURE 4.34: Plot of the normalized I_c with respect to I_c(15 T) for FFJ tapes of type 16059-N2 (the same as in Fig. 4.28), displayed in black, and type 6919-C, in purple.

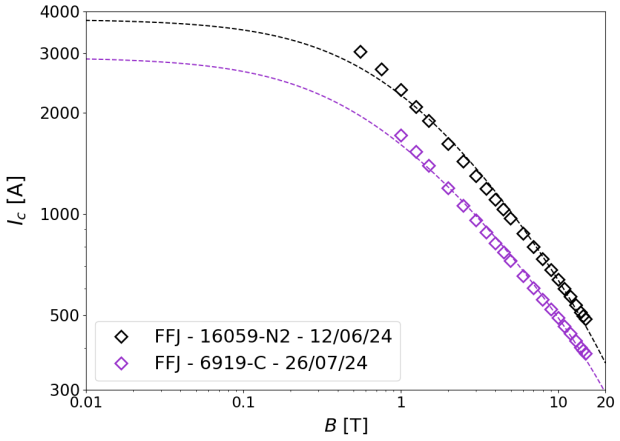

FIGURE 4.35: Scaling of data for FFJ tape 16059-N2 and 6919-C. Parameters are listed in Table 4.7.

the I_c(15 T), which is why the plot reports the normalized I_c with respect to it. The field is not normalized to the B_0 as done previously for Fujikura, see Fig. 4.33, as information lacks about it for this tape. The two datasets result having different field dependence. In particular, the slope of the linear region is lower for type 6919-C than for type N2. The normalized $I_{c,0}$, instead, is very similar.

Let us consider the ratio between $I_{c,0}/I_c$(1 T) = 3794 A / 2345 A = 1.618 for the N2 tape. On one hand, such value might be different (lower) for tape 6919-C. On the other, however, this represents an upper boundary to set in order to not underestimate the $I_{c,0}$. In addition, it is assumed that q = 2 and B_{irr} = 150 T as usual. The resulting scaling parameters and related uncertainties are reported in Table 4.7.

The slope of the linear region ends up being slightly lower for type 6919-C than for 16059-N2, namely 0.55 versus 0.64, as expected from the milder slope in the normalized

FFJ tape	$I_{c,0}$ [A]	α	B_0 [T]	χ^2	$\Delta\alpha$	ΔB_0 [T]
16059-N2	3794	0.64	0.84	86.9	$\pm$0.18	$\pm$0.19
6919-C	2921	0.55	0.53	19.2	$\pm$0.05	$\pm$0.06

TABLE 4.7: Scaling parameters and related uncertainties (they are just of a few amperes for $I_{c,0}$) for the two tape types from FFJ. Let us specify that q is set to 2 to match the exponent in Kramer's law and B_{irr}=150 T from past estimates on the $B_{c,2}$ on cuprates [27].

plot, Fig. 4.34. The crossover field is also lower, being 0.53 T versus 0.84 T, as well as the intercept, 2921 A versus 3794 A. The resulting fitting with the scaling law is shown in the double logarithmic plot in Fig. 4.35 from 0.01 T up to 20 T.

4.4.2.4 Shanghai ST

One last manufacturer is considered in this section, SST, shown also in Fig. 4.27. A second sample of type ST1910 from the same spool was tested on 19/01/24 and one from a different spool on 17/11/23. Then, one sample of type ST2311 was tested on 25/04/24, as displayed in Fig. 4.36. However, data are incomplete, since the lowest field available is 2.5 T for the test on 17/11/23, 1.5 T for the test on 19/01/24, and 0.5 T for the test on 25/04/24.

To scale those data, the ratios of the I_c of tests with respect to those of the 'full' test of 16/01/24 were considered, at the corresponding field levels. Table 4.8 shows that the ratios remain basically constant for each tape over the field domain. Therefore, the limit on the $I_{c,0}$ was set using the ratios with respect to the data at the lowest field available, i.e. 2.5 T for the test on 17/11/23, 1.5 T for the test on 19/01/24, and 0.5 T for the test on 25/04/24.

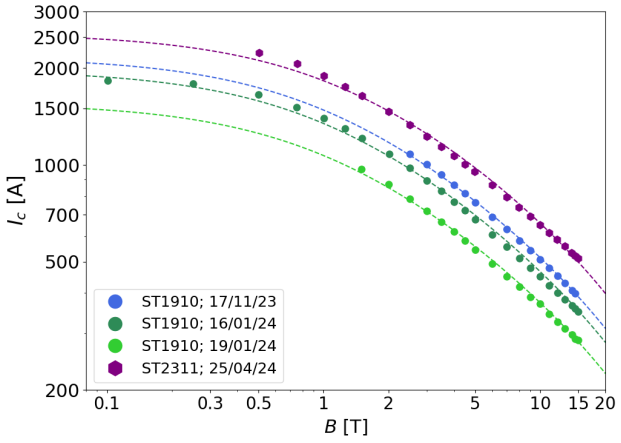

FIGURE 4.36: Scaling of incomplete data from SST tapes ST1910, tested on 17/11/23 and 19/01/24, as well as ST2311, tested on 25/04/24.

	I_c [A]						
B [T]	16/01/24 (ref)	19/01/24	*ratio*	17/11/23	*ratio*	25/04/24	*ratio*
0.0	1841	-	-	-	-	-	-
0.5	1657	-	-	-	-	2231	1.346
1.0	1396	-	-	-	-	1894	1.357
1.5	1210	970	0.801	-	-	1642	1.357
2.0	1082	872	0.806	-	-	1465	1.354
2.5	977	786	0.804	1084	1.11	1332	1.363
3.0	895	721	0.805	1005	1.12	1226	1.370
5.0	676	546	0.808	765	1.13	953	1.410
10.0	451	371	0.822	508	1.13	652	1.445

TABLE 4.8: Ratios of the critical current for the two additional tests on SST tape ST1910 and on ST2311, with respect to the reference, conducted on 16/01/24.

The same α and B_0 were adopted for samples of tape ST1910, since the pinning structure remains the same. In doing so, the variability in performance is attributed exclusively to the $I_{c,0}$. This results to be 1543 A for the test on 19/01/24 and 2125 A for the test on 17/11/23. The error bars on the scaling parameters are the same as in Table 4.5.

We also note that tape ST2311 has very similar I_c field dependence. For this reason, the same B_0 = 1.06 T is kept while the α is allowed to change. This corresponds to assuming that the density of APCs is the same, however the field dependence might change slightly. As a result, α = 0.52, slightly lower than 0.56 of tape ST1910, and $I_{c,0}$ = 2610 A.

It is an even more challenging task to apply the scaling law on datasets that are limited to the intermediate field range. This is the case of tape SST ST2306 tested on 07/08/24 and displayed in Fig. 4.37. In spite of the limited data available, such tape has a considerably different field dependence when compared to tape ST2311 tested on 25/04/24

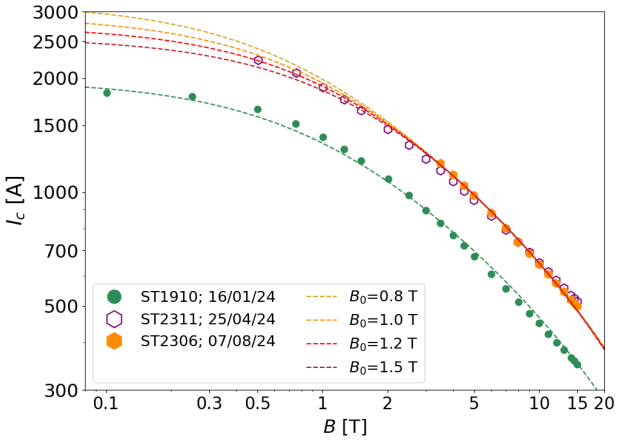

FIGURE 4.37: Scaling of incomplete data of the SST ST2306 tape. The tapes ST1910 and ST2311 are also displayed for comparison.

B_0 [T]	$I_{c,0}$ [A]	$\Delta I_{c,0}/I_{c,0}$	α	$\Delta\alpha/\alpha$
0.8	3157	8.1%	0.56	-1.8%
1.0	2920	0%	0.57	0%
1.2	2749	-5.9%	0.58	1.8%
1.5	2563	-12.2%	0.61	7.0%

TABLE 4.9: Percentage variation of the intercept and the slope of the linear region as a function of the variation of the crossover field. The percentage error margin is also specified for both parameters.

and tape ST1910 tested on 16/01/24, which are also reported for comparison. Four scenarios for scaling the data of tape ST2306 are analyzed. In particular, the B_0 is allowed to vary from 0.8 T (the resulting scaling is in yellow in Fig. 4.37), 1.0 T (orange), 1.2 T (red), and 1.5 T (dark red), corresponding to the range of expected crossover field values at 4.2 K. The derived $I_{c,0}$ and α are reported in Table 4.9.

The relative variations in the table are referred to the case of B_0 = 1 T. The slope of *Region II* changes by 7 % at most. Instead, the $I_{c,0}$ is lowest at 2563 A for 1.5 T field and highest at 3157 A for 0.8 T crossover field, namely it varies by ∼20 %. Based on the previous results on SST tapes, 1.0 T - 1.2 T is the reasonable range for the crossover field, resulting in an acceptable 6% variation on the $I_{c,0}$.

To conclude this section 4.4.2, it is relevant to clarify that the solution of each case is not identical and one might wonder whether a general approach could rather be elaborated. The point to make here is that there is no 'recipe' to fit a partial transport dataset, when no other information is at hand. The only way is complementing the transport measurements with the magnetic hysteresis cycles. In the next chapter, a methodology to compare the field dependence given by the two techniques is put forward, which is then useful to scale the magnetization data in a reliable way.

4.4.3 Statistics on tape performance

Multiple tape samples have been tested for some of the tapes presented above, see also [30]. They were not necessarily the best ones of their respective batches, while rather those tested successfully up to high current levels, typically 2000 A or higher and low applied fields, which is relevant to apply the scaling law.

4.4.3.1 SuperPower

Fig. 4.38 displays the performance of four tape samples from the SuperPower AP tape. Critical current tests generally start at the highest available field of 15 T and the field is lowered progressively reaching higher I_c. In three cases, tapes were tested down to 0.1 T background field.

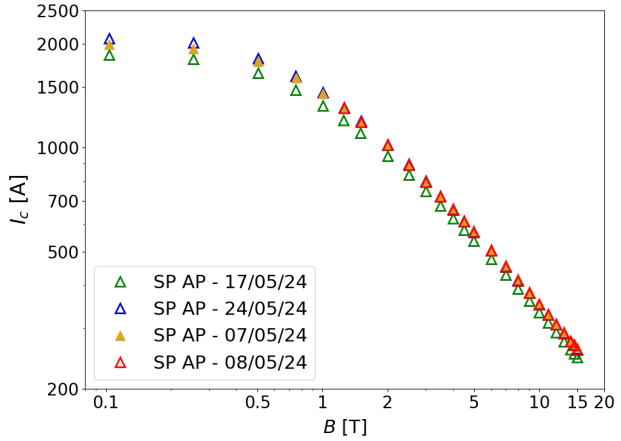

FIGURE 4.38: Statistics on the performance of tape SP AP, of which four different samples have been tested.

As discussed previously, the sample tested on 08/05/24 had similar performance to the others, however a sudden degradation occurred at 1 T, forcing to stop the test. The degradation came from the central region of the holder, where the tape is exposed to the perpendicular field. The maximum difference in performance was between tests on 17/05/24 and 24/05/24 (in green and blue, in Fig. 4.38). This was by 5.6 % at 15 T (247.1 A versus 261.7 A), 6.0 % at 5 T, and it increased up to 10.4 % at 0.1 T (1861 A versus 2078 A).

The typical length of a tape sample is 0.4 m and all four tested samples were extracted consecutively from the same spool. It is also relevant to examine the scaling of these curves, to check for correlations between the parameters. This is shown in Fig. 4.39, where two approaches were tried out. The first one consisted in a 'free' scaling, resulting in α in the range 0.83 - 0.89 for all the curves. In the second one, instead, the same α was set to 0.81, see Table 4.5, for all curves (corresponding to the sample tested on

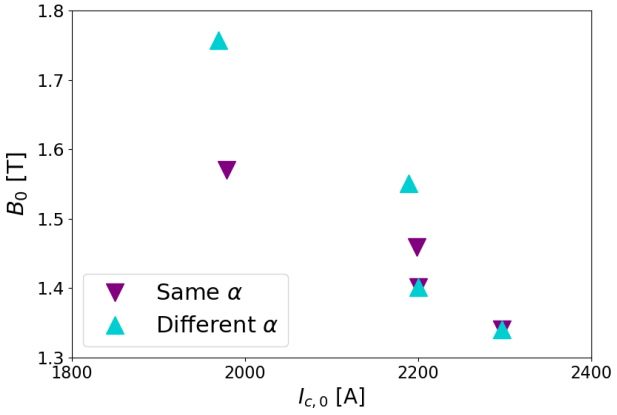

FIGURE 4.39: Effect of setting the same or different (free) α on the B_0 as a function of the intercept, $I_{c,0}$, for tape SP AP.

24/05/24). Both approaches reveal the hint of an inverse relationship between the B_0 and the intercept, $I_{c,0}$. This result suggests that slightly lowering the density of artificial pinning centers might be helpful to improve the zero field performance of tapes at low temperatures.

4.4.3.2 Fujikura

Fig. 4.40 shows the results of the tests on four tape samples from Fujikura 19-0054. The test on 23/07/24 (in red) is the same discussed above for the scaling, see for example Fig. 4.27.

The sample tested on 19/07/24 was also measured down to 0.1 T background field. However, this sample had roughly 36 % lower performance (at 0.1 T, 1567 A versus 2467 A), which is quite remarkable considering that the tape sample was extracted just next to the one tested on 23/07/24. Fig. 4.40 displays the results of two other samples. The test on 03/07/24 was interrupted at 3 T because of a sudden performance degradation, which occurred from one field level to another. The test on 28/03/24, instead, was measured down to 0.3 T background field, then the sample burnt over one of the bent regions. Four additional samples have been tested from the same spool, giving profiles in the same interval defined by those shown here.

4.4.3.3 Faraday Factory

Fig. 4.41 shows the statistics of the FFJ 16059-N2 and 6919-C tapes together. Three different samples of the tape N2 were tested. Their performance was less than 1 %

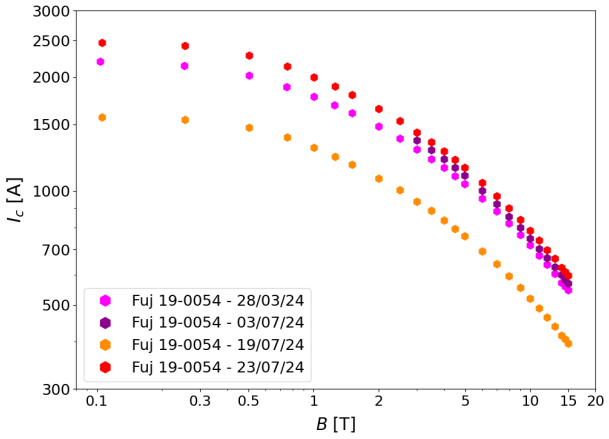

FIGURE 4.40: Statistics on the performance of Fujikura FESC-SCH04 tape. The results on four different samples are shown in this figure, while eight samples have been tested in total. The lowest and highest performance are shown here, in orange (test on 19/07/24) and red (test on 23/07/24), respectively.

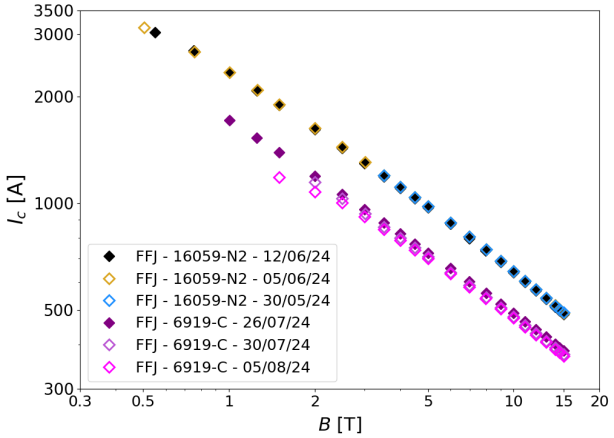

FIGURE 4.41: Statistics on the performance of two types of FFJ tapes. Three different samples have been tested for each.

apart, making it the most consistent tape tested in the campaign. The tape tested on 12/06/24 is the same presented in Fig. 4.28.

The sample tested on 05/06/24 had the same performance down to low fields; in particular, an early beginning of transition was observed even down to 0.5 T background field, giving an extrapolated I_c(0.5 T) = 3130 A. Still, let us specify that it was decided to use the other set to apply the scaling law as the transition was much more evident at 0.55 T. The sample tested on 30/05/24 had a comparable performance to the previous two, however an abrupt degradation was observed at 3.5 T, which is why the data (in light blue) stop there.

Two additional samples were tested for tape 6919-C as well. The test on 30/07/24 was conducted down to 2 T, then the sample suffered from considerable degradation from the transverse region to the field. The performance was lower by 2.5 % with respect to the test on 26/07/24, down to 2.5 T. Then, it increased to 4.1 % in the last run at 2 T. The test on 05/08/24 was lower by 3.4 % down to 5 T, then the degradation increased progressively up to 14.8 % of the last test conducted at 1.5 T. To conclude, even if tape 6919-C had less than 4 % performance variation from tape to tape, it was less capable of withstanding currents above 1000 - 1100 A.

4.4.3.4 Shanghai ST

The SST tape was tested two times, as shown in Fig. 4.36. In particular, the two samples were extracted just adjacent to one another on the same spool. The performance was lower by 18.5 % at 15 T (350.2 A versus 285.3 A), which worsened to 19.1 % at 5 T (675.7 A versus 546.1 A), and further to 19.8 % at 1.5 T (1210 A versus 969.8 A). No data is available below 1.5 T for the test on 19/01/24, as an abrupt degradation occurred in one of the bent regions of the sample.

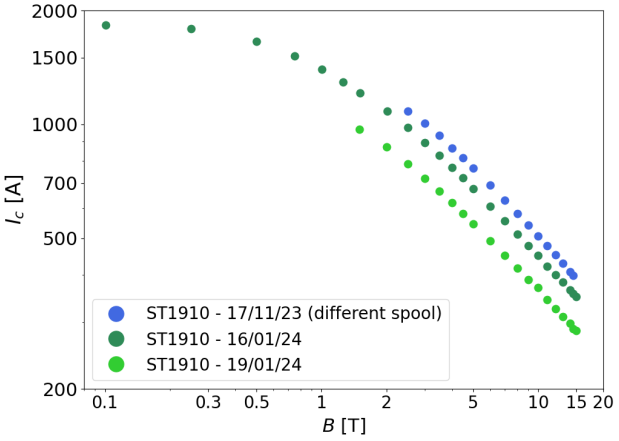

FIGURE 4.42: Statistics on the performance of SST tape of type ST1910. Two samples were from the sample spool (tests on 16/01/24 and 19/01/24), while another one was from a different spool (17/11/23).

A similar plot is reported in Fig. 4.42, where the data of the test on 17/11/23 have been added. In fact, the same type of tape was tested, however coming from a different spool. The performance was ∼13 % higher down to 3 T, then it decreased to 10.5 % just before a strong degradation from one of the bent regions came into play. Overall, the I_c was observed to vary by more than 30 % for this tape type.

4.4.4 Comparison of n-values

Another interesting topic of discussion is the difference of slopes in the V-I curves, i. e. the n-values. Fig. 4.43 and Fig. 4.44 show such quantity for the nine tapes tested in this work with the transport current method.

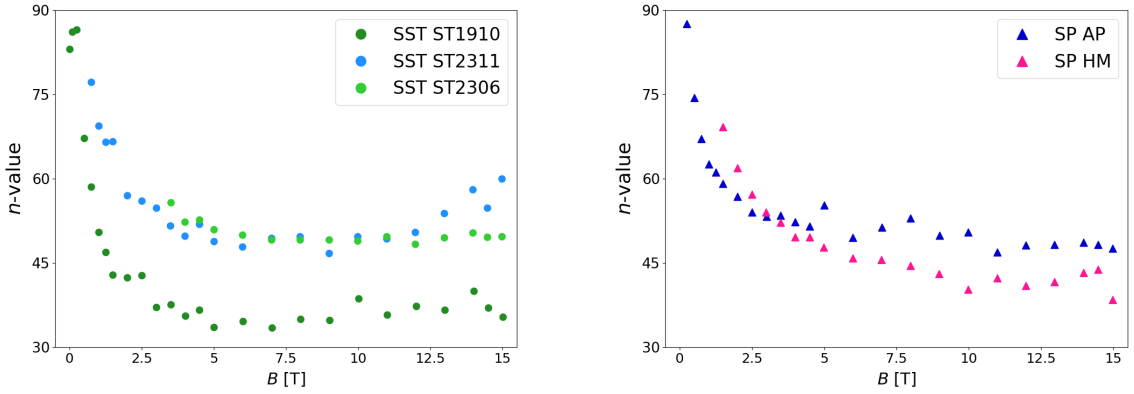

(A) SST (B) SP

FIGURE 4.43: n-values for the three SST and two SP tapes

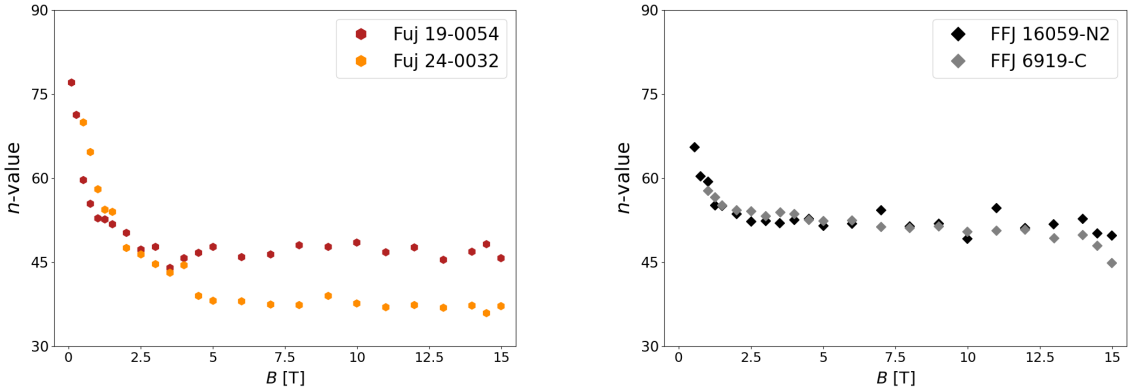

(A) Fujikura (B) FFJ

FIGURE 4.44: n-values for the two Fujikura and FFJ tapes

The n-values are above 70 in the low field region ($B \leq 0.5$ T) for the three tapes SST ST1910, SP AP, and Fuj 19-0054 tested down to 0.1 T background field. The slope of the power law drops rapidly as the field increases to 2 - 3 T, being in the range 50 - 55 for tapes ST2306, ST2311, SP AP, Fujikura 19-0054 and the two FFJ tapes. The SP HM tape has lower n-values than the SP AP above 5 T, being as low as 40. Additionally, n-values are as low as 33.5 and 36.0 for tapes ST1910 and Fuj 24-0032, respectively. Finally, SST tape ST2311 goes again up to 60 from 12 T onward.

4.4.5 Pinning force

To conclude this chapter, Fig. 4.45 presents the pinning force (per unit volume) as a function of the applied magnetic field for the best tapes from the four manufacturers, at 4.2 K. The pinning force is computed as the Lorentz force, the product of the I_c with

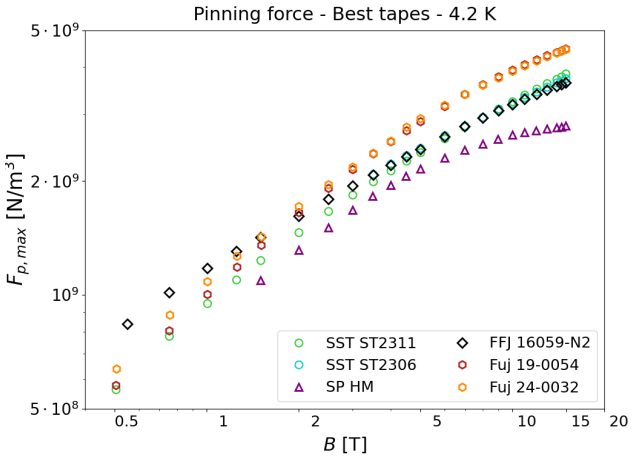

FIGURE 4.45: Pinning force of the best performing tapes.

the applied magnetic field, B, and dividing by the thickness of the REBCO layer, here assumed to be 2 μm.

The pinning force increases for all tapes with increasing field and at 15 T they are still far from the peak. In fact, this is expected between 25 - 30 T, namely $\sim$20 % of B_{irr}. The Fujikura tapes display the highest pinning force, since they had the highest $I_c \approx 600$ A at 15 T, even higher than FFJ N2 tape. The peak is at about $5{\cdot}10^9$ N/m^3, which acts to push the tape laterally against one of the groove edges. This force is successfully withstood by the sample holder, both in the G10 part and at the connections with the copper bars.

Chapter 5

Experimental results: Magnetization

5.1 Magnetization at different temperatures

The measurement of the magnetic moment of high temperature superconductors (HTS) as well as of low temperature superconductors (LTS) is a valuable tool to assess their critical current density, J_c, as a function of both the magnetic field and temperature. In particular, for the case of LTS, which are manufactured in the form of multifilamentary wires, measuring the magnetic moment is useful to derive the interfilamentary coupling losses.

Magnetization measurements constitute an alternative to transport current measurements and present several advantages with respect to them. First, the system does not need a power supply to inject current into the sample, as it is the case of the transport method discussed in the previous chapter. Second, the temperature in magnetization measurements can stretch over a wide range, from 1.7 K up to 100 K, in the system available at CERN. This is allowed thanks to a variable temperature insert (VTI) inside the magnet bore. Conversely, the transport current method is constrained either to the liquid helium temperature, 4.2 K, or the superfluid helium temperature, 1.9 K, as it is available in the installations at CERN.

Furthermore, samples for magnetization measurements are small, being typically a few millimeters long and wide, which limits the material requirement. Samples are easy to insert and extract from the magnet bore and the full characterization of a sample over many temperature levels is accomplished in a single day. This is especially advantageous in the case of Nb_3Sn samples, which are wound around a screw thus facilitating the reaction process. Instead, the sample cooldown, measurement, warm-up, and

extraction takes up to an entire day for a single temperature level in the case of the transport method.

Chapter 3 presented the working principle of the Vibrating Sample Magnetometer (VSM) facility. Let us recall it here briefly. In the VSM technique, a small sample (typically 4 mm wide and 4 mm long) is oscillated inside a background field imposed by a solenoid magnet. The frequency of oscillation is 20.4 Hz and the field ramp rate is typically between 100 - 300 mT/min, such that the sample experiences a quasi-static field during a single oscillation.

Fig. 5.1 shows the magnetic hysteresis cycles of the same SST tape presented in chapter 3. Cycles were recorded at 4.2 K, 6 K, 8 K, 10 K, 20 K, 30 K, 40 K, 50 K, 60 K, 70 K, 77 K, and 82 K. The magnetic moment is expressed in emu (1 emu corresponds to 10^{-3} Am^2 in the SI system). The field in a typical measurement is raised from zero up to 10 T, lowered to -2 T, then increased again to 2 T, and finally reduced to zero, see

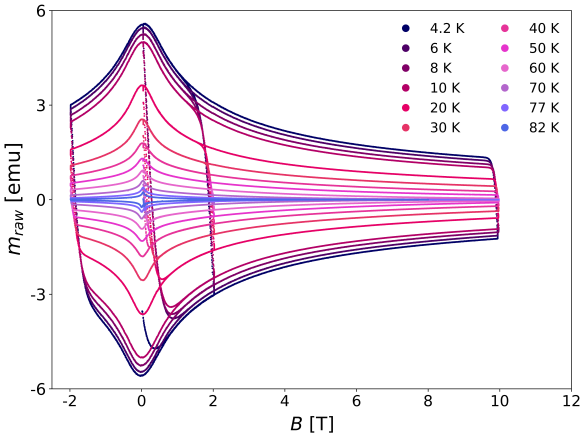

FIGURE 5.1: Magnetic hysteresis cycles for an SST tape, from 4.2 K up to 82 K.

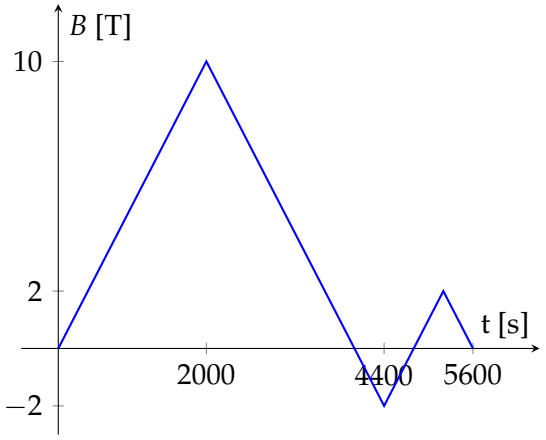

FIGURE 5.2: Magnetic cycle imposed by the background solenoid.

Fig. 5.2. This allows verification of the overlap of data in the initial part of the direct branch. Thus, this confirms the proper running of the measurement (e.g. temperature stability) while saving precious time with respect to conducting a full magnetic cycle.

We call the lower part of the curve from zero to 10 T the *direct* branch, while the upper part from 10 T down to zero the *reversal* branch. The scaling law is applied to the reversal branch of the cycle, since this branch is recorded continuously from the beginning to end. Moreover, the reversal branch is symmetric to the direct branch.

5.2 Analysis of the raw data and related scaling at 4.2 K

Before continuing, the procedure to elaborate and fit the magnetization data applying the scaling law is described. The first operation is to isolate the positive part of the curve ($m > 0$) and sort the reversal branch for $B > B_{peak}$, where B_{peak} is the field level corresponding to the peak magnetization, $m_{peak,4K}$. See Fig. 5.3, where the full raw data are indicated in dark blue as B_{raw}, m_{raw} and the sorted data in orange as B_{sort}, m_{sort}. Here, we still refer to the same SST tape mentioned above, ST1910.

The peak magnetization, $m_{peak,4K}$, is usually located at slightly positive fields. For example, B_{peak}=0.075 T for the curve considered here at 4.2 K. The reason for the peak offset is given later in chapter 6. The next step is to compensate for this discrepancy, see the green curve in Fig. 5.4 which indicates the selected data for fitting with the scaling law, B_{sel} and m_{sel}, where B_{sel} = B_{raw} - B_{peak}. Fig. 5.4 is a closeup on the positive part of the reversal branch only. One can note that the green curve is very close to the original one, since B_{peak} is small compared to the scale of the x-axis in the plot.

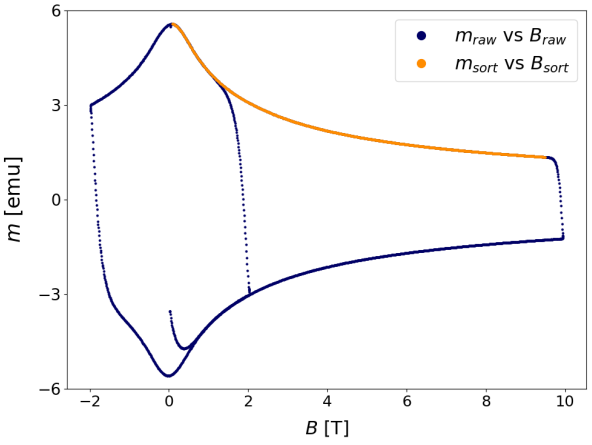

FIGURE 5.3: Raw and sorted data in the magnetic hysteresis cycle of SST tape ST1910, at 4.2 K.

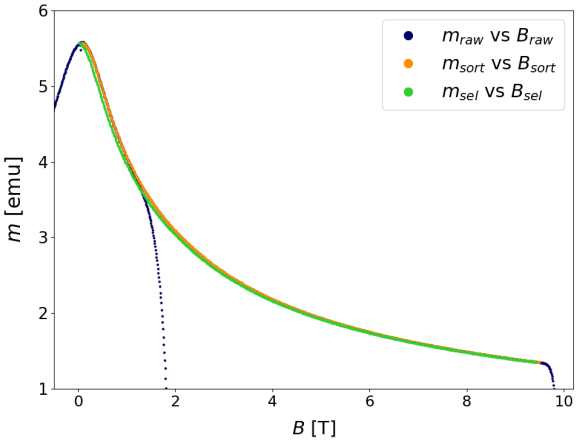

FIGURE 5.4: Selected data for further analysis of SST tape ST1910 at 4.2 K. This figure is a closeup into the positive part of the reversal branch only.

The scaling law is applied on the selected data, namely the green curve. This is reported in Fig. 5.5, which shows only the selected data in light green and the resulting fitting using the scaling with the black dashed line. Scale is log-log. The scaling parameters are reported in Table 5.1.

Table 5.1 also reports two parameters for the quality of the fitting. One is the least square parameter, $\chi^2 = 0.52$. Hundreds of data points are available for the fitting, which makes it a rather good value. Another parameter is also considered, the ratio between the derived m_0 and the peak magnetization, $m_{peak,4K}$. Let us note that here the m_0 is a scaling parameter that substitutes the $I_{c,0}$ in the scaling law. The ratio between $m_0/m_{peak,4K} = 1.071$.

It is relevant to remark that the scaling proposed in Fig. 5.5 with the parameters in Table 5.1 has been obtained assuming $q = 2$, to match the exponent in Kramer's law

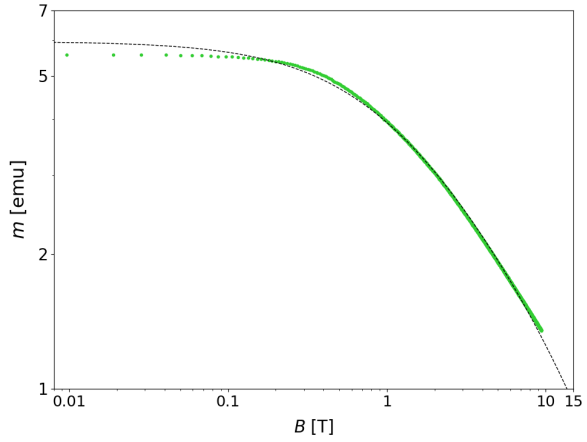

FIGURE 5.5: Fitting of the selected data using the scaling law. Scale is log-log.

	m_0 [emu]	α	B_0 [T]	Δm_0	$\Delta\alpha$	ΔB_0	m_0/m_{peak}	χ^2
SST ST1910	5.97	0.61	1.06	$\pm$0.01	$\pm$0.05	$\pm$0.08	1.071	0.52

TABLE 5.1: Scaling parameters, error margins, and quality of fitting for SST tape ST1910. Let us note that both $\Delta\alpha$ and ΔB_0 are $\sim$8 % of the corresponding values of α and B_0. Then, q is set to 2 to match the exponent in Kramer's law and B_{irr}=150 T from past estimates on the $B_{c,2}$ on cuprates [27].

and B_{irr} = 150 T in accordance with the literature. Let us note, however, that these two parameters here are meant just for fitting, without having an actual physical meaning (see also later). Table 5.1 also reports the error margins on the m_0, α, and B_0.

5.3 Methodology and scaling parameters as a function of temperature

The methodology to compare the results of the transport and magnetization methods is presented in this section. Then, the temperature dependence of the scaling parameters is derived for the same SST tape discussed so far.

5.3.1 Methodology: transport versus magnetization

Fig. 5.6 proposes the comparison between transport and magnetization data for the SST tape at 4.2 K. First of all, let us note that the transport data chosen here are from the test on 16/01/24, as this was the most complete over the field range from zero up to 15 T (see chapter 4).

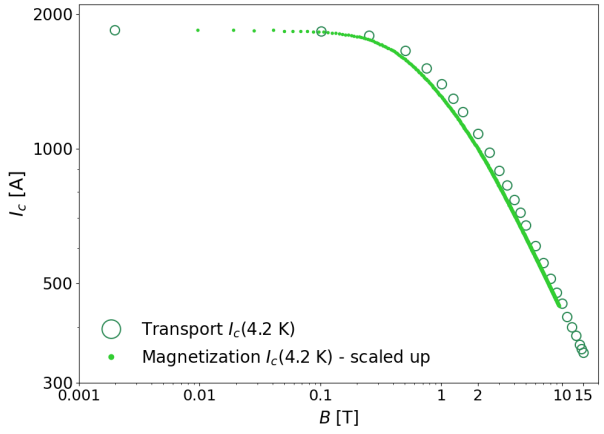

FIGURE 5.6: Transport versus magnetization data (scaled up) for the SST tape at 4.2 K and in perpendicular field.

Remarkably, the plot is filled with data down to a few milliteslas for both methods. To compare the two sets, the latter have been scaled up dividing by the peak magnetization, $m_{peak,4K}$, and multiplying by the transport critical current at zero applied field, $I_{c,T}(0\ \mathrm{T}) = 1841$ A, as indicated in section 5.3.2.

The two curves display a good match between each other at very low fields (below 0.25 T), thanks to the scaling up procedure. The discrepancy is highest at 8.0 % at 2 T, which then decreases to 5 % at 10 T. Fig. 5.7 is a closeup starting from 0.1 T. Fig. 5.8 adds the fitting using the scaling law for both the transport data (dashed line, in red) and the magnetization data (in orange).

The crossover field, B_0, resulting from the fitting of the magnetization data is 1.06 T. It is assumed, as a first approximation, that the B_0 is directly associated to the density of the pinning centers in the REBCO layer. This shall remain the same along a tape spool, especially when one considers that the samples for testing the transport and

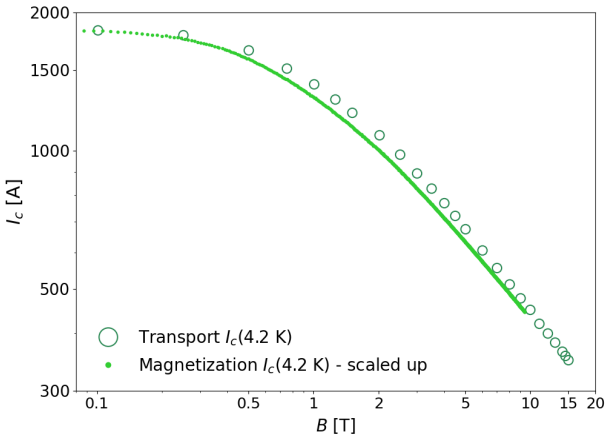

FIGURE 5.7: Closeup of Fig. 5.6 above 0.1 T.

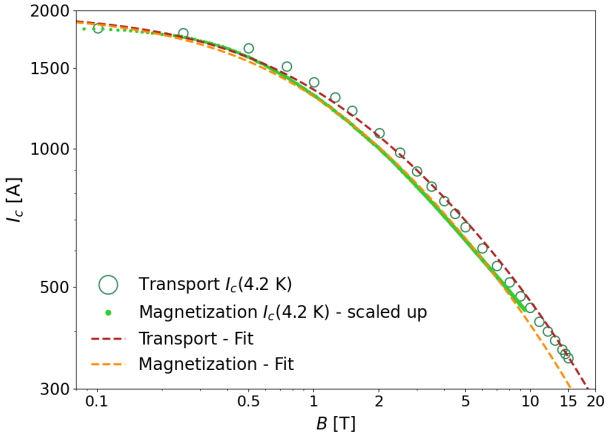

FIGURE 5.8: Fitting of transport and magnetization data applying the scaling law.

SST ST1910	$I_{c,0}$ [A]	α	B_0 [T]	q	B_{irr} [T]	$I_{c,0}$ / I_c(0 T)	χ^2
Magnetization	1971 (scaled)	0.61	1.06	2	150	1.071	0.52
Transport	1974	0.56	1.06	2	150	1.072	28.2

TABLE 5.2: Scaling parameters for the SST ST1910 tape both for the magnetization and transport data. The error bars on the scaling parameters of the magnetization data is ∼8 %, as shown in Table 5.1. The fitting of transport data (indicated in red in Fig. 5.8) differs by a 10% at most to the fitting of magnetization data (in orange in the same figure).

magnetization performance presented here have been extracted at a distance of just a few meters from each other. In fact, it was decided to keep the same value for fitting the transport data, while letting the slope of the linear region, α, associated to the strength of the pinning centers, as well as the intercept, $I_{c,0}$, free to vary.

Table 5.2, which extends Table 5.1, reports the comparison between the two resulting fittings with the scaling law. The $I_{c,0}$ shown for the magnetization method, which can be addressed as $I_{c,0,M}$, was obtained dividing m_0 by $m_{peak,4K}$ and multiplying by $I_{c,T}$ at zero applied field. Thanks to the fact that transport data are available down to zero applied field, the derived transport $I_{c,0,T}$ and the scaled up $I_{c,0,M}$ turn out to be very close to each other, namely 1974 A versus 1971 A.

The slope of the linear region resulting from the two methods is expected to differ. In fact, the α is 0.61 for the magnetization method while it is lower, 0.56, for the transport method. In turn, the fitting of transport data differs at most by 10% from the magnetization data. The least square parameter, χ^2, is very low for the magnetization data, but still acceptable for the transport as it is comparable to the number of data points.

Despite such difference, all the previous plots show that a rather good match of the field dependence *exists* between the transport and the scaled up magnetization measurements at 4.2 K. The method proposed, which consists in scaling up the magnetization measurements by $I_{c,T}$(0 T) / $m_{peak,4K}$ has the potential to scale up the magnetization curves at the other temperature levels, thus deriving the absolute value of the currents involved.

To conclude this section, it is important to highlight a few key aspects. First, both I_c datasets are plotted as a function of the applied background field, therefore the tape self-field is included in both. The self-field is not uniformly distributed across the tape width [111]. However, the most relevant impact of self-field is expected to occur below 0.5 T, where the currents are the highest, but the field dependence fades. The curves in Fig. 5.6 and in the similar following plots suggest that the self-field might be comparable for both datasets, allowing for a fair comparison between the two.

No upper limit is set on the $I_{c,0}$, resulting in a slight overshoot by roughly 7 % above the measured $I_{c,T}$ at zero applied field. This is capable to account for the augmented performance in absence of the tape self-field, which is the actual objective of the scaling

law. The second aspect is that the $I_{c,0,M}$ is chosen to scale up the other temperature levels and will be indicated just as $I_{c,0}$.

5.3.2 Derivation of scaling parameters as a function of temperature

The utility of these curves lies especially in deriving the parameters in the scaling law. Fig. 5.9 shows the resulting temperature dependence of $I_{c,0}$ for the SST tape, where the starting value at 4.2 K is 1974 A (see Table 4.5 in chapter 4). The region below 10 K is of particular interest, since the concavity of the curve is different from the region above 10 K. To further investigate on this, we refined the measurements in the low temperature region, namely at 4.2 K, 6 K, 8 K, and 10 K for the other tapes tested in this work as well.

Fig. 5.10 presents the temperature dependence of B_0 and α. The crossover field starts from 1.06 T, in agreement with Table 5.1 and, after following a slow initial reduction, it

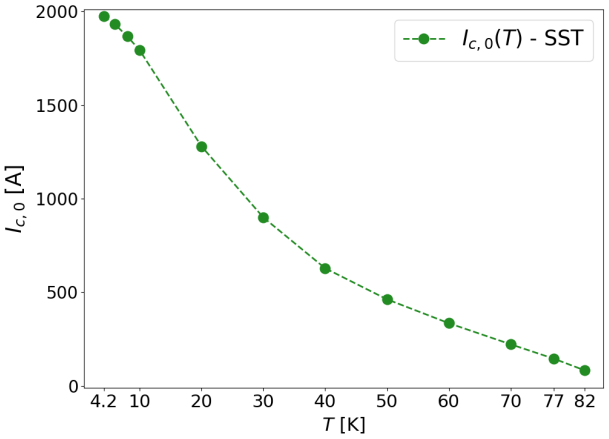

FIGURE 5.9: Intercept $I_{c,0}$ for the SST tape as a function of temperature. Error bars are comprised within the symbols.

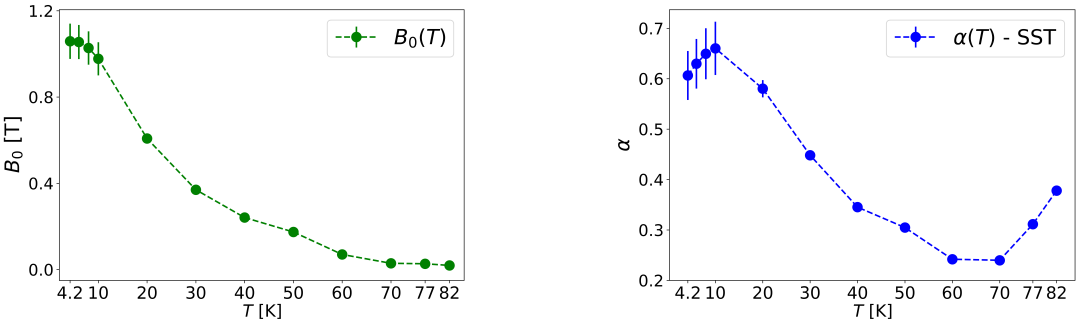

(A) Crossover field

(B) Slope of the linear region.

FIGURE 5.10: Crossover field (left) and slope of the linear region (right) for the SST tape as a function of temperature. Plots are complemented with the error bars.

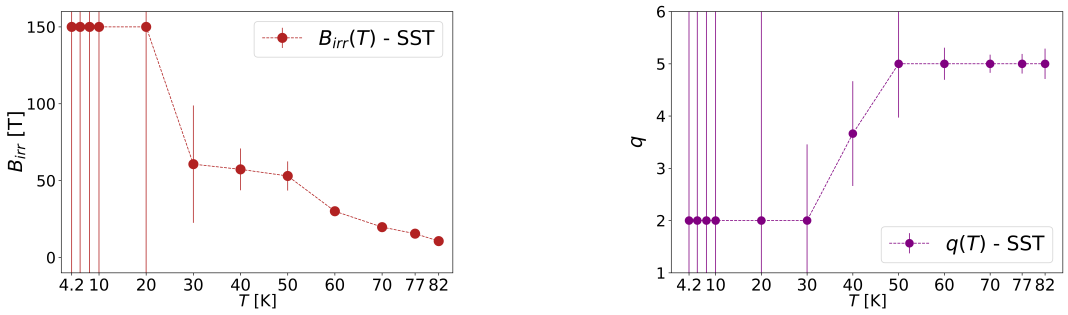

(A) Irreversibility field

(B) q-slope

FIGURE 5.11: B_{irr} (left) and q-slope (right) for the SST tape as a function of temperature. Plots are complemented with the error bars. Points below 20 K are affected by great uncertainty. In fact, any value could be used to fit the measurements in that range, where B_{irr}=150 T and q=2 are just fixed based on physics considerations.

declines mildly with increasing temperature. Conversely, the slope of the linear region starts from 0.61 at 4.2 K, it goes up until 10 K reaching 0.66, then drops progressively to 0.24 at 60 K, and it increases finally to 0.37 at 82 K. This is a sign that different pinning mechanisms might intervene at different temperatures. The plots also report the error bars on the estimation of the parameters. The errors are highest between 4.2 K and 10 K, namely of about $\pm$0.05 T on the B_0 and of $\pm$0.05 on the α, due to the difficulty of fitting over this temperature range.

Fig. 5.11 shows the temperature dependence also of the last two scaling parameters, B_{irr} and q. B_{irr} starts from 150 T at 4.2 K and it remains so up to 20 K before it decreases. While we keep such constant value in this temperature range for the scope of this work, we are aware that it is not physically realistic. The error bars confirm that both B_{irr} and q are affected by great uncertainty from 4.2 K to 20 K, as any value of these two parameters could be used to fit the data. Then, the error reduces above 30 K, and q is still 2 at 30 K, then it jumps to 5 at 50 K, with an intermediate step of 3.64, at 40 K. The shift is because the drop in performance is much more rapid at middle-to-high temperatures than at low temperatures.

5.4 Extension of results to other tape manufacturers

We now extend the methodology described in the previous section to the other tapes tested from SuperPower, Fujikura and Faraday Factory Japan.

5.4.1 SuperPower

Fig. 5.12 shows the comparison between the transport and magnetization data at 4.2 K. Transport data are available down to 0.1 T background field in this case, where $I_{c,T}$(0.1 T)

= 2078 A. The magnetization data have been scaled up by the factor $I_{c,T}(0.1\ \mathrm{T})/m_{peak,4K}$.

The two datasets overlap very nicely between each other across the entire field range, which spans from a few hundreds of milliteslas up to 7 T. The reason why magnetization data stop at 7 T, instead of 10 T like for the SST tape, is that the measurements were conducted using a different system at the University of Geneva.

In addition, Fig. 5.13 proposes the scaling of the transport data (in red) and of the magnetization data (in orange). Analogously to Table 5.2, Table 5.3 reports the resulting fitting with the scaling law in the two cases. Let us remark that the $I_{c,0}$ shown for the magnetization method was obtained dividing the m_0 by $m_{peak,4K}$ and multiplying by $I_{c,T}(0.1\ \mathrm{T})$. The crossover field, $B_0 = 1.42$ T from fitting the magnetization data using the scaling law. For the same reason given in the case of the SST tape, the same value of

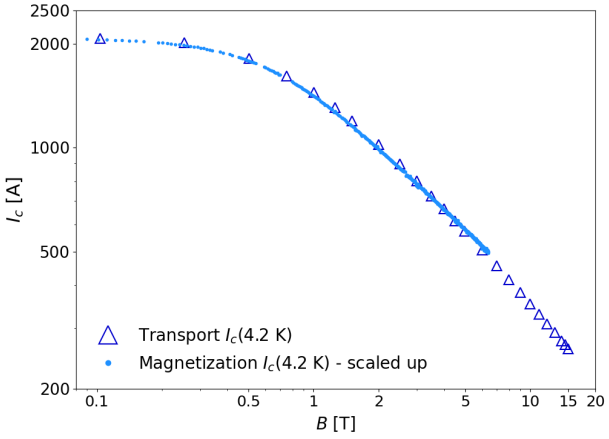

FIGURE 5.12: Transport versus magnetization data (scaled up) for the SP tape at 4.2 K and in perpendicular field.

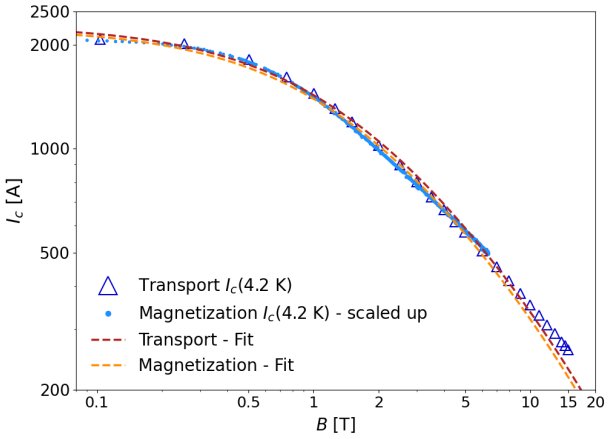

FIGURE 5.13: Fitting of transport and magnetization data for the SP tape applying the scaling law.

SP AP	$I_{c,0}$ [A]	α	B_0 [T]	q	B_{irr} [T]	$I_{c,0}/I_c$(0.1 T)	χ^2
Magnetization	2245 (scaled)	0.87	1.42	2	150	1.080	0.51
Transport	2284	0.85	1.42	2	150	1.099	32.5

TABLE 5.3: Scaling parameters for the SP AP tape both for the magnetization and transport data. The error bars on the scaling parameters of the magnetization data are ∼35%, as shown in Fig. 5.19 and Fig. 5.20. The fitting of transport data (indicated in red in Fig. 5.13) differs by a 5% at most to the fitting of magnetization data (in orange in the same figure).

B_0 is used to fit the transport data. The resulting $I_{c,0}$ are practically identical, therefore also the ratio $I_{c,0}/I_c$(0.1 T).

The slope of the linear region is slightly higher for the VSM data, 0.87 versus 0.85. The resulting discrepancy between the fitting of the transport data and the magnetization data is by less than 5 %. However, we would like to note that the magnetization data stop at 7 T, namely a dataset extended to 10 T might have resulted in α being even closer to that of the transport measurement. The least square parameter, χ^2, is very low for the magnetization data, and still acceptable for the transport as it is comparable to the number of data points.

The match between the transport and the scaled up magnetization measurements at 4.2 K is very good and the proposed methodology allows deriving the absolute values of the critical currents at the other temperature levels.

5.4.2 Fujikura

Fig. 5.14 shows the comparison between the transport and magnetization data at 4.2 K. Both datasets are available down to 0.1 T background field in this case, where $I_{c,T}$(0.1 T) =

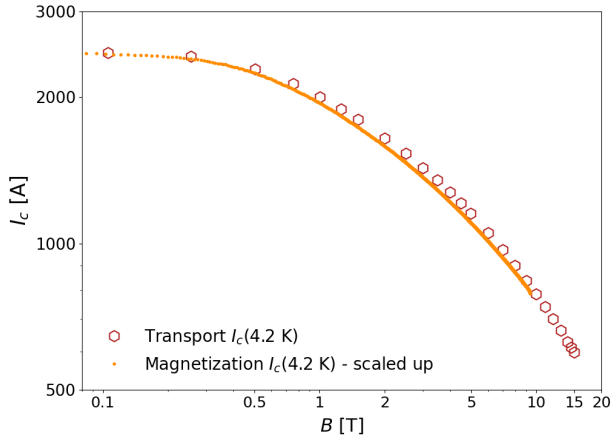

FIGURE 5.14: Transport versus magnetization data (scaled up) for the Fujikura tape at 4.2 K and in perpendicular field.

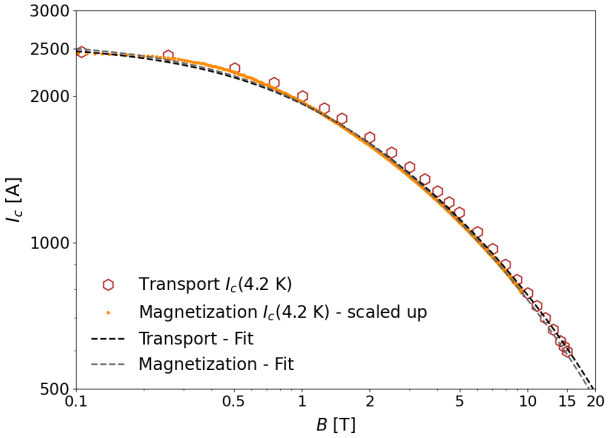

FIGURE 5.15: Fitting of transport and magnetization data for the Fujikura tape applying the scaling law.

2467 A. The magnetization data have been scaled up by the factor $I_{c,T}$(0.1 T) / $m_{peak,4K}$. Similarly to the case of the SuperPower tape, the two datasets overlap nicely with each other across the entire field range, which spans from a few hundreds of milliteslas up to 10 T.

Then, Fig. 5.15 shows the resulting fitting applying the scaling law, where the black dashed line is for the transport data, while the grey dashed line is for the magnetization data. Table 5.4 reports the scaling parameters in the two cases. Let us remark that the $I_{c,0}$ shown for the magnetization method was obtained dividing the m_0 by $m_{peak,4K}$ and multiplying by $I_{c,T}$(0.1 T).

The two $I_{c,0}$ are just a few amperes apart and the ratio $I_{c,0}/I_c$(0.1 T) is also similar. The slope of the linear region is slightly higher for the magnetization than for the transport data, being 0.52 versus 0.51. This translates into a variance of the fitting of transport data from the magnetization data smaller than 5 %. Finally, the least square parameter, χ^2 = 7.01 for the transport data, which is the best value so far, while as usual it is very low for the magnetization data.

FESC-SCH04	$I_{c,0}$ [A]	α	B_0 [T]	q	B_{irr} [T]	$I_{c,0}/I_c$(0.1 T)	χ^2
Magnetization	2597 (scaled)	0.52	1.39	2	150	1.053	0.23
Transport	2650	0.51	1.39	2	150	1.074	7.01

TABLE 5.4: Scaling parameters for the Fujikura FESC-SCH04 tape both for the magnetization and transport data. The error bars on the scaling parameters of the magnetization data are ∼9%, as shown in Fig. 5.19 and Fig. 5.20. The fitting of transport data (indicated in black in Fig. 5.15) differs by a 5% at most to the fitting of magnetization data (in grey in the same figure).

5.4.3 Faraday Factory

Fig. 5.16 shows the comparison between the transport and magnetization data at 4.2 K for the tape from Faraday Factory Japan. This time, the transport dataset is available only down to 0.55 T, since the power supply was limited in current to 3000 A (see chapter 4). Let us note that the derived I_c(0.55 T) = 3040 A.

As explained in chapter 4, the $I_{c,0}$ was estimated by considering the performance of a similar tape from the same manufacturer tested one year earlier. The resulting $I_{c,0}$ = 3794 A, which is 24.8 % higher than the I_c(0.55 T). This time, the magnetization data have been scaled up by the ratio $I_{c,0,T}/m_{peak,4K}$, since the information on I_c at zero applied field is lacking. The two datasets shown in Fig. 5.16 are in very good agreement between each other, proving that the scaling up procedure of the magnetization data is reliable even in the case of partial data across the magnetic field domain.

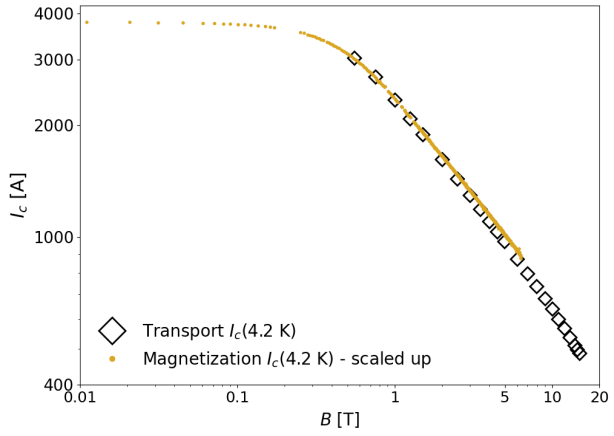

FIGURE 5.16: Transport versus magnetization data (scaled up) for the FFJ tape at 4.2 K and in perpendicular field.

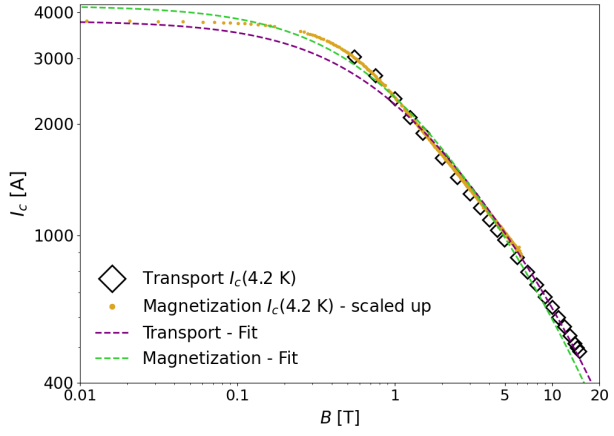

FIGURE 5.17: Fitting of transport and magnetization data for the FFJ tape applying the scaling law.

FFJ 16059-N2	$I_{c,0}$ [A]	α	B_0 [T]	q	B_{irr} [T]	$I_{c,0}/I_c$(0 T)	χ^2
Magnetization	4165 (scaled)	0.71	0.84	2.0	150	1.098	0.68
Transport	3794	0.64	0.84	2.0	150	n.a.	86.9

TABLE 5.5: Scaling parameters for the FFJ 16059-N2 tape both for the magnetization and transport data. The error bars on the scaling parameters of the magnetization data are ∼25%, as shown in Fig. 5.19 and Fig. 5.20. The fitting of transport data (indicated in purple in Fig. 5.17) differs by a 10% at most to the fitting of magnetization data (in green in the same figure). Note that the ratio $I_{c,0}/I_c$(0 T) is not reported for the transport dataset, since the critical current is available only down to 0.55 T.

Fig. 5.17 further displays the fitting applying the relevant scaling law. The dashed line in purple is for the fitting of the transport data, while in green is for the magnetization data. Table 5.5 sums up the resulting scaling parameters. B_0 is 0.84 T from the magnetization data, which is the lowest value of the crossover field found so far. The same value is adopted for fitting the transport data. In this case, the ratio $I_{c,0}/I_c$(0 T) is not available for the transport method.

The slope of the linear region results to be 0.64 for the transport data and 0.71 for the magnetization data. Consequently, the divergence on the fitting of transport data with respect to magnetization data is 10 %. The least square parameter ends up being quite high for the transport data, which can be explained by the lack of data in the low-field region. This does not constitute an issue, however, since the resulting fitting is close to the fitting of the magnetization data, which is much more accurate.

5.5 Temperature dependence of the scaling parameters

Fig. 5.18 - 5.20 show the scaling parameters of the tapes presented in the previous sections. Fig. 5.18 is for the $I_{c,0}$: as it has been mentioned, curves of the magnetic moment at each temperature level are scaled dividing by $m_{peak,4K}$ and multiplying by the I_c(4.2 K, 0.1 T) obtained by the transport method. For the FFJ tape, curves are multiplied by the $I_{c,0}$ since transport data are missing below 0.55 T.

The FFJ tape has much higher performance than the other three tapes. The distinctive feature of the SuperPower AP tape is the relatively slow decrease of the $I_{c,0}$ between 4.2 K and 10 K. The other tapes, instead, tend to experience a faster initial drop. In general, the region below 10 K is of great interest, since the concavity of the curve is different from the region above 10 K. Such behavior confirms what was observed already in [29], which is unexpected from the theoretical standpoint. The rest of the temperature domain, from 10 K up to 82 K (85 K for SP and 87 K for FFJ) is defined by a mild slope in all cases.

Table 5.6 sums up much information about the tapes and we refer to it diffusely in the following. First, it is worth commenting on α and B_0 together. Noticeably, the FFJ tape

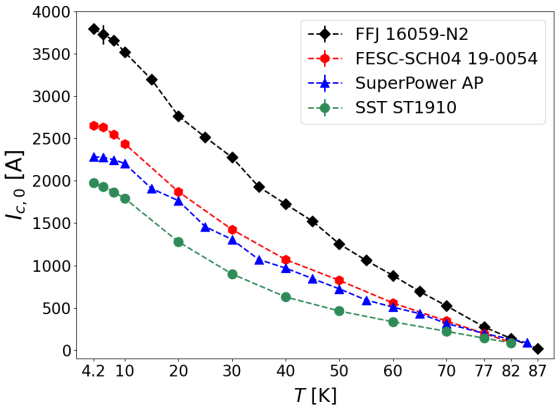

FIGURE 5.18: Critical current at zero background field from 4.2 K up to 87 K, for the same tapes tested by the transport method in chapter 3.

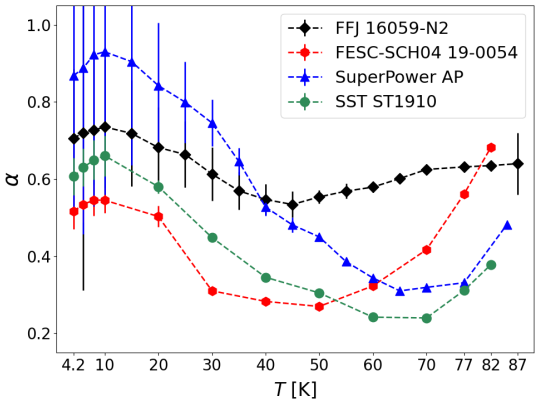

FIGURE 5.19: Slope of the linear region from 4.2 K up to 87 K, for the same tapes tested by the transport method in chapter 3. The high uncertainty of the FFJ and SP tapes below 20 K is attributed to the limited testing up to 7 T.

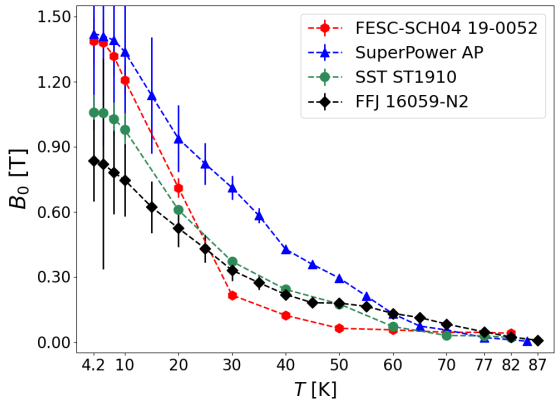

FIGURE 5.20: Crossover field from 4.2 K up to 87 K for the same tapes tested by the transport method in chapter 3. The high uncertainty of the FFJ and SP tapes below 20 K is attributed to the limited testing up to 7 T.

(in black) displays some high values of α from the intermediate to high temperature range, 50 K onwards. Similarly, the B_0 is quite high for this tape over the same interval. A high B_0 means a delayed performance drop, which is relevant for high temperature applications where the fields involved are contained below a few teslas at most. Despite the high values of α, this tape might be employed at all temperatures, see Table 5.6, thanks to the remarkable $I_{c,0}$ values. In fact, Y_2O_3 nanoparticles [24] act as effective pinning centers over a wide range of temperatures, as explained in [46].

Before continuing in the discussion, it is worth commenting on the error bars of both the α and B_0, shown in Fig. 5.19 and Fig. 5.20. For example, the uncertainty on the FFJ tape (at 1 σ) is $\pm$0.19 for α and $\pm$0.18 T for B_0, at 4.2 K. The uncertainty of this tape is highest at 6 K, where it is $\pm$0.41 for α and $\pm$0.48 T for B_0. Something similar occurs for the SP tape, which has $\pm$0.36 and $\pm$0.44 T for the two quantities at 4.2 K, respectively. Only above 20 K, the uncertainties reduce considerably for both tapes. This is attributed to the limited testing only up to 7 T, which makes it difficult to properly fit the low-field region at low temperatures. Instead, the Fujikura and SST tapes have been measured up to 10 T and result in low error bars already from 4.2 K, in the order of $\pm$0.05 for the α and $\pm$0.05 T for the B_0.

The Fujikura tape (in red) behaves differently. α values are comprised between 0.52 - 0.55 below 10 K, which are the lowest among all tapes, while B_0 stays above 1.2 T. In comparison, the SST tape (in green) has slightly higher α, between 0.61 - 0.66, and lower B_0 = 0.98 T - 1.06 T in the same temperature range. The combination of α and B_0 keeps the performance of these two tapes very close to each other, and they are preferable from low to middle temperature applications, indicatively below 60 K.

The B_0 of the Fujikura tape drops rapidly below 300 mT already at 30 K and then gently reduces to zero approaching T_c, see Fig. 5.20. In contrast, the α raises to high values close to T_c (it is 0.68 at 82 K), see Fig. 5.19. This is the sign that a different pinning mechanism kicks in from middle to high temperatures and it might be interpreted by means of the BHO nanorods indicated in Table 5.6.

Manufacturer	SP	SST	Fujikura	**FFJ**
Route	IBAD+MOCVD	IBAD+PLD	IBAD+PLD	IBAD+PLD
SC layer	(Y,Gd)BCO	GdBCO	EuBCO	YBCO
Pinning	BZO nanorods	No APC	BHO nanorods	Y_2O_3 nanop.
α (<10 K)	0.87 - 0.93	0.61 - 0.66	0.52 - 0.55	0.71 - 0.74
α (>60 K)	0.31 - 0.48	0.24 - 0.38	0.32 - 0.68	0.58 - 0.64
B_0(<10 K) [T]	1.34 - 1.42	0.98 - 1.06	1.21 - 1.39	0.75 - 0.84
Appl. range	Above 60 K	Overall	Below 60 K	Overall

TABLE 5.6: Manufacturing route, REBCO layer, types of pinning centers, scaling parameters, and inferred application range of the tapes tested for the scope of this work.

The SST tape undergoes a similar trend in terms of α, however the values are quite low over the entire temperature domain. This makes this tape suitable also in the rest of the temperature domain, namely above 60 K. Instead, B_0 decreases gently with increasing temperature. A single pinning mechanism might be involved in this case, which cannot be attributed to advanced pinning centers (marked as 'No APC' in Table 5.6), but rather to stacking faults, as it was shown in [59].

The SP tape (in blue) starts from some high values of α, between 0.87 - 0.93, as well as of B_0 = 1.34 T - 1.42 T below 10 K. Then, the latter decreases smoothly with increasing temperature, similarly to the SST tape. The presence of BZO nanorods in the superconducting layer may be at the origin of this behavior [23]. This mechanism fades

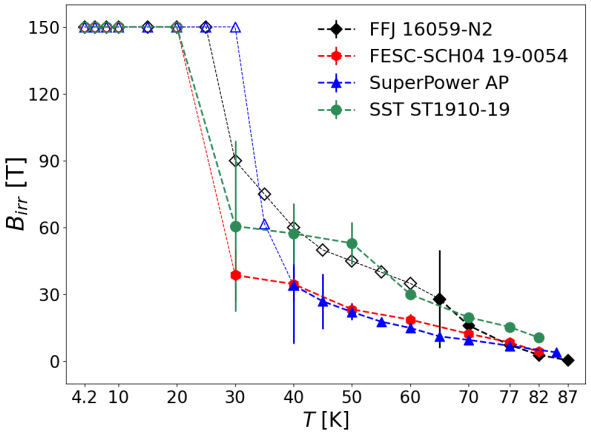

FIGURE 5.21: B_{irr} from 4.2 K up to 87 K for the same tapes tested by the transport method in chapter 3. Open symbols below 30 K - 40 K (65 K for the FFJ tape) correspond to error bars that are out of scale, see the example in Fig. 5.11. B_{irr} was chosen to 150 T because of past estimates on $B_{c,2}$, at low temperatures, on cuprates [27].

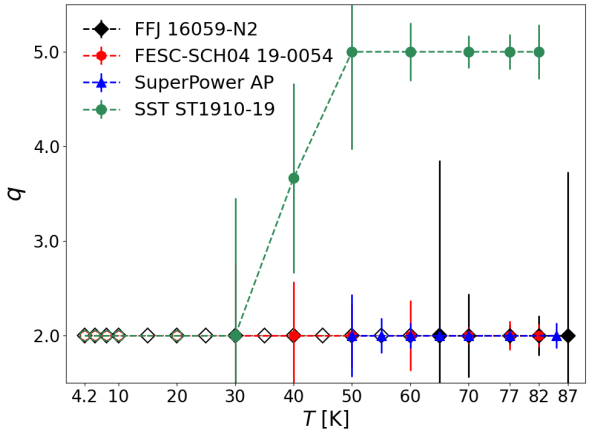

FIGURE 5.22: q slope from 4.2 K up to 87 K for the same tapes tested by the transport method in chapter 3. Open symbols below 30 K - 40 K (65 K for the FFJ tape) correspond to error bars that are out of scale, see the example in Fig. 5.11. q was chosen to 2, at low temperatures, to match the exponent in Kramer's law.

gradually as the temperature rises. For such reasons, the SP tape is best suited for applications above 60 K, as the combination of α and B_0 is competitive with SST in this temperature range. A common feature observed for SST, SP, and Fujikura tapes is that the slope of the linear region raises at high temperatures, having slightly different onsets starting at 50 - 60 K, see Fig. 5.19. This might be attributed to creep, which becomes increasingly important at high temperatures.

For completeness, Fig. 5.21 and Fig. 5.22 sum up the dependence of the irreversibility field, B_{irr}, and of the associated slope of the third term in the scaling law, q, with temperature. Full symbols are complemented with the error bars, which are relatively limited above 30 K for the SST and Fujikura tapes, above 40 K for the SP tape, and above 65 K for the FFJ tape. The error bars are out of scale below such temperatures, as it was the case presented in Fig. 5.11 and the related data points are reported with open symbols. This is attributed to the hysteresis data being limited to very low fractions of the irreversibility field, which makes the open symbols just fitting parameters and not values with an actual physical meaning. As a reference, q was set to 2 from 4.2 K to match the exponent in Kramer's law, while B_{irr} was set to 150 T because of past estimates on the $B_{c,2}$ on cuprates [27].

The two plots suggest that the SP and Fujikura tapes have similar phenomenology. In fact, they share a common trend of B_{irr} from 40 K onward. In addition, the q slope stays to 2 all over the temperature range for both. On the other hand, FFJ and SST tapes might belong to a second category, given the similar high values of B_{irr} from 40 K onward.

5.6 Methodology and scaling parameters for partial transport data

In the previous sections, the methodology for comparing the transport and magnetization data for four tapes from SuperPower, Fujikura, Shanghai ST, and Faraday Factory Japan presented at the Applied Superconductivity Conference (ASC) in 2024 was discussed [30]. It is the objective of this section to present additional tapes for which transport and magnetization data were extracted on a limited field range as well as deriving the temperature dependence of the scaling parameters.

5.6.1 Fujikura 24-0032

Fig. 5.23 shows the comparison between the transport and magnetization data of tape FESC-SCH04 from Fujikura, type 24-0032. The two datasets match up with a difference of less than 4 % between each other across the field range from 0.5 T to 10 T. Transport

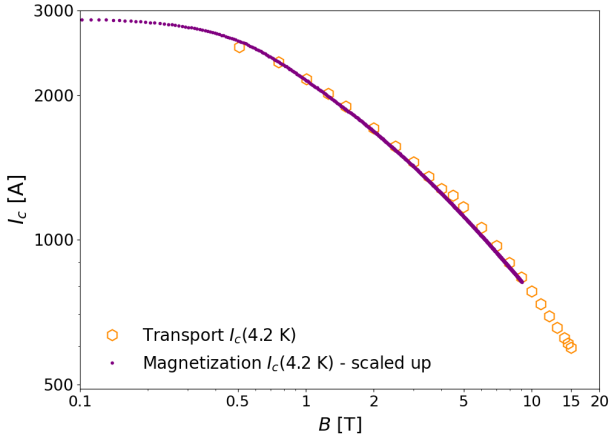

FIGURE 5.23: Transport and magnetization data for tape 24-0032 from Fujikura.

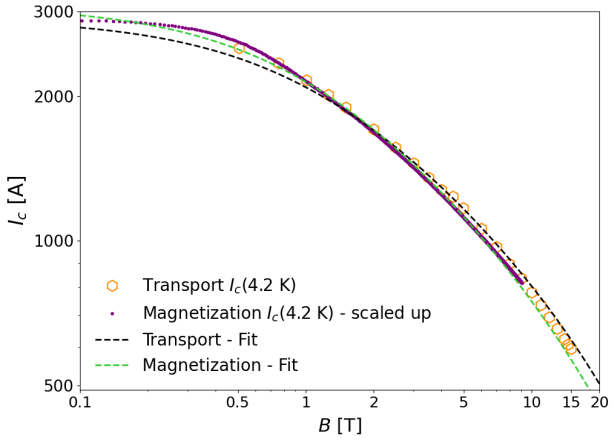

FIGURE 5.24: Fitting of transport and magnetization data for tape 24-0032 from Fujikura.

data are available down to 0.5 T, where I_c(0.5 T) = 2523 A. Therefore, it is not possible to scale up the magnetization data by the I_c(0.1 T) as shown in the previous cases. The option of scaling up by the I_c(0.5 T) is also not viable since it would result in a non negligible error.

Consequently, magnetization data are scaled up diving by $m_{peak,4K}$ and multiplying by $I_{c,0,T}$, namely the $I_{c,0}$ obtained by the transport method. Let us recall that the $I_{c,0}$ is a scaling parameter which is usually slightly higher than the actual measured I_c in zero applied field. Then, Fig. 5.24 shows the resulting fitting with the scaling law for both the transport data, see the black dashed line, and the magnetization data, see the green dashed line.

In the case where both the magnetization data and its fitting were scaled up by the I_c(0.1 T), the obtained $I_{c,0,M}$ and $I_{c,0,T}$ were very close, see Table 5.2 for SST tape ST1910. Instead, in this case, $I_{c,0,M}$ is quite higher than the $I_{c,0,T}$, as can be seen from Fig. 5.24

Fuj 24-0032	$I_{c,0}$ [A]	α	B_0 [T]	q	B_{irr} [T]	$I_{c,0}/I_c$(0 T)	χ^2
Magnetization	3092	0.56	1.14	2	150	1.066	0.54
Transport	2902	0.50	1.14	2	150	n.a.	26.9

TABLE 5.7: Scaling parameters for the Fujikura 24-0032 tape both for the magnetization and transport data. The error bars on the scaling parameters of the magnetization data are ∼12%, as shown in Fig. 5.35 and Fig. 5.38. The fitting of transport data (indicated in black in Fig. 5.24) differs by a 10% at most to the fitting of magnetization data (in green in the same figure). Note that the ratio $I_{c,0}/I_c$(0 T) is not reported for the transport dataset, since the critical current is available only down to 0.5 T.

and Table 5.7. Let us point out that the scaling law is applied on the transport data using the same B_0 found fitting the magnetization data.

In brief, we consider the fitting of the transport data as a pragmatic method to estimate the I_c at zero applied field, which then is used to scale up the magnetization data. The resulting maximum discrepancy between the fitting of the transport data and the magnetization data is by 10 %. Nevertheless, the fit of magnetization data is more accurate and we advise keeping it as the useful reference for modelling actual applications.

5.6.2 SST ST2306

The same exercise is repeated for the SST tape ST2306, however transport data are available only down to 3.5 T in this case. Fig. 5.25 shows the comparison of the transport and magnetization data for this tape.

A similar reasoning as provided for the Fujikura tape 24-0032 is repeated here: transport data are fitted applying the scaling law and the derived $I_{c,0,T}$ is used to scale up the magnetization data. The resulting fitting of the two curves is shown in Fig. 5.26 and scaling parameters are reported in Table 5.8. Once again, the resulting $I_{c,0,M}$ is

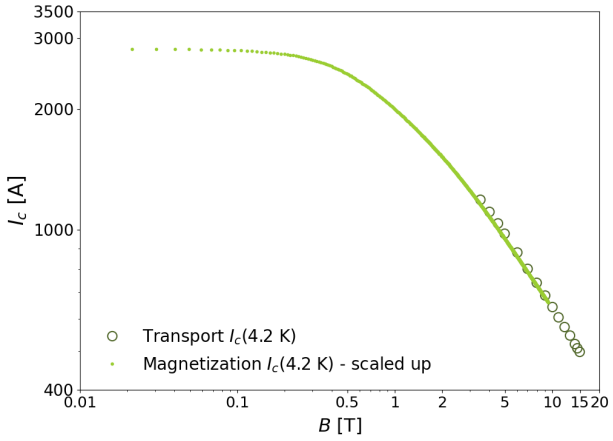

FIGURE 5.25: Transport versus magnetization data for tape ST2306 from SST at 4.2 K and in perpendicular field.

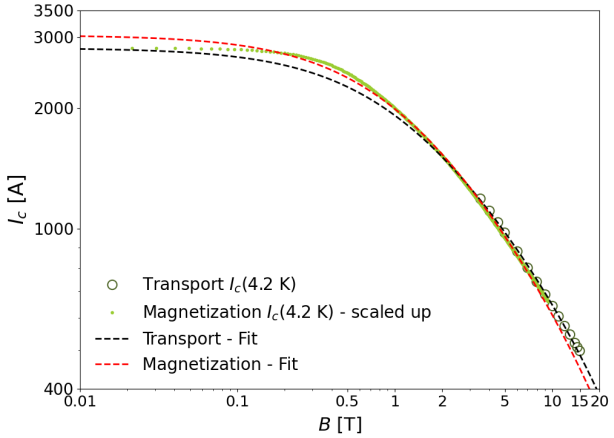

FIGURE 5.26: Fitting of the transport and magnetization data for tape ST2306 from SST.

SST ST2306	$I_{c,0}$ [A]	α	B_0 [T]	q	B_{irr} [T]	$I_{c,0}/I_c$(0 T)	χ^2
Magnetization	3038	0.63	1.10	2	150	1.076	0.67
Transport	2822	0.58	1.10	2	150	n.a.	1.11

TABLE 5.8: Scaling parameters for the SST ST2306 tape both for the magnetization and transport data. The error bars on the scaling parameters of the magnetization data are ∼9%, as shown in Fig. 5.34 and Fig. 5.37. The fitting of transport data (indicated in black in Fig. 5.26) differs by 8% at most to the fitting of magnetization data (in red in the same figure). Note that the ratio $I_{c,0}/I_c$(0 T) is not reported for the transport dataset, since the critical current is available only down to 3.5 T.

higher than the $I_{c,0,T}$. The resulting maximum discrepancy of fitting the transport data to the magnetization data is by 8 %. Nevertheless, the fit of magnetization data is more accurate and it is advised to adopt it for modelling actual applications.

5.6.3 SST ST2311

Fig. 5.27 shows the comparison of transport and magnetization data for SST tape ST2311. Transport data are available down to 0.5 T, corresponding to I_c(0.5 T) = 2231 A. Magnetization data stop at 7 T, which is specific of tapes tested with the VSM facility of the University of Geneva.

Fig. 5.28 shows the resulting scaling of both the transport and magnetization data. This figure is a closeup in the field range above 0.1 T. The orange dashed line is for the fitting of the transport data, while the black dashed line is for the magnetization data. Scaling parameters are reported in Table 5.9.

The resulting $I_{c,0,M}$ is 7 % higher than the $I_{c,0,T}$. The maximum difference between the fitting of the transport data and the magnetization data is 15 %. The scaling of the

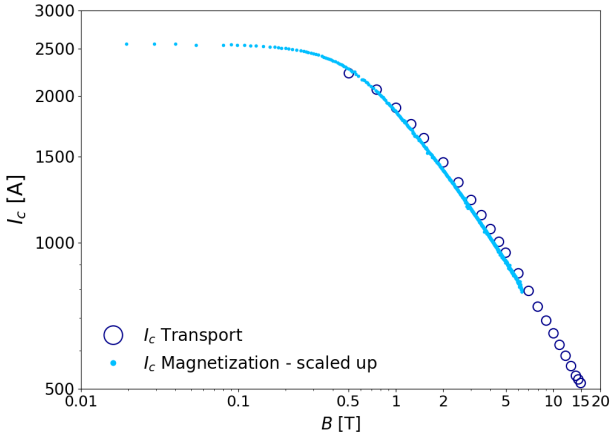

FIGURE 5.27: Transport versus magnetization data for tape ST2311 from SST at 4.2 K and in perpendicular field.

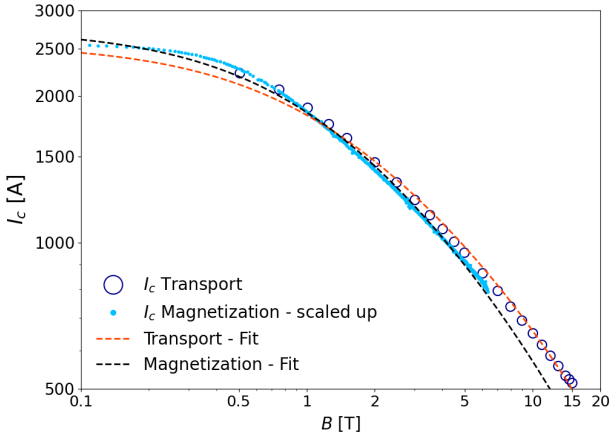

FIGURE 5.28: Fitting of transport and magnetization data for tape ST2311 from SST.

SST ST2311	$I_{c,0}$ [A]	α	B_0 [T]	q	B_{irr} [T]	$I_{c,0}/I_c$(0 T)	χ^2
Magnetization	2752	0.66	1.26	2	150	1.073	0.25
Transport	2566	0.56	1.26	2	150	n.a.	2.96

TABLE 5.9: Scaling parameters for the SST ST2311 tape both for the magnetization and transport data. The error bars on the scaling parameters of the magnetization data are ∼30%, as shown in Fig. 5.34 and Fig. 5.37. The fitting of transport data (indicated in red in Fig. 5.28) differs by 15% at most to the fitting of magnetization data (in black in the same figure). Note that the ratio $I_{c,0}/I_c$(0 T) is not reported for the transport dataset, since the critical current is available only down to 0.5 T.

magnetization data has much lower standard deviation, χ^2, therefore this is considered as the most accurate one.

5.6.4 FFJ 6919-C

Let us analyze the case of tape 6919-C from Faraday Factory Japan. Fig. 5.29 shows the comparison between the transport and magnetization data. Transport data are available down to 1 T, since the tape burnt below this field level. Magnetization data are available up to 7 T, since this tape was tested at the University of Geneva.

Transport data were fitted applying the scaling law by imposing an upper limit on the $I_{c,0}$, given by the ratio between $I_{c,0}/I_c(1\ \mathrm{T})$ = 1.618 of tape 16059-N2, as presented in chapter 4. The ratio was increased by a 5 % tolerance to get 1.7. The resulting $I_{c,0,T}$ = 2921 A.

The magnetization data have been scaled up by such factor and the two datasets end up displaying a good match over the intermediate field range, *Region II*. Then, Fig. 5.30

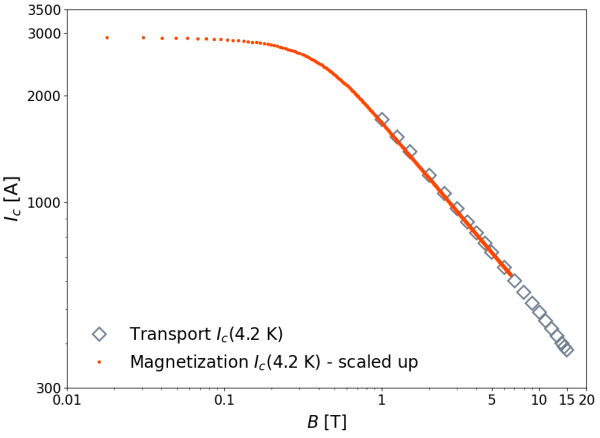

FIGURE 5.29: Transport versus magnetization data for FFJ tape 6919-C, at 4.2 K and in perpendicular field.

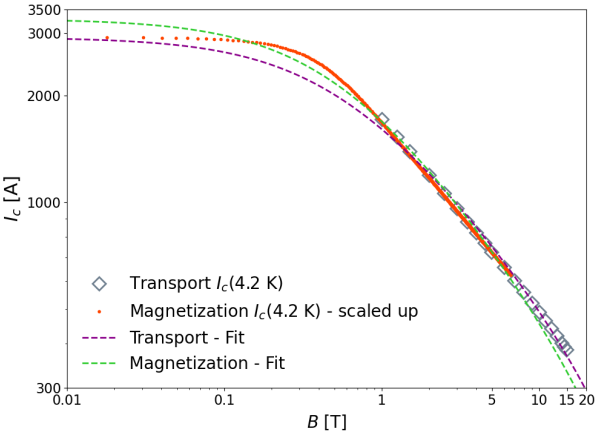

FIGURE 5.30: Fitting of transport and magnetization data for FFJ tape 6919-C applying the scaling law.

FFJ 6919-C	$I_{c,0}$ [A]	α	B_0 [T]	q	B_{irr} [T]	$I_{c,0}/I_c$(0 T)	χ^2
Magnetization	3292	0.62	0.53	2	150	1.127	5.96
Transport	2921	0.55	0.53	2	150	-	19.2

TABLE 5.10: Scaling parameters for the FFJ 6919-C tape both for the magnetization and transport data. The error bars on the scaling parameters of the magnetization data are ∼10%, as shown in Fig. 5.36 and Fig. 5.39. The fitting of transport data (indicated in purple in Fig. 5.30) differs by 11% at most to the fitting of magnetization data (in green in the same figure). Note that the ratio $I_{c,0}/I_c$(0 T) is not reported for the transport dataset, since the critical current is available only down to 1 T.

reports the resulting fitting of the two curves by means of the scaling law. Let us note that the fitting of the magnetization data has also been scaled up by $I_{c,0,T}/m_{peak,4K}$, therefore the resulting $I_{c,0,M}$ = 3292 A > $I_{c,0,T}$. Table 5.10 lists the scaling parameters.

The maximum difference between the fitting of transport data and magnetization data is 11 %. The scaling of the magnetization data has much lower standard deviation, χ^2, therefore this is considered as the most accurate one.

5.7 Further comparison of results

Scaling parameters as a function of temperature for the additional four tapes presented in section 5.6 are discussed. Parameters are compared to those presented already for the first four tapes. Plots in this section are divided into three groups. Three different tapes from SST have been tested by both the transport and magnetization methods: ST1910, represented in dark green, ST2306 in light green, and ST2311 in light blue. Two FESC-SCH04 tapes from Fujikura have also been tested: type 19-0054 and 24-0032, shown in red and orange, respectively. The scaling parameters for the SuperPower AP tape are also displayed, in blue, together with the previous two. Finally, the temperature dependence of the scaling parameters of two tapes from Faraday Factory, 16059-N2 and 6919-C, is shown in black and grey.

5.7.1 Intercept, $I_{c,0}$

The resulting $I_{c,0}$ temperature dependence is displayed in Fig. 5.31 - 5.33.

To begin with, the $I_{c,0}$ of SST tapes is quite variable at 4.2 K, roughly between 2000 A and 2800 A. Tape ST1910 was manufactured in 2023, while the other two, having considerably higher performance, in 2024. The two Fujikura tapes have comparable performance to the two recent SST tapes. The SuperPower AP tape has lower $I_{c,0}$ than the Fujikura tapes between 4.2 K - 10 K, namely of about 2200 A, then it remains quite close to them over the rest of the temperature range.

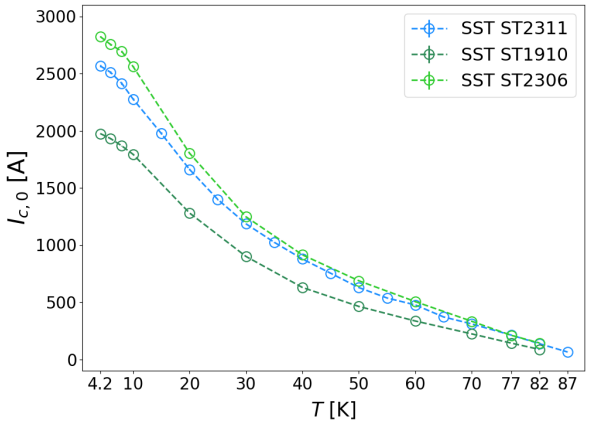

FIGURE 5.31: Intercept, $I_{c,0}$, for the three SST tapes as a function of temperature. Error bars are comprised within the symbols.

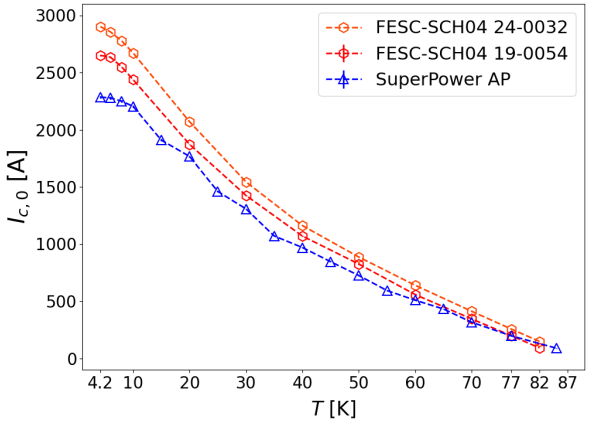

FIGURE 5.32: Intercept, $I_{c,0}$, for the two Fujikura tapes and the SP AP tape as a function of temperature. Error bars are comprised within the symbols.

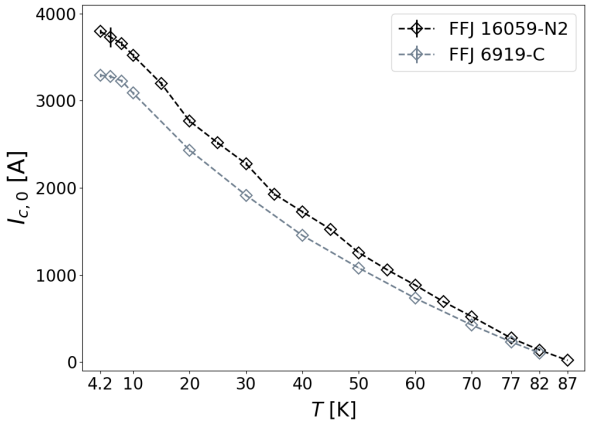

FIGURE 5.33: Intercept, $I_{c,0}$, for the two FFJ tapes as a function of temperature. Error bars are comprised within the symbols.

We note the extremely high performance of tape 16059-N2. In fact, let us recall that 3000 A were injected in this tape at 0.55 T background field, which is the highest performance achieved with any 4 mm tape tested in this work. Then, the estimated $I_{c,0}$ = 3794 A at 4.2 K, as shown in Fig. 5.33. The performance of tape 6919-C is also very good, given the $I_{c,0}$ = 3292 A at 4.2 K. In fact, this is above all the other tapes from SST, SP, and Fujikura that have just been discussed. The intercept drops quite rapidly between 4.2 K - 10 K for tape 16059-N2, while it reduces more slowly in the case of tape 6919-C. Then, the drop takes place at a relatively constant rate over the rest of the temperature domain for both.

5.7.2 Slope of the linear region, α

Considering SST tapes, the α starts from values between 0.6 - 0.65 at 4.2 K, which increase to 0.65 - 0.7 up to 10 K. Then, curves drop and reach the minimum of 0.25 - 0.3, at 60 - 65 K. These low values of the slope of the linear region mean a slow rate of performance drop, which is favorable for applications in this temperature range. The α increases again up to 0.4 - 0.45 at 82 K. Another data point close to 0.8 is available for tape ST2311 at 87 K, a sign that the performance drops very rapidly close to T_c.

It is relevant to comment about the uncertainties. Of the eight tapes shown in Fig. 5.34 - Fig. 5.36, five tapes have very low error bars, $\ll \pm 0.1$ across the entire temperature spectrum. Nevertheless, tape ST2311, SP AP, and 16059-N2 are characterized by large error bars below 20 K. These are even up to ± 0.41 for 16059-N2 at 6 K. While this is rather troublesome, it is useful to note that the same three tapes have been tested in magnetic fields only up to 7 T. Consequently, this limits the ability to accurately fit the linear region at low temperatures, explaining the high uncertainties. Then, the

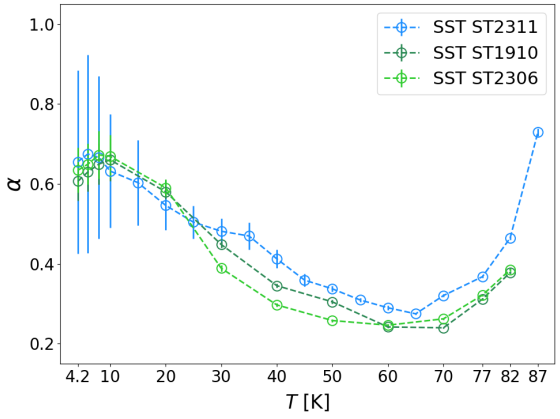

FIGURE 5.34: α for the three SST tapes as a function of temperature. The high error bars of tape ST2311 below 20 K are attributed to the limited testing only up to 7 T.

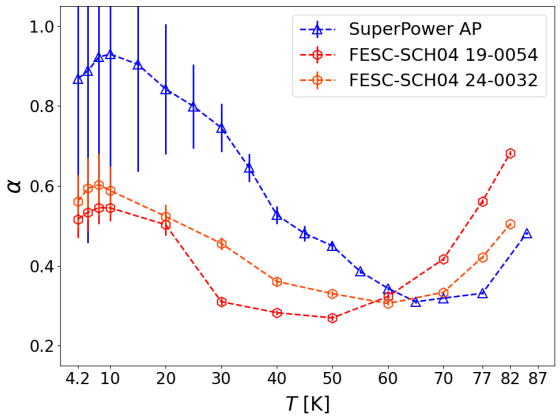

FIGURE 5.35: α for the two Fujikura tapes and the SP AP tape. The high error bars of tape SP AP below 20 K are attributed to the limited testing only up to 7 T.

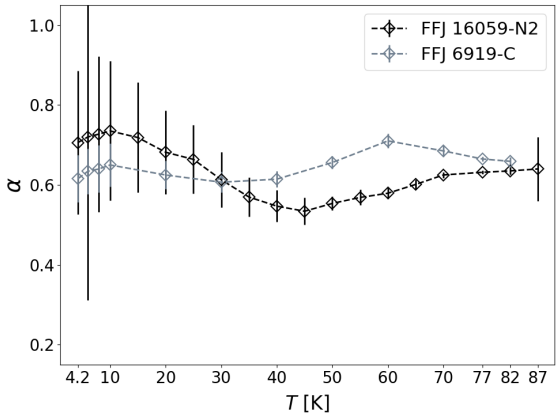

FIGURE 5.36: α for the two FFJ tapes as a function of temperature. The high error bars of tape 16059-N2 below 20 K are attributed to the limited testing only up to 7 T.

error bars of these three tapes also reduce to a maximum ± 0.05 across the rest of the temperature domain.

The evolution of α for the Fujikura tapes recalls that of the SST tapes. Values are between 0.5 - 0.55 at 4.2 K, which increase to 0.55 - 0.6 at 10 K. While they follow the same kind of trend in the rest of the temperature domain, values actually differ considerably. Tape 19-0054 features a sharp drop from 0.5 at 20 K to 0.31 at 30 K. It reaches the minimum at 50 K (0.27), then it rises as the temperature gets to 82 K, reaching even higher values (α=0.68 at 82 K) than in the low temperature region. Instead, tape 24-0032 has a gentle slope from 10 K to 60 K, where it reaches its minimum (0.31). It increases again up to 82 K, but the final value is lower than at 4.2 K (0.5 versus 0.56, respectively). In this sense, this tape is more similar to the SST tapes.

The α of tape 16059-N2 grows to 0.62 at 70 K with modest slope, then it continues to increase with lower slope, reaching 0.64 at 87 K. α raises to 0.71 at 60 K for the other

tape, however it decreases to 0.66 at 82 K. These α values are quite high compared to the other tapes, with only SP being actually comparable to tape 16059-N2 between 4.2 K to 45 K.

5.7.3 Crossover field, B_0

The crossover field, B_0, of SST tapes are very close to each other, similarly to what seen for the α. Values at 4.2 K are of 1.0 T - 1.1 T for tape ST1910 and ST2306, while of 1.26 T for ST2311. Then, they decrease with a similar trend up to T_c.

Regarding the uncertainties, similar considerations as in section 5.7.2 can be elaborated. We note that tapes ST2311, SP AP, and 16059-N2 displaying large error bars, are those tested in magnetic fields only up to 7 T. Consequently, this limits the ability to accurately fit the linear region at low temperatures, explaining the high uncertainties. Then, the error bars of these three tapes also reduce to a maximum ± 0.05 T across the rest of the temperature domain.

B_0 of Fujikura tape 19-0054 starts from 1.39 T at 4.2 K, drops to just 0.22 T at 30 K, and it goes down to zero as the temperature approaches T_c. Instead, tape 24-0032 has a slightly lower value of 1.14 T at 4.2 K, then gently declines with increasing temperature. In fact, B_0 of this tape surpasses that of tape 19-0054 already at 30 K (0.35 T versus 0.22 T).

In the case of the SP tape, the B_0 starts from 1.42 T at 4.2 K, being close to that of the Fujikura tape 19-0054, then it declines much more slowly. The SP tape and the two Fujikura tapes have similar crossover fields above 70 K. In general, high values of B_0 have the effect of counterbalancing high values of α. As a matter of fact, higher B_0 translates in a delayed drop of performance, while higher α indicates a faster drop with

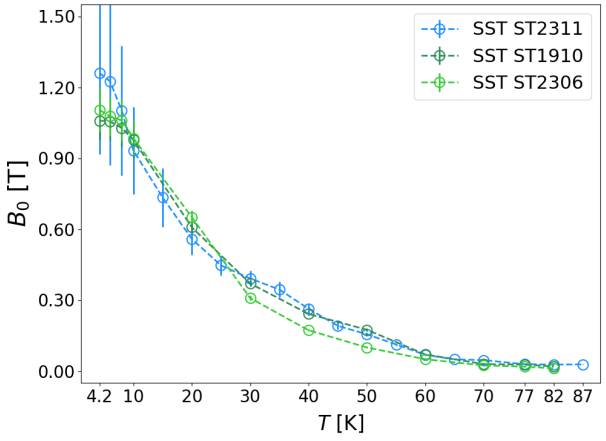

FIGURE 5.37: B_0 for the three SST tapes as a function of temperature. The high error bars of tape ST2311 below 20 K are attributed to the limited testing only up to 7 T.

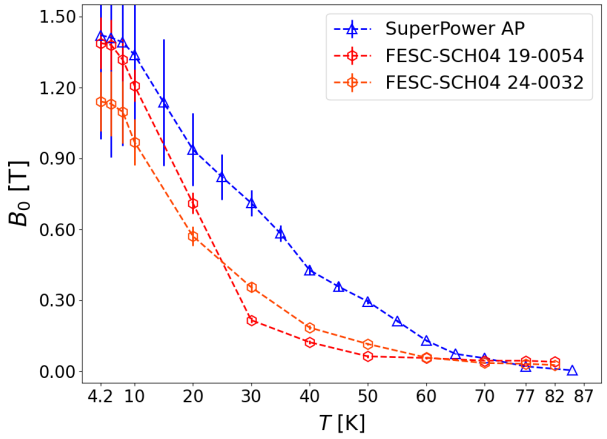

FIGURE 5.38: B_0 for the two Fujikura tapes and the SP AP tape as a function of temperature. The high error bars of tape SP AP below 20 K are attributed to the limited testing only up to 7 T.

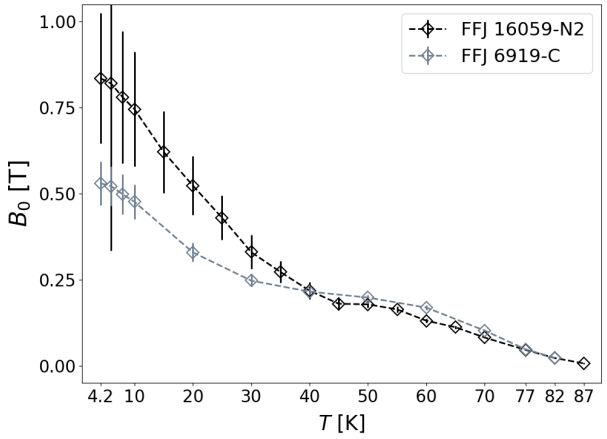

FIGURE 5.39: B_0 for the two FFJ tapes as a function of temperature. The high error bars of tape 16059-N2 below 20 K are attributed to the limited testing only up to 7 T.

increasing field. In this case, however, the difference between the α of the SuperPower and of the Fujikura tapes is too high to 'compensate' for the delayed B_0 of SuperPower. For all these reasons, the two Fujikura tapes represent a good option for applications over the entire temperature domain, whereas SuperPower could be better suited for high temperatures, above 50 - 60 K.

Another peculiar feature of FFJ tapes are the modest values of the crossover field. Fig. 5.39 shows that tape 16059-N2 starts from 0.84 T at 4.2 K, while tape 6919-C even from 0.53 T. The former decreases with modest slope up to 45 K, where it displays a plateau-like feature up to 55 K. Then, it goes smoothly to zero approaching T_c. The latter has mild slope from 10 K to 30 K, then it decreases at a lower pace, to finally drop faster again from 60 K. Let us note that values of the two tapes are very similar from 40 K onward.

5.7.4 Irreversibility field and q-slope

As a final section to this chapter, Fig. 5.40 - 5.42 depict the irreversibility field and the q-slope for the full set of tapes.

It is relevant to comment about the uncertainties. As discussed previously in Fig. 5.21 and Fig. 5.22, the error bars are reported only above some temperature threshold. This is 30 K for tapes ST1910, ST2306, Fujikura 19-0054, 40 K for SP AP and Fujikura 24-0032, 50 K for ST2311, and even 65 K for the two FFJ tapes. In fact, the error bars are out of scale below such temperatures, see Fig. 5.11, and both q and B_{irr} are just fitting parameters without an actual physical meaning. This is attributed to the maximum available field, either 7 T or 10 T, being much lower than the irreversibility field, thus not allowing to observe *Region III*.

Tape ST1910 is peculiar in the sense that it displays a first 'step' of B_{irr} between 30 K - 50 K, then decreases progressively up to 82 K. The other two tapes show a smooth decline from 42 T in the case of ST2306 and 68 T of ST2311. They stay at 150 T in the low-intermediate temperature range, meaning that the available experimental data are still fully in *Region II* and do not allow to identify the actual value.

The q-slope of tape ST1910 jumps from 2.0 at 30 K to 5.0 at 50 K with an intermediate step of 3.64 at 40 K. The other two tapes have a constant q=2 over the entire range, meaning that the performance drop remains mild over *Region III*. Similarly among all the other tapes, the q slope equals 2 across the entire temperature range. B_{irr} seems to differ considerably between the two FFJ tapes. It is 90 T at 30 K for 16059-N2, 16 T at 70 K, 2.9 T at 82 K and 0.5 T at 87 K, which is quite remarkable to observe. Conversely, tape 6919-C detaches from the upper limit at 60 K, where B_{irr} = 67 T. It drops to 9.5 T at 70 K and 2.5 T at 82 K.

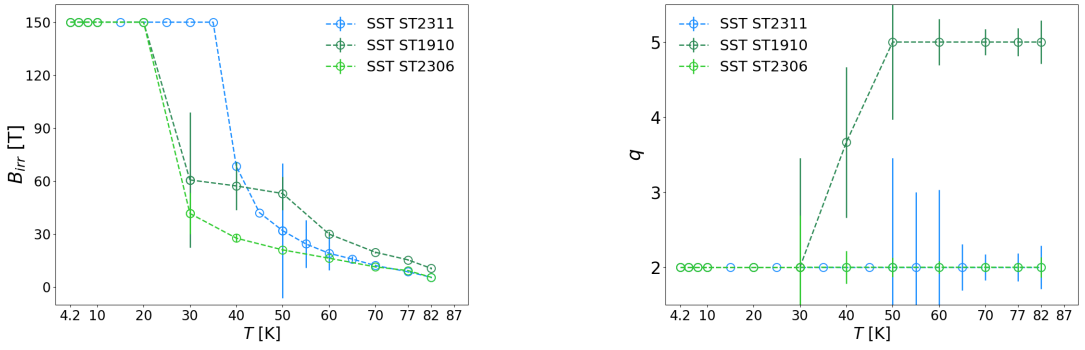

(A) Irreversibility field (B) q-slope

FIGURE 5.40: B_{irr} (left) and q-slope (right) for all three SST tapes as a function of temperature. Error bars below 30 K (50 K for ST2311) are not reported since they are out of scale, which is attributed to the maximum field available, either 7 T or 10 T, being far from B_{irr} at such temperatures.

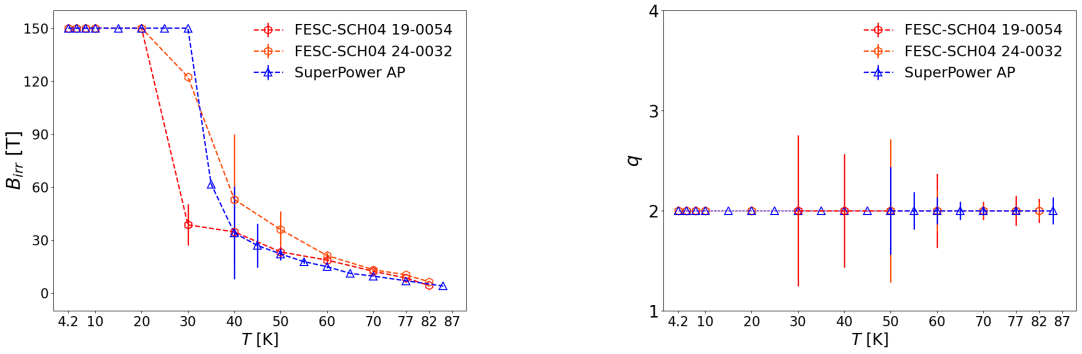

(A) Irreversibility field (B) q-slope

FIGURE 5.41: B_{irr} (left) and q-slope (right) for the two Fujikura and the SP tapes as a function of temperature. Error bars below 30 K - 40 K are not reported since they are out of scale, which is attributed to the maximum field available, either 7 T or 10 T, being far from B_{irr} at such temperatures.

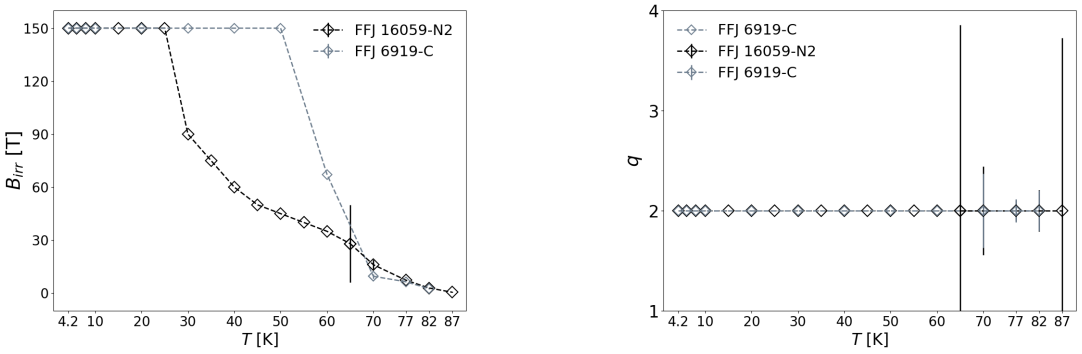

(A) Irreversibility field (B) q-slope

FIGURE 5.42: B_{irr} (left) and q-slope (right) for the two FFJ tapes as a function of temperature. Error bars below 65 K are not reported since they are out of scale, which is attributed to the maximum field available, either 7 T or 10 T, being far from B_{irr} at such temperatures.

The B_{irr} departs from the upper limit of 150 T between 30 K to 40 K as also noticed for the SST tapes. One data point stands out for tape 24-0032, which has 122 T irreversibility field at 30 K. On the other hand, the first useful data point is 39 T at 30 K for tape 19-0054 and 62 T at 35 K for SuperPower AP. The rest of the temperature domain is characterized by a smooth descent for all three tapes. Tape 24-0032 remains higher up to 50 K (50 T versus 23 T of tape 19-0054 and 22 T of SP AP), then values are very similar approaching the T_c.

To summarize, the two FFJ tapes studied in this work have much higher intercept than tapes from the other manufacturers. The slope of the linear region is quite high at all temperature levels, implying a fast performance drop, which is further enhanced by the low values of the crossover field. Nevertheless, the performance remains very

competitive with the other tape manufacturers, which makes FFJ applicable over the full temperature domain, confirming the labeling in Table 5.6.

5.8 Summary

The results and the related analysis presented in this chapter make a brief summary useful. The full measured magnetization data of eight REBCO tapes from four manufacturers have been presented. First, the methodology to compare the results of transport and magnetization experiments at 4.2 K was put forward. The agreement between the field dependence of the two methods show that the proposed methodology can be applied to scale up the magnetization curves at all temperature levels using the transport data at 4.2 K. On one side, this allows inferring the absolute values of the current at different temperatures and, on the other, the temperature dependence of the scaling parameters in the scaling law.

Scaling parameters show similar patterns among different tapes from the same manufacturers as it is, for example, the case of SST and Fujikura. In fact, given the similar trends of the slope of the linear region and of the crossover field, one might infer that the manufacturers could be adopting similar pinning mechanisms and densities of the pinning centers. Instead, this is not the case of FFJ, which displays different patterns and values for the two tapes tested. Scaling parameters of the SP tape are also very much different with respect to the other tapes.

The scaling law can be re-written as

$$I_c(B,T,\theta=0) = I_{c,0}(T)\cdot\left[1+\frac{B}{B_0(T)}\right]^{-\alpha(T)}\cdot\left[1-\frac{B}{B_{irr}(T)}\right]^{q(T)} \tag{5.1}$$

which here is presented in terms of both the magnetic field and temperature dependence of the critical current for the field orientation parallel to the c-axis, θ = 0°. The availability of the temperature dependence of the scaling parameters derived through the experimental campaign described in chapter 4 and in this chapter allows for such a full characterization of the tape properties.

Extending the effort to each type of tape from the manufacturers, or at least to each 'family' of similar tapes, would provide a very valuable tool to magnet designers. Thus, this would relieve from the tedious characterization process, which was the initial aim and the truly advantageous point made in this chapter.

5.9 A potential step forward

Despite being particularly effective, the scaling law proposed tends to underestimate the performance between 0.5 - 2 T by up to 7 - 8 %, while it remains generally below 5 % in the rest of the field domain. An improvement in the region affected by minor accuracy can be achieved by introducing an inner exponent in the second term of the law, such as:

$$\left[1 + \left(\frac{B}{B_0}\right)^{\beta/\alpha}\right]^{-\alpha} \tag{5.2}$$

which would 'squeeze' the transition between *Region I* and *Region II* even more. In the expression, $\beta \approx 2$.

Chapter 6

Numerical modelling of the magnetization experiment

6.1 Initial considerations

The governing equations to describe the electromagnetic evolution of REBCO coated conductors are the Maxwell equations and the superconducting material is described by means of a non-linear E-J characteristics, which takes into account the transition from the superconducting to the normal state [113].

Maxwell equations are used to describe electromagnetic phenomena at the macroscopic scale and several formulations can be derived depending on which state variables are chosen to solve for. These equations are independent of the material and need to be coupled with constitutive laws that describe the electromagnetic properties of the materials involved as well as appropriate boundary conditions in order to obtain a solvable system.

Maxwell equations are usually formulated by means of scalar, ϕ, or vector, $\vec{A}$, magnetic potentials supplied with some appropriate gauge conditions. Independently of the used formulation, for non-linear materials or in the presence of conductors with sharp corners, the discretization by the FEM method of the second-order differential operator, $\nabla \times \nabla \times$ and the use of nodal elements give rise to ill-conditioned matrices and the iterative solution converges slowly.

The use of edge elements overcomes the problems mentioned above. The distinctive property of these elements is that they are curl conforming by construction. Namely, in the case of strong discontinuities of the materials properties and in the presence of sharp corners, they guarantee the physical requests for the magnetic field $\vec{H}$ on the boundaries of the elements. These are the continuity of the tangential component and the possible discontinuity of the normal component.

In fact, the main disadvantage of FEM models with nodal elements is that a correction has to be applied at each node in order to satisfy the divergence-free equation $\vec{\nabla} \cdot \vec{H} = 0$. This results in a large set of constraints and the solution can be harmed by the increase of the null space of the stiffness matrix. Instead, edge elements of the first-order have zero divergence by construction, and they are also curl conforming, as mentioned above.

This method presents several advantages.

1. Using the magnetic field components as state variables avoids any issue linked to the choice of the gauge.
2. The magnetic field components used as state variables of the problem allow to easily impose the boundary conditions.
3. The magnetic field variables are directly available from the solution, and they do not need to be calculated by differentiating electromagnetic potentials, which usually introduces inaccuracy in the numerical values.

In simulations, one has to deal with many different types of materials, such as:

- The superconductor. This is described by a non-linear resistivity, $\rho(J)$, and $\vec{B} = \mu_0 \vec{H}$.
- Normal conducting materials. These are described by means of a constant resistivity and by $\vec{B} = \mu_0 \vec{H}$, replaced by μ for magnetic materials.
- The air or vacuum surrounding the conductor. It is an insulating material with $\vec{B} = \mu_0 \vec{H}$.

6.1.1 A couple of words on the power law

The electromagnetic behaviour of HTS is highly non-linear, therefore it is described through a non-linear *E-J* constitutive relation. The most diffused is the Bean critical state model [35], which assumes a step change in the electric field when the current density surpasses the critical current density, J_c. However, this model does not account for flux creep, namely the way how the current density induced in the superconductor evolves in time while the external excitation remains unchanged. To account for flux creep, the step change can be substituted by functions that also show a fast but gradual change of the electric field near j_c, such as *E-J* power laws. In fact, the Bean model can be seen as the limit of the *E-J* power law when the exponent goes to infinity.

The most widely used relation is the non-linear power law:

$$\rho = \frac{E_c}{J_c}\left|\frac{J}{J_c}\right|^{n-1} \tag{6.1}$$

6.1.2 A digression on edge elements

Edge elements are commonly used in FEM simulations, as they are the most appropriate to represent vector fields characterized by specific boundary conditions [114].

In the case of a magnetic field, using finite elements satisfies the continuity of the tangential component along the boundary between two domains of different permeability, thanks to the continuity of the approximation functions across the common edge of adjacent mesh elements.

Edge shape functions are couple of polynomials (therefore, vectors) defined in each element, such that the tangential component has a unitary value along one edge and zero in the others of the same element. In this way, the degrees of freedom are assigned to the edges of the elements, not to the nodes. As an example, given a triangular mesh in a 2D problem, the field $U^e(x)$ in the element Ω^e is:

$$\mathbf{U}^e(\mathbf{x}) = \sum_{j=1}^{3} U_j^e \mathbf{N}_j^e(\mathbf{x}) \ \ , if\ x \in e \tag{6.2}$$

$$\mathbf{N}_j^e(\mathbf{x}) = 0\ , if\ x \notin e \tag{6.3}$$

also:

$$\mathbf{N}_j^e(\mathbf{x}) \cdot \mathbf{t}_j \ \ , if\ x \in j - edge \tag{6.4}$$

$$\mathbf{N}_j^e(\mathbf{x}) \cdot \mathbf{t}_k \ \ , if\ x \in two\ other\ edges \tag{6.5}$$

where $\mathbf{t}_j$ is the tangent vector to the edge j. $\mathbf{N}_j^e(\mathbf{x})$ is defined only in the element e and it is null elsewhere.

In two adjacent elements e and e' with edges j and j', the continuity of the tangential component implies that $U_j^e = U_{j'}^{e'}$.

These shape functions can also be built in the interior of the elements, such that:

$$\vec{\nabla} \cdot \mathbf{N}_j^e(\mathbf{x}) = 0 \tag{6.6}$$

$$\vec{\nabla} \times \mathbf{N}_j^e(\mathbf{x}) = \mathbf{j}_j^e(\mathbf{x}) \tag{6.7}$$

The first equation above already provides the condition of zero divergence of the magnetic field.

6.2 Formulations

6.2.1 The magnetic field, or *H* formulation

The H formulation is elaborated starting from Faraday's law:

$$\vec{\nabla} \times \vec{E} = -\frac{\partial \vec{B}}{\partial t} \tag{6.8}$$

both the constitutive relation of the superconductor, $\vec{E} = \rho \vec{J}$, and of the magnetic materials, $\vec{B} = \mu \vec{H}$, are implemented. Substituting into Faraday's law:

$$\vec{\nabla} \times (\rho \vec{J}) = -\mu \frac{\partial \vec{H}}{\partial t} \tag{6.9}$$

Considering Ampere's law:

$$\vec{\nabla} \times \vec{H} = \vec{J} \tag{6.10}$$

and again, substituting into the previous equation, one gets:

$$\vec{\nabla} \times \left(\rho \vec{\nabla} \times \vec{H} \right) = -\mu \frac{\partial \vec{H}}{\partial t} \tag{6.11}$$

which is the equation of the H formulation [115], where the state variable is $\vec{H}$. Note that in the first term, the resistivity is variable in space, therefore it cannot be brought out of the curl.

Gauss' law is another relevant equation for the H formulation:

$$\vec{\nabla} \cdot (\mu \vec{H}) = 0 \tag{6.12}$$

Solving both Eq. 6.11 and Eq. 6.12 results in an over-constrained system, requiring another procedure. The simplest approach was proposed in [116] and consists in taking the divergence of Eq. 6.11. The first term becomes zero by definition, whereas the divergence and time derivative can be exchanged in the second, obtaining:

$$\mu \frac{\partial}{\partial t} \left(\vec{\nabla} \cdot \vec{H} \right) = 0 \tag{6.13}$$

namely, $\vec{\nabla} \cdot \vec{H}$ is constant at all times. If $\vec{\nabla} \cdot \vec{H} = 0$ at a given instant of time, then the expression is zero at all other instants. Usually, the initial condition is set in this way. Let us note that the magnetic induction being divergence-free is obtained only by the analytical structure and not by the edge elements used in the discretization process.

In 2D, the $\vec{H}$ and $\vec{E}$ vectors have only two transverse and one longitudinal component: $\vec{H} = [H_x(x,y), H_y(x,y), 0]$ and $\vec{E} = [0, 0, E_z(x,y)]$. Eq. 6.11 can be re-written as:

$$\mu \frac{\partial H_x}{\partial t} + \frac{\partial E_z}{\partial y} = 0 \tag{6.14}$$

$$\mu \frac{\partial H_y}{\partial t} - \frac{\partial E_z}{\partial x} = 0 \tag{6.15}$$

The constitutive relation becomes $E = \rho(J)J$, whereas the current density is:

$$J = \frac{\partial H_y}{\partial x} - \frac{\partial H_x}{\partial y} \tag{6.16}$$

The resistivity of the superconductor is non-linear and it is modelled by means of a power law, see also section 6.1.1.

6.2.1.1 Advantages and disadvantages

The uniqueness of the solution in the H formulation is guaranteed by the absence of gauges, as instead is the case when magnetic vector or scalar potentials are used. Boundary conditions are easy to implement, since the magnetic field can be directly specified and it is intuitive by nature. Additionally, the magnetic field is the computed

quantity, thus does not require further calculations. Other advantages of the H formulation have been well described in [113].

The H formulation poses also some disadvantages. The full vector field has to be solved in the non-conducting domains, which increases the size of the matrices involved. To avoid the circulation of currents in the non-conducting domains, a high dummy resistivity is imposed, typically of $100\ \Omega \cdot m$. This can degrade the matrix conditioning and increase considerably the computation time.

6.2.2 The magnetic vector potential, or A formulation

The A formulation is used, similarly to the H formulation, in the solution of electromagnetic problems and it has been widely employed for solving the field and current distribution in HTS bulks, wires and tapes. The state variable in this formulation is the magnetic vector potential, $\vec{A}$, whose curl corresponds to the magnetic field $\vec{B}$:

$$\vec{B} = \vec{\nabla} \times \vec{A} \tag{6.17}$$

This solution is not unique, since Eq. 6.17 is satisfied also by summing the vector potential with the gradient of a scalar potential, $\vec{A}' = \vec{A} + \vec{\nabla}\psi$. The trivial solution is $\psi = 0$, which reduces the number of degrees of freedom of the problem.

Substituting Eq. 6.17 into Faraday's law and exchanging the time derivative and the curl on the right-hand side,

$$\vec{\nabla} \times \vec{E} = \vec{\nabla} \times \left(-\frac{\partial \vec{A}}{\partial t} \right) \tag{6.18}$$

One obtains,

$$\vec{E} = -\frac{\partial \vec{A}}{\partial t} \tag{6.19}$$

which is also satisfied by:

$$\vec{E} - \vec{\nabla}\varphi = -\frac{\partial \vec{A}}{\partial t} \tag{6.20}$$

where φ is the electric scalar potential. Again, this quantity is not uniquely determined, as we can relate it to φ as $\varphi' = \varphi + \partial\psi/\partial t$ which also satisfies the equation. However, considering the trivial solution for the electric scalar potential, $\varphi = 0$, the electric field is:

$$\vec{E} = -\frac{\partial \vec{A}}{\partial t} \tag{6.21}$$

Another way is to set a so-called *gauge fixing*, which is usually the Lorentz gauge:

$$\vec{\nabla} \cdot \vec{A} + \mu\varepsilon \frac{\partial \varphi}{\partial t} \tag{6.22}$$

Let us now consider Ampere's law, $\vec{\nabla} \times \vec{B} = \mu\vec{J}$. Substituting Eq. 6.17,

$$\vec{\nabla} \times \left(\vec{\nabla} \times \vec{A} \right) = \mu\vec{J} \tag{6.23}$$

and Ohm's law, $\vec{J} = \sigma\vec{E}$, becomes:

$$\vec{\nabla} \times \left(\vec{\nabla} \times \vec{A} \right) = \mu\sigma \frac{\partial \vec{A}}{\partial t} \tag{6.24}$$

Recalling the identity: $\vec{\nabla} \times (\vec{\nabla} \times \vec{A}) = \vec{\nabla}(\vec{\nabla} \cdot \vec{A}) - \nabla^2 \vec{A}$ and assuming the so-called Lorentz gauge given in Eq. 6.22, the resulting governing equation is:

$$\nabla^2 \vec{A} = -\mu\sigma \frac{\partial \vec{A}}{\partial t} \tag{6.25}$$

As previously stated, the A formulation presents similar advantages to the H formulation. In 2D, however, it requires a lower number of DOFs compared to the H formulation, since it needs only the z-component of the magnetic vector potential, A_z.

6.2.3 The H-A formulation

The H formulation, despite being powerful and capable to model several applications, from AC losses in HTS tapes [113], [117], [118], [119], to levitation of permanent magnets over HTS bulks [120], presents several limitations.

In fact, the use of $\vec{H}$ in the non-conducting domains requires to impose a high 'dummy' resistivity (typically, 100 Ωm) to avoid the circulation of eddy currents in these domains. Other than being non-physical, this degrades the matrix conditioning [121] and leads to unwanted currents. Also, the use of a vector variable in these domains adds superfluous degrees-of-freedom (DOFs) to the model.

The H-A formulation is the first example of a mixed formulation, where two conventional formulations are put together to model different domains. For example, in the case of a single tape surrounded by air, the H formulation is used to solve the magnetic field in the tape, whereas the A formulation is used in the non-conducting domain of the air.

The implementation of the *H-A* formulation requires to couple the two formulations at the boundaries of the shared domains. First, one must ensure the continuity of the tangential component of the electric field $\vec{E}$ across the boundary of the superconducting and air domain, namely:

$$\hat{n} \times (\vec{E}_A - \vec{E}_H) = 0, \; across \; \Gamma_H \tag{6.26}$$

this expression is specified on the boundary of the H domain, Γ_H. Then, one must also ensure the continuity of the tangential component of the magnetic field across the boundary between the two domains, which is expressed as:

$$\hat{n} \times (\vec{H}_A - \vec{H}_H) = 0, \; across \; \Gamma_A \tag{6.27}$$

this expression is specified on the boundary of the A domain, Γ_A. We must note here that the sheet current density at the boundary is considered to be equal to zero.

6.2.4 The magnetic scalar potential, or ϕ formulation

The magnetic field $\vec{H}$ is solved in this formulation using the magnetic scalar potential, ϕ. In fact, the assumption is of a null current density, $\vec{J}$=0, which applying Ampere's law allows defining:

$$\vec{H} = -\vec{\nabla}\phi \tag{6.28}$$

Applying Gauss' law, the resulting equation to be solved is:

$$\vec{\nabla} \cdot \vec{\nabla}\phi = 0 \tag{6.29}$$

namely the Laplace equation, where the unknown is a scalar field. This is much more convenient with respect to the vector field $\vec{H}$ [121] and is ideal to solve electromagnetic problems in dielectric materials.

6.2.5 The H-ϕ formulation

The *H-*ϕ formulation implements a similar approach to the *H-A* formulation. In this case, the H formulation is used to solve the superconducting domain, Ω_{sc}, whereas the ϕ formulation is employed in the air or, more generally, in non-conducting domains, Ω_{nc}. The ϕ formulation requires only one DOF per mesh element, a property that is

preserved in 3D domains. As a comparison, in the mixed H-A formulation, the A formulation requires another three DOFs per mesh element when passing from 2D to 3D. Therefore, using the ϕ formulation in non-conducting domains allows reducing the computational time by much.

The governing equation in Ω_{sc} is Eq. 6.11 for the H formulation:

$$\vec{\nabla} \times \left(\rho \vec{\nabla} \times \vec{H} \right) = -\mu \frac{\partial \vec{H}}{\partial t} \tag{6.30}$$

whereas the governing equation in Ω_{nc} is Eq. 6.29:

$$\vec{\nabla} \cdot \vec{\nabla} \phi = 0 \tag{6.31}$$

This setting of the model avoids imposing a dummy resistivity in the air, as described in section 6.2.1, which is the case when the H formulation is employed both in Ω_{sc} and Ω_{nc}. In Comsol®, curl (edge) elements are used in Ω_{sc} to solve for $\vec{H}$. Lagrange (nodal) elements are used in Ω_{nc} to solve for ϕ.

This formulation can be implemented in two different ways in Comsol®. The H formulation is always set using the *General Form PDE* module. The ϕ formulation is set either by the *Weak Form PDE* (as described in [121]) or the *Magnetic Fields, No Currents* module (as described in [28]). The modelling of the magnetization experiment has be conducted using this specific formulation, as shown in section 6.3.

The two formulations are coupled by imposing the continuity of the tangential component of the magnetic field strength $\vec{H}$, across the boundary of the H formulation:

$$\hat{n} \times (\vec{H}_\phi - \vec{H}_H) = 0, \ across \ \Gamma_H \tag{6.32}$$

as well as imposing the continuity of the normal component of $\vec{B}$, in the ϕ formulation,

$$(\vec{B}_\phi - \vec{B}_H) \cdot \hat{n} = 0, \ across \ \Gamma_\phi \tag{6.33}$$

6.2.6 T and T-ϕ formulation

The material, or medium, on which the T formulation acts is always a surface or a manifold in 3D geometries. Currents are constrained to exist only on such surface, meaning the current vector potential is normal to the sheet:

$$\vec{T} = T\hat{n}_s \tag{6.34}$$

where $\hat{n}_s$ is the unit vector normal to the surface. Here, T is only a scalar field, which helps reducing the number of variables and the computational burden with it.

The T formulation is particularly useful to model REBCO coated conductors. In fact, three main assumptions underlie the T formulation and the deriving mixed formulations:

1. The magnetic field $\vec{H}$ is uniform across the tape thickness, because of the high aspect ratio;
2. The current flow is only in the parallel direction to the tape wide surface;
3. The parallel component of the field to the tape is negligible, meaning the current density in the tape is dominated by the normal component of the field.

One starts from:

$$\vec{\nabla} \cdot \vec{J} = 0 \tag{6.35}$$

which is valid in an isotropic and linear material and neglects capacitive effects. This allows writing:

$$\vec{J} = \vec{\nabla} \times \vec{T} \tag{6.36}$$

where $\vec{T}$ is the current vector potential. Similarly to the A formulation, a gauge has to be imposed in order to obtain a unique solution: $\vec{\nabla} \cdot \vec{T} = 0$. From Ampere's law:

$$\vec{\nabla} \times \vec{H} = \vec{\nabla} \times \vec{T} \tag{6.37}$$

which gives:

$$\vec{H} = \vec{T} - \vec{\nabla}\phi \tag{6.38}$$

Since the solution is not unique, we introduced ϕ, the magnetic scalar potential. Considering Faraday's law:

$$\vec{\nabla} \times \vec{E} = -\frac{\partial \vec{B}}{\partial t} \tag{6.39}$$

substituting Ohm's law, $\vec{E} = \rho\vec{J}$,

$$\vec{\nabla} \times (\rho\vec{J}) = -\mu\frac{\partial\vec{H}}{\partial t} \tag{6.40}$$

Then, considering also Eq. 6.36 and Eq. 6.38,

$$\vec{\nabla} \times (\rho\vec{\nabla} \times \vec{T}) = -\mu\frac{\partial}{\partial t}(\vec{T} - \vec{\nabla}\phi) \tag{6.41}$$

This is the equation of the T-ϕ formulation. From here, the current vector potential, $\vec{T}$, is perpendicular to the surface and can be written as: $\vec{T} = T\hat{n}_s$. Instead, the right-hand side of the equation is a magnetic field source $\vec{H}$ perpendicular to the surface. Substituting:

$$\vec{\nabla} \times (\rho\vec{\nabla} \times (T\hat{n}_s)) = -\mu\frac{\partial}{\partial t}(\vec{H} \oplus \hat{n}_s) \tag{6.42}$$

where the symbol $\oplus$ stays for the element-wise product.

An immediate consequence of this formulation is the derivation of the current across the cross-section, which results to be the product of the original tape thickness, δ, with the difference of the current vector potential at the sheet edges, T_1 and T_2. This is also shown in Fig. 6.1.

$$\begin{aligned} I &= \int\int_{\Omega_T} \vec{J} \cdot \vec{n}_{\Omega_T} dS \\ &= \int\int_{\Omega_T} (\vec{\nabla} \times \vec{T}) \cdot \vec{n}_{\Omega_T} dS \\ &= \oint_{\Gamma_T} \vec{T} \cdot d\vec{l} = \delta(T_1 - T_2) \end{aligned} \tag{6.43}$$

6.2.7 T-A formulation

The state variable solved in the superconducting region is the *current vector potential*, $\vec{T}$, defined already in Section 6.2.6, see [122]:

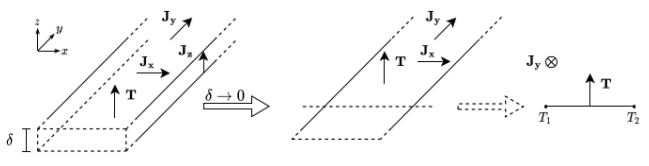

FIGURE 6.1: Thin sheet approximation of a tape, alongside $\vec{J}$ and $\vec{T}$. Credits: [28].

$$\vec{J} = \vec{\nabla} \times \vec{T} \tag{6.44}$$

Instead, the magnetic field is solved using the A formulation in the air region. The T formulation treats the superconducting tapes as thin sheets. In fact, the HTS domain (T domain) is seen from the air domain (A domain) as a boundary.

Let us write $\vec{J}_s$ as the surface current flowing in the tape. This is the current density, $\vec{J}$, given by the T formulation, multiplied by the tape thickness, δ:

$$\vec{J}_s = \delta\vec{J} = \delta(\vec{\nabla} \times \vec{T}) \tag{6.45}$$

The condition to be satisfied in this mixed formulation takes the discontinuity of $\vec{H}$ across the boundary between the T and A formulation, Γ_A:

$$\hat{n} \times (\vec{H}_1 - \vec{H}_2) = \vec{J}_s, \; in \; \Gamma_A \tag{6.46}$$

Please note that the H formulation could also be used for this, in which case one talks about the T-H formulation. The T-A formulation will be employed in section 6.3 together with the H-ϕ formulation to model the magnetization experiment.

6.2.8 T-Ω formulation

As for the T-A formulation, the current vector potential, Eq. 6.44, is used. The current density in the superconductor generates a field, $\vec{H}_s$:

$$\vec{\nabla} \times \vec{H}_s = \vec{J} \tag{6.47}$$

such that the total magnetic field is:

$$\vec{H} = \vec{H}_0 + \vec{H}_s \tag{6.48}$$

where $\vec{H}_0$ is the external magnetic field. We can write:

$$\vec{T} = \vec{H}_s - \vec{\nabla}\Omega \tag{6.49}$$

which satisfies:

$$\vec{\nabla} \times \vec{T} = \vec{\nabla} \times \vec{J} \tag{6.50}$$

The total field is:

$$\vec{H} = \vec{H}_0 + \vec{T} - \vec{\nabla}\Omega \tag{6.51}$$

Given the constitutive equation $\vec{E} = \frac{1}{\sigma}\vec{J}$ and Faraday's law, $\vec{\nabla} \times \vec{E} = -\frac{\partial \vec{B}}{\partial t}$, the previous equation becomes:

$$\vec{\nabla} \times \left(\frac{1}{\sigma}\vec{\nabla} \times \vec{T}\right) = -\mu \frac{\partial}{\partial t}(\vec{H}_0 + \vec{T} - \vec{\nabla}\Omega) \tag{6.52}$$

whereas, Gauss' law, $\vec{\nabla} \cdot \vec{B} = 0$, becomes:

$$\vec{\nabla} \cdot \mu(\vec{H}_0 + \vec{T} - \vec{\nabla}\Omega) = 0 \tag{6.53}$$

For more details on this, see [123].

6.3 3-D modelling of the magnetization experiment

The focus of this work has been the simulation of the magnetization experiment widely discussed in this thesis. Four different models have been developed, adopting the H, H-ϕ, and T-A formulations described above. In particular, the H-ϕ formulation has been investigated with both methods described in section 6.2.5.

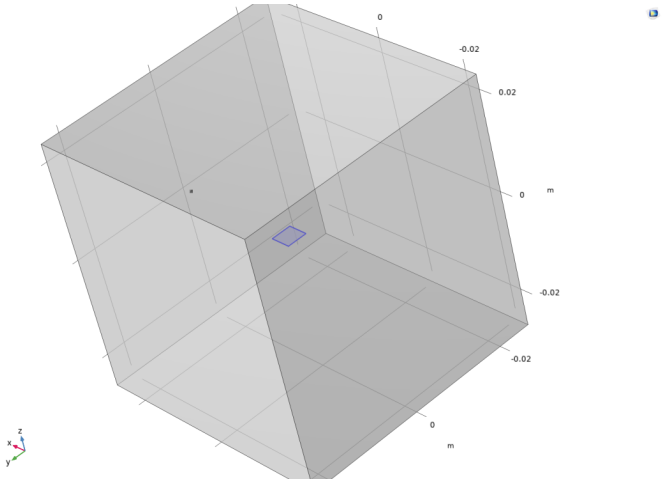

FIGURE 6.2: Geometry of the Comsol® model for reproducing the magnetization experiment. The tape is highlighted in blue at the center.

The models have been built in Comsol® Multiphysics, following the instructions in [28] and the examples on the HTS modelling website [124]. Fig. 6.2 shows the geometry of the models. This is constituted by a square of 4 mm sides located at the center, used to model the REBCO tape sample, and of an outer cube of 50 mm sides for the air. In this section, the results of these four models are compared and then benchmarked with the actual experimental data.

6.3.1 Reason for modelling

Before further introducing the model and the results, it is useful to recall an analytical model to understand whether the critical current density, J_c, could already be derived using a simple formula [125], [126]:

$$J_c(B) = \frac{\Delta M(B)}{t\left(1 - \frac{t}{3w}\right)} \tag{6.54}$$

where M is the magnetization, expressed in A/m, t is the thickness of the REBCO layer, and w is the tape width. In the case of REBCO tapes, where $t/w \rightarrow \infty$, the formula above simplifies to:

$$J_c(B) = \frac{\Delta M(B)}{t} \tag{6.55}$$

To compute the magnetization, the measured magnetic moment, $m(B)$ expressed in Am^2, is divided by the sample volume, namely the product of $w^2 t$ (in the case analyzed here, the sample width and length are the same). Substituting:

$$J_c(B) = \frac{\Delta m(B)}{w^2\ t^2} \tag{6.56}$$

As shown below, such as in Fig. 6.11, $\Delta m(B = 0) \approx 10$ emu $= 10^{-2}$ Am^2. Then, $w =$ 4 mm and assuming $t = 2.5$ μm, which is reasonable for the thickness of the REBCO layer, applying Eq. 6.56, it results in: $J_c(B) = 10^{14}$ A/m^2. This is 500 times higher than expected for a commercial tape carrying 2000 A. Therefore, the actual layer where the currents flow is not so easy to estimate, and it is why a numerical simulation is needed.

6.3.2 Model parameters

Both the H and H-ϕ formulations solve the three components of the field vector, $\vec{H}$, in the superconducting tape. Then, the first one solves them also in the surrounding air,

while the second one uses the single component of the magnetic scalar potential, ϕ. For this reason, the tape sample is defined as a 3-D bulk having a thin thickness and the $J_{c,0}$ in the scaling law is proportioned accordingly. Instead, the tape is seen as a 2-D boundary of the air domain in the *T-A* formulation. Nevertheless, a 'fake' thickness is still used. Table 6.1 summarizes the main features of the model.

The actual thickness of the REBCO layer is usually around 2.5 - 3 μm in commercial tapes. The thickness adopted in the models presented here is 10 μm, namely 3 to 4 times higher. This value has been chosen as a compromise between being as close as possible to the actual REBCO layer, while obtaining a reasonable computation time. In fact, let us note that the aspect ratio of the mesh elements is quite high in the models (typically above 30), which considerably slows down the computation. Parametric studies have been conducted to investigate the influence of both the vertical and horizontal mesh density on the magnetization curve.

The current density at zero field appearing in the scaling law implemented in the model results from the ratio between the *intercept*, mentioned in the previous chapters, and the cross section:

$$J_{c,0} = \frac{I_{c,0}}{w^2 \cdot t} \tag{6.57}$$

therefore it is equal to $5 \cdot 10^{10}$ A/m^2, namely a factor four lower than the expected $2 \cdot 10^{11}$ A/m^2, corresponding to a 2.5 μm thickness of the REBCO layer.

The critical electric field, $E_c = 10^{-4}$ V/m. The n-value is set to 20, even if this can be up to 50 at 4.2 K (chapter 3), to ease the computational burden. The same field cycle is imposed as in the actual magnetization experiment, ramping at a rate dB/dt = 300 mT/min, with 10 T and -2 T reversal fields. Finally, the scaling parameters were set as those found on the measurement of SST tape ST1910, at 4.2 K: B_0 = 1.06 T, α = 0.61, B_{irr} = 150 T, and q = 2.

Parameter	*Symbol*	*Value*
Intercept	$I_{c,0}$	2000 A
Tape sample side (square)	w	4 mm
Modelled thickness	t	10 μm
Resulting current density	$J_{c,0}$	$5 \cdot 10^{10}$ A/m^2
Critical electric field	E_c	10^{-4} V/m
n-value	n	20
Field ramp rate	dB/dt	300 mT/min
Crossover field, at 4.2 K	B_0	1.06 T
Slope of linear region, at 4.2 K	α	0.61
Irreversibility field, at 4.2 K	B_{irr}	150 T
Slope of *Region III*, at 4.2 K	q	2

TABLE 6.1: Simulation parameters in the Comsol® simulation.

The meshing is performed using edge (curl) elements in the domains where the H or A formulation is applied, and nodal (lagrange) elements in the domains solving the T or ϕ formulation.

6.3.3 Field and current density distribution at inversion

To begin with, Fig. 6.3a displays the distribution of the vertical field component, B_z, at t = 2000 s, namely when the applied background field, B_{ext} = 10 T. In-plane meshing is made up by 48x48 elements.

The field is slightly higher than 10 T at the boundaries and lower in the inner core, as expected from Brandt's theory [127]. This is further displayed in Fig. 6.3b, which is the profile of the vertical component of the field, B_z, along the x-axis.

Following the peak of the applied field, the field in the tape decreases starting from the edges. Fig. 6.4a shows the B_z when the applied field reaches zero. Namely, the field is actually negative at the edges, around -0.4 T, and still positive in the core, up to

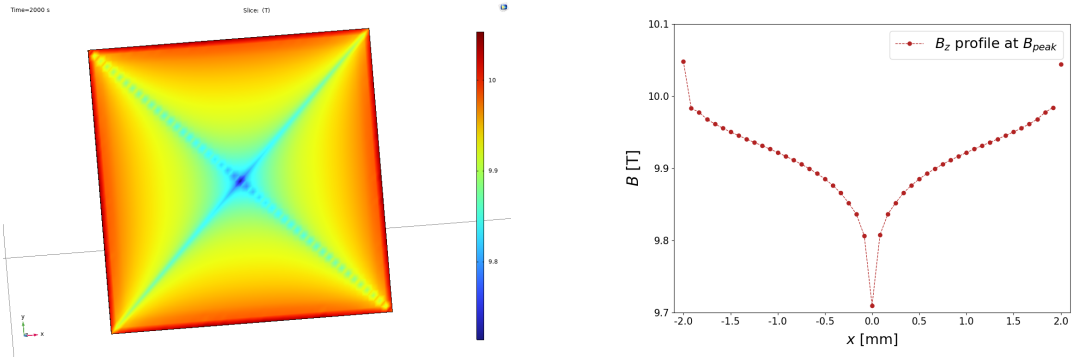

(A) Across the tape midplane. (B) Along x.

FIGURE 6.3: B_z distribution at B_{peak}.

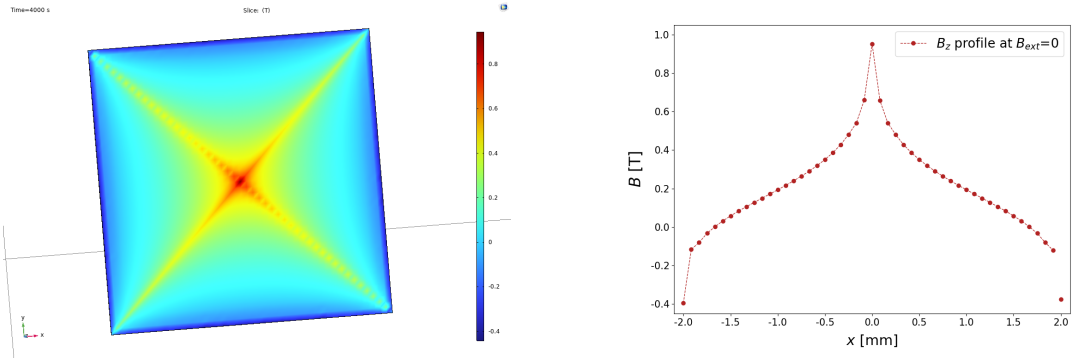

(A) Across the midplane. (B) Along x.

FIGURE 6.4: B_z distribution at B_{ext}=0.

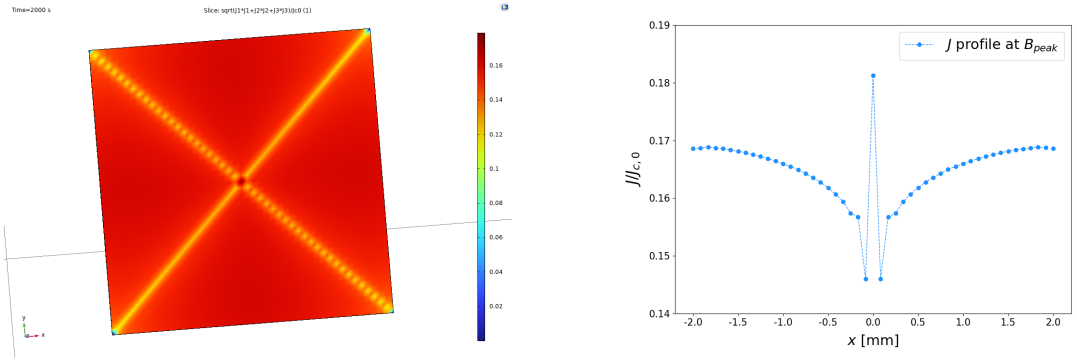

(A) Across the midplane. (B) Along x.

FIGURE 6.5: $J/J_{c,0}$ distribution at B_{peak}.

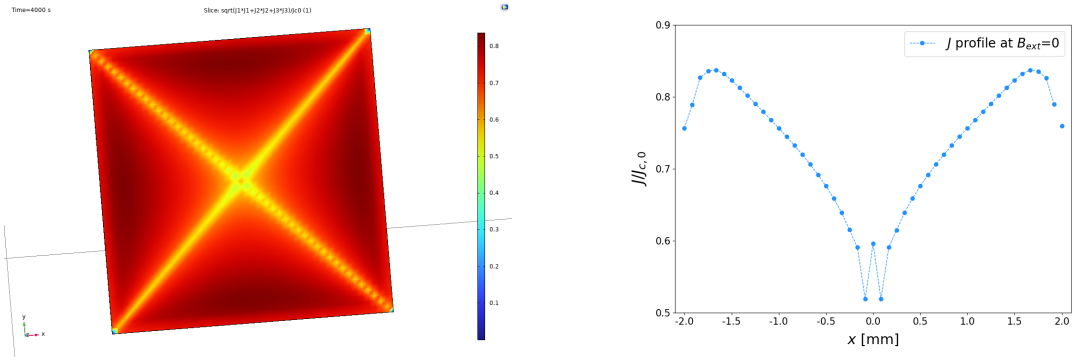

(A) Across the midplane. (B) Along x.

FIGURE 6.6: $J/J_{c,0}$ distribution at B_{ext}=0.

even 0.9 T as shown clearly in Fig. 6.4b. Let us recall that the model implements the full $J_c(B)$ scaling law.

To complete this part, Fig. 6.5 and Fig. 6.6 display the current density distribution normalized by the $J_{c,0}$, which also follows a peculiar pattern across the tape width. Let us note that the local current increase appearing at $x \approx 0$ in Fig. 6.5b and Fig. 6.6b is an artifact of the meshing, while the actual expected profile shall reach an absolute minimum in both cases.

6.3.4 Comparison between different models

In this section, the modelling results of the four models are compared. To begin with, Table 6.2 reports the combinations of the vertical and horizontal meshing adopted for each of the four models.

The H formulation is implemented using the standard mfh module available in Comsol®. The horizontal meshing has been varied between 3 and 18 elements per side, using either one or two vertical elements. The H-ϕ formulation can be built in two ways. Both

Formulation	*Modules*	*Vertical*	*Horizontal*
H	mfh	1, 2	3, 6, 12, 18
H-ϕ	GF + mfnc	1, 2	3, 6, 12, 18, 24
	GF + WF	1, 2, 4	3, 6, 12, 18, 24
T-A	GFb + mf	-	3, 6, 9

TABLE 6.2: Vertical and horizontal meshing for each of the four models built in Comsol®.

implement the *General Form PDE* module, GF for short, to solve the three field components in the superconductor. The surrounding air is modelled using either the *Magnetic Fields No Currents* module, mfnc for short, or the *Weak Form PDE* module, WF.

These methods turned out to be faster, therefore models have been run up to 24 side horizontal elements and 4 vertical elements in the case of the GF + WF. Finally, the *T-A* formulation is modelled through the *General Form Boundary PDE*, GFb for short, and the *Magnetic Fields* module, mf for short, to solve the *A* formulation in the air. The horizontal meshing has been set using either 3, 6 or 9 side lateral elements. No vertical elements are needed in this case, as the tape is treated as a thin sheet.

Fig. 6.7 displays the location of the peak magnetization, m_{peak}, and the corresponding field level, B_{peak}, as a function of the lateral mesh elements in the case of the mfh module. The 'x' symbols are for one vertical element, while the '+' for two vertical elements. Curves in both pairs lie very close to each other. m_{peak} tends to plateauing with increasing mesh density, ending up at 4.05 emu with 18 lateral elements. Something similar occurs for the peak location, B_{peak}, which is slightly negative, 40 - 50 mT as the mesh gets denser.

Then, Fig. 6.8 shows a similar plot for the *H-ϕ* formulation using the GF + mfnc modules. The behavior is qualitatively similar to Fig. 6.7, where this time the mesh extends

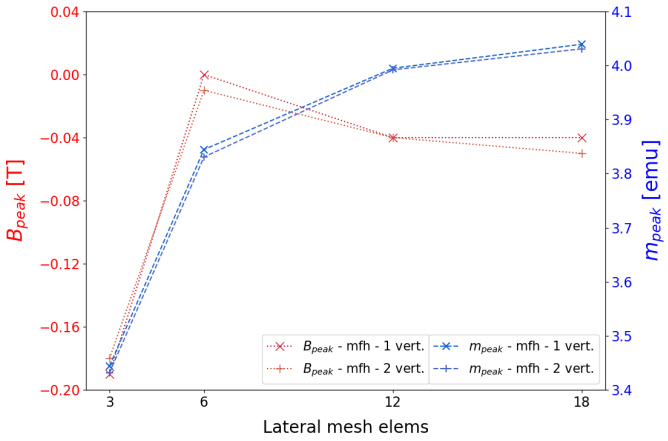

FIGURE 6.7: Peak magnetization and its location for either one and two vertical elements, with the mfh module, as a function of the number of lateral mesh elements.

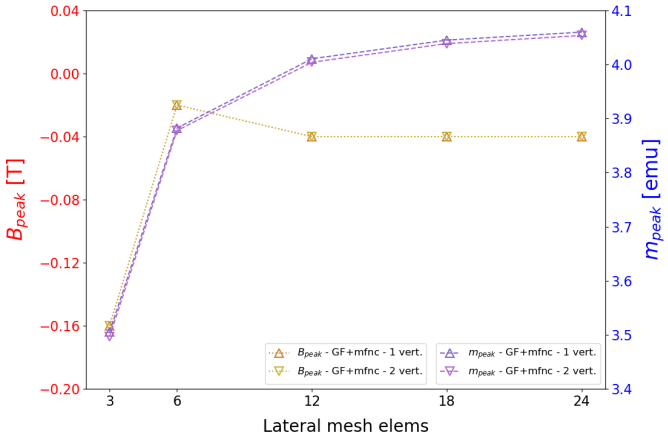

FIGURE 6.8: Peak magnetization and its location for either one and two vertical elements, with the GF+mfnc module, as a function of the number of lateral mesh elements.

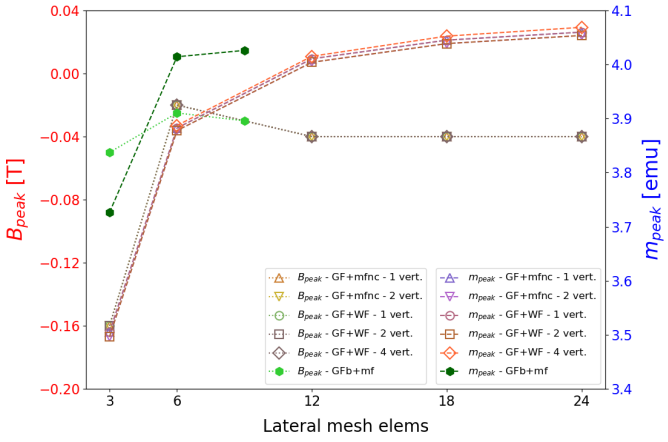

FIGURE 6.9: Extension of Fig. 6.8 to the GF+WF module.

up to 24 lateral elements. The m_{peak} reaches towards convergence, showing further refinement is optional.

Additionally, m_{peak} is just a few percentage points lower in the case of two vertical elements while B_{peak} is identical for both. Fig. 6.9 extends Fig. 6.8 to the case of the GF + WF modules. This implementation turned up to be faster than the previous one, allowing the analysis with four vertical elements. Noticeably, the results of these two implementation methods, corresponding to the same formulation, coincide when the vertical meshing is the same. Therefore, one can observe that four vertical elements give higher m_{peak} than meshing with a single element. The peak locations, B_{peak}, remain the same.

The plot also reports the values for the T-A formulation (in green). Despite the fact that data points are available only up to nine lateral elements, this method seems to

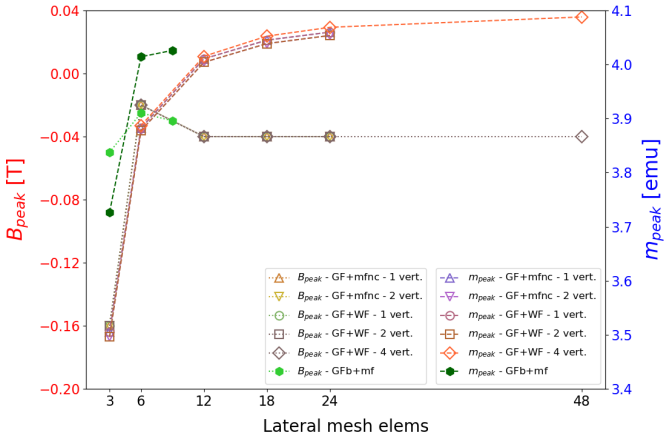

FIGURE 6.10: Additional extension to the most refined model with 48 lateral mesh elements.

converge at a much lower mesh density. The trend followed by the peak locations seems also to align with the other methods.

As a concluding note to this section, Fig. 6.10 presents the additional result of the most refined model, implemented using GF+WF modules, where the tape has been meshed with 48 side lateral and 4 vertical elements. This was used to show the qualitative results in Fig. 6.3 - Fig. 6.6. The curve peak is 4.088 emu, just 0.47 % higher than with 24 lateral elements, while the peak location remains unaltered.

6.3.5 Simulation times

Table 6.3 reports the simulation time for the *mfh* module. Times grow rapidly as the mesh density increases, ending up being even a factor six higher with 18 elements than with 12, both in the case of one and two vertical elements.

This does not come as a surprise, since the H formulation must solve three unknowns per mesh edge element, which slows down the computation considerably. In fact, let us note that the simulation with 18 lateral elements requires 448 minutes (7.5 hours) for one vertical element and up to 660 minutes (11 hours) for two.

Then, Table 6.4 displays the simulation times of the H-ϕ formulation using the GF+mfnc modules. Despite starting from a non-negligible 12.5 minutes with three lateral elements, the simulation time raises by a ratio between 1.5 - 1.6 at each step from 6 to 24 lateral elements, in the case of one vertical mesh element, and between 1.5 - 1.7 at each step for two vertical elements.

Table 6.5 is for the GF+WF modules. Strikingly, simulation times are reduced by a factor 4 - 5 with respect to the same H-ϕ formulation implemented using GF + mfnc,

mfh

Vert. elems	*Horizontal elems*			
	3	*6*	*12*	*18*
1	2.5	9	73	448
2	13	25	102	660

TABLE 6.3: Solution times (in minutes) for the mfh implementation.

GF+mfnc

Vert. elems	*Horizontal elems*				
	3	*6*	*12*	*18*	*24*
1	12.5	15	24	36	54
2	12.5	17	32	54	83

TABLE 6.4: Solution times (in minutes) for the GF+mfnc implementation.

GF+WF

Vert. elems	*Horizontal elems*				
	3	*6*	*12*	*18*	*24*
1	1.5	2.5	4.5	7.5	12
2	2	3	7	12	21
4	-	4	8	15	29

TABLE 6.5: Solution times (in minutes) for the GF+WF implementation.

GFb+mf

Horizontal elems		
3	*6*	*9*
130	130	310

TABLE 6.6: Solution times (in minutes) for the GFb+mf implementation.

and even up to 30 times compared to the mfh module. The most detailed simulation with 48 lateral and 4 vertical elements took 126 minutes, only 4.3 times higher than with 24 lateral and the same vertical meshing.

Finally, Table 6.6 displays the simulation times for the *T-A* formulation implemented through the GFb + mf modules. No vertical meshing is needed in this case, therefore only the number of horizontal elements is reported. A few horizontal elements require a long simulation time already, see for example 310 minutes (5 hours and 10 minutes) for nine horizontal elements. In fact, the computation ends up being quite heavy due to the three components of the magnetic vector potential to be solved on the element edges. Unfortunately, no additional data is available for 12 horizontal elements or higher, since simulations do not converge.

6.3.6 Comparison with experimental data

The reason for modelling the magnetization experiment is to being able to reproduce the measured data. Here, tape SST ST1910 measured at 4.2 K is chosen to compare the measurement and modelling results. The sample was 4 mm wide (as from manufacturing) and cut to 4 $\pm$ 0.1 mm length. Fig. 6.11 shows the magnetization curves of both the experimental data (shown also in Fig. 5.3 in chapter 5) and the resulting curve from the Comsol® modelling using the GF+WF implementation with 48 side lateral elements and 4 vertical elements. The same scaling parameters found for the measurement, listed in Table 6.1, have been implemented in the model.

The first observation is that the modelling curve is lower than the experimental one. In particular, the magnetization peak of the former is $m_{peak,sim}$ = 4.09 emu and $m_{peak,exp}$ = 5.58 emu for the latter, which differ by 36.4%. The respective peaks are located at $B_{peak,meas}$ = 0.075 T and $B_{peak,sim}$ = -0.04 T.

It is useful to comment about a few details. Simulation data span up to a few tenths of tesla above the experimental data points. This is due to the magnet power supply starting lowering the injected current before the field actually reaches 10 T: as a consequence, the actual maximum field is at about 9.9 T. The simulation data also show a 'shoulder'-like shape at -2 T, which is caused by the shape of the smoothing function of the current ramp (used to avoid discontinuous sharp variations in the simulation). Additionally, one expects B_{peak} to be located at positive fields, as it is the case observed in the measurement, because of strong demagnetization effects induced by the current profile, which compresses the flux at the sample edges.

To further investigate on the difference between the two curves presented, Fig. 6.12 displays the two curves normalized by their respective peaks and shifted to zero field

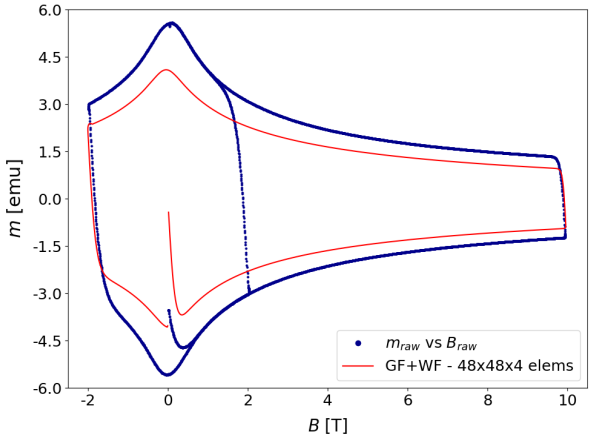

FIGURE 6.11: Measured versus modelled magnetic hysteresis cycle of SST tape ST1910.

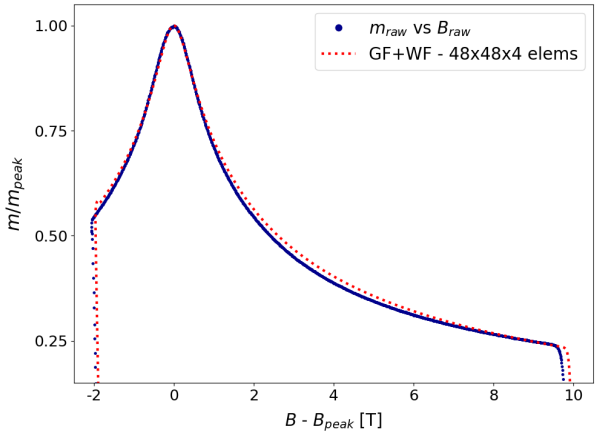

FIGURE 6.12: Normalized measured versus modelled magnetic hysteresis cycle of SST tape ST1910.

with respect to their peak locations. The plot is a closeup onto the positive region of magnetic moments. The resulting datasets match up to a very high degree over the entire field range, with the maximum discrepancy being 4 % between 3 - 4 T. This further proves the quality of the proposed scaling law in being able to approximate the entire field range from zero up to 10 T or above.

A few reasons can be put forward to explain the discrepancy between the measured and modelled data. To begin with, the $J_{c,0}$ imposed in the model is derived dividing the $I_{c,0}$ by the tape cross section. The intercept is found by fitting the magnetization data at 4.2 K and scaling up by the ratio $I_{c,T}$(0 T) / $m_{peak,4K}$, where $I_{c,T}$(0 T) is the transport current measured at zero applied background field. Such quantity includes the self-field, which is particularly relevant above ∼1500 - 2000 A, as it is the case analyzed here. Clearly, the specified quantity is not the current at actual null field, while the J_c should compensate for that.

The same topic was discussed also in chapter 5, where transport and magnetization data were compared. Both datasets showed a very similar field dependence across the field range and down to very low fields, allowing to elaborate two considerations. First, that the impact of self-field might be very similar in both cases, thanks to the overlap across the entire field range. Second, that most of the impact of self-field is below 0.5 T - 1 T, where currents surpass 1500 A. However, this field range corresponds to the transition between *Region II* and *Region I*, where the field dependence fades, therefore having little impact on the scaling. For these reasons, the upper limit for finding the $I_{c,0}$ of the scaling law was estimated to a 10 % higher than the measured $I_{c,T}$(0 T).

An additional factor is the intrinsic variability of tape performance along a spool. The statistics on tape performance has been discussed in chapter 4, revealing a variability up to 30 % on the performance of this SST tape. The combined action of the two

listed factors, the self-field on one side (accounting for a 5 - 10 %) and the variability of performance (by up to 30 %) provides a quantitative explanation for the observed discrepancy of measured and modelled hysteresis cycles.

As an additional comparison, the measured versus modelled data for FFJ tape 6919-C are presented, see Fig. 6.13. Here, $m_{peak,sim}$ = 5.87 emu while $m_{peak,exp}$ = 6.19 emu, which differ only by 5.2 %. In fact, we recall that this FFJ tape had high statistical reproducibility by the transport method (chapter 4), which explains the small discrepancy between the two peaks. This further supports the idea that the 36 % difference in the peaks for the SST tape (Fig. 6.11) can be attributed to the performance variation along the spool length. Nevertheless, the fitting of the transport and magnetization data for this FFJ 6919-C tape was quite challenging due to the absence of transport data at low fields (chapter 5). This accounts for the two curves not matching closely over the field domain, which is also visible in the normalized plot, Fig. 6.14.

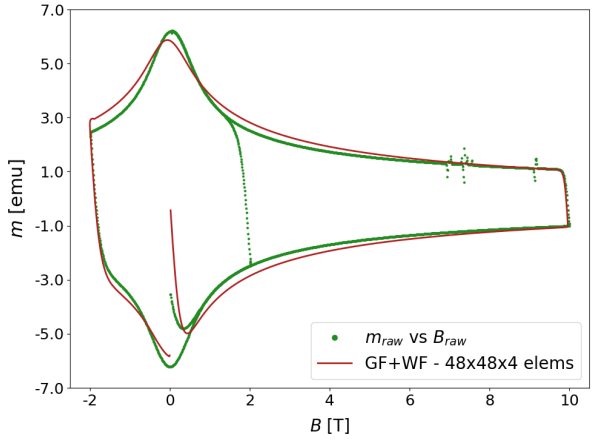

FIGURE 6.13: Measured versus modelled magnetic hysteresis cycle of FFJ tape 6919-C.

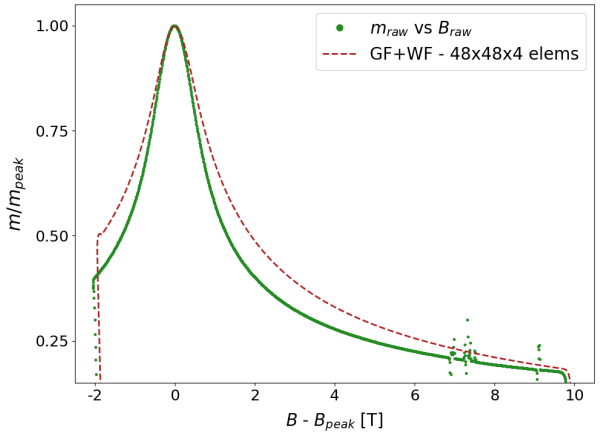

FIGURE 6.14: Normalized measured versus modelled magnetic hysteresis cycle of FFJ tape 6919-C.

Chapter 7

Conclusions

The focus of this thesis was to propose and validate a so-called scaling law to describe the field dependence of the critical current, I_c, of REBCO coated conductors from the millitesla range up to the irreversibility field, B_{irr}, and up to the critical temperature, T_c.

The field dependence of the critical current is distinguished into three regions, which are associated to the relative pinning mechanisms involved. In *Region I*, the density of flux vortices is much lower than the density of pinning centers. As a result, the critical current stays at the value at zero field, $I_{c,0}$. For example at 4.2 K, this regime extends up to 0.3 T and it decreases at higher temperatures, stretching only up to a few milliteslas above 80 K.

The crossover field, B_0, marks the transition to *Region II*, where the critical current is controlled by the collective pinning of vortex bundles confined in a fixed volume. The field dependence is of type $B^{-\alpha}$, which appears as a constant slope in a double logarithmic plot, the usual way of representing the data. A further drop marks the transition to *Region III*, also referred to as the thermal activation regime. In fact, thermal fluctuations play a relevant role from 30 K - 40 K onward, as they are very effective in de-pinning the weak pinning centers when approaching B_{irr}. Since these constitute the majority of pinning centers in the material, only the strong centers are left from intermediate to high temperatures, thus the rapid drop.

This behavior is comparable to LTS, although a few aspects must be highlighted. *Region I* is generally neglected in scaling laws for LTS. However, demagnetization effects are small for LTS, as they are manufactured in thin filaments, hence magnetization losses are generally not an issue. This is not the case for REBCO coated conductors, which are wide single filaments and a similar scaling law as for LTS would result in a potential singularity at low fields, which would mislead the estimation of losses. This is the first reason for extending the description for HTS.

Then, we remark the lack of transport data below 2 - 3 T at 4.2 K in the literature, for 4 mm wide tapes. In turn, this is the actual region for the transition from collective pinning to single vortex pinning and it is critical to determine the B_0 of tapes.

In this work, it has been proposed to add a term to the Kramer expression used in general for LTS, to account for the B_0 and the plateauing of performance in *Region I*. The resulting scaling law is made up of five parameters. The first is the $I_{c,0}$, namely the critical current value at zero field, also called the intercept. Then, B_0 marking the transition to *Region II*, and α, the slope of the linear region. The last two parameters are B_{irr} and q, governing the rapidity of the drop in *Region III*. Let us note that all these terms are a function of temperature; with the exception of $I_{c,0}$, they are also a function of the angular orientation, θ, however this is outside the scope of the work.

The scaling law was first applied to literature data, which showed its potential in describing the field dependence accurately. Moreover, the two reasons provided above drove us to conducting an experimental campaign of tape testing based on two activities, using both direct and indirect methods. The direct method consists in injecting a transport current in a tape immersed in a liquid helium bath at 4.2 K and exposed to background magnetic fields of up to 15 T, perpendicular to the broad face of the tape. The indirect method relies on a vibrating sample magnetometer (VSM) and measures the magnetic moment of tapes which oscillate rapidly inside a slowly ramping magnetic field.

For the transport method, a solenoid test station available in the superconducting laboratory at CERN has been used, which generates a background magnetic field of up to 15 T and injects up to 3 kA in the samples. A sample holder with a 'U' shape has been developed to create a short straight region where the field is perpendicular to the tape in the solenoid bore. In particular, the goal was to explore the region down to low field levels (below 1 T) where the critical current surpasses 1500 A - 2000 A and the relevant scaling parameter B_0 is directly accessible. The design of the holder implemented an inner 1.5 mm groove and six transversal holes into an already existing 4.5 mm groove that hosts the tape, to improve the heat exchange between the tape and the liquid helium. This has been the essential feature to surpass the barrier of 2000 A injected in the sample, that was particularly limiting during the early stages of the work.

For the magnetization method, a small sample (typically 4 mm wide and 4 mm long) oscillates at 20 Hz inside a perpendicular background field imposed by a solenoid magnet that can reach up to 10 T and the resulting magnetic moment is measured. The field ramp rate is such that the sample experiences a quasi-static field during a single oscillation. The VSM technique is powerful in the sense that it allows testing at variable temperatures, from 4.2 K up to T_c. In particular, it allows observing the irreversibility field directly, above 77 K.

In this work, a methodology to compare the results of the two methods was established. By checking that the same field dependence is measured at 4.2 K with both, the transport method is useful to determine the absolute value of the I_c(4.2 K) at zero applied field to scale the curves obtained at the other temperature levels by the magnetization method.

Matching between transport and magnetization data at 4.2 K was verified for all tapes tested in the scope of this work. Once again, let us stress that the magnetization method enables measurements at multiple temperature levels up to T_c, and it was used to infer the temperature evolution of the scaling parameters for eight tapes. Similar patterns in the scaling parameters have been identified among different manufacturers. A correlation with the known pinning landscape has been discussed and the application range for each of them has been outlined.

Numerical modelling has also constituted an important part of this work. A model of the magnetization experiment was built using the Comsol® software. The H, H - ϕ and T - A formulations have been implemented using both the standard modules and partial differential equations modules, since these problems are not covered in general only by the standard modules. The models differed much in the simulation times but resulted in very similar magnetization curves. The comparison with the measurements on actual tape samples showed a good match (within 5 %) in the peak values of a tape sample displaying small performance variation in transport measurements. A much higher difference was observed in another case, which was attributed to the variation in tape performance along the spool length.

7.1 Open questions

While this thesis proposes a solution to the need for a comprehensive scaling law describing the field and temperature dependence of the critical current of REBCO coated conductors, some open questions remain.

- The scaling parameters and the comparison with the pinning mechanisms of the manufacturers (chapter 5) allow inferring some potential links between the two. We believe that an additional effort shall be spent in this direction, possibly in collaboration with the manufacturers, to establish clear relations between the employed pinning mechanisms and the scaling parameters. This would allow defining *standard* scaling parameters for tapes, relieving from the time consuming characterization required at present and thus easing the work of magnet designers.
- Along the same line of thought, is the expansion of a database of tape testing to confirm the observed patterns of the scaling parameters and identify common

trends, as it was the case for the three tapes from Shanghai Superconductor Technology. The elaboration of analytical relations for the temperature evolution of such scaling parameters would be another major advancement. Specifically, this would allow to pass from the 77 K, low field currents (up to 1 T), directly to the 4.2 K in-field performance.

- The modelling of the magnetization experiment is effective in reproducing experimental results. The implemented $J_{c,0}$ was derived from the measured transport $I_{c,0}$ and divided by the tape cross section. However, this method discards the impact of self-field on the $J_{c,0}$ and shall be taken into better consideration in future attempts. Also, clarity shall be assessed on the impact of performance variability along the spool length, which is up to 30 %, and could still account as the main cause of the difference in magnetization between model and experiment.

- The scaling law validated here has shown a good match with experimental results, with a typical 5 % discrepancy and up to a maximum 10 % discrepancy in cases of limited datasets. The description minimizes the number of parameters in the formula (five), nevertheless some modifications could be implemented, as anticipated in chapter 5, to achieve an even better match.

- Finally, the scaling law was validated in this work in perpendicular fields to the tape broad face. It is of primary importance to verify its validity also in the case of parallel fields and, in general, extend it to the angular domain. A proposal to use an established law has been put forward (chapter 3), however it is likely that scaling parameters have an additional angular dependence themselves, which needs further investigation. This would require the development of new sample holders and possibly the use of different test facilities.

Appendix A

Slab in an external field and with transport current

A.1 The Bean critical state model

The first attempt to understand the irreversibility of the magnetization curves in type-II superconductors has been performed by Bean [35], who developed a simple model to deduce the critical current density in the superconductor. The content of this section is extracted from [36].

The force on all vortices is expressed in Eq. 1.63:

$$\vec{F} = \vec{J} \times n\vec{\Phi}_0 \tag{A.1}$$

substituting Ampere's law:

$$\vec{F} = (\vec{\nabla} \times \vec{H}) \times n\vec{\Phi}_0 \tag{A.2}$$

Considering a 1-D slab, the equation becomes:

$$F = \frac{dH}{dx} B \tag{A.3}$$

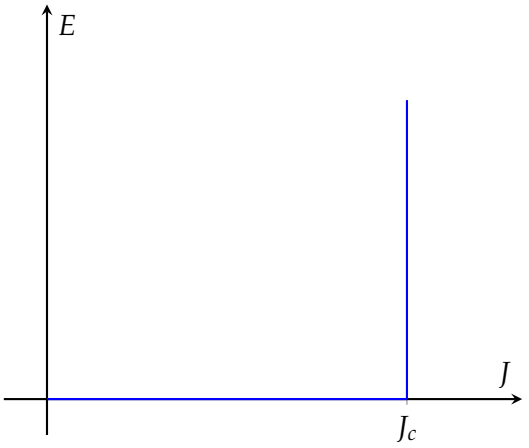

FIGURE A.1: At J_c, the electric field jumps to an infinite value in Bean's critical state model.

We remind, from chapter 1, that the Bean model makes two basic assumptions:

1. There exists a limit value of J that the superconductor can carry, called the critical current density, J_c.

2. Any electric field in the material (no matter how small) induces the circulation of the full J_c, see Fig. A.1.

These two hypotheses remain valid in any critical state model, which differentiate according to the magnetic field dependence of the J_c. An immediate consequence of the assumption that J_c is finite is diffusion and dissipation in the material.

We can write:

$$J(t) = \begin{cases} +J_c, & if\ \exists\ t' < t; E(t') > 0\ then\ \forall t'' \geq t', E(t'') \geq 0 \\ -J_c, & if\ \exists\ t' < t; E(t') < 0\ then\ \forall t'' > t', E(t'') \leq 0 \\ 0, & if\ E(t') = 0\ \forall t' \leq t \end{cases} \tag{A.4}$$

considering t as the present moment. Then, the two main descriptions are:

- Bean's model: J_c is constant, i.e. independent of the field.

- Kim's model: $J_c(B) = J_{c,0}/(1 + B/B_0)$

We consider a slab of thickness $2a$ exposed to an external field B_{ext} parallel to the slab and to a transport current per unit length, i_t, see Fig. A.2. We have:

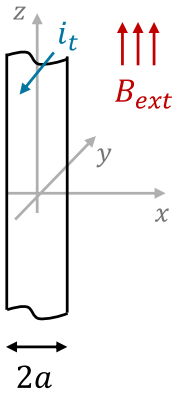

FIGURE A.2: Slab of thickness $2a$ immersed in an external field and subjected to a transport current.

$$\begin{cases} \vec{B} = B(x)\hat{k} \\ \vec{J} = J(x)\hat{j} \end{cases} \tag{A.5}$$

In 1-D, Ampere's law is:

$$\frac{dB}{dx} = \mu_0 J \tag{A.6}$$

which is valid for any material. In a superconductor,

$$\frac{dB}{dx} = \begin{cases} \mu_0 J_c \\ 0 \\ -\mu_0 J_c \end{cases} \tag{A.7}$$

meaning that the resulting field profile is independent of the applied field ramp rate. A rectangular path can be defined around a unit length L of the slab, see Fig. A.3. Integrating along such path, Eq. A.8 is obtained.

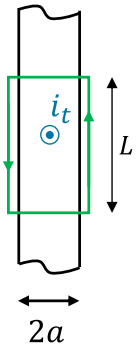

FIGURE A.3: Integration path around the slab

$$2B_t L = \mu_0 i_t L \tag{A.8}$$

Therefore:

$$B_t = \frac{1}{2}\mu_0 i_t \tag{A.9}$$

The boundary conditions are:

$$B(+a) = B_{ext} + \frac{1}{2}\mu_0 i_t$$

$$B(-a) = B_{ext} - \frac{1}{2}\mu_0 i_t$$

A.1.1 Case 1. External applied field

Now, we consider an external cycling field, such as the one represented by the black line in Fig. A.4. Thanks to the absence of derivatives, the problem can be treated as a succession of static steps, namely the black curve produces the same evolution as the red curve in the figure.

Three phases can be distinguished. The first one is from zero to t_1, where the field reaches the peak value, B_{ext}^{max}, starting from zero. Phase 2 goes from t_1 to t_3, which is when the field lowers down to the opposite value, -B_{ext}^{max}. Finally, Phase 3 is from t_3 to t_4, where the field increases back up to zero. Fig. A.5 reports the evolution of the magnetic field and current density penetration in the slab during Phase 1 (divided into four sub-phases, from 1a to 1d).

As soon as B_{ext} is applied, the magnetic field and the current density penetrate the slab up to a' (phase 1a). The current is $+J_c$ on the right and $-J_c$ on the left.

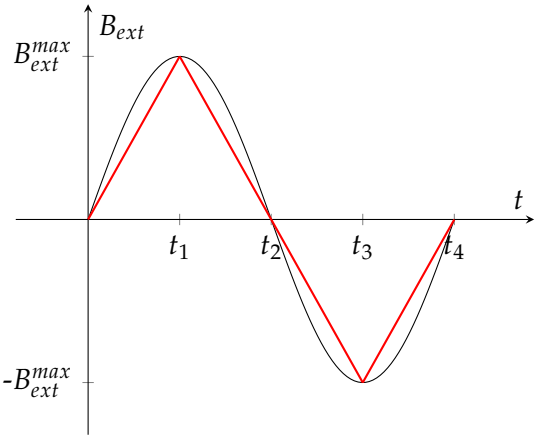

FIGURE A.4: Variation of the external field in time.

$$J(x) = \begin{cases} +J_c & , a' < x \leq a \\ 0 & , -a' \leq x \leq a' \\ -J_c & , -a \leq x < -a' \end{cases} \tag{A.10}$$

The magnetic field appears as a broken line (positive). As the field increases, a' also increases until it equals a (phases 1b and 1c in Fig. A.5). In this situation, the slab is saturated and the saturation field is:

$$B_{sat} = \mu_0 J_c a \tag{A.11}$$

Once B_{ext} surpasses B_{sat}, the field profile shifts upwards rigidly, since the current cannot penetrate further (phase 1d). The field profile is obtained by integration of Eq. A.7 and using the boundary conditions, see Eq. A.12.

$$B(x) = \begin{cases} B_{ext} - \mu_0 J_c (a - x) & , \ a' < x \leq a \\ 0 & , -a' \leq x \leq a' \\ B_{ext} - \mu_0 J_c (a + x) & , -a \leq x < -a' \end{cases} \tag{A.12}$$

The penetration depth, a', is derived as:

$$a' = a - \frac{B_{ext}}{\mu_0 J_c} \tag{A.13}$$

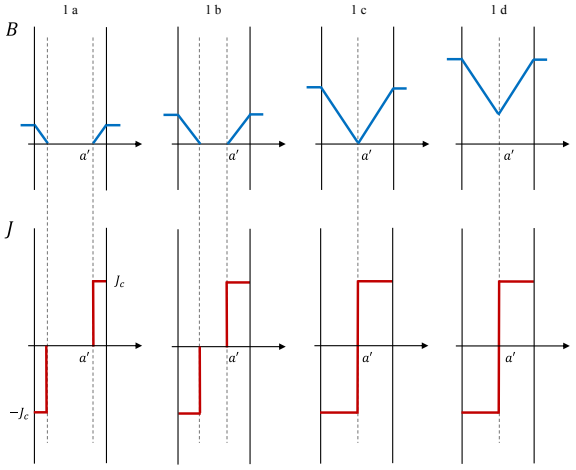

FIGURE A.5: Sequence of magnetic field and current penetration in the slab during Phase 1 (here divided into four sub-phases).

Note: the field-free region in the center of the slab is characterized by B=0 independent of B_{ext} (up to saturation), and such region is characterized by J=0 as well. Instead, $J = J_c$ in the critical regions and the field is determined by J_c and B_{ext} [126].

To calculate the losses, Faraday's law is used to derive the electric field. In the slab:

$$\frac{dE}{dx} = -\frac{dB}{dt} \tag{A.14}$$

and the condition $E(x{=}0) = 0$ holds, since the central spot does not see any electric field. Let us note here, that $\vec{E} = E(x)\hat{i}$. Integrating:

$$E(x) = \begin{cases} \frac{dB_{ext}}{dt}(x - a') & , \ a' < x \leq a \\ 0 & , -a' \leq x \leq a' \\ \frac{dB_{ext}}{dt}(x + a') & , -a \leq x < -a' \end{cases} \tag{A.15}$$

One can also derive the power dissipation:

$$P_v(x) = E(x)J(x) = \begin{cases} J_c\frac{dB_{ext}}{dt}|x - a'| & , \ a' < x \leq a \\ 0 & , -a' \leq x \leq a' \\ J_c\frac{dB_{ext}}{dt}|x + a'| & , -a \leq x < -a' \end{cases} \tag{A.16}$$

Fig. A.6 shows the resulting electric field and power dissipation profiles during Phase 1.

The study has so far been limited to Phase 1, the monotonic part of the curve. Now, we shift the focus to Phase 2, namely where the field decreases between t_1 and t_3. Let us remind that the field at the boundary always corresponds to the applied field. The

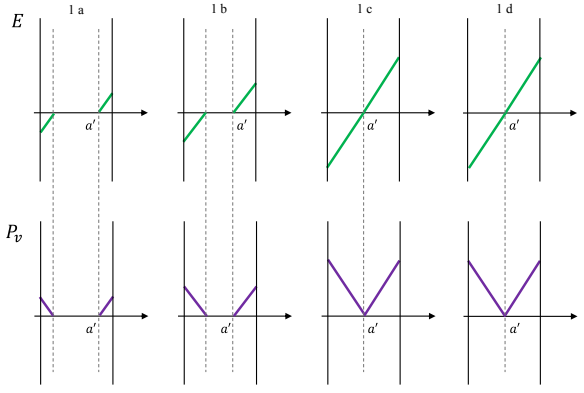

FIGURE A.6: Sequence of electric field and power dissipation in the slab during Phase 1.

problem is governed by the same equation: a layer of currents is induced from the wall, which erases the previous established layer.

The field variation with respect to the inversion point is:

$$\frac{\Delta B}{2} = \mu_0 J_c (a - a'') \tag{A.17}$$

where a'' is the penetration depth of the new layer of currents. Reversing the previous equation:

$$a'' = a - \frac{\Delta B}{2\mu_0 J_c} = a\left(1 - \frac{\Delta B}{2B_{sat}}\right) \tag{A.18}$$

One gets a''=0 when $\Delta B = 2B_{sat}$. Fig. A.7 displays the field and current evolution up to the full inversion, which takes place at t_3 (Phase 2 in subdivided into four sub-phases, similarly to Phase 1). The electric field is always in the same direction of the current, such that it always induces losses. The highest contribution to the losses comes from the external regions of the slab.

The total surface losses are:

$$P_s = \int_{-a}^{+a} EJdx = J_c \left|\frac{dB_{ext}}{dt}\right| (a - a'')^2 \tag{A.19}$$

expressed in W/m^2. Let us also note that when the external field is zero, at t_2, the flux inside the slab is not zero. For this reason, the magnetization in type-II superconductors is *hysteretic*.

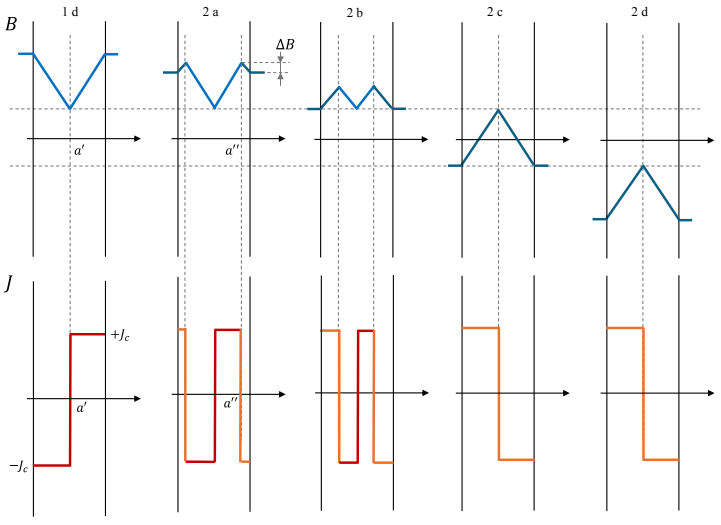

FIGURE A.7: Field and current evolution leading to a full profile inversion during Phase 2 (here divided into four sub-phases and including Phase 1d).

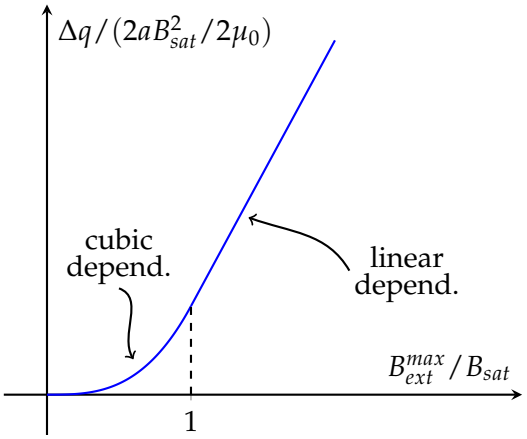

FIGURE A.8: Losses in a magnetic cycle, below and above B_{sat}.

Finally, the field is raised back up to zero in Phase 3. An opposite layer of currents erases those formed during Phase 2. This layer is identical to Phase 1. The penetration depth is now called a''' and the equations are the same as for a'', i.e. Eq. A.18 and Eq. A.19. The energy dissipated in half cycle is:

$$\Delta q = \int_{t_1}^{t_3} P_s(t)dt = \int_{t_1}^{t_2} P_s(t)dt + \int_{t_2}^{t_3} P_s(t)dt \tag{A.20}$$

which becomes:

$$\Delta q = \begin{cases} \dfrac{4a}{3\mu_0 B_{sat}}(B_{ext}^{max})^3 & , B_{ext}^{max} \leq B_{sat} \\ \dfrac{4a}{3\mu_0}B_{sat}B_{ext}^{max} - \dfrac{8a}{3\mu_0}B_{sat}^2 & , B_{ext}^{max} > B_{sat} \end{cases} \tag{A.21}$$

The difference between the two types of behaviour is shown in Fig. A.8. The system A.21 describes the losses for a slab of width $2a$. In the case of an infinitely thin strip of same width $2a$, and writing $\beta = B_{ext}^{max}/B_{sat}$, the magnetization losses are:

$$Q = \begin{cases} \dfrac{2(B_{ext}^{max})^2}{\mu_0}\dfrac{\beta}{3} & , \ \beta \leq 1 \\ \dfrac{2(B_{ext}^{max})^2}{3\mu_0}\left(\dfrac{1}{\beta} - \dfrac{2}{\beta^2}\right) & , \ \beta > 1 \end{cases} \tag{A.22}$$

which are basically the same equations as in the system of Eq. A.21, divided by $2a$ [36].

A.1.1.1 Difference with a perfect conductor

The penetration depth of currents in a perfect conductor is given by:

$$\delta = \sqrt{\frac{2\rho}{\mu_0 \omega}} \tag{A.23}$$

where ω is the frequency of the alternate field. For an ideal material, $\rho \to 0$, therefore $\delta \to 0$, so the intensity of the currents tends to infinity. However, since the thickness of the layer of currents is practically reduced to zero, the dissipation is also zero. The situation is different in a superconductor, where the current density cannot exceed J_c. The external field is thus screened with a higher penetration in the material, causing the dissipation.

A.1.2 Case 2. Transport current

Now, we consider the case of a transport current flowing along the slab. The time variation is the same as the black line in Fig. A.4, where the maxima are replaced by $i_{t,max} < i_c$ and -$i_{t,max}$. The relevant equations are still the system of Eq. A.7:

$$\frac{dB}{dx} = \begin{cases} +\mu_0 J_c \\ 0 \\ -\mu_0 J_c \end{cases} \tag{A.24}$$

together with the boundary condition, Eq. A.1, where B_{ext} is set to zero:

$$B(+a) = +\frac{1}{2}\mu_0 i_t$$

$$B(-a) = -\frac{1}{2}\mu_0 i_t$$

One must also have: $i_t \leq 2aJ_c$. Moreover, $B(\pm a, t) \leq B_{sat}$. Let us note that:

$$i_t = 2J_c(a - a') \tag{A.25}$$

Reversing:

$$a' = a\left(1 - \frac{i_t}{i_c}\right) \tag{A.26}$$

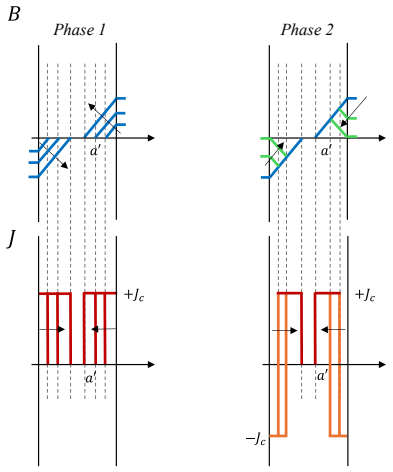

FIGURE A.9: Field and current evolution in a slab carrying a transport current, during both Phase 1 and Phase 2.

Therefore, $i_c = 2aJ_c$ [A/m]. Fig. A.9 (left) shows the resulting field and current profiles while the transport current reaches the critical current during Phase 1.

These are:

$$B(x) = \begin{cases} +\frac{1}{2}\mu_0 i_t - \mu_0 J_c(a-x) & , \ a' < x \leq a \\ 0 & , \ -a \leq x \leq a' \\ -\frac{1}{2}\mu_0 i_t + \mu_0 J_c(a+x) & , \ -a \leq x < -a' \end{cases} \tag{A.27}$$

and

$$J(x) = \begin{cases} +J_c & , \ a' < |x| \leq a \\ 0 & , \ 0 \leq |x| \leq a' \end{cases} \tag{A.28}$$

Please note that the evolution is summed up in a single figure, Fig. A.9, for both the current and the field. The arrows indicate the direction of the profile evolution into the slab.

Applying Ampere's law, the electric field is:

$$E(x) = \int_0^x \frac{\partial B(x')}{\partial t} dx' \tag{A.29}$$

Resulting in:

$$E(x) = \begin{cases} \frac{1}{2}\mu_0 \frac{di_t}{dt}(x - a') & , \ a' < x \leq a \\ 0 & , -a' \leq x \leq a' \\ -\frac{1}{2}\mu_0 \frac{di_t}{dt}(x + a') & , -a \leq x < -a' \end{cases} \tag{A.30}$$

This means that the electric field varies linearly in space and the same happens for the losses. The current decreases in Phase 2, ending up in creating a reversal layer of currents, see again Fig. A.9, on the right. The innermost profiles indicate the layers of currents at t_2, when the overall current is zero. Nevertheless, the slab is penetrated by both a direct and a reverse layer of currents, on each side with respect to the middle line. The losses per cycle are given by:

$$\Delta q = \frac{\mu_0}{6} \frac{i_c^4}{i_{t,max}^2} \tag{A.31}$$

it is relevant noticing that the losses strongly depend on the value of $i_{t,max}$. Then, the total power is: $P = \Delta q \cdot f$. To conclude, one cannot really define these as losses associated to a magnetization cycle, while it is more appropriate to talk about transport or self-field losses.

A.1.3 Magnetic moment and magnetization

The magnetic moment of a body of general shape and volume τ is:

$$\vec{m} = \frac{1}{2} \int_\tau \vec{r} \times \vec{J} \, d\vec{r} \tag{A.32}$$

which is measured in A·m^2, and $\vec{J}$ in the formula is the current distribution in the volume. The same magnetic moment can be generated by the current flowing along a circumference, as represented in Fig. A.10.

The magnetization is then defined as:

$$\vec{M} = \frac{\vec{m}}{\tau} \tag{A.33}$$

and it is measured in A/m.

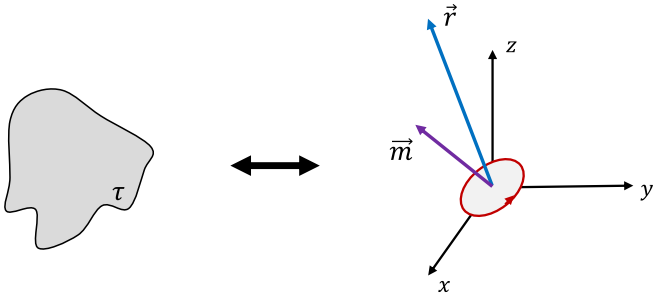

FIGURE A.10: Equivalence between a generic volume τ and a circle having the same magnetic moment.

In the case of a slab, Eq. A.32 becomes:

$$m_z = -\int_{-a}^{+a} xJdx \tag{A.34}$$

which is negative, since it reacts in the opposite direction to an external field. Please note that the resulting unit is A, since here the magnetization is expressed per unit length. Substituting Ampere's law:

$$m_z = -\frac{1}{\mu_0}\int_{-a}^{+a} x\frac{\partial B}{\partial x}dx \tag{A.35}$$

This is solved per parts:

$$m_z = -\frac{1}{\mu_0}[xB]_{-a}^{+a} + \frac{1}{\mu_0}\int_{-a}^{+a} Bdx \tag{A.36}$$

$$= -\frac{1}{\mu_0}2aB_{ext} + \frac{1}{\mu_0}\int_{-a}^{+a} Bdx \tag{A.37}$$

$$= -2a\frac{B_{ext}}{\mu_0} + \frac{2a}{\mu_0} < B > \tag{A.38}$$

$$= 2a\frac{< B > -B_{ext}}{\mu_0} \tag{A.39}$$

where $< B >$ is the average field in the slab. The magnetization is:

$$M = \frac{m}{2a} = \frac{< B > -B_{ext}}{\mu_0} \tag{A.40}$$

This implies that the magnetization profile in the slab can also be derived from the knowledge of the J profile.

Recalling Fig. A.5, we write:

$$\Delta a = a - a' = \frac{B_{ext}}{\mu_0 J_c} \tag{A.41}$$

Summing the areas of the two triangles on the left and right:

$$< B > = \frac{1}{2a} \cdot 2\left(\frac{1}{2}\frac{B_{ext}}{\mu_0 J_c}\right) B_{ext} = \frac{1}{2}\frac{B_{ext}^2}{B_{sat}} \tag{A.42}$$

Finally:

$$\mu_0 M = -\frac{1}{2} B_{sat}\left[2\frac{B_{ext}}{B_{sat}} - \left(\frac{B_{ext}}{B_{sat}}\right)^2\right] \tag{A.43}$$

considering that $\mu_0 M_{max} = -\frac{1}{2} B_{sat}$, the previous equation can be rewritten as:

$$\frac{M}{M_{max}} = -\frac{B_{ext}}{B_{sat}}\left[2 - \left(\frac{B_{ext}}{B_{sat}}\right)\right] \tag{A.44}$$

The magnetization saturates above B_{sat} and remains constant up to the inversion point.

In the general case:

$$\mu_0 M = \frac{1}{2} B_{sat}\left[2\frac{\Delta B}{B_{sat}} - 2\left(\frac{\Delta B}{B_{sat}}\right)^2 - 1\right] \tag{A.45}$$

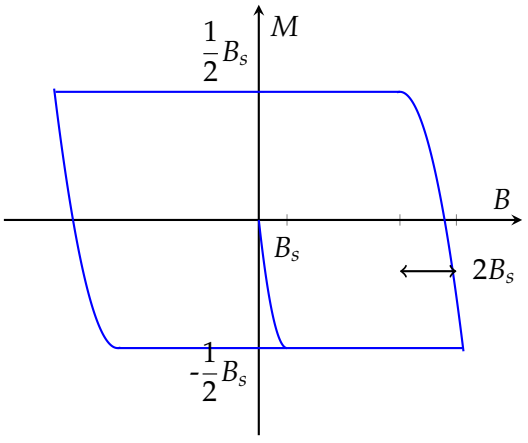

FIGURE A.11: Magnetization cycle in the Bean model. B_s indicates the saturation field.

This last formula is valid until $\Delta B \leq 2B_{sat}$. At inversion, the curve goes backwards and it stays constant until the next inversion, see also Fig. A.11, as already presented in Fig. 1.15. This corresponds to the magnetization cycle, similarly to the case of traditional materials, which is also why the term 'hysteretic' has been adopted for superconductors as well. The overall losses in a cycle are:

$$\Delta q = -\oint m \, dB_{ext} = -2a \oint M \, dB_{ext} \tag{A.46}$$

expressed in $\mathrm{J/m^2}$.

A.1.3.1 Ways to reduce the losses

Diving a superconductor in N filaments, the losses of the single filament drop as $1/N^2$, which must then be multiplied by the number of filaments, giving the overall reduction of losses as $1/N$.

The reduction is actually lower, since currents can flow from one filament to another through the matrix, the so-called *coupling currents*. In LTS, filaments are also transposed, such that the current paths are as shortened as possible. In HTS, some examples of transposed conductors are the Roebel and the CORC cable. Another technique to reduce the losses is to close the gaps in between tapes. This way, the field is never perpendicular to the current.

Superconductors are also subjected to losses each time they are exposed to a field ramp. This has a huge impact on operation, especially on the refrigeration side. Losses can be reduced by acting on the materials, on the conductors (magnetic shields, filamentization), or on the geometry of the application, for example to achieve flux expulsion.

Appendix B

Magnetic field generated by a thin strip

B.1 Outside the tape

Let us consider a tape of width $2a$ and a point P located on the same axis of the strip, at a distance D from the strip, as indicated in Fig. B.1. The strip has thickness d. A current density $j(x,z)$ flows in the strip and one can define the so-called *sheet current density*, $J(x)$:

$$J(x) = \int_{-d/2}^{d/2} j(x,z)dz \tag{B.1}$$

flowing along the y-direction, $J(x) = J_y(x)$. In the case where the width-to-thickness ratio is sufficiently high, as it is the case of REBCO tapes, the distribution along the z-axis can be disregarded and all considerations can be made on the $J(x)$. The total current flowing in the tape is:

$$I = \int_0^{2a} J(x)dx \tag{B.2}$$

It follows directly that the infinitesimal current flowing at position x is: $dI(x) = J(x)dx$. If the current density is uniform, namely $J(x) = J = \frac{I}{w}$, then $dI = \frac{I}{w}dx$. The magnetic field generated in point P by this infinitesimal current can be found by Ampere's law:

$$\oint_l \vec{B} \cdot d\vec{l} = \mu_0 I \tag{B.3}$$

which, at a distance R is:

$$B \cdot 2\pi R = \mu_0 I \tag{B.4}$$

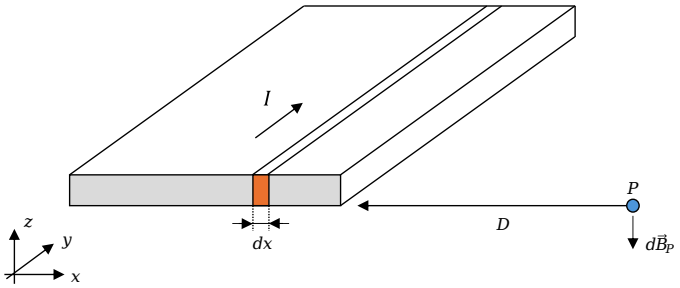

FIGURE B.1: Infinitesimal field generated by an infinitesimal current line in dx.

and then:

$$B = \frac{\mu_0 I}{2\pi R} \tag{B.5}$$

Therefore, the infinitesimal field dB_p generated by the infinitesimal current dI is:

$$dB_{P,z} = \frac{\mu_0}{2\pi}\frac{dI}{(D+x)} = \frac{\mu_0 I}{2\pi w}\frac{dx}{(D+x)} \tag{B.6}$$

Integrating on the tape width w, one obtains the total field:

$$B_{P,z} = \frac{\mu_0 I}{4\pi a}\int_0^{2a}\frac{dx}{D+x} \tag{B.7}$$

which gives:

$$B_{P,z} = \frac{\mu_0 I}{4\pi a}\Big[ln|D+x|\Big]_0^{2a} \tag{B.8}$$

namely:

$$B_{P,z} = \frac{\mu_0 I}{4\pi a}\Big[ln(2a+D) - ln(D)\Big] \tag{B.9}$$

Finally:

$$B_{P,z} = \frac{\mu_0 I}{4\pi a}\left[ln\left(1+\frac{2a}{D}\right)\right] \tag{B.10}$$

B.2 Inside the tape

Computing the field generated in the strip by the current flowing in the strip itself requires taking two locations inside the strip into account. The first one is the point of interest, located in x, while the other one is the actual source point, located in x'. The infinitesimal contribution of the current $J(x')dx'$ to the field in x is:

$$dB_z(x,x') = \frac{\mu_0}{2\pi}\frac{J(x')dx'}{|x-x'|} \tag{B.11}$$

where we use the module, since x can be on either sides of x'. The resulting field in a strip of width $2a$ is obtained by integration of all these infinitesimal contributions:

$$B_z(x) = \frac{\mu_0}{2\pi}\int_{-a}^{a}\frac{J(x')dx'}{|x-x'|} \tag{B.12}$$

which is valid for a generic current distribution in the tape, $J(x)$. Also, the tape extends from $-a$ to $+a$. Eq. B.12 is used in Eq. (1) in [128] as well as Eq. (2) in [129].

In the case where J is uniform over the tape width, we can write: $J(x') = \frac{I}{2a}$, and:

$$B_z(x) = \frac{\mu_0 I}{4\pi a}\int_{-a}^{a}\frac{dx'}{|x-x'|} \tag{B.13}$$

The integral can be solved using the Cauchy principal value method:

$$\int_{-a}^{a}\frac{dx'}{|x-x'|} = \lim_{\varepsilon\to 0}\left\{\int_{-a}^{x-\varepsilon}\frac{dx'}{|x-x'|} + \int_{x+\varepsilon}^{a}\frac{dx'}{|x-x'|}\right\} \tag{B.14}$$

which brings to:

$$\int_{-a}^{a}\frac{dx'}{|x-x'|} = \lim_{\varepsilon\to 0}\left\{\Big[ln|x-x'|\Big]_{-a}^{x-\varepsilon} + \Big[ln|x-x'|\Big]_{x+\varepsilon}^{a}\right\} \tag{B.15}$$

then:

$$\int_{-a}^{a}\frac{dx'}{|x-x'|} = \lim_{\varepsilon\to 0}\left\{ln|\varepsilon| - ln|x+a| + ln|x-a| - ln|\varepsilon|\right\} \tag{B.16}$$

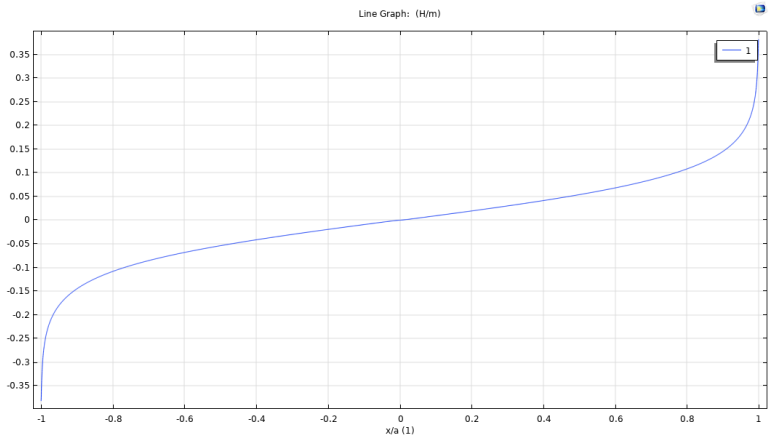

FIGURE B.2: Field distribution in the strip for a uniform transport current, I_t=1000 A.

Simplifying:

$$\int_{-a}^{a} \frac{dx'}{|x-x'|} = ln\frac{|x-a|}{|x+a|} \tag{B.17}$$

Therefore:

$$B_z(x) = \frac{\mu_0 I}{4\pi a} ln\frac{|x-a|}{|x+a|} \tag{B.18}$$

The analytical field profile given in Eq. B.18 was also reproduced by means of a simulation in Comsol® in the case of a transport current of 1000 A, see Fig. B.2.

Appendix C

Thin strip in an external field and with transport current

We present now the complementary case of a field perpendicular to an infinitely thin strip. For such purpose, we use the method of image currents and the Joukowski mapping. The calculation is developed on the basis of [130].

C.1 Transport current

C.1.1 Source current - magnetic potential

Let us consider a line current $+I$. The field generated by this current can be calculated starting from the Ampere's law:

$$\vec{\nabla} \times \vec{B} = \mu_0 \vec{J} \tag{C.1}$$

Integrating:

$$\int_S (\vec{\nabla} \times \vec{B}) \cdot d\vec{S} = \int_S \mu_0 \vec{J} \cdot d\vec{S} \tag{C.2}$$

The right-hand side (RHS) can be transformed into a line integral using Stokes' theorem:

$$\int_S (\vec{\nabla} \times \vec{B}) \cdot d\vec{S} = \oint_l \vec{B} \cdot d\vec{l} \tag{C.3}$$

Then,

$$\oint_l \vec{B} \cdot d\vec{l} = \int_S \mu_0 \vec{J} \cdot d\vec{S} \tag{C.4}$$

which around a circle of radius R is:

$$B \cdot 2\pi R = \mu_0 I \tag{C.5}$$

Therefore:

$$B = \frac{\mu_0 I}{2\pi R} \tag{C.6}$$

In vectorial form:

$$\vec{B} = B_\theta \hat{\theta} = \frac{\mu_0 I}{2\pi R} \hat{\theta} \tag{C.7}$$

Let us recall that the magnetic vector potential is defined as:

$$\vec{B} = \vec{\nabla} \times \vec{A} \tag{C.8}$$

Since $\vec{B} = B_\theta \, \hat{\theta}$, then $\vec{\nabla} \times \vec{A} = (\vec{\nabla} \times \vec{A})_\theta$. In cylindrical coordinates:

$$\vec{\nabla} \times \vec{A} = \begin{vmatrix} \hat{r} & \hat{\theta} & \hat{z} \\ \dfrac{\partial}{\partial r} & \dfrac{1}{r}\dfrac{\partial}{\partial \theta} & \dfrac{\partial}{\partial z} \\ A_r & A_\theta & A_z \end{vmatrix} \tag{C.9}$$

Therefore:

$$\left(\vec{\nabla} \times \vec{A}\right)_\theta = -\left(\frac{\partial A_z}{\partial r} - \frac{\partial A_r}{\partial z}\right) \tag{C.10}$$

Since A_r does not vary along the z-coordinate, the second term in the previous equation is zero. Then, going back to Eq. C.7, we can write:

$$-\frac{\partial A_z}{\partial r} \hat{\theta} = \frac{\mu_0 I}{2\pi R} \hat{\theta} \tag{C.11}$$

Isolating the modulii, and since A_r depends only on z:

$$-\frac{dA_r}{dz} = \frac{\mu_0 I}{2\pi R} \tag{C.12}$$

Integrating:

$$A_z(r) = -\frac{\mu_0 I}{2\pi} ln(R) + C \tag{C.13}$$

where here, R is a distance and the integration constant is neglected. Let us now consider a source current $+I$ in a location $(x_0; 0)$ and a generic point $(r; \theta)$. Using Eq. C.13, we write:

$$A_z(r;\theta)|_{x_0} = -\frac{\mu_0 I}{2\pi} ln\Big\{(x_0 - rcos\theta)^2 + r^2 sin^2\theta\Big\}^{1/2} \tag{C.14}$$

namely:

$$A_z(r;\theta)|_{x_0} = -\frac{\mu_0 I}{4\pi} ln(x_0^2 + r^2 - 2rx_0 cos\theta) \tag{C.15}$$

C.1.2 Image current - magnetic potential

The same calculation can be repeated for an image current line $-I$, which is located in $x_0^* = R^2/x_0$. Let us note that R is the radius of a reference circle.

$$A_z(r;\theta)|_{x_0^*} = +\frac{\mu_0 I}{4\pi} ln\left[\frac{R^4}{x_0^2} + r^2 - 2r\frac{R^2}{x_0} cos\theta\right] \tag{C.16}$$

Collecting the term $\dfrac{R^2}{x_0^2}$:

$$A_z(r;\theta)|_{x_0^*} = +\frac{\mu_0 I}{4\pi} ln\left\{\frac{R^2}{x_0^2}\left[R^2 + r^2\frac{x_0^2}{R^2} - 2rx_0 cos\theta\right]\right\} \tag{C.17}$$

Finally:

$$A_z(r;\theta)|_{x_0^*} = +\frac{\mu_0 I}{4\pi} ln\left[R^2 + r^2\frac{x_0^2}{R^2} - 2rx_0 cos\theta\right] + \frac{\mu_0 I}{2\pi} ln\frac{R}{|x_0|} \tag{C.18}$$

The image current has opposite sign with respect to the source current and it is located such that the field component normal to the rim of the circle of radius R is zero.

Summing up:

$$A_{z,tot}(r;\theta) = A_z(r;\theta)\Big|_{x_0} + A_z(r;\theta)\Big|_{x_0^*} \tag{C.19}$$

which gives:

$$A_{z,tot}(r;\theta) = \frac{\mu_0 I}{4\pi} ln \frac{R^2 + r^2\frac{x_0^2}{R^2} - 2rx_0 cos\theta}{x_0^2 + r^2 - 2rx_0 cos\theta} + \frac{\mu_0 I}{2\pi} ln \frac{R}{|x_0|} \tag{C.20}$$

On the rim of the circle:

$$A_{z,tot}(r = R;\theta) = \frac{\mu_0 I}{2\pi} ln \frac{R}{|x_0|} \tag{C.21}$$

The radial component of the field can be found as:

$$B_r(r;\theta) = \frac{1}{r}\frac{\partial A_z}{\partial \theta} \tag{C.22}$$

In Eq. C.20, calling 'N' the numerator and 'D' the denominator of the first logarithm, we obtain:

$$B_r(r;\theta) = \frac{1}{r}\frac{\mu_0 I}{4\pi}\left\{\frac{D}{N}\frac{2rx_0 sin\theta \cdot D - 2rx_0 sin\theta \cdot N}{D^2}\right\} \tag{C.23}$$

Therefore:

$$B_r(r;\theta) = \frac{1}{r}\frac{\mu_0 I}{4\pi}\left\{\frac{2rx_0 sin\theta}{R^2 + r^2\frac{x_0^2}{R^2} - 2rx_0 cos\theta} - \frac{2rx_0 sin\theta}{x_0^2 + r^2 - 2rx_0 cos\theta}\right\} \tag{C.24}$$

On the rim of the circle:

$$B_r(r;\theta)|_{r=R} = 0 \tag{C.25}$$

namely there is no normal component of the field to the rim of the circle, as it can be seen from Fig. C.1. To sum up, the image current $-I$ is located in such a way (at $x_0^* = R^2/x_0$) to counterbalance the source current $+I$ in x_0 and cancel the field inside the circle. Also, the resulting magnetic field is only tangent to the rim of the circle.

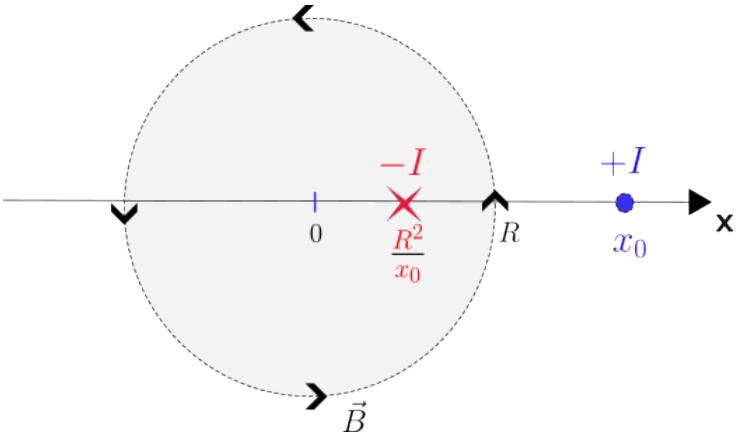

FIGURE C.1: Source and image currents around a circle of radius R. The field vector $\vec{B}$ is tangent to the rim of the circle everywhere along the circumference.

C.1.3 Equivalent current distribution

It is now the objective to find an *equivalent* current distribution to the source and image currents, on the rim of the circle. We consider Fig. C.2. Starting from Ampere's law:

$$\vec{\nabla} \times \vec{B} = \mu_0 \vec{J} \tag{C.26}$$

Integrating:

$$\int_S (\vec{\nabla} \times \vec{B}) \cdot d\vec{S} = \int_S \mu_0 \vec{J} \cdot d\vec{S} \tag{C.27}$$

Let us isolate the LHS:

$$\int_S (\vec{\nabla} \times \vec{B}) \cdot d\vec{S} = \oint_l \vec{B} \cdot d\vec{l} \tag{C.28}$$

From Fig. C.2, we choose the path OAA'OBB'O. Consequently,

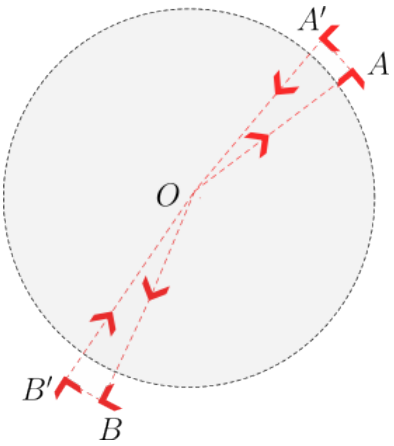

FIGURE C.2: Path to derive the relation between J and B_θ.

$$\oint \vec{B} \cdot d\vec{l} = \int_{OAA'OBB'O} \vec{B} \cdot d\vec{l} = B_\theta(R;\theta)(Rd\theta) + B_\theta(R;-\theta)(-Rd\theta) \tag{C.29}$$

The contribution from segments OA, A'O, OB, and B'O is zero, since the field is zero inside the circle. Please note that the term $(Rd\theta)$ here is an arc length. By symmetry, $B_\theta(R;-\theta) = -B_\theta(R;\theta)$. Therefore,

$$\oint \vec{B} \cdot d\vec{l} = B_\theta(R;\theta)(Rd\theta) + B_\theta(R;\theta)(Rd\theta) = 2B_\theta(R;\theta)Rd\theta \tag{C.30}$$

Then, the RHS is:

$$\int_S \vec{J} \cdot d\vec{S} = J(R;\theta)(Rd\theta) + J(R;-\theta)(Rd\theta) \tag{C.31}$$

note that here, instead, $(Rd\theta)$ is an area. By symmetry: $J(R;-\theta) = J(R;\theta)$. This leads to:

$$\int_S \vec{J} \cdot d\vec{S} = 2J(R;\theta)(Rd\theta) \tag{C.32}$$

Putting everything back together:

$$2B_\theta(R;\theta)Rd\theta = 2J(R;\theta)Rd\theta \cdot \mu_0 \tag{C.33}$$

We derive that:

$$J(R;\theta) = \frac{1}{\mu_0} B_\theta(R;\theta) \tag{C.34}$$

which is the relation between the current density and the tangential component of the field on the rim of the circle. This implies that finding the expression at the RHS for B_θ allows finding the current distribution. In particular,

$$B_\theta = -\frac{\partial A_z}{\partial r} \tag{C.35}$$

In fact, let us recall that $\partial A_r/\partial z = 0$ in the determinant for computing $\vec{B}$, Eq. C.9.

$$B_\theta = -\frac{\mu_0 I}{4\pi} \cdot \frac{\partial}{\partial r} \left\{ ln \frac{R^2 + r^2 \frac{x_0^2}{R^2} - 2rx_0 cos\theta}{x_0^2 + r^2 - 2rx_0 cos\theta} \right\} \tag{C.36}$$

calling 'N' the numerator and 'D' the denominator in the logarithm, we get:

$$B_\theta = -\frac{\mu_0 I}{4\pi}\frac{D}{N}\cdot\frac{\left[2r\frac{x_0^2}{R^2}-2x_0 cos\theta\right]\cdot D - N\cdot\left[2r-2x_0 cos\theta\right]}{D^2} \tag{C.37}$$

Then,

$$B_\theta = B_\theta(r;\theta) = -\frac{\mu_0 I}{2\pi}\cdot\left\{\frac{r\frac{x_0^2}{R^2}-x_0 cos\theta}{R^2+r^2\frac{x_0^2}{R^2}-2rx_0 cos\theta} - \frac{r-x_0 cos\theta}{x_0^2+r^2-2rx_0 cos\theta}\right\} \tag{C.38}$$

Finally:

$$B_\theta(r=R;\theta) = -\frac{\mu_0 I}{2\pi R}\cdot\frac{x_0^2-R^2}{x_0^2+R^2-2Rx_0 cos\theta} \tag{C.39}$$

Units are T. The resulting current distribution on the rim of the circle is derived using Eq. C.34:

$$J(r=R;\theta) = -\frac{I}{2\pi R}\cdot\frac{x_0^2-R^2}{x_0^2+R^2-2Rx_0 cos\theta} \tag{C.40}$$

Now, let us consider another source current $+I$, this time located in $(-x_0;0)$ and its associated image current $-I$ in $(-R^2/x_0;0)$, see also Fig. C.3. In this case,

$$B_\theta\big|_{-x_0} = -\frac{\mu_0 I}{2\pi R}\cdot\frac{x_0^2-R^2}{x_0^2+R^2+2Rx_0 cos\theta} \tag{C.41}$$

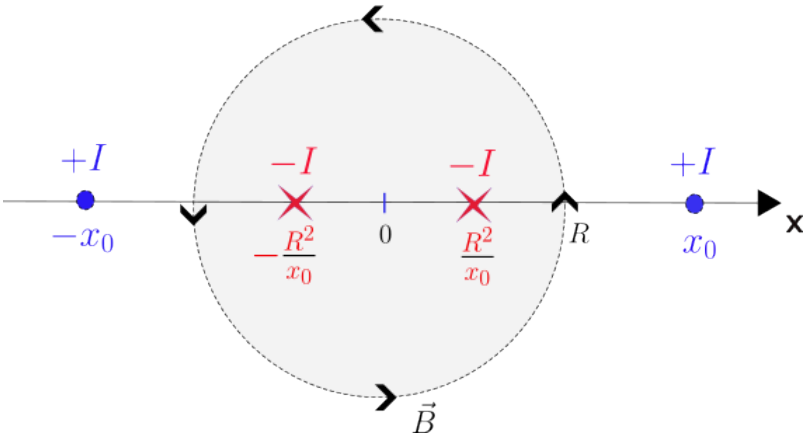

FIGURE C.3: Source and image currents mirrored on the negative side.

Summing up:

$$B_{\theta,tot} = B_{\theta,x_0} + B_{\theta,-x_0} \tag{C.42}$$

namely:

$$B_{\theta,tot} = -\frac{\mu_0 I}{2\pi R}(x_0^2 - R^2)\left\{ \frac{1}{(x_0^2 + R^2) - 2Rx_0 cos\theta} + \frac{1}{(x_0^2 + R^2) + 2Rx_0 cos\theta} \right\} \tag{C.43}$$

developing the calculation:

$$B_{\theta,tot} = -\frac{\mu_0 I}{2\pi R}(x_0^2 - R^2)\frac{2(x_0^2 + R^2)}{(x_0^2 + R^2)^2 - (2Rx_0 cos\theta)^2} \tag{C.44}$$

which gives:

$$B_{\theta,tot} = -\frac{\mu_0 I}{\pi R} \cdot \frac{x_0^4 - R^4}{(x_0^2 + R^2)^2 - (2Rx_0 cos\theta)^2} \tag{C.45}$$

Transforming using Eq. C.34, we get:

$$J_{\theta,tot} = -\frac{I}{\pi R} \cdot \frac{x_0^4 - R^4}{(x_0^2 + R^2)^2 - (2Rx_0 cos\theta)^2} \tag{C.46}$$

which is the current distribution on the rim of the circle. The following objective is to 'squeeze' the circle to obtain the current distribution in a thin strip. This is achieved thanks to the Joukowski mapping.

C.1.4 Joukowski mapping

The Joukowski mapping is defined in the complex plane, and it acts such that:

$$w = u + iv = \frac{1}{2}\left(z + \frac{R^2}{z}\right) \tag{C.47}$$

For example, the circle: $z = Re^{i\theta}$ becomes:

$$w = \frac{1}{2}\left[Re^{i\theta} + \frac{R^2}{Re^{i\theta}}\right] = \frac{1}{2}\left[Re^{i\theta} + Re^{-i\theta}\right] \tag{C.48}$$

namely:

$$w = Rcos\theta \tag{C.49}$$

which is a line segment $[-R; +R]$, or a strip. Considering the line current in $(x_0; 0)$, this is transformed in:

$$w = u + iv = \frac{1}{2}\left(x_0 + \frac{R^2}{x_0}\right) \tag{C.50}$$

Then,

$$u_0 = \frac{1}{2}\left(x_0 + \frac{R^2}{x_0}\right) \tag{C.51}$$

which becomes:

$$x_{0_{1,2}} = u_0 \pm \sqrt{u_0^2 - R^2} \tag{C.52}$$

The negative sign is used to map the interior of the strip to the interior of the circle, while the positive sign is used to map the exterior of the strip to the exterior of the circle. In the following, we keep the positive sign:

$$x_0 = u_0 + \sqrt{u_0^2 - R^2} \tag{C.53}$$

Elevating to the square:

$$x_0^2 = u_0^2 + 2u_0\sqrt{u_0^2 - R^2} + (u_0^2 - R^2) = 2u_0^2 - R^2 + 2u_0\sqrt{u_0^2 - R^2} \tag{C.54}$$

Then:

$$x_0^2 + R^2 = 2u_0\left[u_0 + \sqrt{u_0^2 - R^2}\right] \tag{C.55}$$

Squaring also Eq. C.54, and developing the calculation, we get:

$$x_0^4 = (x_0^2)^2 \tag{C.56}$$
$$= 4u_0^4 + 4u_0^2(u_0^2 - R^2) + R^4 + 8u_0^3\sqrt{u_0^2 - R^2} - 4u_0^2R^2 - 4u_0\sqrt{u_0^2 - R^2}R^2 \tag{C.57}$$
$$= 8u_0^4 - 4u_0^2R^2 + R^4 + 8u_0^3\sqrt{u_0^2 - R^2} - 4u_0^2R^2 - 4u_0\sqrt{u_0^2 - R^2}R^2 \tag{C.58}$$
$$= 8u_0^4 - 8u_0^2R^2 + 8u_0^3\sqrt{u_0^2 - R^2} - 4u_0\sqrt{u_0^2 - R^2}R^2 + R^4 \tag{C.59}$$
$$= 8u_0^2(u_0^2 - R^2) + 4u_0\sqrt{u_0^2 - R^2}(2u_0^2 - R^2) + R^4 \tag{C.60}$$
$$= 8u_0^2(u_0^2 - R^2) + 4u_0\sqrt{u_0^2 - R^2}(u_0^2 - R^2) + 4u_0^3\sqrt{u_0^2 - R^2} + R^4 \tag{C.61}$$

this continues as:

$$x_0^4 = (u_0^2 - R^2)\left[8u_0^2 + 4u_0\sqrt{u_0^2 - R^2}\right] + 4u_0^3\sqrt{u_0^2 - R^2} + R^4 \tag{C.62}$$
$$= 4u_0(u_0^2 - R^2)\left[2u_0 + \sqrt{u_0^2 - R^2}\right] + 4u_0^3\sqrt{u_0^2 - R^2} + R^4 \tag{C.63}$$
$$= 4u_0(u_0^2 - R^2)\left[u_0 + \sqrt{u_0^2 - R^2}\right] + 4u_0^2(u_0^2 - R^2) + 4u_0^3\sqrt{u_0^2 - R^2} + R^4 \tag{C.64}$$
$$= 4u_0(u_0^2 - R^2)\left[u_0 + \sqrt{u_0^2 - R^2}\right] + 4u_0^2\sqrt{u_0^2 - R^2}\left[\sqrt{u_0^2 - R^2} + u_0\right] + R^4 \tag{C.65}$$
$$= 4u_0\sqrt{u_0^2 - R^2}\left[u_0 + \sqrt{u_0^2 - R^2}\right]^2 + R^4 \tag{C.66}$$

Therefore:

$$x_0^4 - R^4 = 4u_0\sqrt{u_0^2 - R^2}\left[u_0 + \sqrt{u_0^2 - R^2}\right]^2 \tag{C.67}$$

Then:

$$J(R;\theta) = -\frac{I}{\pi R}\frac{4u_0\sqrt{u_0^2 - R^2}\left[u_0 + \sqrt{u_0^2 - R^2}\right]^2}{4u_0^2\left[u_0 + \sqrt{u_0^2 - R^2}\right]^2 - 4R^2\left[u_0 + \sqrt{u_0^2 - R^2}\right]^2 cos\theta} \tag{C.68}$$

from which:

$$J(z) = -\frac{I}{\pi R}\frac{u_0\sqrt{u_0^2 - R^2}}{u_0^2 - u^2} \tag{C.69}$$

where $u = Rcos\theta$. Note that J is a line current density, in [A/m]. The conservation of current must also be considered when switching from the z-coordinate to u-coordinate.

$$J(u)du = J(z)dz \tag{C.70}$$

Since $z = Re^{i\theta}$, $dz = Rd\theta$, while $u = Rcos\theta$, $du = -Rsin\theta d\theta$. Then:

$$J(u) = J(z)\frac{dz}{du} \tag{C.71}$$

which is:

$$J(u) = J(z)\left(-\frac{1}{sin\theta}\right) \tag{C.72}$$

From trigonometry:

$$sin\theta = \sqrt{1 - cos^2\theta} \tag{C.73}$$

We have: $u = Rcos\theta$, therefore:

$$sin\theta = \sqrt{1 - \left(\frac{u}{R}\right)^2} = \frac{1}{R}\sqrt{R^2 - u^2} \tag{C.74}$$

which is dimensionless. Eq. C.71 becomes:

$$J(u) = -J(z)\frac{R}{\sqrt{R^2 - u^2}} \tag{C.75}$$

Putting Eq. C.69 and Eq. C.75 together, we get:

$$J(u_0; u) = -\frac{I}{\pi R}\frac{u_0\sqrt{u_0^2 - R^2}}{u_0^2 - u^2}\left(-\frac{R}{\sqrt{R^2 - u^2}}\right) \tag{C.76}$$

$$\tag{C.77}$$

$$= +\frac{I}{\pi}\frac{u_0\sqrt{u_0^2 - R^2}}{\sqrt{R^2 - u^2}(u_0^2 - u^2)} \tag{C.78}$$

this is again a line current density, and substituting q=R (in accordance with [130]), Eq. C.78 can be written as:

$$J(u_0;u) = +\frac{I}{\pi}\frac{u_0\sqrt{u_0^2-q^2}}{\sqrt{q^2-u^2}(u_0^2-u^2)} \tag{C.79}$$

To proceed further and compute the distribution of current density, we note that I in the formula is actually the critical current density in the strip, $J_c = I_c/2a$. Then, a line current density can be obtained by integration, which is the actual objective of the computation.

The source current is distributed from q to a, which is the reason why we integrate. In addition, we add a factor 2 because of symmetry. Then,

$$J(u) = \frac{J_c}{\pi}\cdot 2\int_q^a \frac{u_0\sqrt{u_0^2-q^2}}{\sqrt{q^2-u^2}(u_0^2-u^2)}du_0 \tag{C.80}$$

This is:

$$J(u) = \frac{J_c}{\pi\sqrt{q^2-u^2}}\cdot 2\int_q^a \frac{u_0\sqrt{u_0^2-q^2}}{u_0^2-u^2}du_0 \tag{C.81}$$

The integral is solved as:

$$J(u) = \frac{2J_c}{\pi\sqrt{q^2-u^2}}\left\{\sqrt{u_0^2-q^2} - \sqrt{q^2-u^2}\; arctg\Big(\frac{\sqrt{u_0^2-q^2}}{\sqrt{q^2-u^2}}\Big)\right\}\Bigg|_q^a \tag{C.82}$$

which gives:

$$J(u) = \frac{2J_c}{\pi\sqrt{q^2-u^2}}\left\{\sqrt{a^2-q^2} - \sqrt{q^2-u^2}\; arctg\left(\frac{\sqrt{a^2-q^2}}{\sqrt{q^2-u^2}}\right)\right\} \tag{C.83}$$

and:

$$J(u) = \frac{2J_c}{\pi}\left\{\frac{\sqrt{a^2-q^2}}{\sqrt{q^2-u^2}} - \; arctg\left(\frac{\sqrt{a^2-q^2}}{\sqrt{q^2-u^2}}\right)\right\} \tag{C.84}$$

Actually, the first term produces a singularity in $u = \pm q$, which must be eliminated. To do that, we notice that a constant current on the rim of the circle does not produce any field component normal to the circle itself (thanks to the right-hand rule).

A constant current can also be associated to a constant current density, J_0. Transforming into the strip:

$$J_{unif}(u) = J_0\left(-\frac{R}{\sqrt{R^2-u^2}}\right) \tag{C.85}$$

and with $q = R$,

$$J_{unif}(u) = -\frac{J_0 q}{\sqrt{q^2-u^2}} \tag{C.86}$$

Integrating:

$$J(u) = -J_0\, q\, 2\int_q^a \frac{1}{(a-q)\sqrt{q^2-u^2}} du_0 \tag{C.87}$$

where we divide by the factor $(a-q)$, to keep the correct units A/m. Therefore:

$$J(u) = -J_0 \frac{q}{a-q}\cdot\frac{2(a-q)}{\sqrt{q^2-u^2}} \tag{C.88}$$

$$= -J_0 \frac{2q}{\sqrt{q^2-u^2}} \tag{C.89}$$

Then, choosing:

$$\frac{2J_c}{\pi}\frac{\sqrt{a^2-q^2}}{\sqrt{q^2-u^2}} = -J_0\frac{2q}{\sqrt{q^2-u^2}} \tag{C.90}$$

We obtain:

$$J_0 = -\frac{J_c}{\pi q}\sqrt{a^2-q^2} \tag{C.91}$$

$$= -\frac{J_c}{\pi}\sqrt{\left(\frac{a}{q}\right)^2-1} \tag{C.92}$$

Finally:

$$J(u) = \frac{2J_c}{\pi} arctg\left(\frac{\sqrt{a^2-q^2}}{\sqrt{q^2-u^2}}\right) \tag{C.93}$$

This is the expression for the current distribution in the strip, for $q < u \leq a$ in the case of a transport current, as displayed in Fig. C.4. The transport current in strip geometry generates a self-field that wraps around the strip and has a discontinuity between the top and bottom surfaces. As a result, currents flow across the entire width of the film:

$$J_y(x) = \begin{cases} J_c & , \ q < |x| \leq a \\ 2\frac{J_c}{\pi} arctg\left(\sqrt{\frac{a^2-q^2}{q^2-x^2}}\right) & , \ |x| \leq q \end{cases} \tag{C.94}$$

see also Fig. C.4. The penetration depth is:

$$q = a\sqrt{1-\left(\frac{i_t}{i_c}\right)^2} \tag{C.95}$$

the dependence from the transport current, i_t, is non linear.

The field distribution given by a generic current distribution is:

$$B_z(x) = \frac{\mu_0}{2\pi}\int_{-a}^{a} \frac{J(x')dx'}{|x-x'|} \tag{C.96}$$

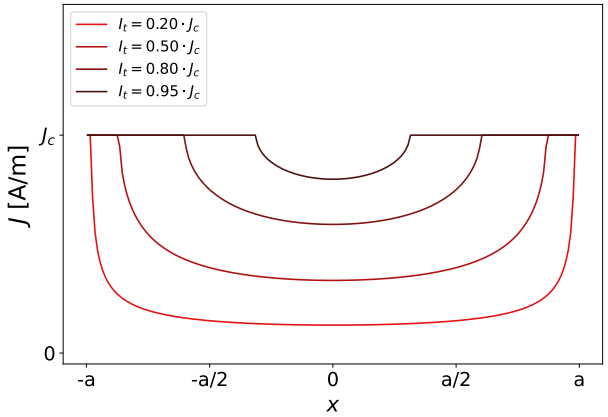

FIGURE C.4: Current distribution resulting from a transport current in the strip.

Integrating (Eq. C.96), one obtains the magnetic field:

$$B_z(x) = \begin{cases} 0, & |x| \leq q \\ \dfrac{J_c}{\pi}\dfrac{x}{|x|}\ln\dfrac{\sqrt{x^2-q^2}+\sqrt{a^2-q^2}}{\sqrt{|x^2-a^2|}}, & |x| \geq q \end{cases} \tag{C.97}$$

which is shown in Fig. C.5. Now, we integrate to obtain the current in the strip.

$$I = \int_{-a}^{a} J(u)du \tag{C.98}$$

$$= 2\int_0^q \frac{2J_c}{\pi} arctg\left(\frac{\sqrt{a^2-q^2}}{\sqrt{q^2-u^2}}\right)du + 2J_c(a-q) \tag{C.99}$$

where the factor 2 in front of the first integral is for symmetry, while the second term results from the full critical current density flowing in the edges, namely from $-a$ to $-q$ and from q to a. Then,

$$I = 4\frac{J_c}{\pi}\left\{\sqrt{a^2-q^2}arctg\left(\frac{u}{\sqrt{q^2-u^2}}\right)\right. \tag{C.100}$$

$$\left. - a\cdot arctg\left(\frac{\sqrt{a^2-q^2}}{\sqrt{q^2-u^2}}\frac{u}{a}\right) - u\cdot arctg\left(\frac{\sqrt{a^2-q^2}}{\sqrt{q^2-u^2}}\right)\right\}\Bigg|_0^q + 2J_c(a-q) \tag{C.101}$$

For $u = q$, all the *arctg* arguments are equal to $\dfrac{\pi}{2}$, and zero for $u = 0$. Therefore,

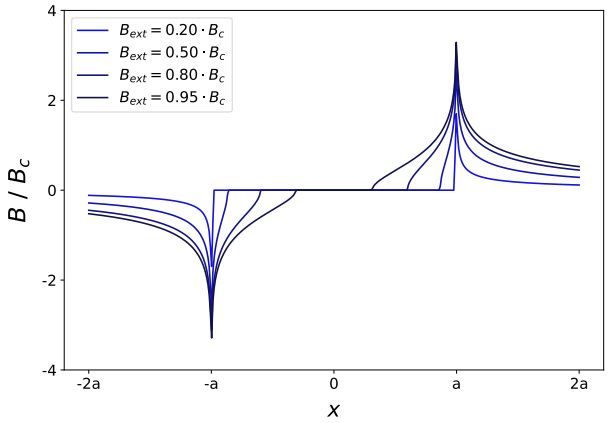

FIGURE C.5: Field distribution resulting from a transport current in the strip.

$$I = 4\frac{J_c}{\pi} \cdot \frac{\pi}{2}\left\{\sqrt{a^2 - q^2} - a - q\right\} + 2\sigma_c(a - q) \tag{C.102}$$

$$\tag{C.103}$$

$$= 2J_c\left(\sqrt{a^2 - q^2} - a + q\right) + 2J_c(a - q) \tag{C.104}$$

$$\tag{C.105}$$

$$= 2J_c\left(\sqrt{a^2 - q^2}\right) \tag{C.106}$$

Then,

$$\frac{I}{2J_c} = \sqrt{a^2 - q^2} \tag{C.107}$$

giving:

$$\frac{I}{2\frac{I_c}{2a}} = \sqrt{a^2 - q^2} \tag{C.108}$$

and:

$$\frac{I}{I_c} = \frac{1}{a}\sqrt{a^2 - q^2} \tag{C.109}$$

which leads to:

$$\frac{I}{I_c} = \sqrt{1 - \left(\frac{q}{a}\right)^2} \tag{C.110}$$

And the so-called penetration depth is:

$$q = a\sqrt{1 - \left(\frac{I}{I_c}\right)^2} \tag{C.111}$$

The current-free region is also field-free in the slab. The important difference with the strip geometry is that the current flows everywhere across the entire width despite the presence of the field free region.

C.2 Applied perpendicular field

In section A, we analyzed the case of a slab immersed in a parallel field. Here, we consider a perpendicular field to a thin strip, such as could be a REBCO coated conductor. This system is displayed in Fig. C.6.

The strip can be seen as an infinitesimal layer of the slab. We make the assumption that in a slab or film of width $2a$, infinite along the y-direction, currents flow only along y, if an external field is applied along the z and/or y direction. Namely:

$$\vec{J} = J_y \hat{j} = -\frac{1}{\mu_0}\left(\frac{\partial B_z}{\partial x} - \frac{\partial B_x}{\partial z}\right)\hat{j} \tag{C.112}$$

In the case where the slab is infinite also along z, then the B_x component becomes zero by symmetry and only the first term survives, which is the case analyzed in section A. However, when considering the thin strip ($d << a$), the second term plays the most relevant role.

This term originates from the flux lines being wrapped around the sample, causing a discontinuity of B_x between the top and bottom surfaces:

$$B_x\left(x, z = -\frac{d}{2}\right) = -B_x\left(x, z = \frac{d}{2}\right) \tag{C.113}$$

The continuity of such tangential component on the top and bottom surfaces is guaranteed by a very high gradient $\partial B_x/\partial z$ across the sample thickness. As it happens, the first term on the RHS of Eq. C.112 is proportional to $1/a$, which is negligible with respect to the second, proportional to $1/d$. This is due to the strong demagnetization

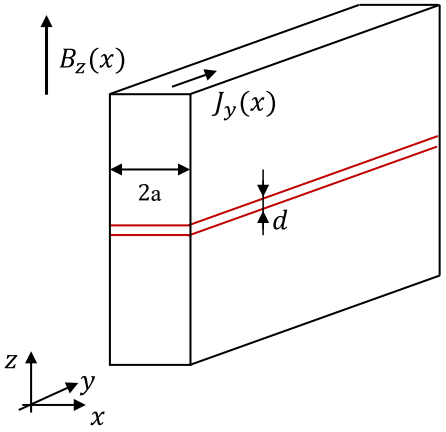

FIGURE C.6: Schematics of a slab and strip that are infinite along y. The magnetic field is oriented along the vertical direction, z.

effects occurring in the thin strip geometry, which expels the field lines from the edges of the strip.

In [128], Ampere's law is used to compute the parallel component of the field to the strip resulting from a transport current, as:

$$\vec{\nabla} \times \vec{B} = \mu_0 \vec{J} \tag{C.114}$$

Integrating:

$$\int_S (\vec{\nabla} \times \vec{B}) \cdot d\vec{S} = \mu_0 \int_S \vec{J} \cdot d\vec{S} \tag{C.115}$$

The RHS becomes:

$$\oint_l \vec{B} \cdot d\vec{l} = \mu_0 I \tag{C.116}$$

Then,

$$\oint_l \vec{B} \cdot d\vec{l} = \left(2aB_{//}\right) \cdot 2 \tag{C.117}$$

Continuing:

$$4a \cdot B_{\parallel} = 4a \cdot B_x \left(x; \frac{d}{2}\right) = \mu_0 I \tag{C.118}$$

which gives,

$$B_x \left(x; \frac{d}{2}\right) = \frac{\mu_0 I}{4a} \tag{C.119}$$

and:

$$B_x \left(x; \frac{d}{2}\right) = \frac{1}{2}\mu_0 \left(\frac{I}{2a}\right) = \frac{1}{2}\mu_0 J_y(x) \tag{C.120}$$

Finally:

$$B_x\left(x;\frac{d}{2}\right)=\frac{1}{2}\mu_0 J_y(x) \tag{C.121}$$

One can write:

$$J_y(x)=\frac{1}{\mu_0 d}\left[B_x\left(x,z=-\frac{d}{2}\right)-B_x\left(x,z=\frac{d}{2}\right)\right] \tag{C.122}$$

Eq. C.121 is important, in the sense that the parallel field component is completely determined by the closest current path (local relationship). This means that measuring B_x, the current distribution is immediately known: $J(x)=2B_x(x)/\mu_0$.

Instead, the perpendicular component of the field, Eq. C.96, is generated by all current paths (non-local relationship). If B_z is measured, Eq. C.96 must be inverted to obtain I. This means that one has to find the current distribution which at the specimen surface generates a perpendicular field B_z that vanishes everywhere except at a given position $(x-x')$. This problem is solved using the method of complex functions, and the solution is: [127], [129]:

$$I(x)=\frac{2}{\pi}\int_{-a}^{a}\frac{B_z(x')}{x-x'}\sqrt{\frac{a^2-x'^2}{a^2-x^2}}dx' \tag{C.123}$$

For a uniform applied field, $B_a << \mu_0 J_c$, this gives the current profile that screens the field from the interior of the strip. Namely $B(x)=0$ for $-a<x<a$, which is achieved by the shielding current:

$$I(x)=\frac{2xB_a}{\mu_0\sqrt{a^2-x^2}} \tag{C.124}$$

Here, we present the method for computing the current and field distribution in the strip.

C.2.1 Shielding current in response to the edge critical current

Let us consider an external transverse field, $B_a=\mu_0 H_a$, to a superconducting strip. The critical state of a thin strip is set up such that the full critical current density flows at $\pm J_c=\pm I_c/2a$ from the edges to establish a field-free region of width $2b<2a$ in the central part of the strip.

A shielding current is necessary in the field-free region to compensate for the field generated by the edge current itself. This can be obtained as for the case of the transport current, while allowing the critical current flowing in opposite directions at the edges. Let us remind that for a source current $+I$ located in $(x_0; 0)$, the shielding current is given by Eq. C.40:

$$J_s(R;\theta)|_{x_0} = -\frac{I}{2\pi R} \cdot \frac{x_0^2 - R^2}{x_0^2 + R^2 - 2Rx_0 cos\theta} \tag{C.125}$$

In this case, we locate a source current $-I$ in $(-x_0, 0)$ and its associated image current $+I$ in $(-R^2/x_0, 0)$.

The shielding current corresponding to this second pair of source and image currents is:

$$J_s(R;\theta)|_{-x_0} = \frac{I}{2\pi R} \cdot \frac{x_0^2 - R^2}{x_0^2 + R^2 + 2Rx_0 cos\theta} \tag{C.126}$$

Summing up the two:

$$J_{tot} = \frac{I}{2\pi R}(x_0^2 - R^2)\left\{ \frac{1}{x_0^2 + R^2 - 2Rx_0 cos\theta} - \frac{1}{x_0^2 + R^2 + 2Rx_0 cos\theta} \right\} \tag{C.127}$$

$$\tag{C.128}$$

$$= \frac{I}{2\pi R}(x_0^2 - R^2)\left\{ \frac{-4Rx_0 cos\theta}{(x_0^2 + R^2)^2 - (2Rx_0 cos\theta)^2} \right\} \tag{C.129}$$

$$\tag{C.130}$$

$$= -\frac{I}{\pi}(x_0^2 - R^2)\frac{2Rx_0 cos\theta}{(x_0^2 + R^2)^2 - (2Rx_0 cos\theta)^2} \tag{C.131}$$

As in the previous case, we want to transform into the Joukowski plane.

$$x_0 = u_0 + \sqrt{u_0^2 - R^2} \tag{C.132}$$

Elevating to the square:

$$x_0^2 = u_0^2 + (u_0^2 - R^2) + 2u_0\sqrt{u_0^2 - R^2} \tag{C.133}$$

$$= 2u_0^2 + 2u_0\sqrt{u_0^2 - R^2} - R^2 \tag{C.134}$$

Then:

$$x_0^2 + R^2 = 2u_0\left[u_0 + \sqrt{u_0^2 - R^2}\right] \tag{C.135}$$

also:

$$x_0^2 - R^2 = 2u_0\left[u_0^2 + u_0\sqrt{u_0^2 - R^2} - R^2\right] \tag{C.136}$$

$$= 2\sqrt{u_0^2 - R^2}\left[u_0 + \sqrt{u_0^2 - R^2}\right] \tag{C.137}$$

Substituting into Eq. C.131:

$$J_{s,tot} = -\frac{I}{\pi}2\sqrt{u_0^2 - R^2}\left[u_0 + \sqrt{u_0^2 - R^2}\right]\cdot \tag{C.138}$$

$$\frac{2R\left[u_0 + \sqrt{u_0^2 - R^2}\right]cos\theta}{4u_0^2\left[u_0 + \sqrt{u_0^2 - R^2}\right]^2 - 4R^2cos^2\theta\left[u_0 + \sqrt{u_0^2 - R^2}\right]^2} \tag{C.139}$$

$$\tag{C.140}$$

$$= -\frac{I}{\pi}\frac{cos\theta\sqrt{u_0^2 - R^2}}{u_0^2 - R^2cos^2\theta} \tag{C.141}$$

Then, we notice that $u = Rcos\theta$, and reversing: $cos\theta = u/R$. This becomes:

$$J_{s,tot} = -\frac{I}{\pi R}\frac{u\sqrt{u_0^2 - R^2}}{u_0^2 - u^2} \tag{C.142}$$

Let us recall that the change of plane implies the conservation of current:

$$J(u)du = J(z)dz \tag{C.143}$$

giving Eq. C.75:

$$J(u) = -J(z)\frac{R}{\sqrt{R^2 - u^2}} \tag{C.144}$$

Eq. C.142 becomes:

$$J_{s,tot}(u) = -\frac{I}{\pi R}\frac{u\sqrt{u_0^2 - R^2}}{u_0^2 - u^2}\left[- \frac{R}{\sqrt{R^2 - u^2}}\right] \tag{C.145}$$

$$= \frac{I}{\pi}\frac{u\sqrt{u_0^2 - R^2}}{\sqrt{R^2 - u^2}(u_0^2 - u^2)} \tag{C.146}$$

This must be integrated between $R = q$ and a. As in the previous case, we note that the current $+I$ is rather a current density, A/m, and by symmetry, we multiply by 2.

$$J_{s,tot}(u) = \frac{J}{\pi\sqrt{q^2 - u^2}} \cdot 2u \int_q^a \frac{\sqrt{u_0^2 - q^2}}{u_0^2 - u^2} du_0 \tag{C.147}$$

Let us note that:

$$\frac{\sqrt{u_0^2 - q^2}}{u_0^2 - u^2} = \frac{1}{\sqrt{u_0^2 - q^2}} - \frac{q^2 - u^2}{(u_0^2 - u^2)\sqrt{u_0^2 - q^2}} \tag{C.148}$$

Therefore:

$$\int_q^a \frac{\sqrt{u_0^2 - q^2}}{u_0^2 - u^2} = \int_q^a \left\{ \frac{1}{\sqrt{u_0^2 - q^2}} - \frac{q^2 - u^2}{(u_0^2 - u^2)\sqrt{u_0^2 - q^2}} \right\} du_0 \tag{C.149}$$

Then:

$$\int_q^a \frac{\sqrt{u_0^2 - q^2}}{u_0^2 - u^2} = ln\left[u_0 + \sqrt{u_0^2 - q^2}\right]\Big|_q^a - \int_q^a \frac{q^2 - u^2}{(u_0^2 - u^2)\sqrt{u_0^2 - q^2}} du_0 \tag{C.150}$$

$$= ln\left\{ \frac{a + \sqrt{a^2 - q^2}}{q} \right\} - \int_q^a \frac{q^2 - u^2}{(u_0^2 - u^2)\sqrt{u_0^2 - q^2}} du_0 \tag{C.151}$$

$$\tag{C.152}$$

Substituting:

$$\mu = \frac{u}{u_0}\sqrt{\frac{u_0^2 - q^2}{q^2 - u^2}} \tag{C.153}$$

deriving:

$$\frac{d\mu}{du_0} = \frac{u}{\sqrt{q^2-u^2}} \cdot \frac{d}{du_0}\left\{\frac{\sqrt{u_0^2-q^2}}{u_0}\right\} \tag{C.154}$$

$$= \frac{u}{\sqrt{q^2-u^2}} \frac{\frac{1}{2\sqrt{u_0^2-q^2}} \cdot 2u_0 \cdot u_0 - \sqrt{u_0^2-q^2}}{u_0^2} \tag{C.155}$$

$$= \frac{u}{\sqrt{q^2-u^2}} \cdot \frac{q^2}{u_0^2\sqrt{u_0^2-q^2}} \tag{C.156}$$

Also,

$$\frac{1}{1+\mu^2} = \frac{1}{1+\frac{u^2}{u_0^2}\frac{u_0^2-q^2}{q^2-u^2}} \tag{C.157}$$

$$\tag{C.158}$$

$$= \frac{u_0^2(q^2-u^2)}{u_0^2(q^2-u^2)+u^2(u_0^2-q^2)} \tag{C.159}$$

$$\tag{C.160}$$

$$= \frac{u_0^2(q^2-u^2)}{q^2(u_0^2-u^2)} \tag{C.161}$$

and:

$$\frac{d}{du_0}\left[arctg(\mu)\right] = \frac{1}{1+\mu^2}\frac{d\mu}{du_0} \tag{C.162}$$

$$\tag{C.163}$$

$$= \frac{u_0^2(q^2-u^2)}{q^2(u_0^2-u^2)} \cdot \frac{u}{\sqrt{q^2-u^2}} \cdot \frac{q^2}{u_0^2\sqrt{u_0^2-q^2}} \tag{C.164}$$

$$\tag{C.165}$$

$$= \frac{u\sqrt{q^2-u^2}}{(u_0^2-u^2)\sqrt{u_0^2-q^2}} \tag{C.166}$$

this is the integral in Eq. C.152. In fact,

$$J_{s,tot}(u) = \frac{J}{\pi\sqrt{q^2-u^2}} \cdot 2u \int_q^a \frac{\sqrt{u_0^2-q^2}}{u_0^2-u^2} du_0 \tag{C.167}$$

$$= \frac{2J \cdot u}{\pi\sqrt{q^2-u^2}} \cdot \int_q^a \left\{ \frac{1}{\sqrt{u_0^2-q^2}} - \frac{q^2-u^2}{(u_0^2-u^2)\sqrt{u_0^2-q^2}} \right\} du_0 \tag{C.168}$$

$$= \frac{2J \cdot u}{\pi\sqrt{q^2-u^2}} \cdot \int_q^a \frac{du_0}{\sqrt{u_0^2-q^2}} - \frac{2J}{\pi} \cdot \int_q^a \frac{u\sqrt{q^2-u^2}}{(u_0^2-u^2)\sqrt{u_0^2-q^2}} du_0 \tag{C.169}$$

$$= \frac{2J \cdot u}{\pi\sqrt{q^2-u^2}} \cdot ln\left[\frac{a+\sqrt{a^2-q^2}}{q}\right] - \frac{2J}{\pi}\int_q^a \frac{d}{du_0}[arctg(\mu)]du_0 \tag{C.170}$$

$$\tag{C.171}$$

The second term is:

$$-\frac{2J}{\pi}\int_q^a \frac{d}{du_0}[arctg(\mu)]du_0 = -\frac{2J}{\pi}\int_q^a d\left[arctg\left(\frac{u}{u_0}\sqrt{\frac{u_0^2-q^2}{q^2-u^2}}\right)\right] \tag{C.172}$$

$$= -\frac{2J}{\pi} arctg\left(\frac{u}{a}\frac{\sqrt{a^2-q^2}}{\sqrt{q^2-u^2}}\right) \tag{C.173}$$

Finally:

$$J_{s,tot}(u) = \frac{2J \cdot u}{\pi\sqrt{q^2-u^2}} \cdot ln\left[\frac{a+\sqrt{a^2-q^2}}{q}\right] - \frac{2J}{\pi} arctg\left(\frac{u}{a}\frac{\sqrt{a^2-q^2}}{\sqrt{q^2-u^2}}\right) \tag{C.174}$$

which is the shielding current in the field-free region, originating in response to the critical current density, J_c, at the edges of the strip. In turn, this is a consequence of the external applied field.

C.2.2 Shielding current in response to the applied field

The current distribution in Eq. C.174 shields the flux-free region of the strip from the critical current generated at the strip edges in response to the external field. An additional current distribution, $J_a(u)$, is needed in the field-free region to cancel the applied field and also to eliminate the singularity given by the logarithmic term in the shielding current, at $|u| = q$.

As we know already from Eq. C.96, the field produced by a current distribution $J_a(u)$ is:

$$B_z(u) = \frac{\mu_0}{2\pi}\int_{-q}^{+q}\frac{J_a(u_0)}{u-u_0}du_0 \tag{C.175}$$

This can be inverted as [131]:

$$J_a(u) = \frac{2}{\pi\mu_0}\int_{-q}^{+q}\frac{B_z(u_0)}{u_0-u}\sqrt{\frac{q^2-u_0^2}{q^2-u^2}}\,du_0 \tag{C.176}$$

If the field is uniform, $B_z(u_0) = \mu_0 H_a$, then:

$$J_a(u) = \frac{2\mu_0 H_a}{\pi\mu_0\sqrt{q^2-u^2}}\int_{-q}^{+q}\frac{\sqrt{q^2-u_0^2}}{u_0-u}du_0 \tag{C.177}$$

$$\tag{C.178}$$

$$= \frac{2uH_a}{\sqrt{q^2-u^2}} \tag{C.179}$$

The resulting current distribution is:

$$J_{overall}(u) = J_{s,tot}(u) + J_a(u) \tag{C.180}$$

$$= -\frac{2J}{\pi}arctg\left[\frac{u}{a}\frac{\sqrt{a^2-q^2}}{\sqrt{q^2-u^2}}\right] \tag{C.181}$$

Eq. C.181 happens by setting:

$$\frac{2uH_a}{\sqrt{q^2-u^2}} = \frac{2J\cdot u}{\pi\sqrt{q^2-u^2}}\cdot ln\left[\frac{a+\sqrt{a^2-q^2}}{q}\right] \tag{C.182}$$

therefore:

$$\frac{H_a}{J/\pi} = ln\left[\frac{a}{q}+\sqrt{\left(\frac{a}{q}\right)^2-1}\right] \tag{C.183}$$

Let us note that:

$$arccosh(x) = ln\left(x+\sqrt{x^2-1}\right) \tag{C.184}$$

Therefore:

$$\frac{H_a}{J/\pi} = arccosh\left(\frac{a}{q}\right) \tag{C.185}$$

if $I = I_c$, then we have also $J_c = I_c/2a$,

$$\frac{H_a}{J_c/\pi} = arccosh\left(\frac{a}{q}\right) \tag{C.186}$$

Then, $J_c/\pi = H_c$, the critical field strength, and:

$$\frac{H_a}{H_c} = arccosh\left(\frac{a}{q}\right) \tag{C.187}$$

Reversing:

$$\frac{a}{q} = cosh\left(\frac{H_a}{H_c}\right) \tag{C.188}$$

Finally:

$$q = \frac{a}{cosh\left(\frac{H_a}{H_c}\right)} \tag{C.189}$$

This is the expression for the penetration depth as a function of the applied field, $\mu_0 H_a$. The current density is given by:

$$J_y(x) = \begin{cases} +J_c & , -a \leq x < -a' \\ -2\frac{J_c}{\pi} arctg\left[\frac{x}{a}\frac{\sqrt{a^2-q^2}}{\sqrt{q^2-x^2}}\right] & , -a' \leq x \leq a' \\ -J_c & , a' < x \leq a \end{cases} \tag{C.190}$$

which is shown in Fig. C.7. The net field is obtained by the integration of:

$$B_z(x) = B_{ext} + \frac{\mu_0}{2\pi}\int_{-a}^{+a} \frac{J_y(x')}{x'-x} dx' \tag{C.191}$$

bringing to:

$$B_z(x) = \begin{cases} 0, & |x| \leq q \\ \dfrac{J_c}{\pi} \cdot ln \dfrac{|x|\sqrt{a^2 - q^2} + a\sqrt{x^2 - q^2}}{q\sqrt{|x^2 - a^2|}}, & |x| \geq q \end{cases} \tag{C.192}$$

which is displayed in Fig. C.8. This analytical solution shows that the penetrating flux front has a vertical slope. Fig. C.7 and Fig. C.8 demonstrate that the slab and the strip react in a very different way in response to an external field. The critical region is characterized by $J = J_c$ for both geometries. The field (vortex)-free region, is current-free in the case of the slab, whereas the current density is continuous and non-zero in the strip.

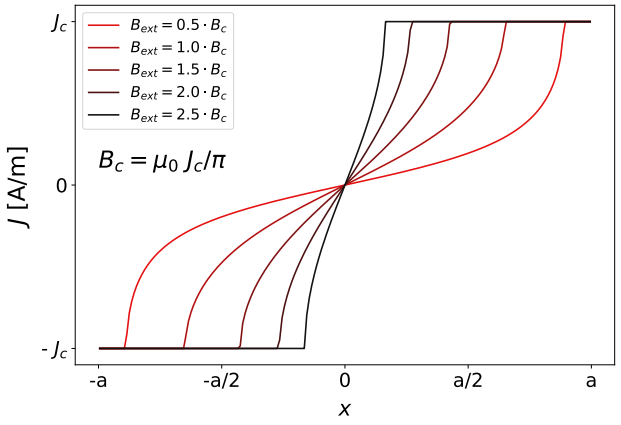

FIGURE C.7: Current distribution in response to an external field perpendicular to the strip.

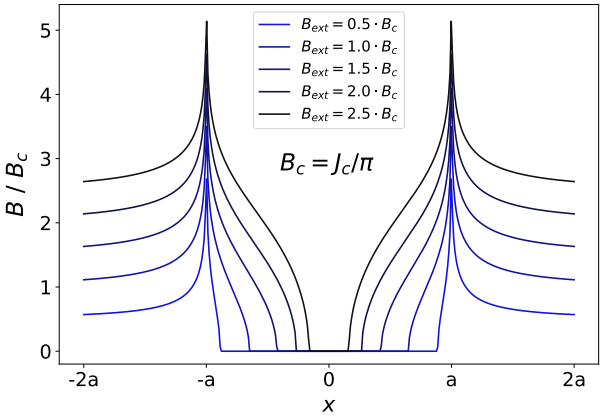

FIGURE C.8: Field distribution in response to an external field perpendicular to the strip.

In addition, the penetration depth is linear in the slab geometry, Eq. A.13, while strongly non-linear in the strip:

$$q = \frac{a}{cosh\left(\frac{B_{ext}}{B_c}\right)} \tag{C.193}$$

where $B_c = \mu_0 J_c / \pi$. Finally, the magnetization is given by:

$$\frac{M}{M_{max}} = -\sqrt{1 - \left(\frac{q}{a}\right)^2} = -tgh\left(\frac{B_{ext}}{B_c}\right) \tag{C.194}$$

The magnetization losses of a strip with finite thickness b are given by [127]:

$$Q = 4a^2 b\ J_c B_{ext}^{max}\ g(x) \tag{C.195}$$

expressed in $\mathrm{J/m^2}$, where

$$g(x) = \frac{2}{x}\ ln\Big[cosh(x) - tgh(x)\Big] \tag{C.196}$$

with $x = B_{ext}^{max} / B_c$ and $B_c = \mu_0 J_c / \pi$.

C.2.3 Current distribution across the thickness

Note that the currents described in Eq. C.94 and Eq. C.190 flow in two surface layers of thickness λ, the magnetic penetration depth. In flux-free regions, one has in general that [127]:

$$j(x,y) = J(x)\frac{cosh(y/\lambda)}{2\lambda \cdot sinh(d/2\lambda)} \tag{C.197}$$

or nearly constant if the thickness $d < \lambda$.

C.2.4 Elliptical strip

If the strip is elliptical, the saturation field in the perpendicular configuration is:

$$B_{sat,\perp} = \mu_0 J_c \frac{b}{\pi}\left\{ln\left[1 + \left(\frac{a}{b}\right)^2\right] + 2\frac{a}{b}arctg\left(\frac{b}{a}\right)\right\} \tag{C.198}$$

with a and b being the major and minor axes of the ellipse. If a transport current flows through the strip, Norris' formulae for an elliptical shape and an infinitely thin strip are used:

$$Q = \frac{I_c^2 \mu_0}{\pi} \cdot \begin{cases} (1-i)ln(1-i) + (2-i)\dfrac{i}{2} & , \, ellipse \\ \\ (1-i)ln(1-i) + (1+i)ln(1+i) - i^2 & , \, strip \end{cases} \tag{C.199}$$

where $i = I_{peak}/I_c$, also equal to $I_{peak}/(J_c S_{tot})$. These formulae have been extracted from [36].

References

[1] H. K. Onnes. Investigations into the properties of substances at low temperatures, which have led, amongst other things, to the preparation of liquid helium. *Nobel Lecture*, 1913.

[2] R. Kleiner and W. Buckel. *Superconductivity, An Introduction*. Wiley-VCH, 2016.

[3] M. Cyrot and D. Pavuna. *Introduction to superconductivity and high-T_c materials*. World Scientific, 1992.

[4] M. Wilson. *Superconducting magnets*. Clarendon Press, 1983.

[5] M. Eisterer. LTS conductors. In *CAS lecture - Normal and Superconducting magnets*, 2023.

[6] D. Larbalestrier. Conductors of Nb_3Sn: what are the key issues? In *CERN academic training lectures*, 2002.

[7] C. Buzea and T. Yamashita. Review of the superconducting properties of MgB_2. *Supercond. Sci. Technol., vol. 14, no. 11, 115-146*, 2001.

[8] R. Liang et al. Lower critical fields in an ellipsoid-shaped $YBa_2Cu_3O_{6.95}$ single crystal. *Phys. Rev. B, vol. 50, no. 6*, 1994.

[9] T. Puig. High temperature superconductors. From the materials to magnet technology. In *Lecture at Applied Superconductivity Conference*, 2024.

[10] F. Kametani et al. Bubble formation within filaments of melt-processed Bi2212 wires and its strongly negative effect on the critical current density. *Supercond. Sci. Technol., vol. 24, Art no. 075009*, 2011.

[11] T. Shen et al. Stable, predictable and training-free operation of superconducting Bi-2212 Rutherford cable racetrack coils at the wire current density of 1000 A/mm^2. *Scientific Reports, vol. 9, Art. no. 10170*, 2019.

[12] X. Ma et al. Rolling characteristics of multi-filamentary Bi-2223/AgAu tapes and roller diameter's effect on transport properties. *Cryogenics, vol. 127, Art no. 103549*, 2022.

[13] J. L. MacManus-Driscoll and S. C. Wimbush. Processing and application of high-temperature superconducting coated conductors. *Nature Reviews, Materials, vol. 6*, 2021.

[14] S.R. Foltyn et al. Material science challenges for high-temperature superconducting wire. *Nature materials, vol. 6, pp. 631-642*, 2007.

[15] B. Ma et al. Inclined-substrate deposition of biaxially textured magnesium oxide thin films for YBCO coated conductors. *Physica C, vol. 366, no. 4, pp. 270-276*, 2002.

[16] C. Barth, G. Mondonico, and C. Senatore. Electro-mechanical properties of RE-BCO coated conductors from various industrial manufacturers at 77 K, self-field and 4.2 K, 19 T. *Supercond. Sci. Techn., vol. 28, Art. no. 045011*, 2015.

[17] Y. Li et al. Progress of REBCO coated conductor program SJTU and SSTC. *IEEE Trans. Appl. Supercond., vol. 28, no. 4*, 2018.

[18] Fujikura. Online website, introduction of Fujikura RE-based HTS wire. *www.fujikura.com*, 2024.

[19] A. Sundaram et al. 2G HTS wires made on 30 μm thick Hastelloy substrate. *Supercond. Sci. Technol., vol. 29, Art. no. 104007*, 2016.

[20] J.-H. Lee et al. RCE-DR, a novel process for coated conductor fabrication with high performance. *Supercond. Sci. Technol., vol. 27, Art. no. 044018*, 2014.

[21] FCC. Online website. *https://fcc.web.cern.ch/*, 2025.

[22] M. Daibo. Recent advances of 2G HTS wires and coils at Fujikura. *Workshop on advanced superconducting materials and magnets*, 2019.

[23] A. Xu et al. Role of weak uncorrelated pinning introduced by $BaZrO_3$ nanorods at low temperature in (Y,Gd)$Ba_2Cu_3O_x$ thin films. *Physical Review B, vol. 86, Art. no. 115416*, 2012.

[24] A. Molodyk et al. Development and large volume production of extremely high current density $YBa_2Cu_3O_7$ superconducting wires for fusion. *Scientific Reports, vol. 11*, 2021.

[25] S. Kang et al. Flux-pinning characteristics as a function of density of columnar defects comprised of self-assembled nanodots and nanorods in epitaxial $YBa_2Cu_3O_{7-\delta}$ films for coated conductor applications. *Physica C, vol. 457, 41-46*, 2007.

[26] L. Civale et al. Influence of crystalline texture on vortex pinning near the ab-plane in $YBa_2Cu_3O_7$ thin films and coated conductors. *Physica C: Superconductivity, vol. 412-414, pp. 976-982*, 2004.

[27] A. I. Golovashkin et al. Low temperature direct measurements of $H_{c,2}$ in HTSC using megagauss magnetic fields. *Physica C: Supercon., vol. 185-189, pp. 1859-1860*, 1991.

[28] D. J. Gameiro Carvalho. Master's degree thesis. *University of Lisbon*, 2023.

[29] G. Succi, A. Ballarino, S. C. Hopkins, C. Barth, and Y. Yang. Magnetic field and temperature scaling of the critical current of REBCO tapes. *IEEE Trans. Appli. Supercond., vol. 34, no. 3*, 2024.

[30] G. Succi, A. Ballarino, S. C. Hopkins, and Y. Yang. Experimental validation of a scaling law for the critical current of commercial REBCO tapes as a function of magnetic field and temperature. *IEEE Trans. Appli. Supercond., vol. 35, no. 5*, 2025.

[31] P. Mangin and R. Kahn. *Superconductivity. An Introduction*. Springer, 2017.

[32] William L. Goodman and Bascom S. Deaver. Detailed measurements of the quantized flux states of hollow superconducting cylinders. *Phys. Rev. Lett., vol.24, no. 16, pp. 870-873*, 1970.

[33] B. B. Goodman. Simple model for the magnetic behaviour of superconductors of negative surface energy. *Phys. Rev. Lett., vol. 6, no. 11, pp. 597-599*, 1961.

[34] P. G. De Gennes. Superconductivity of metals and alloys. *Persus Books*, 1966.

[35] C. P. Bean. Magnetization of high-field superconductors. *Rev. Mod. Physics, vol.36, iss. 1, pp. 31-39*, 1964.

[36] M. Breschi and A. Morandi. Course on superconducting magnets engineering. *University of Bologna, Faculty of Engineering and Architecture*, 2018.

[37] D. Dew-Hughes. Model for flux creep in high t_c superconductors. *Cryogenics, vol. 28*, 1988.

[38] J. Nagamatsu et al. Superconductivity at 39 K in magnesium diboride. *Nature, vol. 410, 63-64*, 2001.

[39] J. G. Bednorz and K. A. Mueller. Possible high T_c superconductivity in the Ba-La-Cu-O system. *Z. Phys. B - Condensed Matter, vol. 64, pp. 189-193*, 1986.

[40] H. Nakagawa et al. The upper critical field and the normal-state resistivity of $YBa_2Cu_3O_{7-\delta}$ thin films in megagauss magnetic fields. *J. Phys.: Condens. Matter, vol. 10, Art. no. 11571*, 2007.

[41] T. Sekitani et al. Measurement of the upper critical field of optimally-doped $YBa_2Cu_3O_{7-\delta}$ in megagauss magnetic fields. *New J. Phys, vol. 9, no. 47*, 2007.

[42] D. C. Larbalestier. Isotropic round-wire multifilament cuprate superconductor for generation of magnetic fields above 30 T. *Nature materials, vol. 13, pp. 375-381*, 2014.

[43] T. Shen et al. Development of high critical current density in multifilamentary round-wire overdoping. *Appl. Phys. Lett., vol. 95, Art. no. 152516*, 2009.

[44] T. Hikata et al. Ag-sheated Bi-Pb-Sr-Ca-Cu-O superconducting wires with high critical current density. *Jpn. J. Appl. Phys., vol. 28, L82*, 1989.

[45] G. Osabe et al. Ni alloy laminated high strength Bi-2223 wire. *SEI technical review, no. 84*, 2017.

[46] T. Puig, J. Gutierrez, and X. Obradors. Impact of high growth rates on the microstructure and vortex pinning of high-temperature superconducting coated conductors. *Nature Reviews Physics, vol. 6, 132-138*, 2024.

[47] D. P. Norton et al. Epitaxial $YBa_2Cu_3O_7$ on biaxially textured nickel (001): an approach to superconducting tapes with high critical current densities. *Science, vol. 274, pp. 575-577*, 1996.

[48] J. Dzick et al. Ion-beam-assisted texturing of YSZ layers. *Physica C, 372-376*, 2002.

[49] M. Bauer et al. Biaxially aligned MgO buffer layers using electron beam evaporation on inclined substrates. *Advances in Superconductivity X*, 1998.

[50] X. Xiong et al. High throughput processing of long-length IBAD MgO and epi-buffer templates at SuperPower. *IEEE Trans. Appl. Supercond., vol. 17, no. 2*, 2007.

[51] A. P. Malozemoff et al. Low-cost YBCO coated conductor technology. *Supercond. Sci. Technol., vol. 13, 473-476*, 2000.

[52] R. Batulin et al. The physical properties of Hastelloy C-276 and Hastelloy C-276 with $Al_2O_3/Y_2O_3/MgO$, $LaMnO_3$ buffer layers down to cryogenic temperatures for applications in superconducting magnets. *Cryogenics, vol. 137, Art. no. 103776*, 2024.

[53] A. Usoskin et al. Long HTS coated conductor processed via large-area PLD/ABAD for high-field applications. *IEEE Trans. Appl. Supercond., vol. 26, no. 3*, 2016.

[54] G. Jiang. Recent development and mass production of high J_{eng} 2G-HTS tapes by using thin hastelloy substrate at Shanghai Superconductor Technology. *Supercond. Sci. Technol., vol. 33, Art no. 074005*, 2020.

[55] V. Chepikov et al. Introduction of $BaSnO_3$ and $BaZrO_3$ artificial pinning centres into 2G HTS wires based on PLD-GdBCO films. Phase I of the industrial R&D programme at SuperOx. *Supercond. Sci. Technol., vol. 30, Art. no. 124001*, 2017.

[56] R. Pratap et al. Growth of high-performance thick film REBCO tapes using advanced MOCVD. *IEEE Trans. Appl. Supercond., vol. 29, no. 5*, 2019.

[57] M. W. Rupich et al. Advances in second generation high temperature superconducting wire manufacturing and R&D at American Superconductor corporation. *Supercond. Sci. Technol., vol. 23, Art. no. 014015*, 2010.

[58] A. Usoskin et al. Long HTS tapes with high in-field performance manufactured via multibeam PLD with 'dynamic' drum concept. *IEEE Trans. Appl. Supercond., vol. 27, no. 4*, 2017.

[59] Y. Zhao. Progress in fabrication of second generation high temperature superconducting tape at Shanghai Superconductor Technology. *Supercond. Sci. Technol., vol. 32, Art no. 044004*, 2019.

[60] H. Kutami. Progress in research and development on long length coated conductors in Fujikura. *Physica C, vol. 469, pp. 1290-1293*, 2009.

[61] Y. Iijima et al. Development for mass production of homogeneous RE123 coated conductors by hot-wall PLD process on IBAD template technique. *Physica C, vol. 469, pp. 1290-1293*, 2014.

[62] Subra. Online website. *www.subra.dk*, 2024.

[63] G. Blatter et al. Vortices in high-temperature superconductors. *Rev. Mod. Phys., vol. 66, 1125*, 1994.

[64] D. R. Nelson and V. M. Vinokur. Boson localization and correlated pinning of superconducting vortex arrays. *Phys. Rev. B, vol. 48, 13060*, 1993.

[65] E. D. Specht et al. Stacking faults in $Y\,Ba_2\,Cu_3\,O_{7-x}$: Measurement using X-ray diffraction and effects on critical current. *Appl. Phys. Lett., vol. 89, Art. no. 162510*, 2006.

[66] B. Dam et al. Origin of high critical currents in $YBa_2Cu_3O_{7-\delta}$ superconducting thin films. *Nature, vol. 399*, 1999.

[67] S. R. Foltyn, H. Wang, L. Civale, B. Maiorov, and Q. X. Jia. The role of interfacial defects in enhancing the critical current density of $YBa_2Cu_3O_7$ coatings. *Supercond. Sci. Technol., vol. 22, no. 12, Art. no. 125002*, 2009.

[68] Ch. Jooss et al. Vortex pinning due to strong quasiparticle scattering at antiphase boundaries in $YBa_2Cu_3O_{7-\delta}$. *Phys. Rev. Lett., vol. 82, no. 3*, 1999.

[69] Y. Chen et al. Enhanced flux pinning by $BaZrO_3$ and $(Gd,Y)_2O_3$ nanostructures in metal organic chemical vapor deposited GdYBCO high temperature superconductor tapes. *Applied Physics Letters, vol. 94, Art. no. 062513*, 2009.

[70] T. Haugan et al. Addition of nanoparticle dispersions to enhance flux pinning of the $YBa_2Cu_3O_{7-\delta}$ superconductor. *Nature, vol. 430, pp. 867-870*, 2004.

[71] S. Zhang et al. Broad temperature study of RE-substitution effects on the in-field critical current behavior of REBCO superconducting tapes. *Supercond. Sci. Technol., vol. 31, Art. no. 125006*, 2018.

[72] J. A. Demko et al. Triaxial HTS cable for the AEP bixby project. *IEEE Trans. Appl. Supercond., vol. 17, no. 2*, 2007.

[73] H. Yumura et al. Phase II of the Albany HTS cable project. *IEEE Trans. Appl. Supercond., vol. 19, no. 3*, 2009.

[74] D. C. van der Laan. Compact $GdBa_2Cu_3O_{7-\delta}$ coated conductor cables for electric power transmission and magnet applications. *Supercond. Sci. Techn., vol. 24, Art. no. 042001*, 2011.

[75] A. Ballarino. Development of superconducting links for the LHC machine. *Supercond. Sci. Techn., vol. 27, Art. no. 044024*, 2014.

[76] Nexans. Online website. *www.nexans.com*, 2022.

[77] T. Winkler. The EcoSwing project. *Materials Science Engineering, vol. 502, Art. no. 012004*, 2019.

[78] H.-W. Lee, K.-C. Kim, and J. Lee. Review of Maglev train technologies. *IEEE Trans. Magnet., vol. 42, no. 7*, 2006.

[79] Central Japan Railway company. Online website. *https://scmaglev.jr-central-global.com/*, 2024.

[80] Lilit Marcus. China debuts train prototype that can hit speeds of 620 kilometers per hour. *CNN*, 2021.

[81] Bruker. Online website. *www.bruker.com*, 2022.

[82] W. D. Markiewicz et al. Design of a superconducting 32 T magnet with REBCO high field coils. *IEEE Trans. Appl. Supercond., vol. 22, no. 3*, 2012.

[83] H. W. Weijers et al. Progress in the development and construction of a 32-T superconducting magnet. *IEEE Trans. Appl. Supercond., vol. 26, no. 4*, 2016.

[84] S. Hahn et al. 45.5-Tesla direct-current magnetic field generated with a high-temperature superconducting magnet. *Nature, vol. 570*, 2019.

[85] B. N. Sorbom et al. ARC: A compact, high-field, fusion nuclear science facility and demonstration power plant with demountable magnets. *Fusion Engineering and Design, vol. 100, pp. 378-405*, 2015.

[86] A. Sykes et al. Compact fusion energy based on the spherical tokamak. *Nuclear Fusion, vol. 58, Art. no. 016039*, 2018.

[87] D. A. Gates et al. Recent advances in stellator optimization. *Nuclear Fusion, vol. 57, Art. no. 126064*, 2017.

[88] M. Benedikt et al. Future circular colliders succeeding the LHC. *Nature Physics, vol. 16, pp. 402-407*, 2020.

[89] M. Xiao et al. Study of CEPC performance with different collision energies and geometric layouts. *Chinese Physics C, vol. 40, Art. no. 087001*, 2016.

[90] E. Todesco. Status and perspectives in high field superconducting magnets for particle accelerators. *Plenary session at Applied Superconductivity Conference*, 2024.

[91] H. C. Freyhardt. YBaCuO and REBaCuO HTS for applications. *Int. J. Appl. Ceram. Technol., vol. 4, no. 3, pp. 203-216*, 2007.

[92] P. Bruzzone et al. High temperature superconductors for fusion magnets. *Nucl. Fusion, vol. 58, no. 10, Art. no. 103001*, 2018.

[93] J. J. Himbele, A. Badel, and P. Tixador. HTS dipole magnet for a particle accelerator using a twisted-stacked cable. *IEEE Trans. Appl. Supercond., vol. 26, no. 3, Art. no. 4005205*, 2016.

[94] L. Rossi and C. Senatore. HTS accelerator magnet and conductor development in Europe. *Instruments, vol. 5, Art. no. 8*, 2021.

[95] D. K. Hilton, A. V. Gavrilin, and U. Trociewitz. Practical fit functions for transport critical current versus field magnitude and angle data from (RE)BCO coated conductors at fixed low temperatures and in high magnetic fields. *Supercond. Sci. Technol., vol. 28, no. 7, pp. 587-604, Art. no. 074002*, 2015.

[96] C. Senatore, C. Barth, M. Bonura, M. Kulich, and G. Mondonico. Field and temperature scaling of the critical current density in commercial REBCO coated conductors. *Supercond. Sci. Technol., vol. 29, no. 1, Art. no. 014002*, 2016.

[97] A. Francis et al. Development of general expressions for the temperature and magnetic field dependence in coated conductors with variable properties. *Supercond. Sci. Technol., vol. 33, no. 4, Art. no. 044011*, 2020.

[98] E. J. Kramer. Scaling laws for flux pinning in hard superconductors. *J. Appl. Phys., vol. 44, no. 3*, 1973.

[99] J. W. Ekin. Unified scaling law for flux pinning in practical superconductors: I. Separability postulate, raw scaling data and parameterization at moderate strains. *Supercond. Sci. Technol., vol. 23, no. 8, Art. no. 083001*, 2010.

[100] J. Fleiter and A. Ballarino. Parameterization of the critical surface of REBCO conductors at Fujikura. *CERN EDMS document no. 1426239*, 2014.

[101] D. Dew-Hughes. Flux pinning mechanisms in type II superconductors. *The Philosophical Magazine: A Journal of Theoretical Experimental and Applied Physics, 30(2), 293–305*, 1974.

[102] L. Krusin-Elbaum. 'Phase diagram' of the vortex-solid phase in Y-Ba-Cu-O crystals: A crossover from single-vortex (1D) to collective (3D) pinning regimes. *Phys. Rev. Lett., vol. 69, no. 15, Art. no. 2280*, 1992.

[103] T. Nishizaki and N. Kobayashi. Vortex-matter phase diagram in $YBa_2Cu_3O_y$. *Supercond. Sci. Technol., vol. 13, no. 1, pp. 1-11, Art. no. 125002*, 2000.

[104] Robinson Research Institute, Victoria University of Wellington. High-temperature superconducting wire critical current database. *https://htsdb.wimbush.eu/*, 2014.

[105] S. C. Wimbush and N. M. Strickland. A public database of high-temperature superconductor critical current data. *IEEE Trans. Appli. Supercond., vol. 27, no. 4*, 2017.

[106] K. Tsuchiya et al. Critical current measurement of commercial REBCO conductors at 4.2 K. *Cryogenics, vol. 85, pp. 1 - 7*, 2017.

[107] K. Tsuchiya et al. Superconducting properties of commercial REBCO conductors with artificial pinning centers. *Supercond. Sci. Techn., vol. 34, no. 10, Art. no. 105005*, 2021.

[108] G. Succi. Sample holders for transport current measurements of REBCO coated conductors in perpendicular and parallel field. *CERN EDMS document no. 3223386*, 2025.

[109] G. Succi, S. C. Hopkins, A. Vande Craen, and B. Medina Clavijo. Calibration of the VSM facility at building 163. *CERN EDMS document no. 3283950*, 2025.

[110] G. Succi, S. C. Hopkins, A. Vande Craen, and B. Medina Clavijo. Operation of the VSM facility at building 163. *CERN EDMS document no. 3283949*, 2025.

[111] C. Xue et al. Field-dependent critical state of high-T_c superconducting strip simultaneously exposed to transpot current and perpendicular magnetic field. *AIP Advances 3, Art. no 122110*, 2013.

[112] J. Jiang et al. High-performance Bi-2212 round wires made with recent powders. *IEEE Trans. Appli. Supercond., vol. 29, no. 15*, 2019.

[113] R. Brambilla, F. Grilli, and L. Martini. Development of an edge-element model for AC loss computation of high-temperature superconductors. *Supercond. Sci. Techn., vol. 20, no. 1*, 2007.

[114] J. Jin. *The Finite Element Method for Electromagnetics*. New York: Wiley, 2002.

[115] B. Shen. Overview of H-formulation: A versatile tool for modeling electromagnetics in high-temperature superconductor applications. *IEEE Access, vol. 8*, 2020.

[116] Kajikawa et al. Numerical evaluation of AC losses in HTS wires with 2D FEM formulated by self magnetic field. *IEEE Trans. Appli. Supercond., vol. 13, no. 2*, 2003.

[117] J. Zhao, Y. Li, and Y. Gao. 3D simulation of AC loss in a twisted multi-filamentary superconducting wire. *Cryogenics, vol. 84, pp.60–68*, 2017.

[118] M. D. Ainslie, T. J. Flack, and A. M. Campbell. Calculating transport AC losses in stacks of high temperature superconductor coated conductors with magnetic substrates using FEM. *Physica C: Superconductivity, vol. 472, no. 1*, 2012.

[119] F. Grilli et al. Computation of losses in HTS under the action of varying magnetic fields and currents. *IEEE Transactions on Applied Superconductivity, vol. 24, no. 1*, 2014.

[120] F. Grilli, A. Morandi, F. De Silvestri, and R. Brambilla. Dynamic modeling of levitation of a superconducting bulk by coupled H-magnetic field and arbitrary lagrangian-eulerian formulations. *Superconductor Science and Technology, vol. 31, no. 12*, 2018.

[121] A. Arsenault, F. Sirois, and F. Grilli. Implementation of the H-ϕ formulation in COMSOL Multiphysics for simulating the magnetization of bulk superconductors and comparison with the H-formulation,. *IEEE Trans. Appli. Supercond., vol. 31, no. 2*, 2021.

[122] H. Zhang, M. Zhang, and W. Yuan. An efficient 3D finite element method model based on the T–A formulation for superconducting coated conductors. *Supercond. Sci. Techn., vol. 30*, 2016.

[123] N. Amemiya et al. Numerical modelings of superconducting wires for AC loss calculations. *Physica C, vol. 310*, 1998.

[124] HTS modelling workgroup. Online website. *https://htsmodelling.com*, 2018.

[125] X. Chen and G. B. Goldfarb. Kim model for magnetization in type-II superconductors. *J. Appl. Phys., vol. 66, no. 6*, 1989.

[126] E. Zeldov et al. Magnetization and transport currents in thin superconducting films. *Phys. Rev. B, vol. 49, no. 14*, 1994.

[127] E. H. Brandt and M. V. Indenbom. Type-II superconducting strip with current in perpendicular magnetic field. *Phys. Rev. B, vol. 48, no. 17*, 1993.

[128] E. H. Brandt, M. V. Indenbom, and A. Forkl. Type-II superconducting strip in perpendicular magnetic field. *Europhys. Lett., vol. 22, no. 9*, 1993.

[129] E. H. Brandt. Determination of currents in flat superconductors. *Phys. Rev. B, vol. 46, no.13*, 1992.

[130] Y. Yang. Critical states of a thin superconducting strip. *Lectures on superconudctivity, University of Southampton*, 2024.

[131] G. W. Swan. Current distribution in a thin superconducting strip. *Journal of mathematical physics, vol. 9, pp. 1308-1312*, 1968.